N-64-9

RTD-TDR-63-4096
Part I

INVESTIGATION OF BORIDE COMPOUNDS FOR VERY HIGH TEMPERATURE APPLICATIONS

TECHNICAL DOCUMENTARY REPORT NO. RTD-TDR-63-4096
Part I
December 1963

AF Materials Laboratory
Research and Technology Division
Air Force Systems Command
Wright-Patterson Air Force Base, Ohio

Project No. 7350, Task No. 735001

(Prepared under Contract No. AF33(657)-8635
by ManLabs, Inc., Cambridge, Massachusetts;
Larry Kaufman and Edward V. Clougherty, authors)

NOTICES

When Government drawings, specifications, or other data are used for any purpose other than in connection with a definitely related Government procurement operation, the United States Government thereby incurs no responsibility nor any obligation whatsoever; and the fact that the Government may have formulated, furnished, or in any way supplied the said drawings, specifications, or other data, is not to be regarded by implication or otherwise as in any manner licensing the holder or any other person or corporation, or conveying any rights or permission to manufacture, use, or sell any patented invention that may in any way be related thereto.

Qualified requesters may obtain copies of this report from the Defense Documentation Center, Cameron Station, Alexandria, Va. 22314

This report has been released to the Office of Technical Services, U.S. Department of Commerce, Washington 25, D. C., for sale to the general public.

Copies of this report should not be returned to the Research and Technology Division unless return is required by security considerations, contractual obligations, or notice on a specific document.

FOREWORD

This report was prepared by the Research Division ManLabs, Inc., with the assistance of the following subcontractors: U. S. Borax Research Corp., Lexington Laboratories, Inc. and Arthur D. Little, Inc., under J.S.A.F. Contract No. AF33(652)-8635. This contract was initiated under Project No. 7350 "Refractory, Inorganic Non-Metallic Materials" Task 735001 "Non-Graphitic". The work was administered under the direction of the A.F. Materials Laboratory, Research and Technology Division with J. D. Latva and S. A. Mersol acting as project engineers.

This report covers the period of work from April 1962 to September 1963.

ManLabs personnel participating in this study included L. Kaufman, E. V. Clougherty, H. Bernstein, L. D. Blackburn, R. Pober, J. Elling, W. Lindonen, L. Lindonen, R. Gould, C. Gallagher, S. Linowski and A. Sarney.

ABSTRACT

A comprehensive study of the properties of high purity well characterized samples of TiB_2, ZrB_2, HfB_2, NbB_2, and TaB_2 has been performed. Floating zone refining and high pressure hot pressing were used to prepare single crystal and polycrystalline material respectively. An investigation of the sintering mechanism of TiB_2 was performed. Powder purification procedures by acid leaching and vacuum heating were examined. Properties measured included lattice parameter, X-ray thermal expansion, linear thermal expansion, electrical resistivity and microhardness. These quantities were obtained for materials which satisfied the sample requirements for the various experiments. Measurements were generally performed between room temperature and 1000°C. Thermal conductivity measurements between 1000° and 2000°C are in progress. Thermal properties measured included specific heat, vapor pressure, and heat of formation. The latter is in progress. Phase boundary experiments were performed in Zr-B system and the current status of the phase diagrams of these materials was reviewed.

Kinetic studies were performed to elucidate the mechanism of oxidation and to study the nature of protective coatings which are produced by some of there materials in oxidizing atmospheres. An integrated thermodynamic analysis of the diborides was completed.

On the basis of current vapor pressure and oxidation data, HfB_2 and ZrB_2 are shown to be the most likely candidates for high temperature applications requiring oxidation resistance. The available description of the compositional dependence of the boron activity in these compounds indicates that metal-rich deviations from stoichiometry in these compounds will probably result in additional enhancement of the oxidation resistance. Other variations in composition suggested by the results of the present study include additions of Ta and Nb or Y and La. These elements might serve to impede diffusion of oxygen through the oxide surface layer. Additions of silicon to the pure diborides might also provide enhanced oxidation resistance.

This technical documentary report has been reviewed and is approved.

W. G. Ranke
Chief, Ceramics and Graphite Branch
Metals and Ceramics Division
A. F. Materials Laboratory

TABLE OF CONTENTS

LIST OF FIGURES

List of Figures (continued)

List of Figures (continued)

List of Figures (continued)

List of Figures (continued)

List of Figures (continued)

LIST OF TABLES

LIST OF TABLES (Cont'd)

List of Tables (continued)

List of Tables (continued)

List of Tables (Continued)

I. INTRODUCTION AND SUMMARY

A. Introduction

Interstitial compounds of the transition metals offer a number of attractive features as future high-strength, high-temperature materials. The advantages of these compounds stem from the strong atomic binding which are due to high packing density of atoms, i.e., small atoms such as B, C, and N occupying the interstices between the metal atoms. The combination of high bond strength with the low relative masses of the hexagonal diborides of Ti, Zr, Hf, Nb, and Ta leads to a unique series of compounds which offer the possibility of refractoriness, oxidation resistance and high strength-to-weight ratios.

Realization of the full potential of borides as future high temperature materials require a thorough knowledge of their properties and behavior under diverse conditions of temperature, environment and stress states. Although applications of these compounds may require alloying or composite structures, a rational basis for such departures requires a thorough knowledge of the properties of the pure compounds. In order to determine the factors which control the behavior of these materials an integrated research program has been designed and implemented. The basis used in designing this program is as follows:

Fully dense single phase materials of high purity must be available for this study. Measurements of the physical, thermal, and strength properties will be performed up to 1500°C. Before extending the temperature range of such measurements it is necessary to explore the oxidation behavior and the thermodynamic stability of these compounds above 1500°C. The availability of the oxidation and thermodynamic information at high temperatures will permit the design of critical high temperature property measurements. Moreover, the interpretation

---

Manuscript released by the authors October 1963 for publication as an RTD Technical Documentary Report.

of high temperature physical, mechanical, and thermal data would be greatly facilitated. This program should provide an efficient means of generating back-up data required to initiate later studies at temperature between 1500°C and the melting point. In addition, it may provide some important clues which will help indicate the types of additives which might improve the high temperature properties of these compounds.

The current phase of this investigation includes activities in the following areas: materials preparation, determination of physical and mechanical properties, oxidation studies, and thermodynamic stability studies. A very brief account of the results obtained to date is given below. More detailed descriptions of each subtask are to be found in appropriate later sections of this report. In each case the name and affiliation of the research worker responsible for the subtask is indicated on the first page of the subtask report.

B. Summary of Research Results

1. Procurement of Raw Materials and Specimen Preparation

High purity powders of all the diborides of interest were obtained, characterized, and introduced into various subtask investigations. An unsuccessful attempt was made to procure sound pyrolytically deposited diboride sheet (see Section II).

Purification studies on TiB_2 and ZrB_2 using high temperature vacuum treatment, non-oxidizing acid leaching, and fused salt leaching have been carried out. These studies produced powders containing about 99.5% metal plus boron with 0.4% oxygen as the major contaminant. Other impurities were generally present in quantities less than 0.1%.

Zone melted specimens of ZrB_2, HfB_2, NbB_2 and TaB_2 have been prepared in single crystal or coarse grained polycrystalline form. This

material, which is of high purity and is well characterized, is ideal for thermochemical studies. However the occurrence of microcracks limits the use of this material in some aspects of the program. The relatively higher vapor pressures of TiB_2 precluded specimen fabrication by this technique. High density (93-99% of theoretical), fine grained specimens of TiB_2, ZrB_2 and HfB_2 have been fabricated by high pressure hot pressing in the range 2000-2500°C and 300,000 psi. To date, NbB_2 and TaB_2 samples corresponding to 83-91% of theoretical X-ray density have been prepared. Studies of the mechanism and kinetics of sintering of TiB_2 (and to a more limited extent ZrB_2 and NbB_2) covering the range 1850 to 2500°C have been performed. These studies indicate that the limiting density is primarily dependent upon sintering temperature and that temperatures in excess of 2400°C are required to produce 90% dense specimens of pure TiB_2. This is interpreted on the basis of competing material transport by vaporization-condensation and diffusion. Additives increase the density limit at low temperatures but become less effective as the sintering temperature increases. The highest density achieved was 95% of theoretical in Cr doped TiB_2 at 2200°C.

2. Physical and Mechanical Property Measurements

Lattice parameter measurements have been made on all the diborides between room temperature and 1500°C. These data yield expansion in the "a" and "c" directions and indicate slight anisotropy, the "c" expansion being larger. In addition, measurements of the amplitude of atomic vibrations perpendicular and parallel to the basal plane in ZrB_2 and HfB_2 have been carried out yielding Debye temperatures for these compounds. The latter are compared favorably with suitable specific heat data on these compounds. Linear expansion data have been obtained on hot pressed specimens of TiB_2 and TaB_2, zone melted rods of ZrB_2 and NbB_2, and hot pressed as well as zone melted specimens of HfB_2 between

25°C and 1000°C. Expansion coefficients and anisotropy ratios derived from these measurements compare reasonably well with the X-ray expansion data. Specimens which are suitable for thermal conductivity and emissivity measurements (1000°C-2000°C) have been prepared. These measurements will be performed during the next six months and reported at a later date. Measurements of the rupture strength and modulus of bending have been similarly postponed until the next phase of this study. Measurements of the electrical resistivity of zone refined and hot pressed specimens of the diboride between 25°C and 1000°C using a variety of contact and lead-wire configurations are reported. Measurements of the hardness as a function of load have been performed for zone refined and hot pressed NbB_2 and HfB_2 and for hot pressed TiB_2 and ZrB_2 at 25°C. In addition, hardness vs. temperature data for zone refined and hot pressed ZrB_2 and HfB_2 and hot pressed TiB_2 between 25°C and 1000°C in vacuum are reported. Anisotropy of the hardness on the basal plane was noted in these studies.

3. Oxidation Studies

Data on the rate of oxygen pickup of all the pure diborides as well as a specimen of Carborundum's ZrB_2-$MoSi_2$ composite are presented covering the temperature range 1200 to 2000°K and at pressures between 10 and 40 torr oxygen pressure. These data cover the behavior of high pressure hot pressed TiB_2 and HfB_2, zone refined ZrB_2, NbB_2, TaB_2 and HfB_2 and the conventionally hot pressed ZrB_2-$MoSi_2$ composite. The oxygen pickup data have been coupled with metallographic and X-ray studies in order to derive some insight into the mechanisms controlling oxidation of the borides. The results indicate that HfB_2 is the most oxidation resistant of the pure diborides there being little difference in the behavior of the zone refined (single crystal or coarse grained) materials

and the fine grained high pressure hot pressed samples. For both HfB_2 and ZrB_2, it was found that the temperature of the monoclinic tetragonal transition in the metal dioxide is accompanied by a sharp change in oxidation behavior and/or mechanism. The low temperature monoclinic form imparted greater oxidation resistance than the high temperature tetragonal form. Measurements on the Carborundum composite at 1866°K yielded a parabolic rate constant for oxygen pickup which was five times larger than for pure HfB_2 thus indicating that this material was poorer at this temperature than HfB_2. At the same temperature, the ZrB_2-$MoSi_2$ composite was superior to pure ZrB_2. However, the important comparison between the HfB_2 and the composite remains to be made above 2000°K where the phase transition in HfO_2 takes place.

4. Studies of Thermodynamic Stability

Measurements of the specific heat of TiB_2, NbB_2 and TaB_2 are reported covering the range 5°K to 350°K. These data are presented along with similar data for ZrB_2 and HfB_2 obtained on a companion R.T.D.-sponsored program. The data have been analyzed in order to obtain a physical description of the vibrational and electronic specific heat contributions. The latter description has been used to compute the specific heats and free energy of formation functions for all the diborides up to their melting points. High purity specimens of all the diborides have been transmitted to Argonne and Los Alamos National Laboratories for measurements of the enthalpy of formation at room temperature. These measurements are to be performed using fluorine bomb and combustion calorimetry. The results will be reported at a later date. Currently available data on the enthalpy and free energy of formation of diborides have been used to develop an approximate method for estimating the enthalpy of formation. This method when coupled with the Δfef values permit calculation of the free energy of formation of all the

diborides up to their melting points. A review of binary phase diagrams between the pertinent metal components and boron is presented along with the results of diffusion couple and two-phase alloy studies in the Zr-B system. A quantitative application of the Schottky-Wagner model of compound phases to the diborides has been presented. This description permits calculation of the vapor pressures of metal and boron over the single phase diboride as a function of composition and temperature. Graphical illustration of the pressure-temperature-composition space shows the variation in congruently vaporizing composition as a function of temperature for each of the diborides. The predicted compositions for congruent vaporization of TiB_2, ZrB_2 and HfB_2 compare favorably with experimental values. Vaporization studies on Nb, two phase Nb_3B_4-NbB_2 mixtures and single phase "NbB_2" covering the composition range $NbB_{1.9}$ to $NbB_{2.1}$ have been performed. The vaporization results can be used to compute the variation in boron activity across the single phase diboride field at 2150°K. Comparison of this data with theoretical predictions yields excellent agreement.

C. Assessment of Research Results and Future Plans

The results obtained thus far permit a relatively good description of the high temperature stability (Section XX) and oxidation behavior (Section XIV) of diborides. Although this description is not completely detailed at present, sufficient information is available to permit identification of the specific research directions in which additional effort will most likely provide significant advances. Such progress can be made by continuing the determination of fundamental data and applying the available background information to the practical applications for these materials.

On the basis of current vapor pressure and oxidation data, HfB_2 and ZrB_2 appear to be the most likely candidates for high temperature applications requiring

oxidation resistance. The available description of the compositional dependence of the boron activity in these compounds indicates that metal-rich deviations from stoichiometry in these compounds will probably result in additional enhancement of the oxidation resistance. Consequently, preparation and oxidation studies of HfB_2, and ZrB_2 specimens containing controlled deviations from stoichiometry should provide important data on the efficacy of such methods in improving oxidation resistance and may result in significant improvement in oxidation resistance. Other variations in composition which are suggested by the results of the present study include Ta and Nb or Sc and La which might serve to impede diffusion of oxygen through the oxide surface layer. Finally, additions of silicon to the pure diborides might provide enhanced oxidation resistance.

Preparation of fully dense specimens of doped or alloyed compounds exhibiting a fine grain size microstructure can be accomplished by utilization of the high pressure hot pressing technique (Section VI). Development of this technique may provide a useful method for significantly increasing the strength of these materials.

At present, the largest gap which exists in the description of the physical and mechanical properties of the diborides include data on thermal conductivity and mechanical strength. Measurements of thermal conductivity are presently underway and should become available in time for the next interim report. It seems appropriate to defer the modulus of rupture measurements until the most promising oxidation resistant compositions have been defined. Once such a definition has been made, rupture strength measurements can be made on these candidate compositions.

Apart from the possible application of borides in situations requiring refractoriness and oxidation resistance, a number of other possible applications exist. These include, radiation resistant materials for control rod applications in nuclear reactors, abrasion resistant materials and tooling, high temperature electrical conductors and thermionic emitters, and crucible and electrode materials for liquid metals and other corrosive substances. Although the subject matter presented in this report hardly provides all of the information required to evaluate the potentialities of the diborides for the aforementioned applications, the information provided is necessary to each.

II. PROGRAM MANAGEMENT

A. Introduction

In view of the diverse nature of the present study, it is being performed as a group effort in which ManLabs, Inc. is serving as prime contractor with Larry Kaufman serving as principal investigator and Edward V. Clougherty as group leader. In this capacity ManLabs provides management responsibility in addition to performing "in-house" research. Several other laboratories have participated in this study and further additions to the research group are anticipated. A detailed description of the composition of the research group is given below.

B. Subcontracting Laboratories

Official award of Contract AF33(657)-8635 was made to ManLabs on 15 April 1962. This contract stipulated "in-house" research at ManLabs in addition to research at the following subcontractor laboratories: Arthur D. Little, Inc. of Cambridge, Mass., Lexington Laboratories, Inc. of Cambridge, Mass., and Advance Metals Research Corp. of Somerville, Mass.

On 29 May 1962 ManLabs initiated a solicitation for proposals covering powder purification studies numbered AF33(657)-8635 RFP-1. This RFP was sent to thirteen different laboratory groups which had indicated interest in participating in the above mentioned study. Award of this subcontract was made to U. S. Borax Research Corp. of Anaheim, California.

The initially planned program included the procurement of pyrolytically deposited flat sheets of TiB_2, ZrB_2, HfB_2, NbB_2 and TaB_2 in thicknesses of 0.080 inches and several inches square. These sheets were required in fine grained form, fully dense and of high purity. After receiving

several bids to provide such material for this program from a number of qualified groups, ManLabs, Inc. contracted to purchase four 1 3/4" x 6" x 0.080" sheets of each of the above-mentioned diborides from High Temperature Materials Inc. of Brighton, Massachusetts. This order was placed on 4 October 1962 on a fixed price basis.

At the time H.T.M. accepted the order they knew the range of temperature, pressure, and flow rates required for the deposition process and counted on being able to optimize these conditions in short order so as to provide ManLabs with the required materials. In the initial experiments at H.T.M. the optimization was accomplished using TiB_2 as the test material. Under the optimum conditions fine grained films of TiB_2 were readily deposited on graphite substrates in thicknesses 0.010-0.030 inches thick. However, deposition of thicker sheets, without cracking presented considerable difficulties. After about five months of effort H.T.M. withdrew the offer to supply the pyrolytic sheet. They have indicated that the source of difficulty might be eliminated by proper matching of the expansion coefficients of boride and substrate.

Further efforts in the direction of procuring suitable pyrolytically deposited sheet material are presently under consideration.

On 15 January 1963, ManLabs initiated request for proposal AF33(657)-8635 (RFP-2) concerning "Measurements of the Bending Strength and Modulus" of the diborides. Eight organizations were solicited and six proposals were received. At the time this RFP was initiated, it was anticipated that single crystal material suitable for these measurements would be available from the zone-refining subtask. However, as indicated in Section V, problems

concerning the mechanical integrity of the single crystal bars have arisen. Regretfully, the procurement of additional subcontracting services to cover this task was postponed until a later date.

On 15 August 1963 a subcontracting agreement between the University of Cincinnati and ManLabs, Inc. was reached for measurements of thermal conductivity and emissivity on the diborides. These measurements will be performed by Professor Michael Hoch of the Department of Materials Science.

C. Dissemination of Program Information

In addition to many informal meetings and technical discussions of "research in progress", two formal meetings of all subcontractors were held at ManLabs, Inc. on 7 September 1962 and 8 March 1963. These meetings were held prior to issuance of semi-annual reports on 1 October 1962 and 1 April 1963. These reports, which received limited distribution, provided interim information on the present study. The results and conclusions of the earlier reports have been subject to alteration with time and are superceded by the present summary report.

In January 28 and 29, 1962, Arthur D. Little, Inc. and ManLabs held a jointly sponsored conference on "The Preparation, Characterization, and Thermodynamics of Group IV-A Diborides" at Acorn Park, Cambridge. This meeting which was attended by seventy research personnel from industry, university, and government was quite successful in defining the current status of information on boride compounds.

A number of papers based on the current program have been presented orally and are in preparation for future publication.

III. PROCUREMENT OF STARTING MATERIALS*

A. Introduction

The procurement of high purity, well characterized starting material is an important part of the present investigation because the scope of this program focuses attention on the fundamental properties of the compounds.

The diboride powders and in addition crystalline boron powder are used without further purification for the performance of the sintering (VII) single crystal growth (V), high pressure hot pressing (VI), X-ray measurements of lattice parameters, thermal expansion, and Debye temperature (VIII) subtasks. In addition, powder samples are also used for specific heat measurements on TiB_2 (XV) and heat of formation measurements (XVII). The remaining subtasks necessitate fabricated material which must be machinable to the required specimen geometries. Many of the subtasks can not be carried out unless crack-free specimens can be delivered. High purity samples of metals are also required for high pressure hot pressing (VI) and phase boundary studies (XVIII). Many property measurements will be made on material fabricated by either zone-refining or high pressure hot pressing. The sample requirements for the two fabricating techniques differ. The former effects purification as well as fabrication; the latter provides fabricated material without effecting purification. Appropriate measurements will be performed to determine the effect of fabricating procedure on properties such as oxidation behavior, hardness, resistivity, etc.

A detailed list of various diboride suppliers whose materials were used in this investigation is presented in Appendix A. It should be emphasized that

---

*E. V. Clougherty, ManLabs, Inc.

commercial specifications are generally listed for 'typical' materials and that there are no guarantees as to the availability of such materials at any given time.

B. Chemical Analysis

The future developments and uses of ceramic refractory materials will depend in part on an integrated evaluation of the measurements of their chemical, physical, thermal, and mechanical properties. The results of the chemical analyses of these materials will play an important role in this evaluation. Several of the properties which make these materials attractive for applied purposes also render accurate and precise chemical analysis a difficult task. Thus, high melting point and chemical inertness at high temperature are characteristics of materials which are difficult to dissolve in acids and bases at convenient temperatures without contamination. The preliminary grinding of these materials in order to obtain a representative sample for analysis is complicated by their extreme hardness.

The analytical problems are further complicated for the refractory metal diborides by the absence of certified standards. The results of the analyses must be evaluated on the basis of the summation of the analyses of all the constituents and on the precision of the individual methods as far as this has been determined in recognized laboratories. In addition, it will be possible in the progress of the present investigation to compare the analytical results of different laboratories and different techniques on the same sample.

A recent compilation[1] contains the methods of analysis for a large variety of refractory materials and an evaluation of the accuracy and the precision of these techniques. Chemical analyses are obtained for the following

elements: Refractory Metal, Boron, Carbon, Nitrogen, Oxygen, and Iron. It should be noted that analytical procedures for boron afford a measure of the total boron present. As yet no method is available which will provide an analysis for free and combined boron.

C. Procurement

1. Diboride Powders

Appropriate quantities of each of the five diborides have been obtained from commercial sources. Each material has been characterized by a qualitative emission spectrographic analysis and quantitative chemical analysis for metal, boron, carbon, nitrogen, oxygen, and iron. Average results of analyses are presented in Table 1; results of individual analyses are presented in detail in Appendix A. The averaged compositions of metal, boron, and the atomic ratio of boron to metal are compared with the calculated compositions for the stoichiometric compounds in Table 2. These experimental results represent total percentage of a given material; no distinction as to free and combined elements can be made at this time.

2. Boron

Crystalline boron was purchased from U.S. Borax. The results of the qualitative spectrographic analysis of this material are presented in Table 3.

Single crystal rods of zone refined boron were purchased from The Eagle-Picher Company for the phase boundary determinations using diffusion couples.

3. Metals

High purity metals were obtained from various sources of supply including the ManLabs inventory stock. These materials were routinely analyzed qualitatively by emission spectrographic analysis. The results of the latter were used to select pertinent quantitative analyses where required. The analytical results are summarized in Table 3.

Table I

Characterization* Of Metal Diboride Powders

Averaged Quantitative Results (w/o)

Material	Supplier	M	B	C	N	O	Fe
TiB_2 (#1)	U.S. Borax	68.68	30.97	0.101	0.065	0.44	0.09
TiB_2 (#2)	Millmaster	68.85	30.48	0.10	0.18	0.06	0.06
ZrB_2 (#1)	U.S. Borax	80.67	18.05	0.33	0.19	0.53	0.046
HfB_2 (#1)	Wah Chang	89.0	10.6	0.14	0.017	0.10	0.083
NbB_2 (#2)	U.S. Borax	80.75	18.6	0.09	0.05	0.11	0.10
TaB_2 (#1)	Kawecki	88.80	10.37	0.38	0.0098	0.68	0.11

Qualitative Results (Range w/o)

Material	Supplier	0.1	0.01-0.10	0.001-0.01	0.001
TiB_2 (#1)	U.S. Borax	——	Co	Al, Ca, Cu, Si, Mn, V	Na, Mg, Cr, Ni, Zr, K
TiB_2 (#2)	Millmaster	Cr, Co	Si, Ni	Mg, Al, Mo	Cu, Ge, Sn, Mn, Ag, Cd
ZrB_2 (#1)	U.S. Borax	———	Ca, Cr, Ti	Na, Mg, Co, Ni, Mo	Fe, Nb, Ag, Mn, Al, Cu, V
HfB_2 (#1)	Wah Chang	———	———	Al, Ti, Mn	Cu, Mg, Cr
NbB_2 (#2)	U.S. Borax	Ti	Al, Si, Cr, Ni, Mg	Sn, Ag, Cu	Ge, Mn
TaB_2 (#1)	Kawecki	———	Al, Ni, Zr	Mg, Si, Ca, Ti, Mn, Zr, Cu, Cr, Mo, Ti	Na, V, K

---

*Detailed analytical results and supplier information are presented in Appendix A.

Table 2

Summary of Averaged Results for Metal and Boron Analyses

		Composition						
		Calculated			Experimental*			
Material	Supplier	w/o M	w/o B	B/Me	w/oM	w/o B	Σ M + B	B/Me
TiB_2	U.S. Borax	68.88	31.12	2.00	68.68	30.97	98.97	1.99
ZrB_2	U.S. Borax	80.83	19.17	2.00	80.67	18.05	98.72	1.89
TaB_2	Kawecki	89.32	10.68	2.00	88.80	10.37	99.17	1.95
HfB_2	Wah Chang	89.19	10.81	2.00	89.0	10.6	99.6	1.97
NbB_2	U.S. Borax	81.11	18.89	2.00	80.75	18.6	99.35	1.98
TiB_2	Millmaster	68.88	31.12	2.00	68.85	30.48	99.33	1.98

---

*Detailed analytical results are presented in Appendix A.

Table 3

Characterization of Boron and Metals

Qualitative Results (Range w/o)**

Element	Supplier	0.1-1	0.01-0.1	0.001-0.01	0.001
B (crystalline)	U.S. Borax	Mn, Si	Mg, Al, Fe, Cu	Ca, Ti, Ni	———
Zr (powder)	ManLabs*	———	Ti, B	Na, Al, Cr, Zn, Sr,	Mg, Si, Ca, Mn, Ni, Cu, Ag, Sn, Ba, Pb
Zr (rod)	ManLabs*	———	———	Co	Al, Cu, Pb
Nb (rod)	ManLabs*	———	———	Cu, Zn, Ga, Ge, As, Rb	Mo
Ta (rod)	ManLabs*	———	———	———	Fe

Quantitative Results (w/o)***

Element	Supplier	
B (crystalline)	U.S. Borax	———
Zr (powder)	ManLabs*	0.005 N
Zr (rod)	ManLabs*	15 ppm H; < 2 ppm N; 0.01% O
Nb (rod)	ManLabs*	———
Ta (rod)	ManLabs*	———

*Laboratory stock inventory.

**Results obtained from emission spectrographic analysis by Jarrell Ash Co., Newtonville, Mass.

***Results obtained by D. Gurnsey, Metallurgy Department, M.I.T.

REFERENCES

1. Kriege, O.H., "The Analysis of Refractory Borides, Carbides, Nitrides, and Silicides," Los Alamos Scientific Laboratory of the University of California, Los Alamos, New Mexico, LA-2306.

IV. PURIFICATION OF DIBORIDE POWDERS*

A. Introduction

In the determination of the fundamental properties of the refractory metal diborides, it is most important to obtain starting material with sufficiently high purity so that the measured quantities will be representative of the pure materials. This subcontract was assigned to study the methods for reducing the impurity levels in presently available refractory diboride powders. The overall program includes an investigation of TiB_2, ZrB_2, HfB_2, NbB_2 and TaB_2; the work which has been completed covers only the initial investigations of TiB_2 and ZrB_2.

An investigation has been made into methods for the purification of TiB_2 and ZrB_2 powders which were prepared by the carbothermic reduction of the mixed oxides. The principal contaminants in these materials were C, N, O, and Fe. Three purification procedures have been studied: high-temperature vacuum treatment, non-oxidizing acid leaching, and fused salt leaching. In the study of the TiB_2 the fused salt leach provided few advantages over aqueous acid leaching and was much more difficult and expensive to perform. Therefore, most of the work has centered around high-temperature vacuum treatment and acid leaching. A combination of these two procedures applied to the highest grade of TiB_2 available (Sample #392-21-A, see Table 7) gave a product (Sample #392-[illegible], see Table 9) which contained 0.03% C, 0.045% N, 0.31% O, and 0.08% Fe. Spectrographic analysis indicated no other significant contamination.

Hydrofluoric acid leaching alone appeared to give the best sam[illegible] ZrB_2. A hafnium-free material (Sample #392-15-A, see Table 12) treat[illegible]

---

*J.L. Boone and G. W. Campbell, Jr., U. S. Borax Research Corp.

this manner gave a product (Sample #386-68-E, see Table 15) which contained 0.16% C, 0.05% N, 0.47% O, and 0.03% Fe. Spectrographic analysis also indicated 0.028% Ti and about 0.014% Si. Although high-temperature vacuum treatment reduced the carbon content further, it also increased the oxygen content. The effect of the various procedures on the impurity levels in this particular sample can be seen in Fig. 3. The acid leaching presumably leaves the surface as the cleanest part of the individual particles with the remaining impurities diffused through the rest of the mass. If this is true, they probably have a minor effect on the properties of the product.

The individual procedures which are considered best at this time for the particular impurities in TiB_2 and ZrB_2 are given below:

Impurity in TiB_2	Purification Procedure
C	High-Temperature Vacuum Treatment
N	High-Temperature Vacuum Treatment
Fe	High-Temperature Vacuum Treatment
Si	High-Temperature Vacuum Treatment
O	HF Leaching
Ca	HF Leaching
Mg	HF Leaching
Al	HF Leaching

Impurity in ZrB_2	Purification Procedure
C	HF Leaching
N	HF Leaching
O	HF Leaching
Fe	High-Temperature Vacuum Treatment
Si	High-Temperature Vacuum Treatment
Ti	Not Removed

Although HfB_2, NbB_2, and TaB_2 have not been studied, it appears reasonably certain that similar improvements can be made in these materials by use of hydrofluoric acid leaching and high-temperature vacuum treatment. The latter would almost certainly be more effective even for TiB_2 and ZrB_2 if a better vacuum could be maintained and if higher temperatures could be reached. These conditions would require the use of an inert gas resistance furnace or an induction furnace.

B. Results and Discussion

1. Purification of Titanium Diboride

1.1 Starting Material

The elemental analysis of a diboride at various stages of purification is the only method of detecting changes in its composition. Therefore, the analytical results are extremely important. The difficulty involved in this task increases greatly as the purity of the substance increases. The experimental uncertainty in the analyses of boron plus titanium is equal to the sum of the experimental uncertainties of the independent determinations ($\pm 0.15\% + \pm 0.20\% = \pm 0.35\%$) and thus, if the experimental value of boron plus titanium were 99.25%, the sum of the actual content can vary from 98.90 to 99.60%. Therefore, the only reliable way of determining the quality of the material in question is to give accurate analyses of all the impurities. In general, this is the procedure being employed. An attempt to use X-ray powder patterns to show changes in the levels of impurities of titanium diboride was not successful since even the starting material showed only those lines attributable to the parent compound.

The titanium diboride used in the initial powder purification studies was prepared by the carbothermic reduction of the mixed oxides and had a measured titanium plus boron content of 98.5% (Sample #392-14-A). This was not the best material available, but since the evaluation of the purification methods depends on measuring changes in only small amounts of contaminants, it was decided that this material would be appropriate for these studies. After a satisfactory procedure was established, it was applied to the best titanium diboride powder available (Sample #392-21-A).

1.2 High-Temperature Vacuum Purification

In the early stages of the contract an attempt was made to modify an existing furnace which was used in the high-temperature vacuum purification of elemental boron so that it might be used to purify the diborides. The furnace, which is schematically shown in Fig. 1 , has an evacuated, water-cooled, steel bell jar which encloses a resistively-heated tungsten coil. Power to the coil was supplied by means of a G.E. 33 KVA transformer (air cooled) in series with a G.E. 33 KVA saturable core reactor. Control of the reactor was provided by a selenium rectifier which in turn was controlled by a 115 V.A.C. transformer. Temperatures were measured by a Pt, Pt-13% Rh thermocouple placed just inside the lip of the crucible containing the sample. However, delays caused by the inability of attaining pressures which were consistently below 0.1 mm. and of attaining thermal equilibrium in the reaction zone even with radiation shielding forced an abandonment of this furnace.

Subsequent high-temperature work was performed in the Hevi-Duty tube furnace shown in Fig. 2 , which was modified for continuous operation at 1500°C. A boat composed of bonded alumina and filled with 23.7 grams of

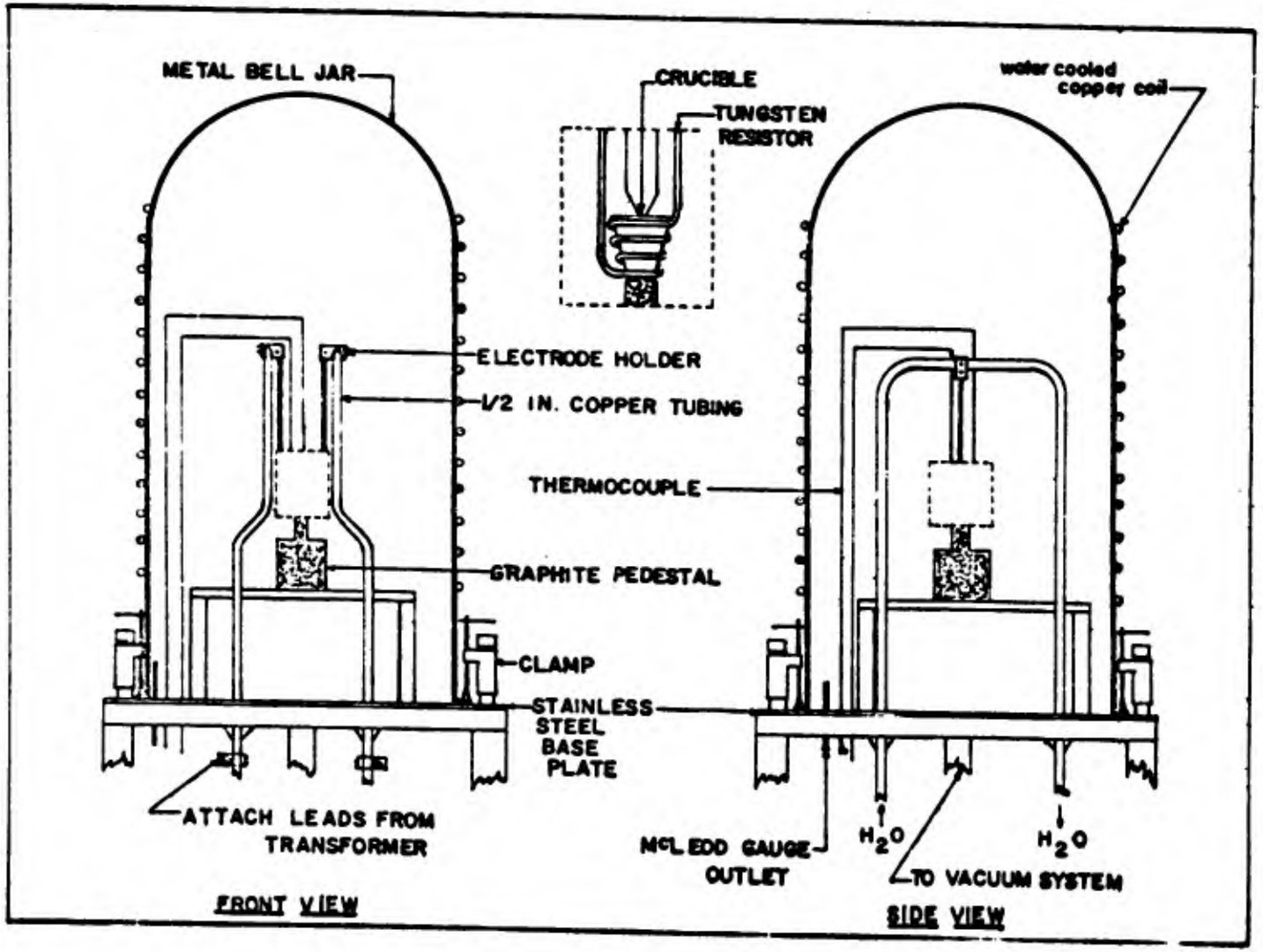

Fig. -1 - High-Temperature Vacuum Bell Jar Furnace.

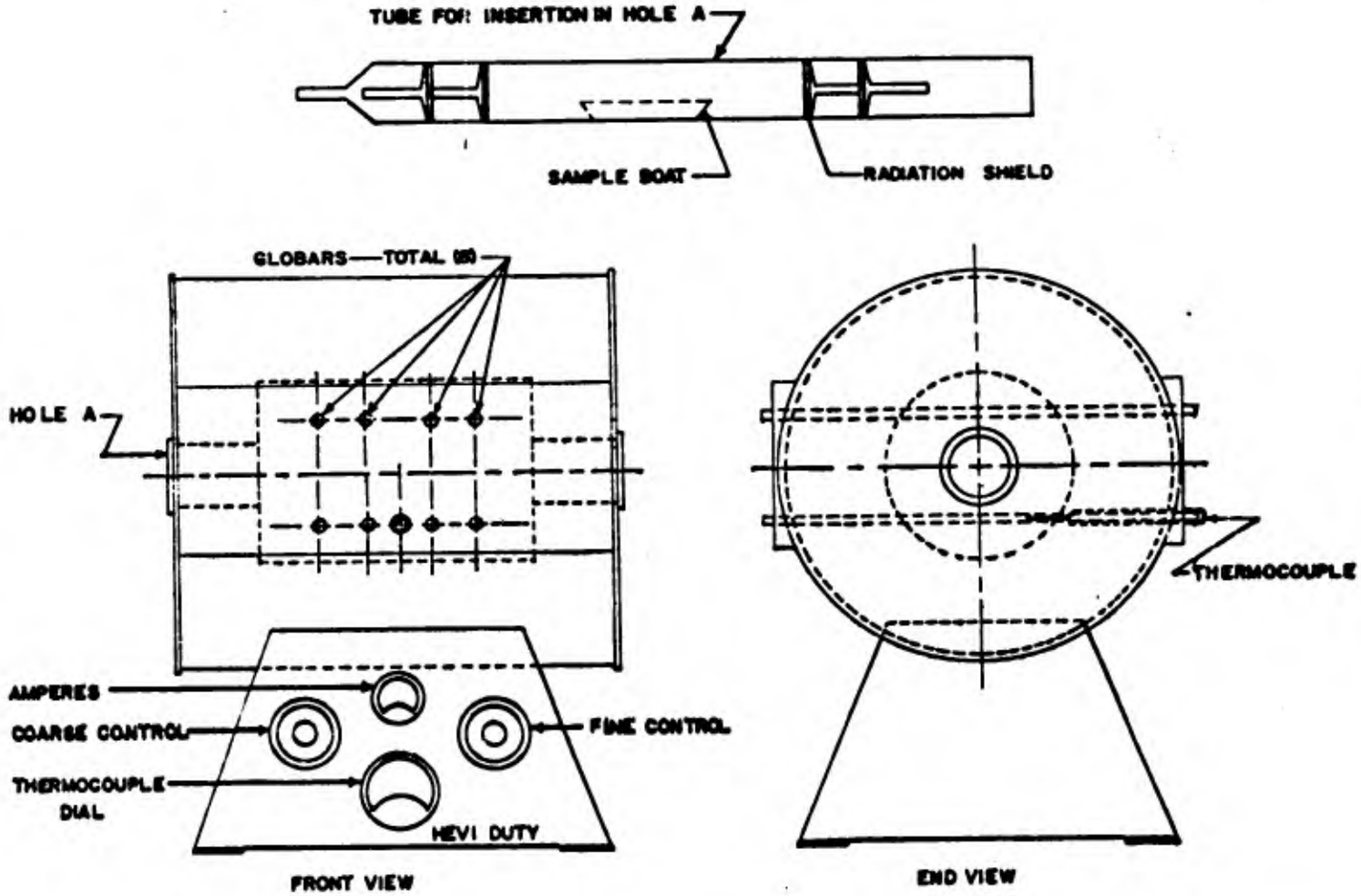

Fig. -2 - Hevi-duty high-temperature tube furnace.

powdered titanium diboride (Sample #392-14-A) was heated in this furnace at 1490-1500°C for 3 hours at $1-8 \times 10^{-3}$ mm. Hg. The sample was then cooled to 25°C under vacuum. Evidence for sintering was indicated by the dimensional stability of the sample after removal from the boat. The maximum weight loss due to volatilization was 1.5 grams (6.3%), but the actual value was probably much less. The major constituents in the volatile material which collected in the cooler parts of the tube were shown by spectrographic analysis to be boron and silicon. The outer surfaces of the titanium diboride were dark and shiny and were obviously contaminated by the boat since the aluminum and calcium contents were considerably higher than those of the starting material. These layers (a maximum of 1.6 grams) were removed before the main body was sampled. An X-ray powder pattern of the product was the same as the starting material and showed no lines other than those due to titanium diboride. The analytical results of the product (Sample #392-8-B) are given in Table 4 .

Table 4

Elemental Analysis of High-Temperature Vacuum Treated TiB_2

	Starting TiB_2 (#392-14-A)	High-Temperature Vacuum Treated TiB_2 (#392-8-B)	Percent Change
C	0.28	0.024	-91
N	0.078	<0.002	-(>97)
O	0.617	1.014	+64
Fe	0.22	0.11	-50
Si	0.056	not detected (<0.005)	-(>91)
Ca	0.030	0.048	+60
Mg	0.0048	0.0028	-42
Al	trace (<0.04)	trace (<0.020)	
Other	nil	nil	

Contamination from the boat probably accounts for both the increase in oxygen and calcium. Silicon would probably be increased also except for the fact that silicon dioxide is converted in a reducing medium to volatile silicon monoxide, presumably leaving oxygen in the titanium diboride matrix. (The absence of silicon in the product has been verified by duplication of the original analysis.) In subsequent work boats made of titanium diboride were used.

1.3 Acid Leach

Fifty-gram samples of titanium diboride were added to 100 ml. of 6 N hydrochloric acid and to 100 ml. of 6 N hydrofluoric acid in high density polyethylene beakers. The two mixtures were then heated to 95-100°C on a steam bath for 3 hours (considerable foaming occurred during the first hour). The boride was washed on a Buechner funnel with water followed by methanol, dried in the atmosphere for 16 hours, and then dried in an oven for 30 minutes at 110°C. The analytical results are given in Table 5 .

Table 5

Elemental Analysis of Acid Leached TiB_2

	Starting TiB_2 (#392-14-A)	Hydrogen Fluoride Leached TiB_2 (#386-22-A)		Hydrogen Chloride Leached TiB_2 (#386-22-B)	
	Percent Components	Percent Components	Percent Change	Percent Components	Percent Change
C	0.28	0.18	-36	0.24	-14
N	0.078	0.046	-41	0.029	-63
O	0.617	0.436	-29	0.611	- 1
Fe	0.22	0.23	+ 5	0.20	- 9
Si	0.056	0.041	-27	0.051	- 9
Ca	0.030	trace (<0.002)	-(>93)	trace (<0.002)	-(> 93)
Mg	0.0048	nil	-(> 80)	0.0042	-12
Al	trace (<0.04)	nil		nil	
Cu	nil	trace (<0.001)		trace (<0.001)	
Other	nil	nil		nil	

The hydrogen fluoride leach gives significant reductions in the carbon, nitrogen, and oxygen contents, but has no measurable effect on the iron. It removed essentially all the aluminum, calcium, and magnesium, and reduced the silicon about 25%. The same general trend was observed for material leached with hydrogen chloride, except that in general the degree of purification was less. The iron is apparently diffused through the sample and is unaffected by surface leaching. The percent recovery in this process was not determined due to loss of material during washing.

1.4 Fused Salt Leach

Part of a mixture containing approximately 100 grams titanium diboride (Sample #392-14-A), 50 grams potassium bifluoride, and 50 grams potassium fluoborate was placed in a graphite boat in the tube furnace shown in Fig. 2 . The system was evacuated and filled with argon several times between 100 and 250°C and then heated under one atmosphere of argon for one hour at 1000-1050°C. It was then cooled under argon, removed, and leached several times in boiling water. The sample was then transferred to a filter paper, washed with water, rinsed with acetone, and dried. Recovery was greater than 85%, but mechanical losses in the procedure did not allow for an accurate determination. The sample was divided into two parts; one was washed further with 6 N hydrofluoric acid and the other with 6 N hydrochloric acid. After one hour at 95-100°C, the samples were diluted to acid strengths of 2 N and heated another 45 minutes. They were then filtered, washed, rinsed with acetone, dried 16 hours in the atmosphere and another 20 minutes at 115°C. The recovery from this acid washing step was greater than 75%. The analytical results are given in Table 6 .

Table 6

Elemental Analysis of Fused Salt Leached TiB_2

	Starting TiB_2 (#392-14-A)[2]	Washed with HF (#392-13-A) Percent Components	Percent Change	Washed with HCl (#392-13-B) Percent Components	Percent Change
Ti	67.85	67.79		67.52	
B	30.60	30.61		30.49	
Total	98.45	98.40		98.01	
B/Ti	2.00	2.00		2.00	
C	0.28	0.30	+ 7	0.33	+18
N	0.078	0.035	-55	0.070	-10
O	0.617	0.455	-26	0.529	-14
Fe	0.22	0.22	0	0.27	+32
Si	0.056	0.054	- 3	trace (<0.005)	-(>91)
Ca	0.030	0.044	+47	not detected (<0.002)	-(>93)
Mg	0.0048	0.0030	-37	0.0034	-29
Al	trace (<0.04)	trace (<0.01)		not detected	
Cu	nil	0.0028		0.0032	
Other	nil	nil		nil	

There was relatively little change in the major contaminants (C, N, O, and Fe), but significant reduction of the minor metallic contaminants occurred in the material washed with hydrochloric acid.

1.5 Purification of High Grade Titanium Diboride

Titanium diboride of approximately 98.5% purity was used in the studies described in sections 1.2 - 1.4 in order to have percentages of impurities which were sufficiently large so that relatively small changes could be measured. From this work it was concluded that heating at high temperatures

under vacuum gave large reductions in the carbon, nitrogen, iron, and silicon contents. In addition, aqueous hydrofluoric acid leaching at 100°C removed most of the calcium and magnesium and gave significant reductions in the oxygen content. This combination of acid leaching and high-temperature vacuum treatment was subsequently applied to the best titanium diboride available in order to prepare a sample of maximum purity.

The starting material (#392-21-A) was from the same batch as the 20 pounds supplied earlier by U.S. Borax Research Corporation to ManLabs, Inc. (cf. Appendix A). It was leached in 6 N Hf for 4 hours at 100°C and then diluted to 2 N HF and heated for another 30 minutes. The slurry was filtered, washed with water followed by acetone, and dried in the atmosphere for 16 hours. There was a 15.2% wt. loss during this first step. The TiB_2 was washed by stirring with 6 N HCl for 30 min. at 100°C and then gradually diluting over a 2 hour period until the total volume was 800 ml. The slurry was filtered and washed with water until no further chloride could be detected with silver ion. The product (#392-21-B) was then rinsed with acetone and dried in the atmosphere for 18 hours. Total loss to this point was 19.3%.

A 2.5-gram sample of #392-21-B was weighed, heated at 98°C for 30 min., cooled in a desiccator, and reweighed. Since the weight loss was only 0.8 mg. or 0.03%, it was concluded that there was no significant oxygen contamination of the sample due to adsorption of moisture.

Two slip-cast and sintered TiB_2 boats, each capable of holding about 13-15 g. of low density TiB_2 powder, were preheated to 1500°C under vacuum and then used in the vacuum heating of #392-21-B. Approximately 28 grams of #392-21-B was heated in each of 5 runs. The temperature of the

furnace was maintained at 1470-1480°C for 4 hours and the pressure was held at 1-3 x 10^{-2} mm. Hg by continuous pumping. After the TiB_2 had cooled to room temperature under vacuum, approximately 3 grams of the original 28 grams was removed from surface of the powder in order to avoid contamination from the furnace. These five samples were combined and thoroughly mixed (#392-37-A). The elemental analyses of samples #392-21-A, #392-21-B, and #392-37-A are given in Tables 7, 8 and 9. Whenever a conflict in values was encountered between the analytical data of LeDoux and that of Kennard and Drake, the LeDoux values were accepted as being more reliable.

Table 7

Elemental Analyses of Sample #392-21-A:
High Grade Titanium Diboride Starting Material

	LeDoux (Reported by ManLabs)		Kennard & Drake	Pacific Spectrochemical	General Atomics
Ti	68.61	68.50	67.92		
B	31.17	30.85	30.59		
Ti + B	99.78	99.35	98.51		
B/Ti	2.003	1.99	1.994		
C	0.094	0.099	0.11		
N	0.073	0.066	0.018		
O	0.43	0.43	0.397		0.74 ± 0.04
Fe	0.10	0.09	0.16	0.12	
Total	100.48	100.04	99.20		
Si				0.046	
Ca				0.017	
Mg				0.0036	
Other				nil	

Table 8

Elemental Analyses of Sample #392-21-B;
High Grade Titanium Diboride after Leaching with HF

	Kennard & Drake		Pacific Spectrochemical		General Atomics
Ti	68.12	67.85			
B	30.69	30.53			
Ti + B	98.81	98.38			
B/Ti	1.994	1.993			
C	0.12	0.12			
N	0.010	0.010			
O	0.268	0.288			0.40±0.08
Fe	0.22	0.17	0.096	0.090	
Total	99.43	98.98			
Si			nil	nil	
Ca			trace (< 0.003)	trace (< 0.003)	
Mg			0.0030	0.0034	
V			trace (< 0.01)	trace (< 0.01)	
Other			nil	nil	

Table 9

Elemental Analyses of Sample #392-37-A:
High Grade Titanium Diboride after Leaching and Heating under Vacuum.

	LeDoux	Kennard & Drake		Pacific Spectrochemical		General Atomics
Ti	69.18	68.20	68.12			
B	30.47	30.78	30.68			
Ti + B	99.65	98.98	98.80			
B/Ti	1.950	1.998	1.994			
C	0.023	0.03	0.03			
N	0.045	0.029	0.016			
O	0.312	0.248	0.332			0.3±0.1
Fe	0.079	0.21	0.14	0.064	0.076	
Total	100.11	99.50	99.32			
Ca				trace (< 0.003)	trace (< 0.003)	
Mg				trace (< 0.001)	trace (< 0.001)	
Other				nil	nil	

The combined acid leaching and high-temperature vacuum treatment reduced the oxygen content by 30%, the carbon by 75%, and the nitrogen by 36%. Iron appeared to be reduced by about 20%. Silicon and calcium, the only significant metal contaminants other than iron, were reduced from 0.017% to less than 0.003% and from 0.046% to less than 0.005% respectively. The magnesium content was little changed, but it was low in the starting material. The X-ray powder patterns of these materials #392-21-A, #392-21-B, and #392-37-A showed only the lines expected for TiB_2 with no variations.

1.6 Analytical Procedures

The elemental analyses for Ti, B, C, N, O, and Fe contained in Tables 4,5 , and 6 were performed by Kennard and Drake, Los Angeles. Their

procedures are given in Table 10. The other data in these Tables were obtained by Pacific SpectroChemical Laboratory, using semi-quantitative spectrographic analysis. The data in Tables 7, 8, and 9 are listed according to their sources and include information from Kennard and Drake, Pacific SpectroChemical, and LeDoux & Company, Inc. The LeDoux procedures are given in Table 11. Tables 7, 8, and 9 also include fast-neutron activation analyses for oxygen which were performed by the General Atomics Division of General Dynamics, San Diego, California.

Table 10

Outline of Method of Analysis for Elements in TiB_2

(Kennard and Drake)

Element	Analytical Method
Ti	Solution in HCl + HNO_3 with few drops of H_2O_2. Undissolved residue fused with $KHSO_4$ and returned to solution. Ti precipitated with NaOH, filtered, and redissolved in 5% H_2SO_4. H_3PO_4 added to mask iron. Ti determined spectrophotometrically.
B	Digested as above. Distill boron as methyl borate-methanol azotrope. Titrated as boric acid with NaOH in presence of mannitol.
C	Combustion.
N	Micro Kjeldahl. ASTM E120-60, p. 503, 1960 Edition.
O	Inert gas fusion. (Leco Vacuum Fusion Analyzer, Model 578-000; temp., 1950°C; time, 3 min.; flux, Pt; crucible, graphite).
Fe	Dissolved as for Ti Tartaric acid and NH_4OH added. Fe precipitated with H_2S, filtered and dissolved in HNO_3. Hydroxylamine hydrochloride and sodium acetate buffer added. Determined spectrophotometrically.

Table 11

Outline of Method of Analysis for Elements in TiB_2

(LeDoux & Company, Inc.)

Element	Analytical Method
Ti	Solution in HF and HNO_3, evaporate to fumes with H_2SO_4; Precipitate with cupferron and ignite; Correct for impurities by spectrographic analysis.
B	Fusion in NaOH, dissolve and filter; Dissolve residue in HCl and reprecipitate; Remove Ti with $BaCO_3$; Titrate H_3BO_3 in presence of mannitol.
C	Combustion and conductometric measurement.
N	Decomposition with HCl, HF, and H_2O_2; Kjeldahl distillation.
O	Inert gas fusion with Pt as flux.
Fe	Orthophenanthroline color procedure.

2. Purification of Zirconium Diboride

2.1 Starting Material

The material (Sample #392-15-A) used in the study of methods for purifying zirconium diboride was the same as the 20 pounds of "Reactor Grade" zirconium diboride supplied earlier to ManLabs, Inc. and referred to in Section III. This is an essentially hafnium-free material of 98.5-98.8% purity. Various analyses of this material are given in Table 12. The main contaminants are oxygen, carbon, nitrogen, and iron. The LeDoux value of 0.30% for tungsten is inconsistent with both the data from Pacific SpectroChemical Laboratory, and that from Jarrell-Ash, as reported by ManLabs in Table 12 and Appendix A. Weak lines in the X-ray powder pattern at 2.68, 2.32, and 1.64 Å may be due to zirconium carbide which gives lines at 2.70, 2.34, and 1.65Å. Other weak unidentified lines were present at 1.723 and 1.401Å.

Table 12

Elemental Analysis of Sample #392-15-A: ZrB_2 Starting Material.

	LeDoux Data from ManLabs		LeDoux Data from USB	Truesdail		Pacific SpectroChemical		General Atomics
Zr	80.42	80.56	80.52	80.10	80.42			
B	18.01	17.87	17.92	18.44	18.13			
Zr + B	98.43	98.43	98.44	98.54	98.55			
B/Zr	1.889	1.871	1.875	1.941	1.901			
C	0.35	0.34	0.45	0.28	0.27			
N	0.20	0.20	0.19	0.20	0.24			
O	0.52	0.52	0.53					0.57±0.04
Fe	0.048	0.051	0.11	0.08	0.11			
	(Semiquantitative Spectrographic)†		(Semiquantitative Spectrographic)†					
Al	-		0.0020			nil (<0.01)		
Ca	-		0.0100			nil		
Co	0.001		0.0020					
Cr	0.007		0.0030					
Cu	0.001		0.0020			nil		
Fe	0.04		0.0700			0.036	0.024	
Mg	0.002		0.0030			trace (<0.001)		
Mn	0.001		0.0005					
Mo	0.01		0.0100					
Na	-		0.0030					
Ni	0.005		0.0100					
Si	0.001		0.0050			0.013		
Ti	0.05		0.0100			0.028	trace (<0.004)	
W	N.D.*		0.3000					
K	N.D.*		0.0020					
Hf	0.01-0.001**					nil	N.D. (<0.05)	
Other						nil	nil	

† Analyses by LeDoux,

* Not detected in Qualitative Spectrographic Analysis.

** Range determined in Qualitative Spectrographic Analysis.

2.2 High-Temperature Vacuum Purification of Zirconium Diboride.

Approximately 125-gram samples of zirconium diboride (Sample #392-15-A) were placed in graphite boats in the mullite tube furnace shown in Fig. 2 and heated to 1470-1480°C for 2 hours at 0.1 mm. They were cooled under vacuum, removed from the furnace, and reweighed. Weight losses amounted to 0.1-0.3 g. or about 0.03-0.10% of the combined weight of boat and sample. The zirconium diboride surface layer was discarded in order to remove any possible contamination. The product (Sample #392-50-A) was then emptied from the boat, taking care not to remove that portion of the sample which adhered to the graphite sides and bottom. The X-ray powder patterns of the top, sides and bottom, and the main body of the sample were all essentially the same and differed from the starting material only in that the weak, unidentified lines at 1.723 and 1.401Å were almost completely removed. The analytical data obtained for this material are given in Table 13.

Table 13

Elemental Analysis of Sample #392-50-A: ZrB_2 after Heating under Vacuum

	LeDoux		Pacific SpectroChemical
Zr	81.07	81.27	
B	18.20	18.20	
Zr + B	99.27	99.47	
B/Zr	1.893	1.888	
C	0.36	0.37	
N	0.18	0.18	
O	0.61	0.61	
Fe	0.04	0.04	0.019
Total	100.46	100.67	
Ti			0.026
Al			0.017
Mg			nil (<0.0005)
Si			0.011
Cu			nil (<0.0003)
Hf			nil
Other			nil

The values indicate an increase in both Zr and B and a slight increase in the B/Zr ratio. However, since the total of the contents of Zr, B, C, N, O, and Fe are considerably above 100%, the values for Zr and B must be considered somewhat questionable. The carbon, nitrogen, and iron contents are all reduced slightly, but the oxygen level has increased. These values are charted in Fig. 3 along with the results from the products of the other ZrB_2 purification procedures.

2.3 High-Temperature Vacuum Purification of Zirconium Diboride followed by Acid Leaching

Part of the zirconium diboride which was heated under vacuum (Sample #392-50-A) was leached in aqueous 6 N HF for 4 hours at 0°C. (A more extensive description of the acid leaching of zirconium diboride is given in the following section.) It was then filtered, rinsed with water followed by acetone, and air dried. The X-ray powder pattern of the product (Sample #392-50-C) had only one weak line at 2.33Å which was not characteristic of zirconium diboride. The elemental analyses of this material are given in Table 14.

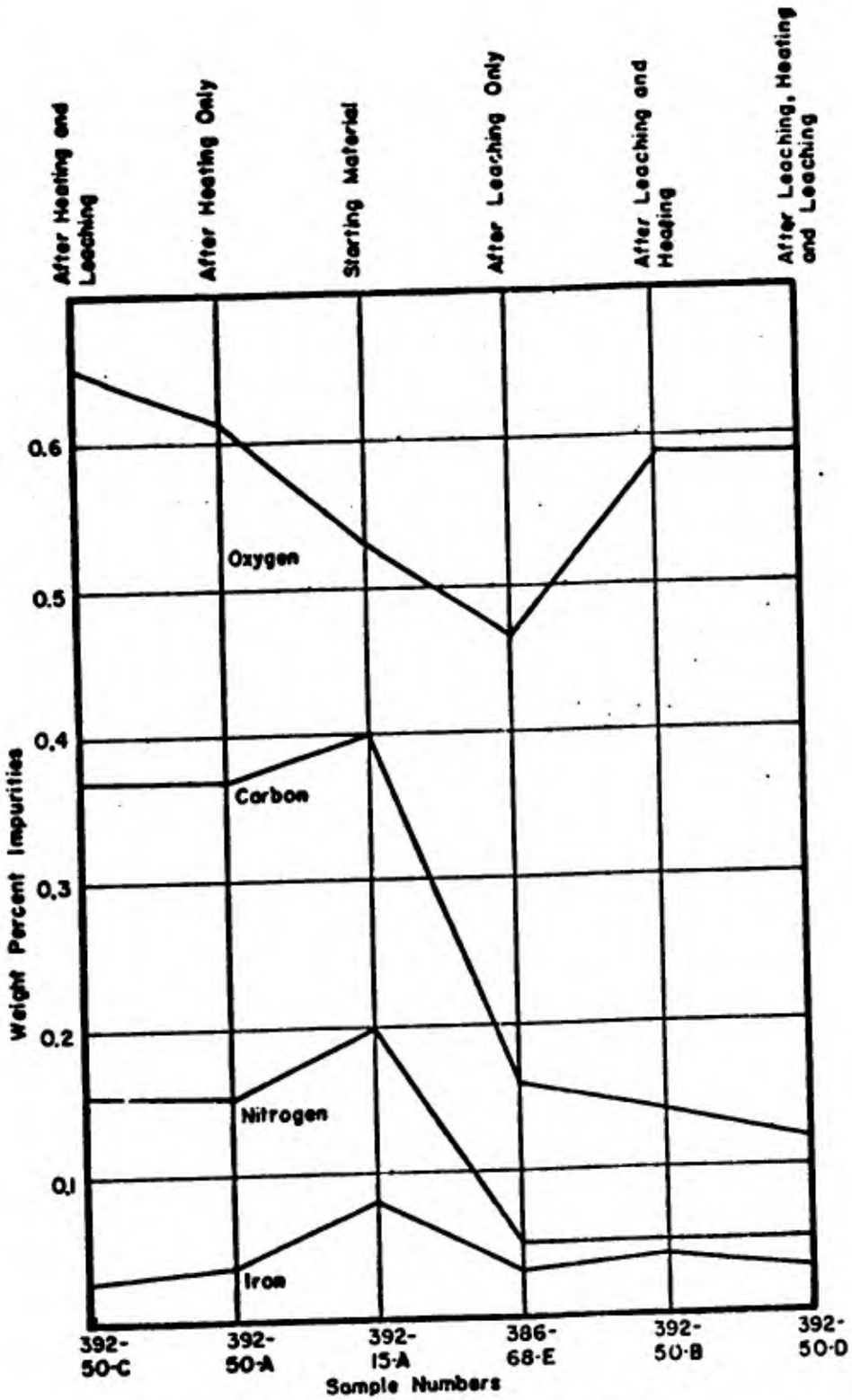

Fig. 3 - Levels of Impurities in Purified ZrB_2

Table 14

Elemental Analysis of Sample #392-50-C:
ZrB_2 after Heating under Vacuum and Acid Leaching

	LeDoux		Pacific SpectroChemical
Zr	80.98	81.13	
B	18.21	18.29	
Zr + B	99.19	99.42	
B/Zr	1.896	1.901	
C	0.35	0.38	
N	0.18	0.18	
O	0.63	0.66	
Fe	0.03	0.03	
Total	100.38	100.67	
Ti			0.032
Al			0.030
Mg			trace (<0.0005)
Si			0.011
Cu			trace (<0.0003)
Hf			nil
Other			nil

The carbon, nitrogen, and iron levels are essentially unchanged from those of zirconium diboride which was heated only (Sample #392-50-A). The oxygen content, however, appeared to be slightly higher (refer to Fig. 3).

2.4 Purification of Zirconium Diboride Powder by Acid Leaching.

Zirconium diboride is much more readily decomposed by hydrofluoric acid than is titanium diboride. When 100-gram samples of "Reactor Grade" ZrB_2 (Sample #392-15-A) were slurried in 240 ml. of 6 N HF at room temperature, an exothermic reaction occurred accompanied by considerable foaming. The temperature was reduced to $0^{\circ}C$ and maintained there for 4 hours.

The samples were diluted, filtered, and washed. They were then stirred in about 400 ml. of water in order to remove any remaining salts, again filtered, washed with water followed by acetone, and air dried. A 10% weight loss was noted for this procedure. The product (Sample #386-68-E) was a free-flowing powder in contrast with the starting material which had a damp appearance and tended to clump. The X-ray powder pattern was also free of extraneous lines. The elemental analyses are given in Table 15 (see also Fig. 3).

Table 15

Elemental Analyses of Sample #386-68-E: ZrB_2 after Acid Leaching.

	LeDoux		Truesdail		Pacific SpectroChemical	
Zr	80.43	80.49	80.11	80.49		
B	18.82	18.84	17.91	17.30		
Zr + B	99.25	99.33	98.02	97.79		
B/Zr	1.973	1.973	1.985	1.812		
C	0.15	0.17	0.10	0.12		
N	0.05	0.05	0.07	0.07		
O	0.47	0.47				
Fe	0.03	0.03	0.12	0.11	0.032	0.032
Total	99.95	100.05				
Ti					0.030	0.026
Al					nil	nil
Mg					trace (<0.001)	trace (<0.0005)
Si					0.014	0.013
Cu					nil	0.00078
Hf					nil	nil
Other					nil	nil

A 200-gram sample of "Reactor Grade" zirconium diboride (#392-15-A) was slurried in 440 ml. of 6 N HCl for 2 hours at 100°C. It was then cooled to 0°C and diluted. The mixture was thick and viscous and difficult to filter even through Whatman #52 filter paper. After filtering, the boride was stirred in 1200 ml. of water made slightly acid with 4 ml. of concentrated HCl in order to remove any adhering salts; it was then filtered, rinsed with water followed by acetone, and air dried. The product appeared damp and tended to clump similar to the starting material. It also showed intensification of the extraneous lines at 2.68 and 2.32 Å in the X-ray powder pattern. The product was not subjected to elemental analysis.

2.5 Purification of Zirconium Diboride by Acid Leaching followed by High-Temperature Vacuum Treatment

The zirconium diboride which was leached with hydrofluoric acid (Sample #386-68-E) was heated to high temperatures in vacuum under the same conditions as those given in section 2.2. The X-ray powder pattern of the product (Sample #392-50-B) was free of extraneous lines. The elemental analyses are given in Table 16 (see also Fig. 3).

Table 16

Elemental Analyses of Sample #392-50-B:

ZrB_2 after Acid Leaching and Heating under Vacuum

	LeDoux		Pacific SpectroChemical
Zr	80.75	80.79	
B	18.70	18.70	
Zr + B	99.45	99.49	
B/Zr	1.952	1.951	
C	0.13	0.14	
N	0.05	0.05	
O	0.53	0.55	
Fe	0.04	0.04	0.028
Total	100.20	100.27	
Ti			0.032
Al			0.044
Mg			trace (<0.0005)
Si			0.0094
Cu			trace (<0.0003)
Hf			nil
Other			nil

2.6 Purification of Zirconium Diboride by Acid Leaching followed by High-Temperature Vacuum Treatment followed by a Second Acid Leaching

Part of the zirconium diboride from the previous section (Sample #392-50-B) which was leached with hydrofluoric acid and then heated under vacuum was again leached with hydrofluoric acid using the procedure described in section 2.4. The X-ray powder pattern of the product (Sample #392-50-D) was essentially free of extraneous lines. The elemental analyses are given in Table 17.

Table 17

Elemental Analyses of Sample #392-50-D: ZrB_2 after Acid Leaching, Heating under Vacuum and a second Acid Leaching.

	LeDoux		Pacific SpectroChemical
Zr	80.74	80.93	
B	18.71	18.75	
Zr + B	99.45	99.68	
B/Zr	1.953	1.953	
C	0.12	0.12	
N	0.05	0.05	
O	0.55	0.53	
Fe	0.03	0.03	0.022
Total	100.20	100.41	
Ti			0.028
Al			0.036
Mg			trace (<0.0005)
Si			0.020
Cu			trace (<0.0003)
Hf			nil
Other			nil

2.7 Comparison of Purification Methods

A survey of the most important data given in the sections on the purification of zirconium diboride is contained in Fig. 3 . The levels of the major impurities (C, N, O, and Fe) are given as a function of the treatment received by a particular sample. Oxygen contents were increased by heating, presumably due to contamination from the mullite tube or diffusion of air through the walls of the tube at high temperature.[1]

[1] Difficulty in obtaining a high vacuum indicated that the tube had some porosity at high temperatures.

The carbon and nitrogen levels were greatly reduced by hydrofluoric acid leaching but not if the sample was first heated under vacuum at approximately 1500°C. The sample of highest purity was considered to be #386-68-E, the material which was acid leached only. It contained a measured zirconium plus boron content of 99.29%, and the sum of the values determined for carbon, nitrogen, oxygen, and iron was 0.71%.

2.8 Analytical Procedures

The analytical data in Tables 12-17 are listed according to the firm which supplied the information. The major part of the chemical analyses were performed by LeDoux & Company, Inc., Teaneck, N. J. (see Table 18 for procedure). Additional information was supplied by Truesdail Laboratories, Inc., Los Angeles (see Table 19 for procedure). The semiquantitative spectrographic analyses were performed by Pacific SpectroChemical Laboratory, Los Angeles, and, in one case, by LeDoux. The General Atomics Division of General Dynamics, San Diego, California, determined the oxygen content reported in Table 12 using fast-neutron activation analysis.

Table 18

Outline of Method of Analysis for Elements in ZrB_2
(LeDoux & Co., Inc.)

Element	Analytical Method
Zr	Digested in HF + HNO_3; Heated to dryness with HF; Salts dissolved in tartaric acid; Zr precipitated with cupferron and ignited; Purity of ZrO_2 determined spectrographically.
B	Fused in NaOH; Dissolved in HCl; Zr precipitated with $BaCO_3$; Boric acid titrated in presence of mannitol.
C	Combustion in presence of Fe + Cu; Conductometric measurement of CO_2.
N	Digested in HF + H_2O_2; Kjeldahl determination.
O	Inert gas fusion using Pt flux.
Fe	Photometric determination of ortho-phenanthroline complex.

Table 19

Outline of Method of Analysis for Elements in ZrB_2

(Truesdail Laboratories, Inc.)

Element	Analytical Method
Zr	Dissolved in $H_2SO_4 + H_2O_2$; Evaporated to dryness and dissolved in HCl; Precipitated Zr with p-bromomandelic acid; Filtered and ignited to ZrO_2.
B	Fusion in $Na_2CO_3 + NaNO_3$; Dissolved in HCl; Precipitated Zr with $BaCO_3$; Boric acid titrated in presence of mannitol.
C	Combustion.
N	Kjeldahl.
Fe	Photometric determination of ortho-phenanthroline complex.

V. SINGLE CRYSTAL GROWTH AND PURIFICATION*

A. Introduction

Single crystals of the refractory metal diborides can be produced by a method of floating-zone melting[1, 2]. The floating-zone method is preferred since there is no sample container needed which might contaminate these high melting compounds (2900°C to 3250°C). Since these materials are most easily obtained in the form of powders (see Section III), specimens for zone melting are prepared by sintering powders into rods approximately 3/8 inch diameter by 8 inches long. Melting is produced by radio frequency induction heating in the apparatus shown in Fig. 4. Power is supplied by a 450 kc 10 kw generator equipped with a manually operated thyratron output control. In most cases boron is added to the diboride powder before sintering so that the excess will compensate for the boron loss due to vaporization at the melting point. Metallographic inspection, X-ray diffraction, and wet chemical analysis of the preliminary zone refined bars are used to determine the proper boron adjustment for a series of fabrication experiments.

Experimental problems stemming from the preferred vaporization of one constituent, prohibit the use of either very slow melting speeds or multiple pass techniques. Therefore, purification by the zone refining method is limited. Impurities which are volatile at the melting temperature will be decreased, but impurities such as refractory metals will for the most part remain. For this reason, high purity starting materials with respect to refractory impurities are needed.

---

*Gerald Clay, Arthur D. Little, Inc.

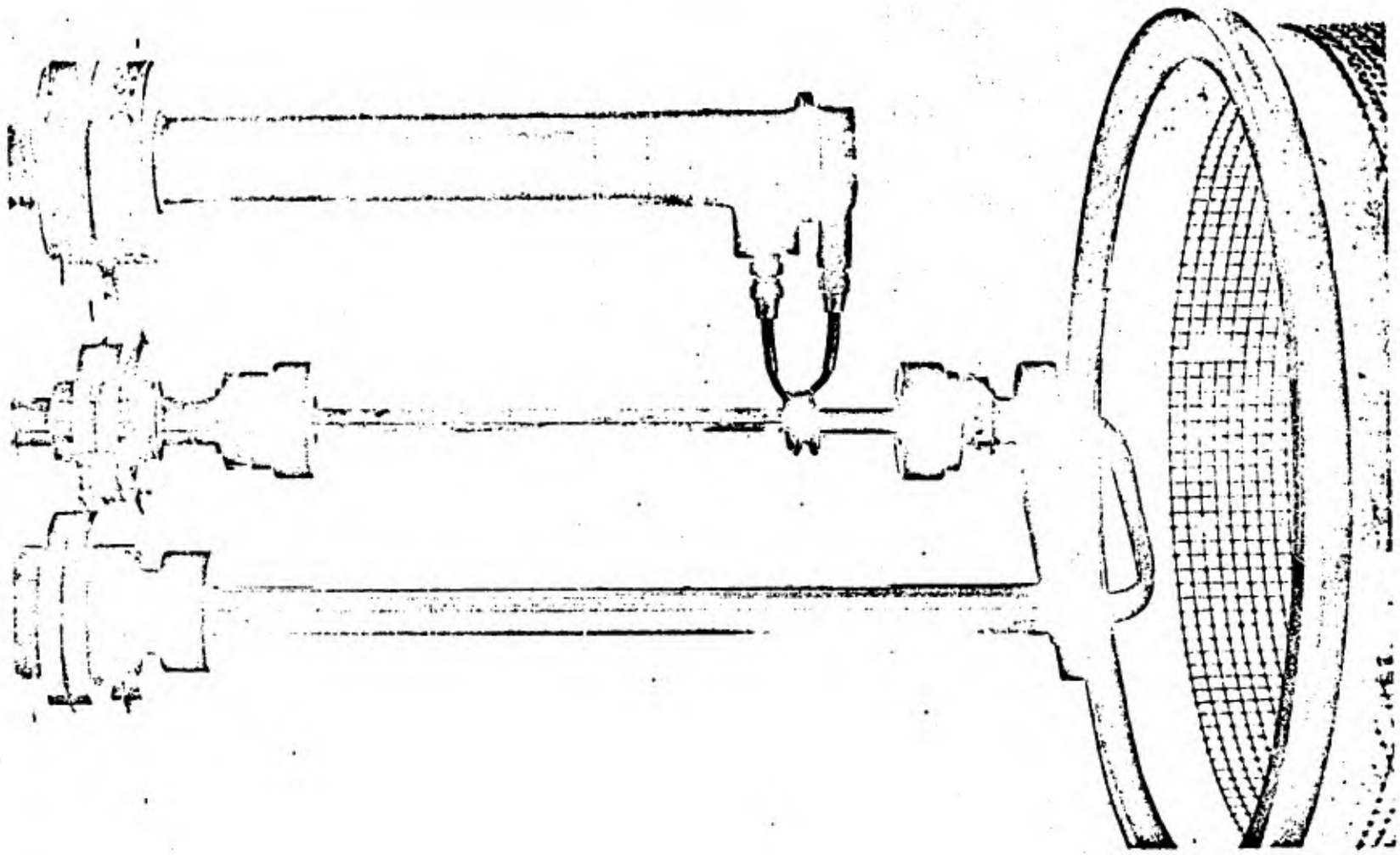

Fig. 4 - Interior of Zone Refiner Showing Movable Coil and Sintered Sample Bar in Place.

Grain size in materials produced by this method increases with distance traveled. It is therefore expected that the beginning of each specimen will be polycrystalline. All samples investigated, however, have a thin polycrystalline skin at the surface, and contain either a large grain polycrystalline area, or single grains within this skin.

B. Niobium Diboride

1. Composition Adjustment - Starting material U.S. Borax NbB_2 (#1)

Several samples of NbB_2 were made with initial boron additions to provide starting mixtures with 7 atomic percent, a/o, excess based on the theoretical content of boron in NbB_2. The product showed a second phase on metallographic examination. By increasing the amount of boron added to the starting material to 10 a/o excess, bars were produced which were single phase as evidenced by metallographic examinations and X-ray diffraction. Bar No. 435 is an example of this group of material. Chemical analysis of this bar, however, indicated that the sample was somewhat boron deficient ($NbB_{1.94}$). By adding 14 a/o excess boron to the NbB_2 powder before sintering, it was possible to make a batch of homogeneous material (Bar Nos. 468 to 532). This boron addition generated problems with the control of the melting. The results at that time indicated that additional boron could not profitably be added, without sacrificing the uniform melting which is necessary to produce single crystals or even large grained material.

The average composition of bars from the latter group is $NbB_{1.968}$ with a range of $NbB_{1.909}$ to $NbB_{1.997}$ compared to the starting composition of $NbB_{1.724}$. Table 20 contains the results of all niobium and boron analyses.

Table 20

Results of Metal and Boron Analyses on NbB_2
(Ledoux and Co., Teaneck, N.J.)

Bar No.	Nb(w/o)	B(w/o)	B + Nb(w/o)	B/Nb
435-2	81.51	18.45	99.96	1.945
469-2A	82.16	17.96	100.12	1.878
473-1	82.01	18.22	100.23	1.909
477-2	81.41	18.69	100.10	1.973
527-2	80.93	18.79	99.72	1.995
531-3	80.51	18.71	99.22	1.997
		Average	99.89	

Bar No. 469 appeared to have formed an oxide coating during sintering. Since the chemical analysis indicated a substantial boron loss, this bar and one other with a surface similar in color were omitted from the lot.

2. Purification

Qualitative spectrographic analyses were used to indicate the general impurity level; wet chemical analyses and quantitative spectrographic analyses were used to determine specific elements.

Carbon, oxygen, nitrogen, and iron were detected in the following amounts:

C - 0.0121%
N - 0.0045%
O - 0.0066%
Fe- 0.0001%

as compared to the starting material: (see Appendix A)

C - 0.033%

N - 0.025%

O - 0.48%

Fe - 0.07%

Table 21 shows the level of the remaining impurities in the melted sample compared to the level in the starting material. The total impurity level is in the range of 0.15% to 0.27%. The average total of Nb and B is 99.89, thus this material is approximately 99.7 to 99.9% pure.

Table 21

Spectrographic Analysis of NbB_2 Impurity Level

Element	After Melting	Starting Material
Ti	0.13%	0.01 - 1.0%
Cr	0.001 - 0.01%	0.01 - 1.0%
Na	0.001 - 0.01%	0.001 - 0.01%
Al	0.001 - 0.01%	0.01 - 0.1%
Mg	0.001%	0.001 - 0.01%
Ca	0.001%	0.001 - 0.1%
Ni	0.001%	0.001 - 0.1%
Cu	0.001%	0.001 - 0.1%
Si	0.001%	

All other elements detectable by spectrographic analysis were 0.001% or less.

3. Crystal Growth

The photo-macrographs in Figs. 5 and 6 show two cross sections of NbB_2 Bar No. 435. The section shown in Fig. 5 was taken from the beginning of the bar approximately 1 inch from the start. It indicates two major grains.

The section shown in Fig. 6 was taken approximately 3 inches from the start: it reveals one major grain and several minor grains at the surface. These photographs also show the problem encountered with cracking in NbB_2 samples.

C. Zirconium Diboride

1. Composition Adjustment - Starting material U.S. Borax ZrB_2(#1)

Preliminary experiments were performed on bars sintered with enough boron to bring the starting material to stoichiometry plus various amounts up to 12^a/o excess. Metallographic analysis on all except the 12^a/o excess bar show a second phase. Fig. 7 shows a section of a bar prepared from starting material with 7^a/o excess boron. Figs. 8 and 9 are sections of a 12^a/o excess bar. Since the homogeneity range of ZrB_2 is quite small, the 12^a/o excess boron composition was considered optimum. Chemical analysis on this bar gave $ZrB_{1.982}$. Table 22 contains the results of chemical analyses for zirconium and boron on typical samples of ZrB_2. From these results the average composition is $ZrB_{1.983}$ with a range from $ZrB_{1.946}$ to $ZrB_{2.023}$. This shows an improvement over the starting material which analyzed as $ZrB_{1.88}$.

Table 22

Chemical Analysis of ZrB_2
(Ledoux and Co., Teaneck, N.J.)

Bar No.	Zr (w/o)	B (w/o)	Zr + B (w/o)	B/Zr
514-5	80.93	19.01	99.94	1.982
548-3	80.74	20.36	100.10	2.023
572-4	80.88	18.65	99.53	1.946
		Average	99.86	1.983

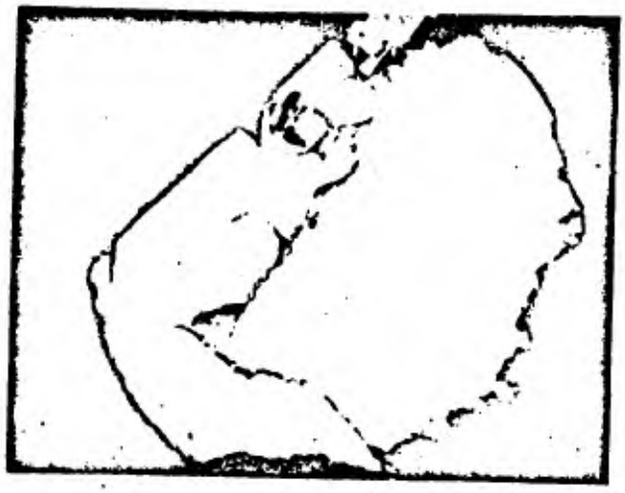

Fig. 5 - NbB_2 No. 435-1C, etched with a 60% glycerin-20% HNO_3 - 20% HF mixture, 10x polarized light.

Fig. 6 - NbB_2 No. 435-4A, as polished, 10x polarized light.

Fig. 7 - ZrB_2 No. 504 (7 a/oxSB) as polished, 50X

Fig. 8 - ZrB_2 No. 514-8 (12a/oxSB) etched with HNO_3-Hf mixture, 50X

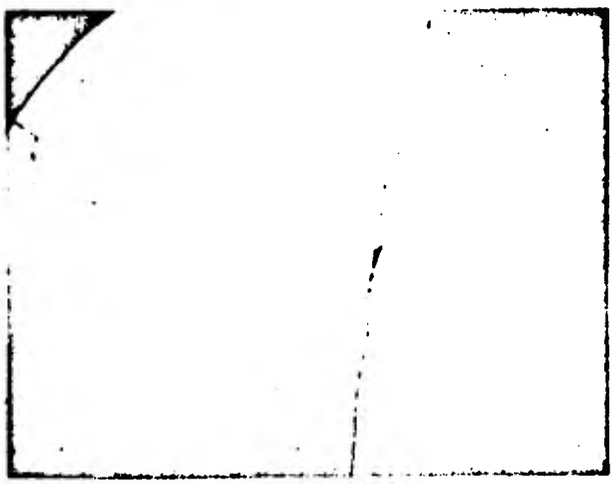

Fig. 9 - ZrB_2 No. 514-8 12 a/oxSB) etched with HNO3-Hf mixture, 10X

2. Purification

Qualitative spectrographic analyses by Jarrell-Ash Company, Newtonville, Massachusetts, showed only the following impurities: (wt.%)

Si - 0.01 - 0.1%

Ca - 0.01 - 0.1%

Ti - 0.001 - 0.1%

Sn - 0.001%

All other impurities detectable by spectrographic analysis were less than 0.0001%. Quantitative spectrographic analyses were made for the following elements and showed:

Ca -	50 ppm
Fe -	50 ppm
Mo -	20 ppm
Na -	20 ppm
Si - Less than	20 ppm
Ti -	100 ppm

Chemical analysis by Ledoux and Company gave:

C - 0.0702% and 0.0232%

N - 0.0040%

O - 0.0074%

Fe - 0.0001%

compared to the starting material (see Table I)

C - 0.33%

N - 0.19%

O - 0.53%

Fe - 0.046%

The lot of ZrB_2 from this information is in the range of 99.9% pure with carbon as the major impurity.

3. Crystal Growth

As in the case of NbB_2, the beginning end of the ZrB_2 bars are polycrystalline as shown in Fig. 10 . Metallography on sections nearer the end indicate grain boundaries only near the surface. Laue photographs taken in the center portion of these cross sections show slight splitting of the spots indicating striations or subgrain boundaries but no major grain boundaries.

D. Titanium Diboride

1. Composition Adjustment - Starting material U.S. Borax TiB_2 (#1)

The average composition of the starting material is $TiB_{1.99}$. Attempts to increase this boron content were entirely unrewarding. Following the general procedure used with the other compounds, bars were sintered with 8, 10 and 12 a/o excess boron. Although the 8 a/o bars sometimes gave single phase material, as determined by metallographic analysis, the melting behavior of this material caused severe experimental difficulties. The major problem was arcing between the sample and the work coil. Increased boron content appeared to alleviate the situation, but this procedure always afforded two-phase material as the product, as shown in Figs., 11 and 12. One such bar (No. 517, 10 a/o excess boron), which represented a starting composition of $TiB_{2.271}$, was analyzed by Schwarzkopf Microanalytical Laboratory, Woodside, New York. The results showed a final composition of $TiB_{2.415}$. This loss of Ti is contrary to what was expected from experience and from vapor pressure considerations. A bar was then made from the starting material ($TiB_{1.98}$); the analysis of this material ($TiB_{1.975}$) indicated that a small amount of boron was

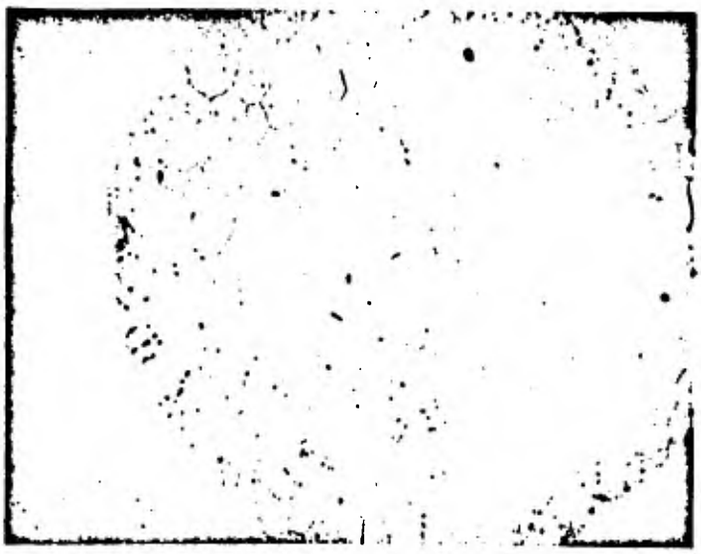

Fig. 10 - ZrB_2 No. 561 As polished 10X

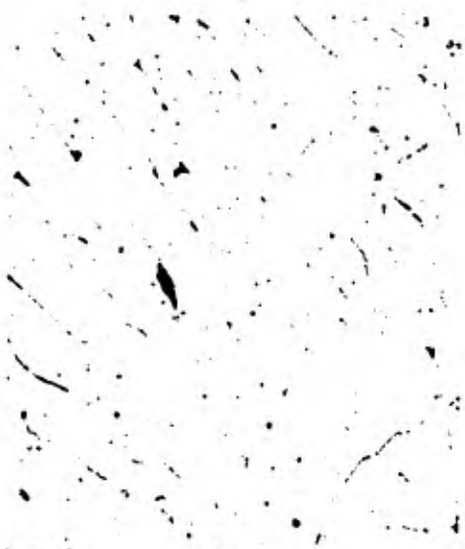

Fig. 11 - TiB_2 No. 522-1
As polished 100X

Fig. 12 - TiB_2 No. 606-4
As polished 400X

lost. Both metallography and X-ray diffraction performed to date indicate that this material is single phase. Although the approximate starting composition has been defined, a considerable amount of additional work is necessary to achieve uniform and controllable melting conditions needed for the preparation of single crystal material.

E. Tantalum Diboride

1. Composition Adjustment - Starting material Kawecki TaB_2 (#1)

Bars were sintered containing up to 12^a/o excess boron. Additions of from 8 to 10^a/o produced single phase material whereas 12^a/o additions produced a two phase sample. Although melting conditions were somewhat better in the case of the 10^a/o addition, chemical analysis showed a boron to metal ratio of 2.05. Thus 9^a/o excess boron was chosen as the optimum addition for the composition adjustment. Table 23 contains the results of chemical analyses for Ta and B on typical samples from the lot.

Table 23

Chemical Analysis of TaB_2*

Bar No.	Ta (w/o)	B (w/o)	Ta + B (w/o)	B/Ta
576-5	89.11	10.92	100.03	2.04
659-3	88.56	11.56	100.12	2.18
679-2	88.55	11.48	100.03	2.16
675-3	89.0	10.9	99.9	2.05
		Average	100.02	2.11

*All analyses by Ledoux and Co., Teaneck, N.J. except sample No. 675-3, analysis by Donald Gurnsey, M.I.T.

2. Purification

Qualitative Spectrographic Analysis of TaB_2 by Jarrell-Ash Co., Newtonville, Massachusetts showed the following impurities:

Mg - 0.001%

Al - 0.001%

Si - 0.001 - 0.01%

Ca - 0.001%

Ti - 0.001 - 0.01%

V - 0.001%

Cr - 0.001 - 0.01%

Fe - 0.001%

Ni - 0.001%

As - 0.001%

Ag - 0.001%

All other elements detectable by spectrographic analysis were 0.0001% or less. Results of quantitative spectrographic analyses for Si, Ti and Cr are forthcoming.

The following results were obtained from Ledoux and Co.

C - 51 ppm and 350 ppm

N - 22 ppm

O - 32 ppm and 25 ppm

compared to starting material (see Table 1)

C - 0.38%

N - 0.0098%

O - 0.68%

Thus the TaB_2 sample has a total impurity level in the range of 0.05% by weight.

3. Crystal Growth

In the case of each of the previously mentioned materials, cracking has been somewhat of a problem. Once single phase, single crystals were obtained, the cracking problem became more severe. Cracking has been a major problem in the fabrication of TaB_2; a section of a cracked sample is shown in Fig. 13. Since the presence of grain boundaries appeared to alleviate the cracking problem somewhat, the samples of TaB_2 were prepared at increased growth speeds in order to expedite sample preparation for some of the measurements which could be performed on this type of material. More work will be needed in order to achieve melting conditions satisfactory for single phase, single crystals.

F. Hafnium Diboride

1. Composition Adjustment- Starting material Wah Chang HfB_2(#1)

Several samples of HfB_2 were melted containing up to 14^a/o excess boron in the starting powder. Both X-ray diffraction and metallography indicated the presence of a second phase in this material. An addition of 14^a/o excess boron produced a sample which contained a two phase region at the beginning, and a single phase region toward the end of a given bar. Since the homogeneity range, is suspected to be extremely small, this addition appeared to be optimum. An addition of 18^a/o excess boron, however, produced a sample which was two phase in a region near the beginning, single phase throughout the central portion, and two phase at the end. The photomicrographs in Figs. 14 and 15 show the appearance of the second phase near the start of the bar at 50 and 400X respectively; the photomicrographs in Figs. 16 and 17 show the appearance of the second phase at the end of the bar at 50 and 400X respectively. From previous experience it appears that the boron vaporizing from the molten zone is condensing on the sintered bar above and effectively adding to the amount of excess boron. For this reason, samples for

chemical analysis were taken immediately after the sections shown in Figs. 14 and 15 , and immediately before those shown in Figs. 16 and 17 . Both analyses, however, showed a boron to metal ratio of 1.97 (see Table 24). This could indicate that the small difference in composition on each side of the homogeneity range is not within the accuracy of the chemical analysis. One other sample from the center portion of a bar was analysed and showed a boron to metal ratio of 2.01.

Table 24

Chemical Analysis of HfB_2
(Ledoux and Co., Teaneck, N.J.)

Bar No.	Hf (w/o)	B (w/o)	Hf + B (w/o)	B/Hf
742-2A	89.32	10.63	99.95	1.97
742-2C	89.35	10.68	100.03	1.97
738-2B	89.33	10.88	100.21	2.01
		Average	100.06	1.98

2. Purification

Qualitative spectrographic anaiysis by Jarrell-Ash Co., Newtonville, Massachusetts showed:

Na - 0.001%

Al - 0.001%

Ti - 0.001%

Ag - 0.001%

All other elements detectable by spectrographic analysis were less than 0.0001%.

The only significant purification of the starting material (see Table 1) here is with respect to Fe, i.e. from 0.1% to 0.0001% by weight.

Fig. 13 - TaB_2 No. 671-2 As polished 100X

Fig. 14 - HfB_2 No. 742-1, as polished 50X (taken 1/4 in. from start of bar)

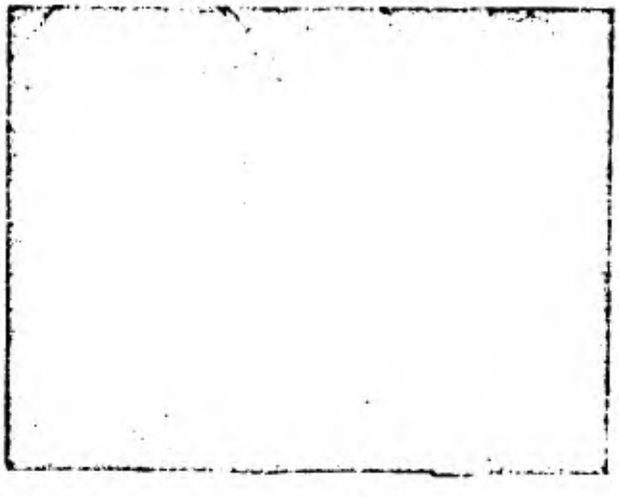

Fig. 15 - HfB_2 No. 742-1, as polished 400X

Fig. 16 - HfB_2 No. 742-3, As polished, 50X (taken 1/4 in. from end of bar)

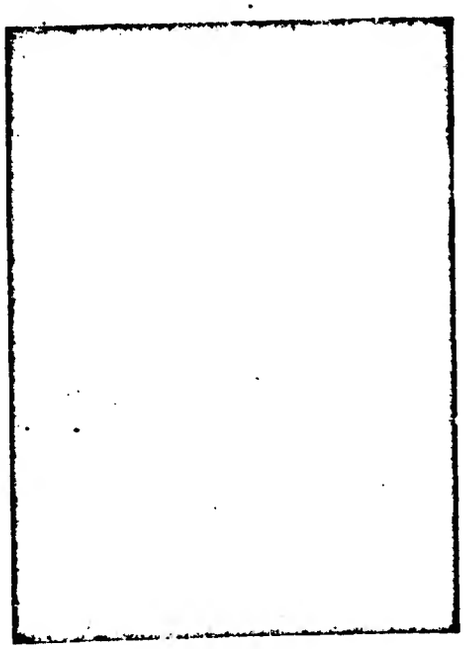

Fig. 17 - HfB_2 No. 742-3, As polished, 400X

One sample of HfB_2 representing two phase material, was analyzed for carbon by Ledoux and Co., and gave 0.111% carbon by weight. Three samples, representing the single phase material, were analyzed, again by Ledoux and Co., and show 254 ppm, 535 ppm and 429 ppm of carbon by weight.

One sample of single phase material and one sample of two phase material were analyzed for oxygen; the results were: 0.011% and 0.024%, respectively. One sample analyzed for nitrogen gave 120 ppm or 0.012% by weight. Thus, the total impurity level is in the order of 0.1% by weight. If two phase material is not considered as a representative sample, then the non-metallic impurities have, in general, been reduced by approximately an order of magnitude.

3. Crystal Growth

The photomacrograph of a longitudinal section of a complete bar of HfB_2 is shown in Fig. 18 . Growth speed for this bar was five inches per hour, whereas the typical samples were grown at ten inches per hour. Note the rapid predomination of the grain of preferred growth. This photograph also shows the previously mentioned polycrystalline skin and the shape of the solid-liquid interface during growth.

G. Areas of Future Work

The experimental difficulty with TiB_2 was caused by excessive volatility at the melting point. This behavior was not encountered with the other diborides for which boron alone was the major volatile constituent. These problems could be minimized by increasing the density of the sintered starter bars to 80% or 90% of the theoretical value. Starting material of this nature would decrease the area for evaporation, reduce the migration of liquid into the sintered bar, and improve the electromagnetic coupling.

Fig. 18 - HfB_2 No. 712-2,
Rough polished 5X

With regard to NbB_2 and TaB_2 these materials have a broader range of homogeneity than ZrB_2 and HfB_2. Thus, the former are easier to prepare as single phase material, but more difficult to prepare with an exact stoichiometry. These problems are complicated because metallography is not a reliable guide to chemical composition. By increasing the number of chemical analyses during the composition adjustment, or possibly by using lattice parameters as a guide to composition, it should be possible to prepare material of any composition within the range of homogeneity.

As previously described, the conditions, under which the zone melting is performed here, leave refractory metal impurities in solid solutions, i.e. the technique becomes a zone levelling process. This procedure can be used for doping or producing mixtures of two or more of the metal diborides. Such mixtures may enhance some of the physical or chemical properties. For example, if the oxidation of a material is diffusion controlled, the addition of metal ions of higher valence will fill anion vacancies in the oxide and thus retard the diffusion of oxygen. The zone melting method would lend itself quite well, for instance, to the addition of tantalum or molybdenum to zirconium or hafnium diboride.

REFERENCES

1. Pfann, W.O., Zone Melting, John Wiley and Sons, Inc., New York, 1958.
2. McClaine, L.A., "Thermodynamic and Kinetic Studies for a Refractory Materials Program," ASD-TDR-62-204 Part I, Arthur D. Little, Inc. January, 1962.

VI. HIGH PRESSURE HOT PRESSING*

A. Introduction

The initial purpose of this subtask was to investigate the feasibility for using high pressure (10-30 kilobars, i.e. 150,000-450,000 psi) and high temperature (2000°-2600°C) to fabricate refractory metal diborides in the form of high density cylinders of approximate dimensions 1 inch length by 0.30 inch diameter. Samples of this size could be processed in this way with the available apparatus at ManLabs and would be adequate for many of the evaluation tests which were planned for this program. The results obtained for TiB_2 demonstrated that this technique could provide high density (95-99% of theoretical), crack free, polycrystalline material fabricated in the above sizes. At the same time in the progress of the overall program it became apparent that the physical integrity of the available zone-refined material would not be adequate for many of the planned evaluation tests.

Accordingly, high pressure hot pressing evolved into a fabricating procedure. Specimens were made for measurement of the following quantities: hot hardness, resistance, thermal expansion, oxidation and thermal conductivity. It is anticipated that this procedure will also supply specimens for future experiments involving strength measurements, phase boundary determinations, the fabrication of composite materials, and the preparation of single phase materials of variable compositions.

B. General Characteristics of the Technique

Before discussing this fabrication procedure it is instructive to define several processes used in powder metallurgy. Sintering is a fabricating process

---

*E. V. Clougherty, ManLabs, Inc.

in which powders are first cold compacted into a desired shape, then heated in vacuo or in an inert atmosphere in the solid state until densification is observed. Hot pressing is a fabricating procedure in which powders are first heated until a definite shrinkage is observed, then pressure is applied while the heat is maintained until final densification is noted. High pressure hot pressing, the technique used in the present subtask, is a fabricating procedure in which powders are first cold compacted in a small hydraulic press, then further cold compacted at high pressure (10 kilobars). Next, the temperature is increased (heating power is supplied by passing current through the pistons and the graphite furnace) and the applied load is maintained constant until densification takes place. The pressure and temperature are then released in a step-wise manner until electrical contact is lost, then the specimen cools to room temperature. The step-wise procedure is designed to avoid cracking of the specimen during cooling after densification. It is generally accepted that hot pressing affords higher densification than sintering. High pressure hot pressing can provide materials with theoretical densities. It is well known that the mechanical properties of materials which are fabricated by powder metallurgical procedures are drastically improved as densification approaches the theoretical limit.[1,2,3,4]

The requirements for starting materials for the high pressure hot pressing procedure differ from those of other fabricating techniques. In particular, the presence of low melting impurities e.g.,Fe, Cr, Ni presents a serious difficulty because these materials must also be retained in the densified product. Excessive amounts of adsorbed and absorbed gases could lead to considerable porosity in the product. Among the powder metallurgical techniques which are designed to produce polycrystalline

materials, the high pressure method has the advantage that recrystallization and grain growth will be decreased.

A previous attempt to use the high pressure hot pressing technique has been reported.[5] In the latter investigation extremely high pressure (55 kilobars) was used in an attempt to prepare high boron alloys. The present investigation is primarily a fabricating technique using considerably less drastic experimental conditions than the above method which was primarily a synthetic technique.

C. Experimental Procedure

The dry powders, used as received, were packed with aid of a hydraulic press into the furnace liner in the apparatus which is shown schematically in Fig. 19. The high pressure components were assembled and the load was raised to 400 psi at room temperature. This load provides a pressure of approximately 10 kilobars on the specimen powders. Next, the powders were heated to the desired temperature for 5 to 10 minutes; the applied load was maintained constant. The temperature is estimated by a linear extrapolation of power input versus temperature curve; the latter is obtained experimentally between room temperature and 1500°C. The load and temperature are gradually reduced in a step-wise manner until electrical contact is lost, then the temperature falls to ambient. In practice, experimental difficulties sometimes cause the temperature to fall to ambient before the pressure can be released. After the experiment is completed, or otherwise terminated, the product is removed from the fabricating assembly and examined as follows:

(1) X-ray Analysis. Contamination from the liner and furnace assembly and the presence of additional metal boron phases resulting from the pressure-temperature treatment are checked.

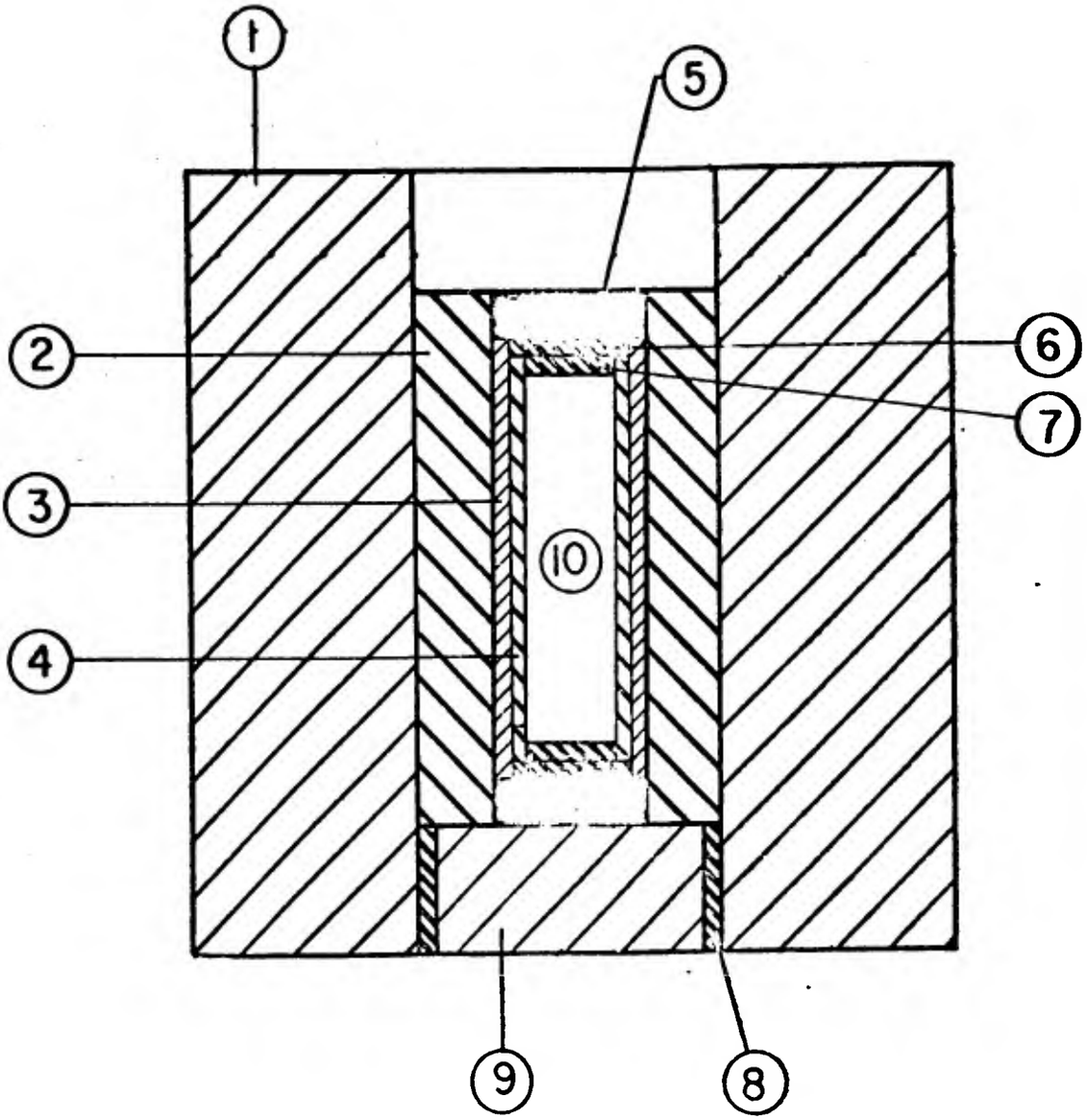

1. DIE (TUNGSTEN CARBIDE)
2. OUTER INSULATION (LAVA)
3. FURNACE (GRAPHITE)
4. LINER (BORON NITRIDE)
5. CARBON PAD
6. BORON NITRIDE PAD
7. BORON NITRIDE PAD
8. LAVA SLEEVE
9. CLOSURE (HARDENED STEEL)
10. SPECIMEN (0.4" DIA. X 1.0" LONG)

Fig. 19 - Schematic diagram of high pressure hot pressing apparatus.

(2) Metallographic Analysis. Specimens are examined in the 'as-polished' and 'etched' condition. Pertinent photomicrographs are taken. Grain size determinations are performed. Physical appearance is noted.

(3) Density Measurement. Specimens are weighed in water and in air and density is computed.

(4) Chemical Analysis. Selected samples are analyzed for boron and metal.

(5) Resistivity. The resistivity is measured at room temperature to check for porosity and excessive cracking.

D. Results and Discussion

1. Evaluation of Fabricated Material

A summary of experimental conditions and product evaluation results for selected high pressure hot pressing experiments on TiB_2, ZrB_2, HfB_2, NbB_2 and TaB_2 are presented in Table 25. A large number of experiments were performed on TiB_2 in the development of the technique. A photograph of eleven specimens of fabricated TiB_2 is shown as Fig. 20. Representative photomicrographs (Figs. 21-25) demonstrate the fine grain structures of material fabricated by this technique. The results to-date indicate significant success for TiB_2, ZrB_2, and HfB_2; the fabricated cylinders of NbB_2 and TaB_2 showed densities in the 90% of theoretical region. It should be pointed out that the initial task in this endeavor was a feasibility study. Accordingly, no effort has been placed on studying the roles of powder treatment and powder particle size as variables in the high pressure hot pressing procedure. It is significant that the starting powders of NbB_2 and TaB_2 are of smaller particle size than the other powders. The smaller particle size limits the

Table 25

High Pressure Hot Pressing Fabrication of Refractory Metal Diborides

Run No.	Average Extrapolated Temperature(°C)	Time (Min.) at Average Temperature(°C)	Physical † Appearance	Density (g./cm^3) Measured	% Theoretical	Resistivity ($\mu\Omega$ cm)
TiB_2-61	2500	5	1	4.38	96.7	-
-63	2575	8.5	1	4.28	94.5	-
-64*	2500	6.5	2	4.33	95.4	-
-70*	2450	5.5	1	4.48	99	-
-71	2450	5	1	4.37	96.4	13.4
-72	2400	3	1	4.37	96.4	13.2
-73	2400	5	2	4.33	95.4	11.6
ZrB_2-1*	2475	6	1	6.03	98.9	10.2
-2	2500	5	2	5.66	92.9	20.2
-3	2500	5	2	5.94	97.4	12.4
-12	2450	6	2	6.00	98.2	10.3
HfB_2-1*	2550	4	2	10.74	97.9	-
-2	2400	4	2	10.64	94.5	10.3
-3	2450	5	2	10.69	95.3	-
NbB_2-1±	2350	2	>4	6.41	89.6	-
-3	2200	4	>4	6.50	90.8	28.2
-9	2500	3	2	6.52	91	20.8
TaB_2-1±	1800	1	2	10.73	85.1	63.4
-12±	2400	4	1	10.53	83.5	49.4

† - Number of pieces removed from the sample cell after completion of a run.
± - Power failure occured at maximum temperature
* - The products of the runs indicated by (*) were analyzed for metal and boron. The results were:

Material Analyzed**	Fabricated M(w/o)	Fabricated B(w/o)	Fabricated B/Me	Fabricated B + M(w/o)	Starting Material M(w/o)	Starting Material B(w/o)	Starting Material B/Me	Starting Material B + M(w/o)
TiB_2-64	69.4	30.39	1.95	99.8	68.7	30.97	1.99	99.7
TiB_2-70	69.3	30.36	1.95	99.7	-- --	-- --	Same --	-- -- --
ZrB_2-1	80.6	17.55	1.83	98.2	80.5	17.97	1.89	98.7
HfB_2-1	88.3	10.51	1.96	98.8	89.0	10.6	1.97	99.6

**Analyses by D. Gurnsey, Metallurgy Department, M.I.T.

Fig. 20 - High pressure hot pressed titanium diboride (actual size).

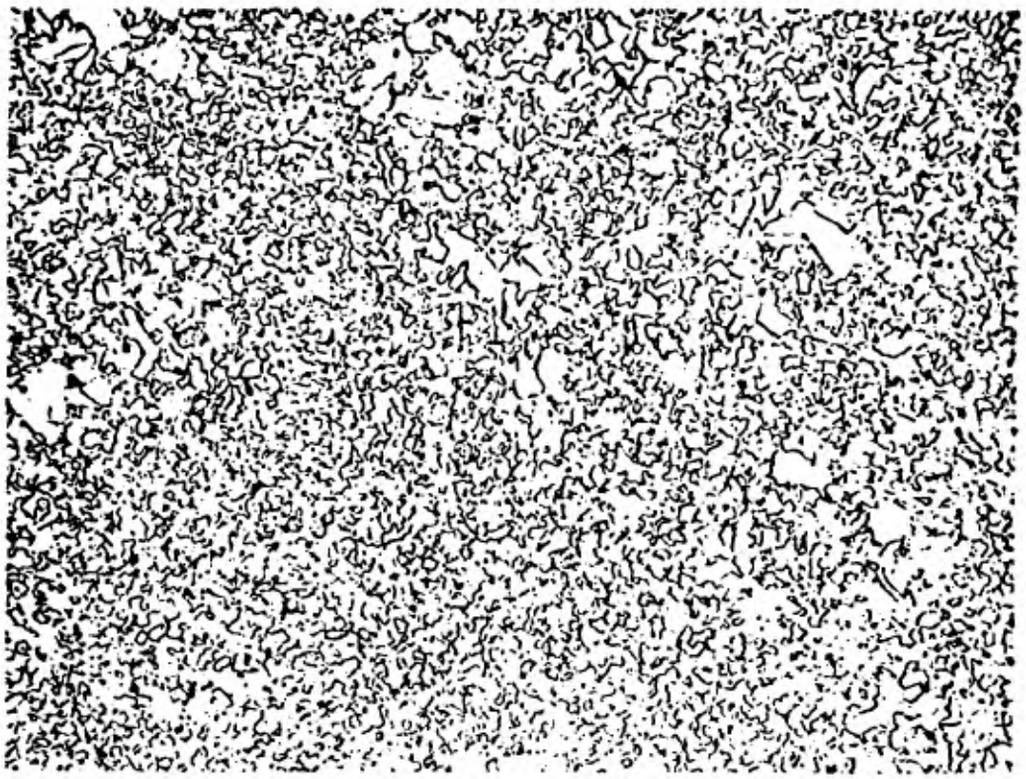

Fig. 21 - Product Run No. TiB_2-64, Etched 500X

Major Area

Etchant 1 HF: 1 HNO_3: 3 Lactic Acid

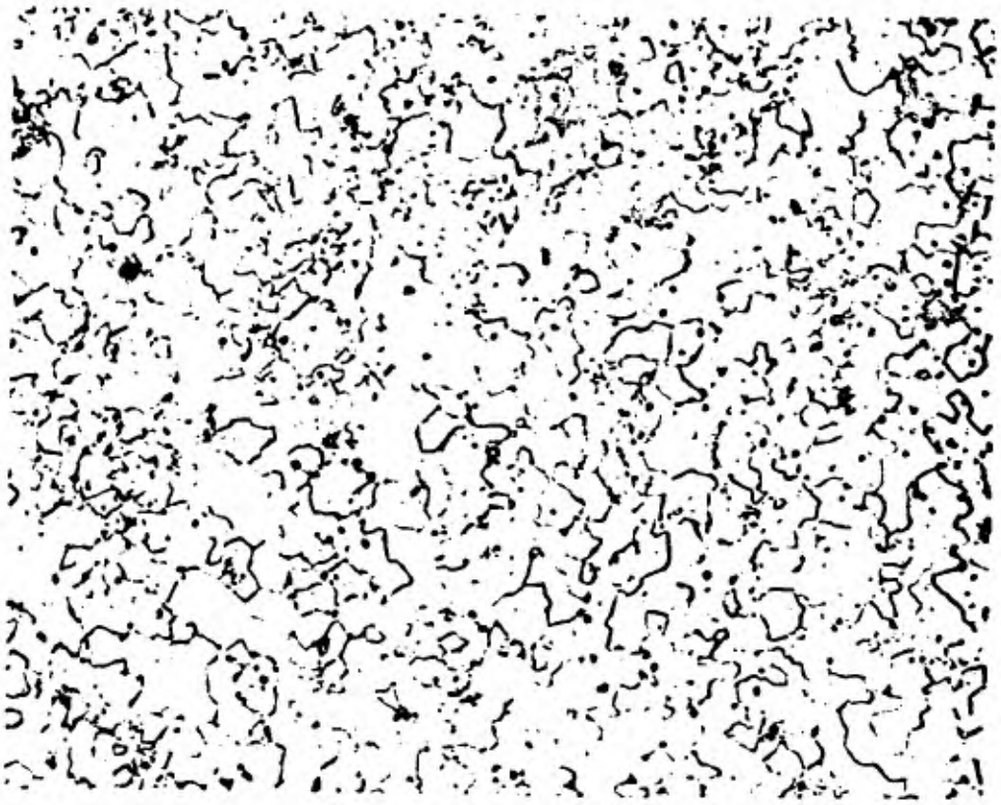

Fig. 22 - Product Run No. ZrB_2-4, Etched 500X

Major Area

Etchant 1 HF: 1 HNO_3: 3 Lactic Acid

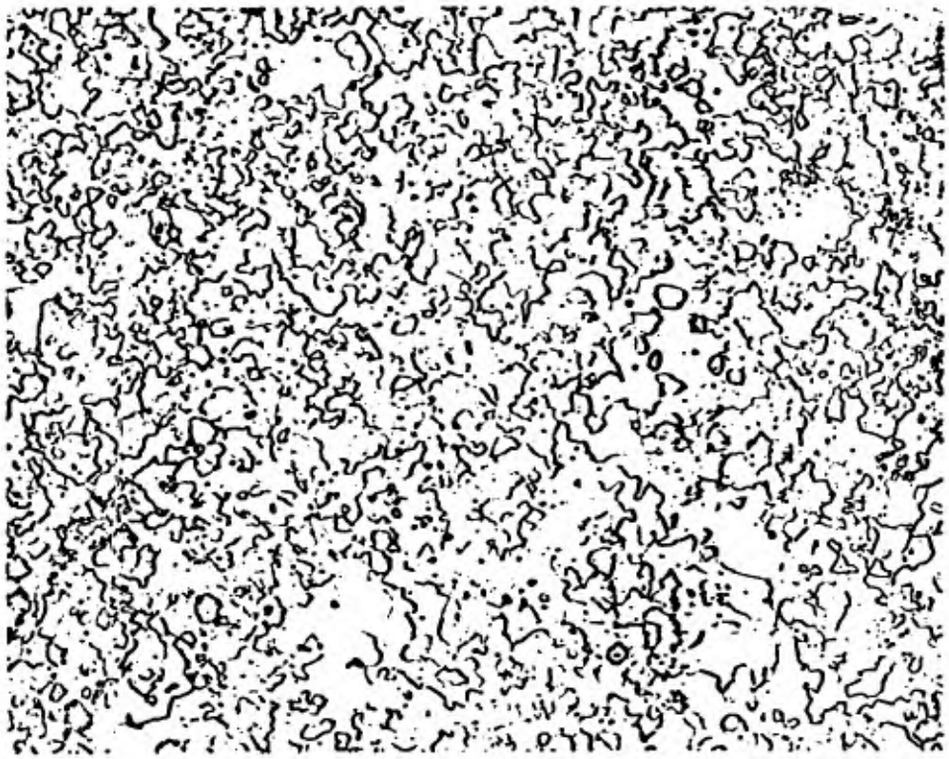

Fig. 23 - - Product Run No. HfB_2-1, Etched 500X

Major Area

Etchant 1 HF: 1 HNO_3: 3 Lactic Acid

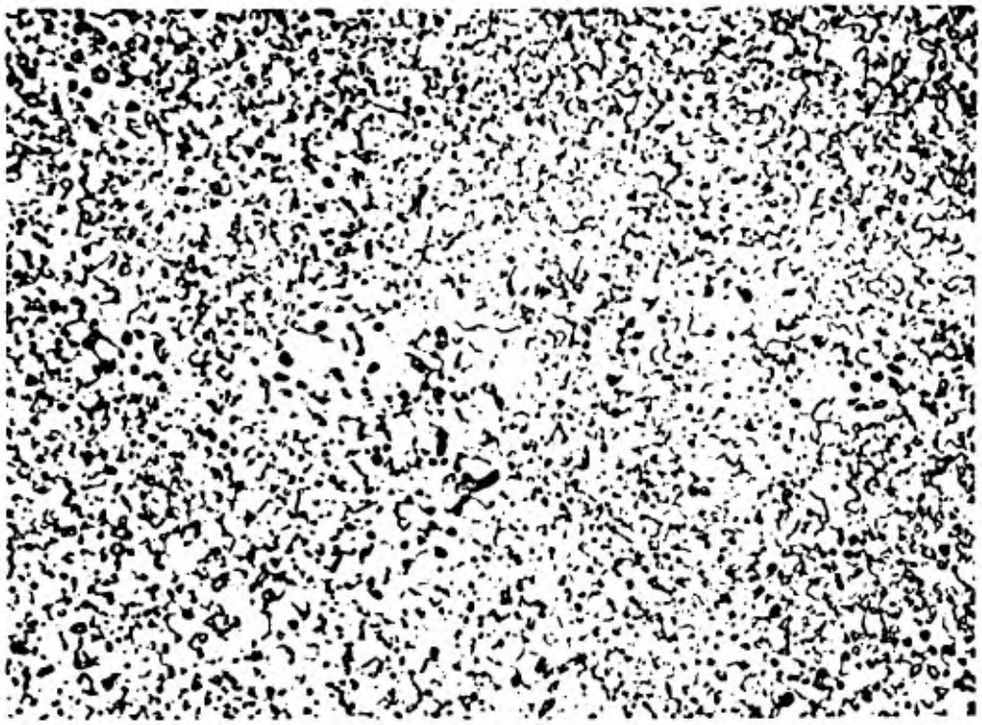

Fig. 24 - Product Run No. NbB_2-1 1500X

Major Area

Etchant 1 HF: 1 HNO_3: 3 Lactic Acid

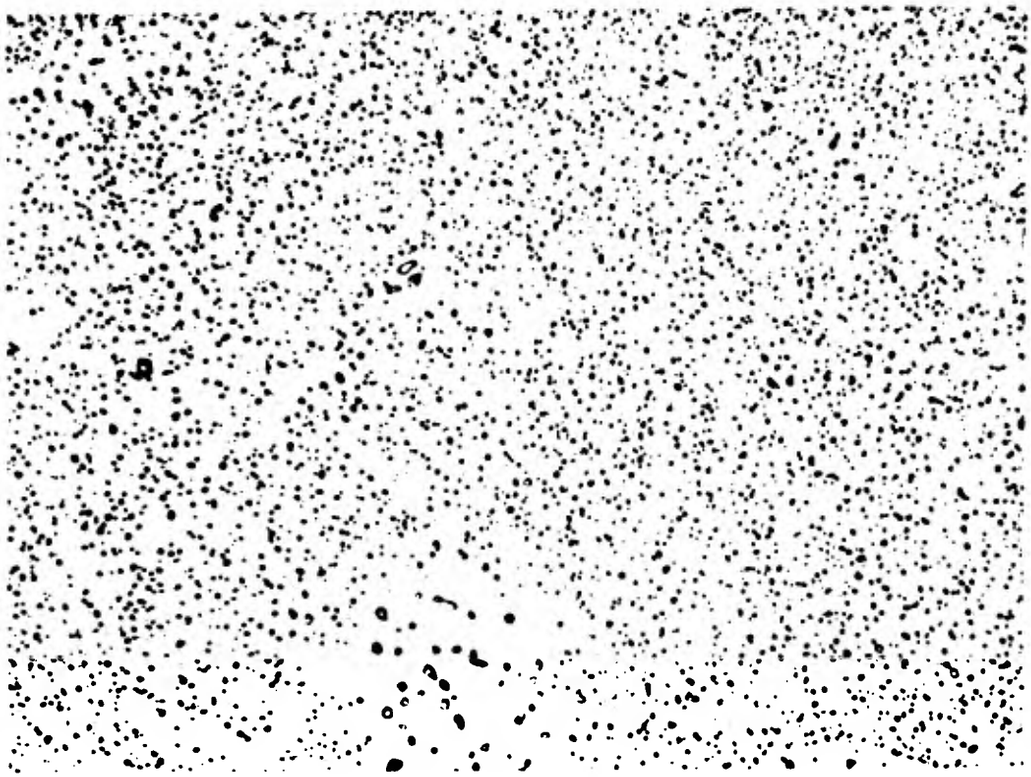

Fig. 25 - Product Run No. TaB_2-1 1500X

Major Area

Etchant 1 HF: 1 HNO_3: 3 Lactic Acid

cold compacted density and increases the relative volume change which takes place in the fabricating procedure at high temperature. In effect, excessive shrinkage of the specimen powder at high temperature causes loss of electrical contact by furnace failure and consequent experimental failure.

The results of the chemical analyses for TiB_2, ZrB_2 and HfB_2 do not indicate any gross change in composition brought about by the fabricating procedure; x-ray results do not show evidence for contamination.

The room temperature resistivity is a sensitive measure of relative porosity and physical integrity of the fabricated diboride samples. The determination can be completed in a relatively short time. The significance of the measured resistivities is discussed in Section XI. The measured resistivity is compared with the extrapolated values for a fully dense material.

It is significant to note that the measured oxidation resistance of HfB_2 fabricated by high pressure hot pressing was equally as good as that measured for HfB_2 single crystals (see Section XIV).

2. Potential Applications

The fabrication of fully-dense, crack-free, fine-grained, samples of refractory metal diborides (and other hard metal compounds) would provide material with optimum physical, electrical and chemical properties. High pressure hot pressing has the potential for a fabricating technique to accomplish this objective with a minimum of sample contamination. In addition, high pressure hot pressing by its very nature can be applied to the important task of providing binary and ternary single phase material of variable composition and composite structures, both of which can be used to further improve the fundamental properties of the pure compounds.

An increase of strength of polycrystalline material with decreasing grain size is well recognised in the fields of metallurgy and ceramics. Murray[1] and Knudsen[2,3] have reported results to confirm this generalization for ceramic materials. Mandorf, et. al.[4] studied the effect of porosity on several physical properties and electrical resistivity for TiB_2; a study of the effect of grain size on the flexural strength was also completed for TiB_2. The material studied by this group was fabricated by conventional hot pressing techniques; the highest density achieved was in the 95% of theoretical region and the lowest grain size of the fabricated material was of the order of 20μ.

In order to illustrate the potential of high pressure hot pressing as a method for fabricating materials with optimum strength properties the data of Mandorf, et. al.[4] for TiB_2 are reproduced in analytical form at a constant grain size of 20μ as a function of P, the fraction of porosity for elastic modulus, E, as

$$E[P]_{\mu} = 78\times10^{6} \exp(-3.74\,P) \text{ psi} \quad (1)$$

for compressive strength, σ_c as

$$\sigma_c[P]_{\mu} = 3.10\times10^{5} \exp(-5.15\,P) \text{ psi} \quad (2)$$

and for flexural strength, σ_F as

$$\sigma_F[P]_{\mu} = 40.5\times10^{3} \exp(-3.19\,P) \text{ psi} \quad (3)$$

The flexural strength of TiB_2 as function of average grain can be represented analytically as

$$\sigma_F[\mu]_P = 7.13\times10^{5} \left(\frac{1}{\mu}\right) + 7550 \text{ psi} \quad (4)$$

This equation was obtained for material of low fractional porosity. Examination of Eqs. 1 through 4 reveal that grain size is more significant in limiting the final strength than does porosity. The latter, however, is still im-

portant for strength considerations and for other properties of these materials. Extrapolation of Eq. 4 to 10μ grain size for high density TiB_2 affords a predicted flexural strength of approximately 80,000 psi. Mandorf et. al.[4] observed an increase in the flexural strength of TiB_2 from room temperature, σ_F = 35,000 psi to 1500°C, σ_F = 44,000 psi; above 1500°C, the flexural strength decreased monotonically to 35,000 psi at 2000°C. The significance of the increase in strength up to 1500°C is uncertain. From these considerations it appears that TiB_2 fabricated by high pressure hot pressing with a 10μ grain size would provide a unique structural material.

REFERENCES

1. Murray, P. J. Iron Steel Inst., (1956) p 125.
2. Knudsen, F.P., J. Am. Cer. Soc., (1959) 42 376-387.
3. Knudsen, F.P., Parker, H.S., Burdick, M.D., J. Am. Cer. Soc., (1960) 43, 641-647.
4. Mandorf, V., Hartwig, J., and Seldin, E.J., Technical Memorandum, TMC-49, "High Temperature Properties of Titanium Diboride" Fostoria Development Laboratory, National Carbon Co., Fostoria, Ohio, 5 April 61.
5. Seybolt, A. U., Trans. ASM, (1960) 52 971-989.

VII. SINTERING*

A. Introduction and Short Summary

The purpose of this sub-task is to investigate the effects of starting material, time, temperature, and additives on the sintering behavior of refractory borides.

Pellets have been prepared from TiB_2 as-received powder, from milled powder, and from mixtures of milled and as-received powder. NbB_2 and ZrB_2 specimens were prepared from milled powder following the procedures found to be useful for TiB_2. The effects of several additives have also been tested on TiB_2. The pressed density ranged from 55 to 65% of theoretical, depending on particle size, particle size distribution, and pressure.

Samples were generally fired at temperatures from ≈ 1850°C to 2650°C with firing times ranging from minutes to hours. The time dependence of densification reveals that TiB_2 behavior is different from that exhibited by most refractory oxides. Specifically, densification proceeds normally for a period of time and then decreases to a low or sometimes negative rate for times of measurement up to 10 hours. Thus, a density limit exists which is a function of temperature for a given powder. The density limit at low temperatures increases with additives and with decreasing initial particle size. At high firing temperatures the density limit appears to be independent of both additives and particle size. Of the additives used, chromium is most effective in promoting densification. The highest density achieved is 95% of theoretical in Cr doped TiB_2 sintered at 2200°C.

---

* R. L. Coble and H. A. Hobbs, Lexington Laboratories, Inc.

The observed behavior is interpreted as resulting from the simultaneous operation of bulk diffusion and evaporation-condensation material transfer mechanisms.

Sintered densities greater than 90% of theoretical can be achieved by sintering above 2400°C or by using selected additives.

B. Experimental

1. Powder Treatment

Initial studies were carried out on TiB_2 powder (-325 mesh) obtained from Millmaster Chemical Company. This powder did not conform to specifications and was exchanged for U. S. Borax Company TiB_2 powder. A size analysis indicated that the size range for this material was between 15 and 35 microns, Fig. 26. NbB_2 powder from U. S. Borax was also obtained and was pressed using the procedure developed for TiB_2. Most of the preliminary studies have been carried out on TiB_2.

The particle size of the as-received powder was too large for pressing pellets or for sintering. All sintering models, regardless of the mechanism of material transport, predict increasing rates with decreasing particle size[1]. Two methods have been used for grinding TiB_2.

1.1 Milling

Ball milling was carried out in an iron mill, with iron balls. The powder was milled dry for twenty hours, and wet for three-quarters of an hour. After milling, the powder was leached with hydrochloric acid eight times; the fluid was decanted from the powder between each leaching.

As received TiB_2 has also been treated in a fluid energy mill (FEM). The mill was teflon lined; abrasion of the lining and contamination of the powder were negligible. No leaching treatment was required after grinding.

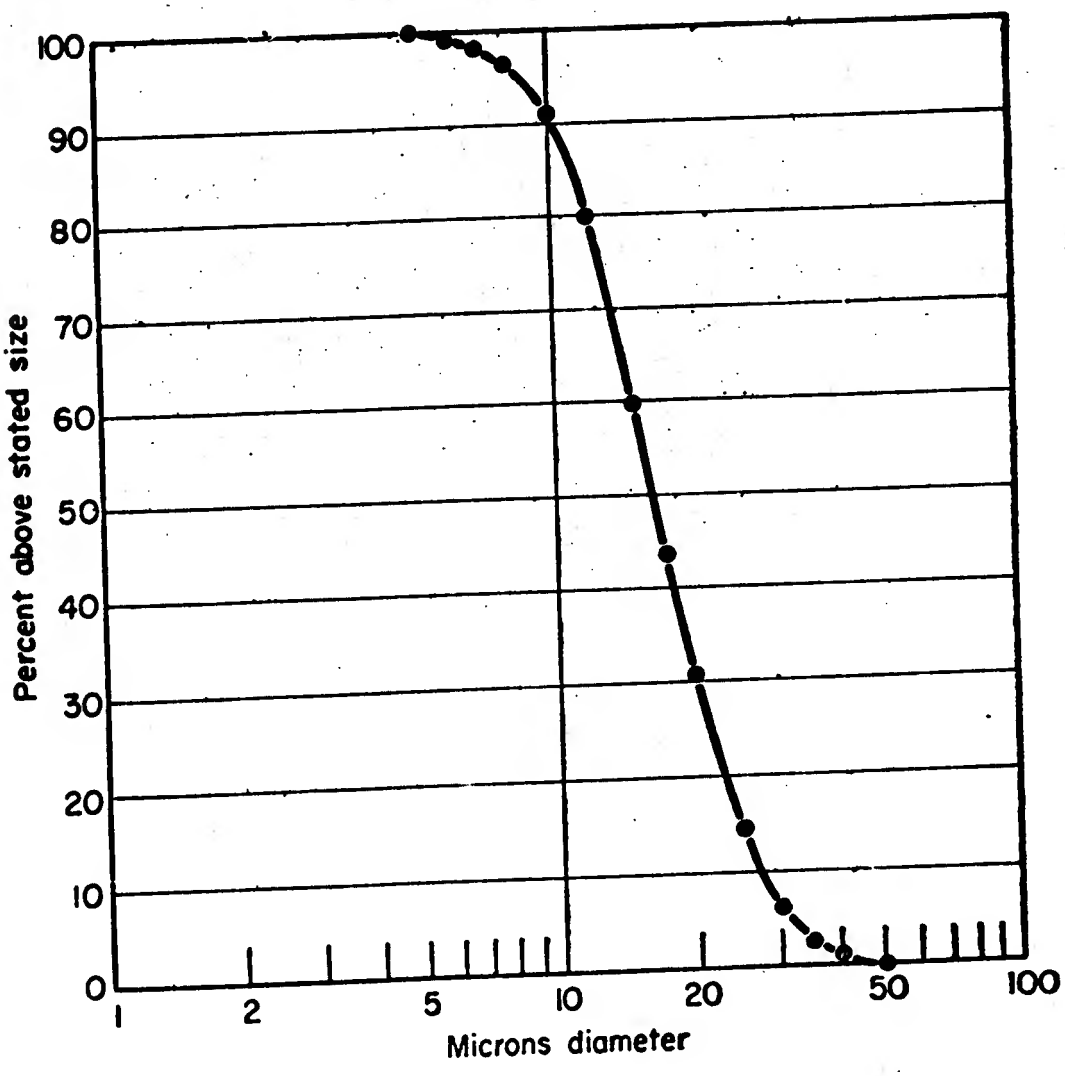

Fig. 26 - Particle Size Analysis of As-Received TiB_2

I.2 Particle Size

The particle size of the as-received powder ranges from 15-35μ (Fig. 26). Measurement of the particle size of the ball milled powder and the fluid energy milled powder have been attempted using a Coulter counter, and by microscopic techniques. The Coulter counter measurement was unsatisfactory because of the formation of agglomerates with both milled powders. Standard light microscopy revealed that the sizes were below the resolution limit. An electron micrograph of a dispersion of the fluid energy milled powder is given in Fig. 27. The smallest individual particles are 0.1μ in diameter. Two classes of agglomerates exist in sizes ranging from 1 to 10 microns (not shown). Some appear to consist of 0.1μ particles, others consist of particles ≈ 1μ in size (as appear in Fig. 27). Firing of the ball milled powder prior to the particle size determination revealed that it was unsatisfactory. Judging from pressing and firing characteristics, its size is intermediate between the as-received and the fluid energy milled powder.

2. Pressing Techniques

Fabrication of sample pellets has been carried out on a Carver Model B laboratory press, capable of applying a 24,000 pound load. Two sets of hardened steel dies were used with this press; the maximum pressures attained are 24,000 and 144,000 psi.

When pressing the dry TiB_2 powder, it was found that the high pressures attained in the small die were insufficient to give satisfactory green strength to allow handling without chipping, breaking, or crumbling of the specimens. This was attributed to the large particle size of the powder.

Because dry pressing alone did not provide satisfactory samples for the sintering studies, several organic binders were incorporated to increase

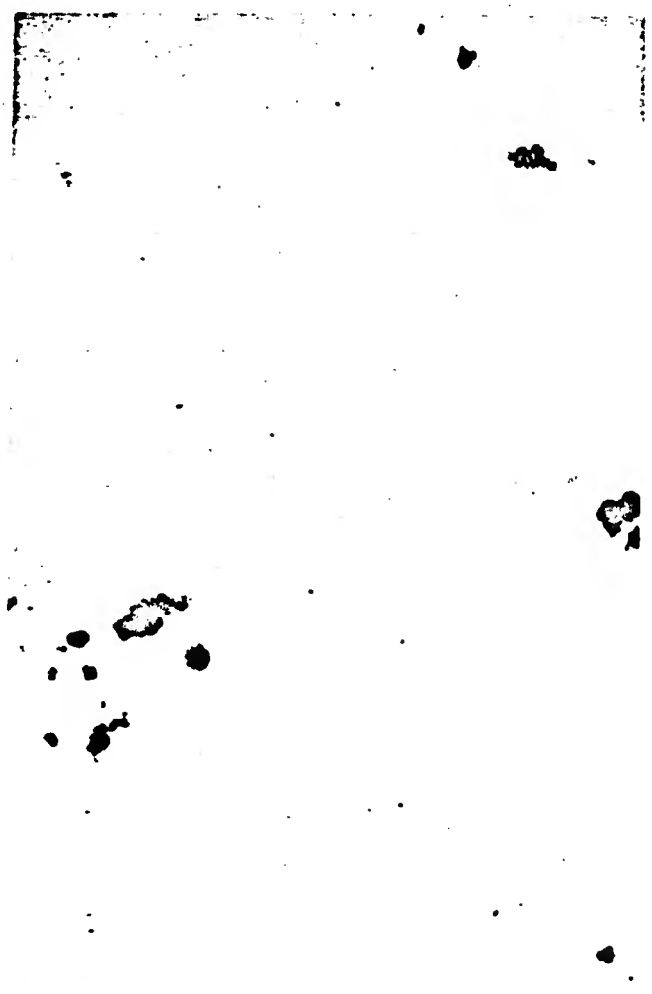

Fig. 27 - Electron Photomicrograph of FEM TiB_2 (magnification = 30,000X individual particles as shown in this field).

the pellet green strength. (This same difficulty was reported by Russian investigators[2] who used ferric chloride as an additive to improve pressing characteristics). Binders included Carbowax, polyvinyl alcohol, and Apiezon type W-100 wax dissolved in toluene. The most successful binder for TiB_2 has been found to be a 5 to 10 weight per cent addition of 10% polyvinyl alcohol solution. Samples pressed with PVA as a binder exhibit satisfactory green strength; they can be handled without crumbling. The minimum pressure for pressing satisfactory pellets is 20,000 psi, which yields a density of 2.5 gm/cm^3 (55% relative density).

2.1 Additives

TiB_2 samples were tested with 1, 5, and 10 weight % additions of iron, nickel, chromium, silicon, and cobalt. Additions were made with nitrate solutions of the respective metals; the slurries were dried prior to vacuum firing to reduce the salts to the metallic state. Additions of impurity metals were also made by using the pure metals. The metal powders were fluid energy milled and added to the TiB_2 powder. Of the two methods outlined above, the pure metal additive proved most effective in enhancing sinterability.

2.2 Firing

Several vacuum systems and furnaces have been used for TiB_2 sintering. It was originally planned to follow the course of densification by continuous observation of the sample with a telescope sighted through a window in the vacuum enclosure. The sample was to be heated with helical wound tungsten wire elements, enclosed within radiation shields. Because of difficulties with the vacuum system (leading to oxidation and failure of the elements)

and creep and failu of the tungsten wire at the necessary sintering temperatures this sys.. was abandoned.

Heat treatments up to 1950°C were conducted in an induction furnace. (Induction heated molybdenum tube, 0.1μ pressure). In these preliminary measurements, sample shrinkage was observed to begin at 1400°C during heating. The shrinkage rate measurement was small and not reproducible because of sample movement during these runs). A new vacuum system was obtained and a rolled tantalum slit-tube heating element enclosed in radiation shields was assembled for boride sintering. Samples have been sintered at 1950° to 2650°C for times ranging from minutes to hours (the heating time to 2300°C is seconds). A tungsten heating element is used for high temperature runs. Pressures in the range 10^{-5} to 10^{-6} mm Hg were obtained during the heating cycles.

As noted below, a weight loss of about 2% was observed during firing of as-received specimens. In order to try to suppress the rate of vaporization (resulting from either oxidation or direct volatilization) one test was conducted in hydrogen in a molybdenum wound alumina tube furnace. The sample was not observed continuously but had melted when observed at 1750°C. Whether this resulted from contamination by impurity pick-up or from boron loss through borane formation was not determined.

3. Density Measurement

The density of sintered specimens was measured by several techniques:

1. Weight and dimensional measurement.
2. Weight and weight change upon immersion in mercury or xylene.
3. Point count of pores in photomicrographs of polished specimens.

The first method was used for samples which did not distort during firing; the second was used on specimens with chipped edges or those which were distorted. When internal cracking (revealed by cutting and polishing) occurred with pellets of excessive length, point counts were then used for density measurement. Because of the possibility of (a) unobserved internal cracking and (b) pull-outs in polished sections, the densities reported may be low. Point count density measurements are higher than the densities measured by mercury immersion. The density reported is from mercury or xylene immersion measurements, unless otherwise noted.

C. Sintering Results

1. As-Received Powder

Pressed samples of as-received TiB_2 were fired for 2 hours at 1850°C in molybdenum furnace at 10^{-4} mm Hg, the density was measured and the samples were re-fired for seven hours at 1850°C under the same conditions.

Fig. 28 is a photomicrograph of the sample after firing for a total of nine hours. The sample with a pressed density of 55%, increased in relative density to 65% after two hours. No further density increase was observed after firing for seven additional hours. The particle size was too large for much shrinkage to occur at the firing temperature. The photomicrograph reveals that the powder was crushed in pressing because the fired grain size is smaller than the original particle size.

2. Ground Powder

Figs. 29 and 30 are photomicrographs of a ball-milled powder sample fired at 1850°C for four hours. The overall density of the sample is approximately 60% of theoretical density, but limited areas (Fig. 29) show densities as high as 68-70%.

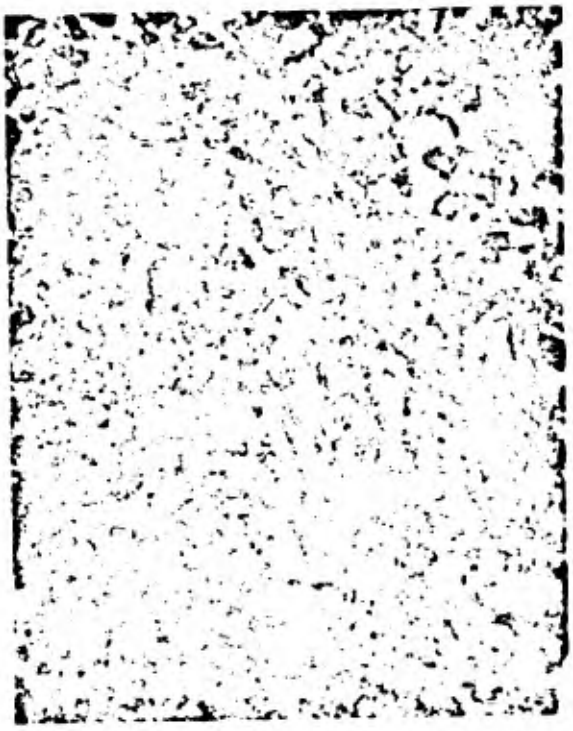

850X

Fig. 28 - Photomicrograph of as-received TiB_2 sintered at 1850°C for 9 hours (as polished).

125X

Fig. 29 - Ball-milled TiB_2 Sample fired at 1850°C 4 hrs. (as polished).

1250X

Fig. 30 - Ball-milled TiB_2 Sample fired at 1850°C 4 hrs. (as polished).

The balled-milled powder was unsatisfactory because of the appreciable weight loss during firing. Measurements of the initial and final lengths and weights of samples of the different powders are shown in Table 26.

Table 26

Characteristics of Samples Fired 4 hours at 1850°C

Sample	Initial length (cm)	Final length (cm)	Initial weight (g.)	Final weight (g.)
As Rec'd I	0.976	0.958	0.603	0.593
As Rec'd II	1.008	0.975	0.625	0.586
Fluid Energy Milled I	1.015	0.989	0.803	0.791
Fluid Energy Milled II	0.960	0.891	0.712	0.668
Ball Milled	0.938	0.847	0.654	0.336

As can be seen from Table 26, the weight loss during firing of the ball-milled powder is much greater than that encountered in either of the other two types of powder. The low-power photomicrograph (Fig. 29) shows quite clearly areas of inhomogeneity in the ball-milled powder. X-ray diffraction analysis of the fired ball-milled sample did not reveal any change in structure or change in relative line intensities.

The initial density of the pellets fabricated from fluid energy milled powder was roughly 60% of the theoretical density. After firing at 1850°C the density of these samples was 75% of theoretical density.

Figs. 31 and 32 are photomicrographs of a fluid energy milled sample which had been fired for four hours at 1850°C. Fig. 31 is a section across the central portion of the sample, showing the porosity as well as the contact area connecting grains. All pores are intersected by grain boundaries, showing that discontinuous grain growth has not enclosed pores within grains. The pores are larger than the original particle size and exhibit marked dihedral angle formation where intersected by grain boundaries.

Fig. 32 is a photomicrograph of the edge of the sample showing exaggerated growth of surface grains through several interior grain diameters. The surface appears to be fully dense, with deep grooving at the intersection of grain boundaries and the surface.

In order to obtain greater green densities, as-received powder was mixed with 30% by weight of milled powder. These samples exhibited higher pressed densities as expected, but less shrinkage occurred during firing; the fired density was less than that of the milled powder alone.

On the basis of these measurements, ball milling for particle size reduction was rejected, as was mixing of particle sizes to achieve higher pressed density. Additional firings at 1850°C-2050°C for shorter and longer times also showed that density changes were complete with one hour firing time; extended firing time did not cause further density increases. Based on the TiB_2 results, NbB_2 and ZrB_2 samples were similarly ground in the fluid energy mill, and pressed with PVA binder prior to sintering.

3. Additives

Separate samples of as-received TiB_2 doped with 1 wt. % Fe, Ni, and Co were sintered at 1950°C for 30 minutes; pure, as-received

1250X

Fig. 31 - FEM sample sintered 4 hours at 1850°C etched with 1 HNO_3: 1 HF: 3 Lactic Acid.

1250X

Fig. 32 - Surface region of FEM sample sintered 4 hours at 1850°C etched with 1 HNO_3: 1 HF: 3 Lactic Acid.

powder and fluid energy milled powder were sintered under the same conditions. The additives affected the flow properties of the powder as well as the sintering characteristics. Pressed and fired densities are shown in Table 27.

From these data, it is apparent that Ni and Co are more effective than iron in promoting densification, and at this temperature are more effective than particle size reduction. A photomicrograph of a Nickel doped specimen sintered 1 hour at 2050°C is shown in Fig. 33. The density measured by mercury immersion is 82%, point count measurement of pores gives a density of 90%. Larger additive contents were prepared for Co, Ni, Cr, Si, and Fe. The density limits for samples sintered at 2200°C are plotted against additive content in Fig. 34. Ni and Co additions beyond 1% gave decreasing limiting density. Silicon is not as effective as Ni or Co. In contrast, the density limit increased with chromium additions up to 10%, at which maximum densities (≈ 95%) were achieved. A photomicrograph of the 10% Cr specimen is given in Fig. 35. The density determined from the pore count is (≈ 95%) in agreement with the gravimetric result. Table 27 is a tabulation of these results.

4. Isothermal Densification

Models for bulk diffusion sintering with the grain boundaries as vacancy sinks for shrinkage above 5% produce equations of the form[3]

$$\frac{\Delta \rho_B}{\Delta t} = \frac{10 D \gamma \Omega}{(GS)^3 k T} \qquad (1)$$

where ρ_B is the relative density, t is time, D is the lattice diffusion coefficient, (GS) is the grain size, k is Boltzmann's constant and T is absolute temperature. The lattice volume, Ω, in equation 1 is given by:

$$\Omega = \frac{m}{\rho n} \qquad (2)$$

Table 27

Sintering Behavior of TiB_2 with and without Additives

Powder	Time (min.)	Pressed Density	Fired Density	Grain Size (Fired)
A) 1950°C				
As Received + 1% Fe	30	60.5%	67%	7.8μ
As Received + 1% Co		62.7%	82%	8.5μ
As Received + 1% Ni		63.5%	82%	7.8μ
FEM		60%	75%	4.0μ
As Received		55%	65%	———
B) 2200°C				
FEM	45	60%	81%	6.6μ
FEM + 1% Co	-8	61.7%	87.5%	DNM*
FEM + 1% Cr	15	63%	78.5%	DNM
FEM + 1% Ni	30	65%	89%	DNM
FEM + 5% Co	8	65.4%	84.9%	DNM
FEM + 5% Cr	15	63.8%	94%	9.2μ
FEM + 5% Ni	30	65.4%	86%	DNM
FEM + 5% Si	10	61.6%	82%	DNM
FEM + 10% Cr	15	66%	95.5%	8.5μ
FEM + 10% Ni	30	67%	83.5%	DNM
FEM + 10% Si	10	60.3%	72.6%	DNM
C) 2050°C				
FEM + 1% Ni	60	62.5%	82%	DNM

*DNM = Did Not Measure

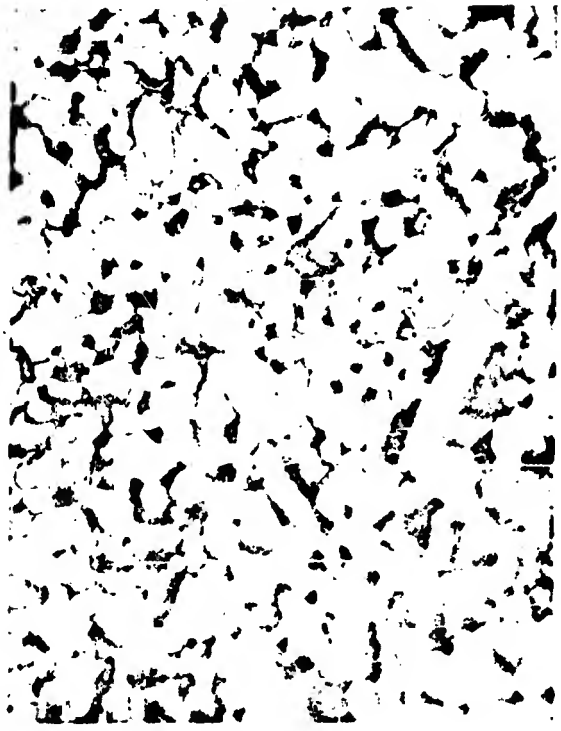

850X

Fig. 33 - Nickel (1 w/o) doped TiB_2 fired 1 hour at 2050°C (etched with 1 HNO_3: 1 HF: 3 Lactic Acid).

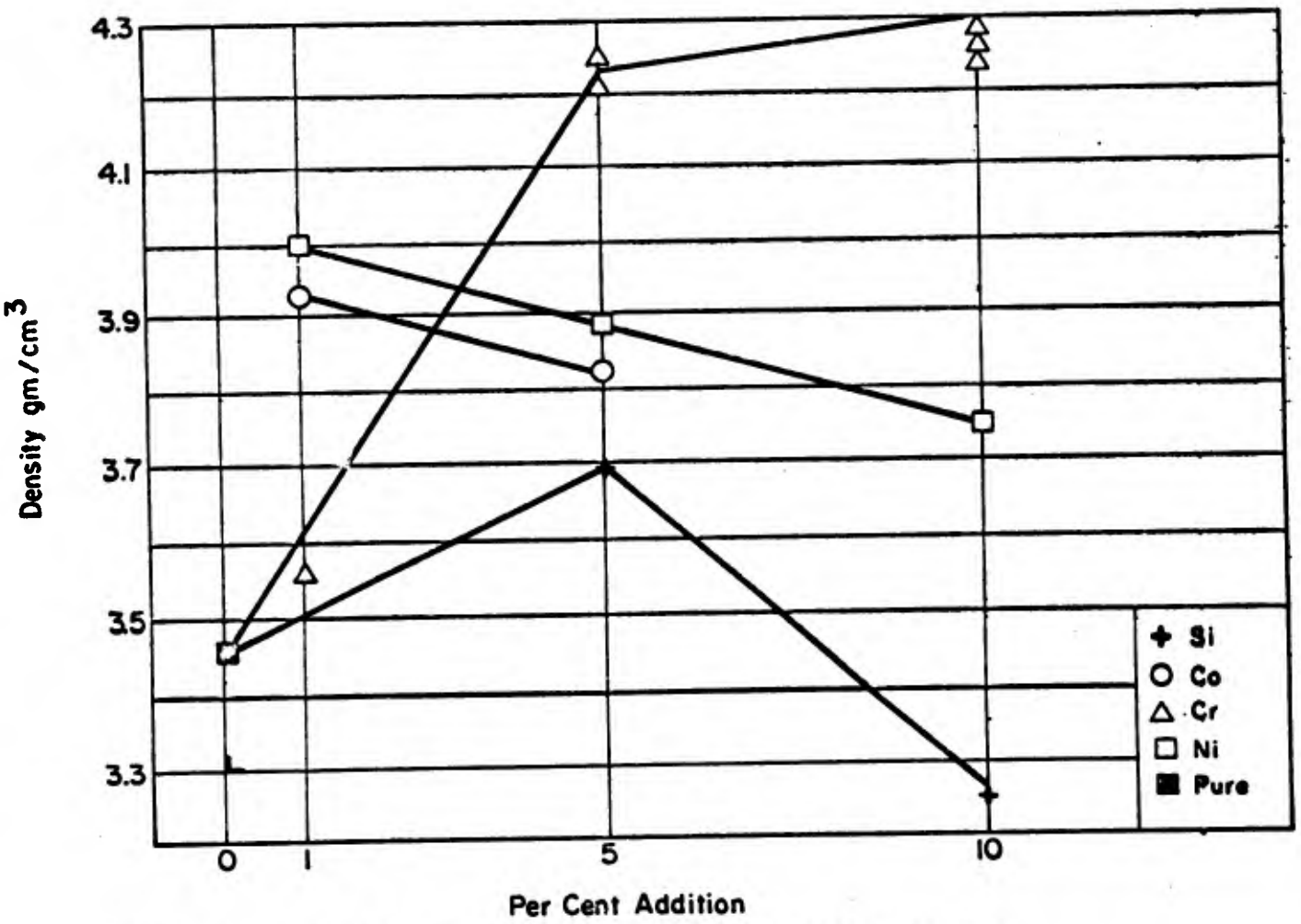

Fig. 34 - Density of TiB_2 (sintered at 2200°C) vs. percent addition.

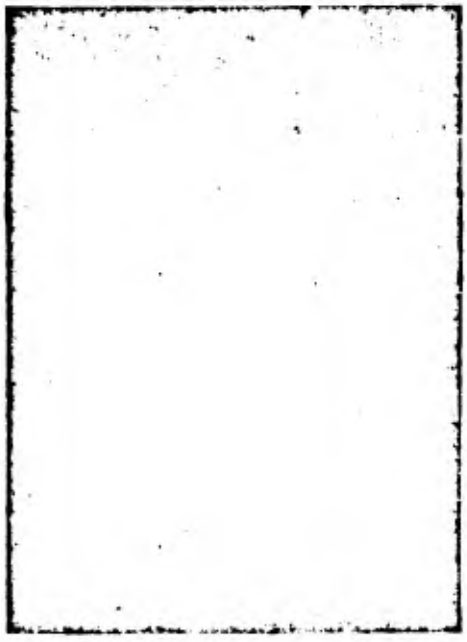

Fig. 35 - 10% Cr doped TiB_2 fired 15 min. at 2200°C, as polished. 400X

where m is the molecular weight, ρ is the density, and n is Avogadro's number.

Because the grain size increases during densification, Equation (1) must be modified; with a grain size increase as the one-third power of time (as observed in Al_2O_3), the density should increase directly with log time[4]. The grain size of TiB_2 specimens is plotted in Fig. 36. There are insufficient data to determine the slope with accuracy. Growth does occur during densification; therefore, the density of isothermal runs are plotted against log times (assuming that the $t^{1/3}$ behavior is followed). The data for pellets of fluid energy milled powder pressed at 42,000 psi and 144,000 psi and sintered at 2200°C, 2250°C, and 2300°C for varying times are plotted in Figs. 37 and 38, respectively. The weight loss for these specimens is given in Table 28. The data of Babich et al.[2] for TiB_2 sintered at 2300°C are also plotted in Fig. 38. The curves may be divided into two segments. The initial segments exhibit linear increases in density with log times; then density limits which are temperature dependent are reached and no further densification occurs. The samples pressed at the lower pressure have not been sintered long enough to determine whether the density limit also depends on the pressed density.

Babich's data for 2300°C exhibits a lower rate initially than our data, but the same density limit exists for both. The higher initial rate observed here is probably due to a smaller initial particle size; this suggests that the density limit is independent of initial particle size. The activation energy for densification calculated from Fig. 37 and 38 is >150 kcal/mole; it increases with the density at which the times are compared because the curves are not parallel.

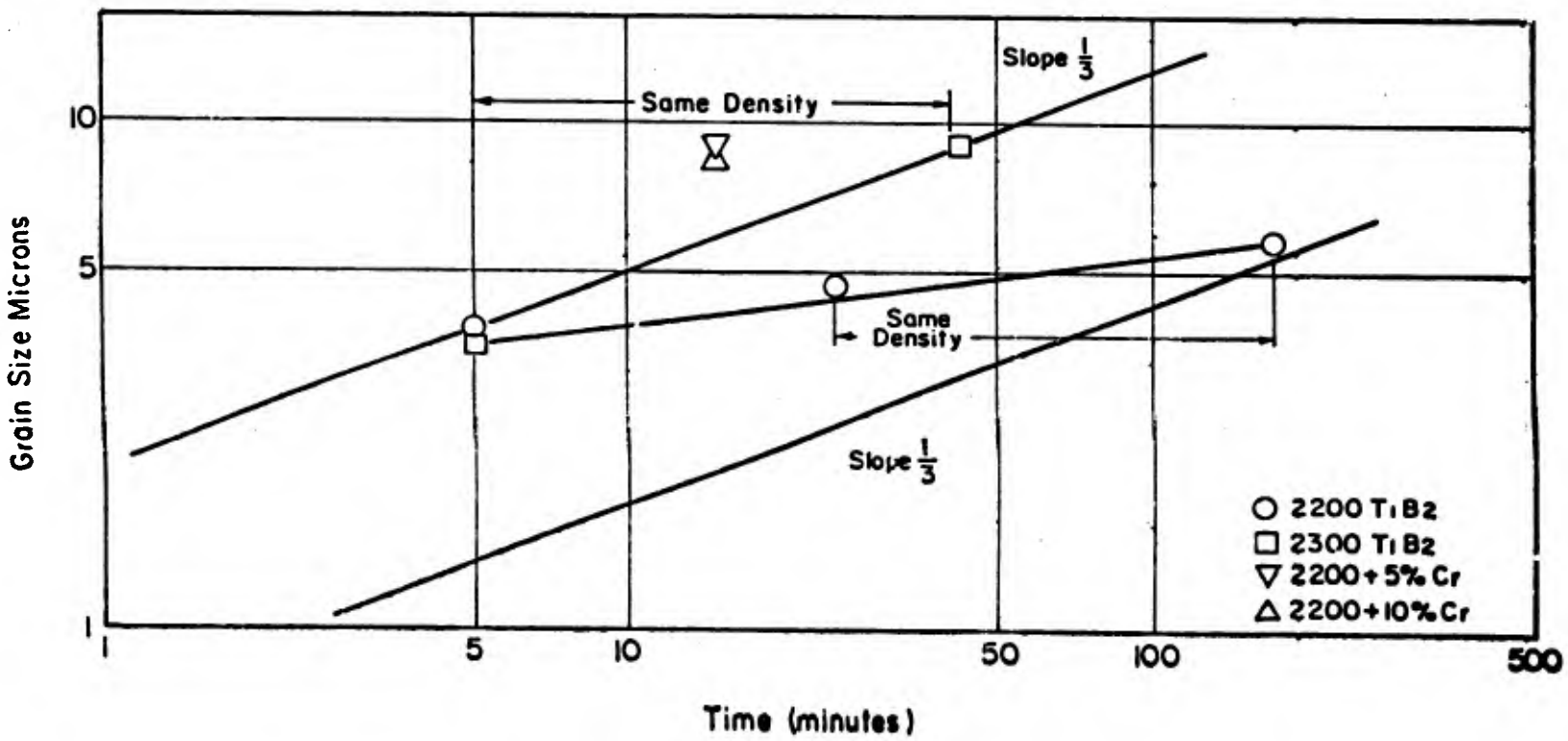

Fig. 36 -Grain Size of Sintered TiB_2 vs. Time.

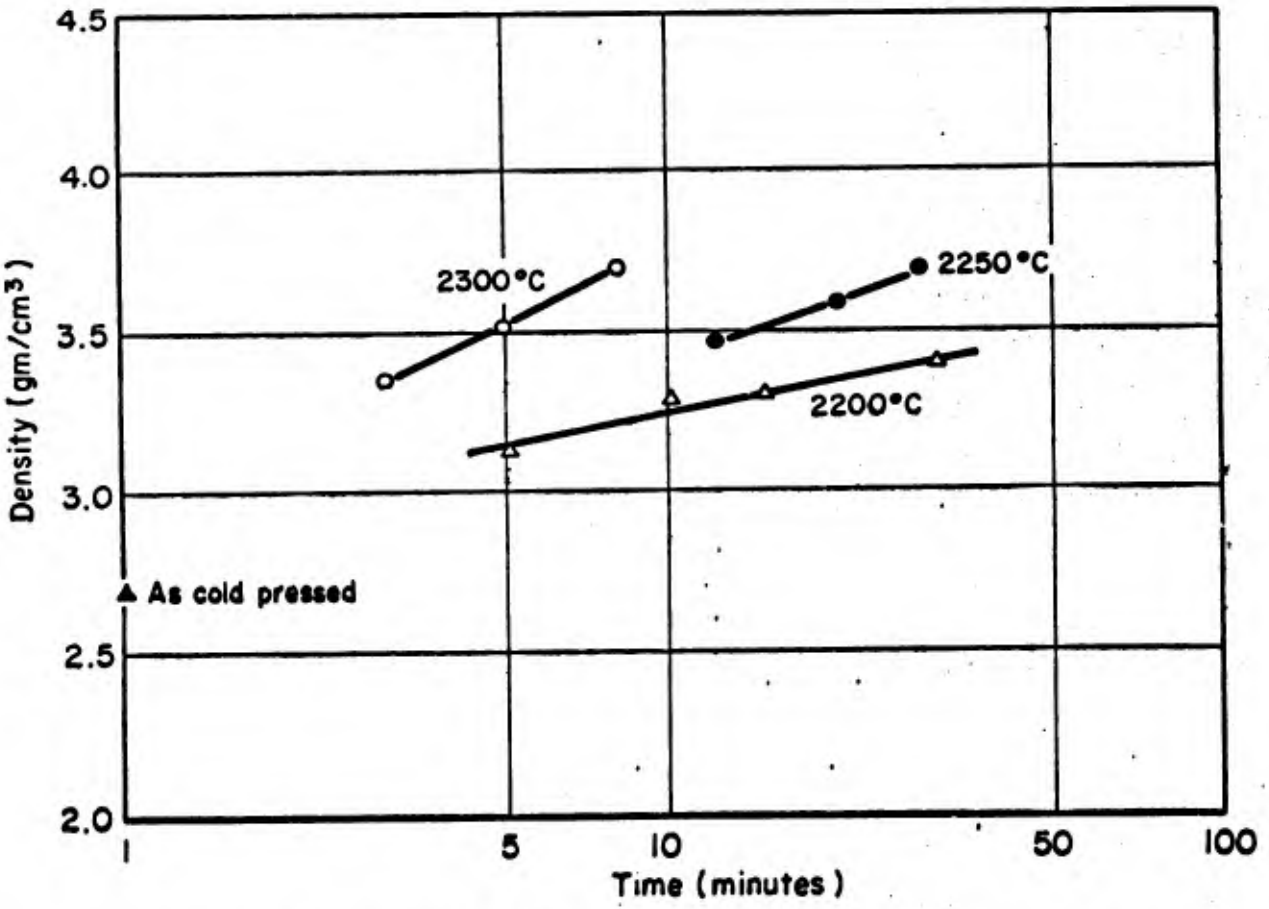

Fig. 37 - Density of FEM TiB_2 pressed at 42,000 psi vs. Time at 2200, 2250, and 2300°C (Density by Mercury Displacement).

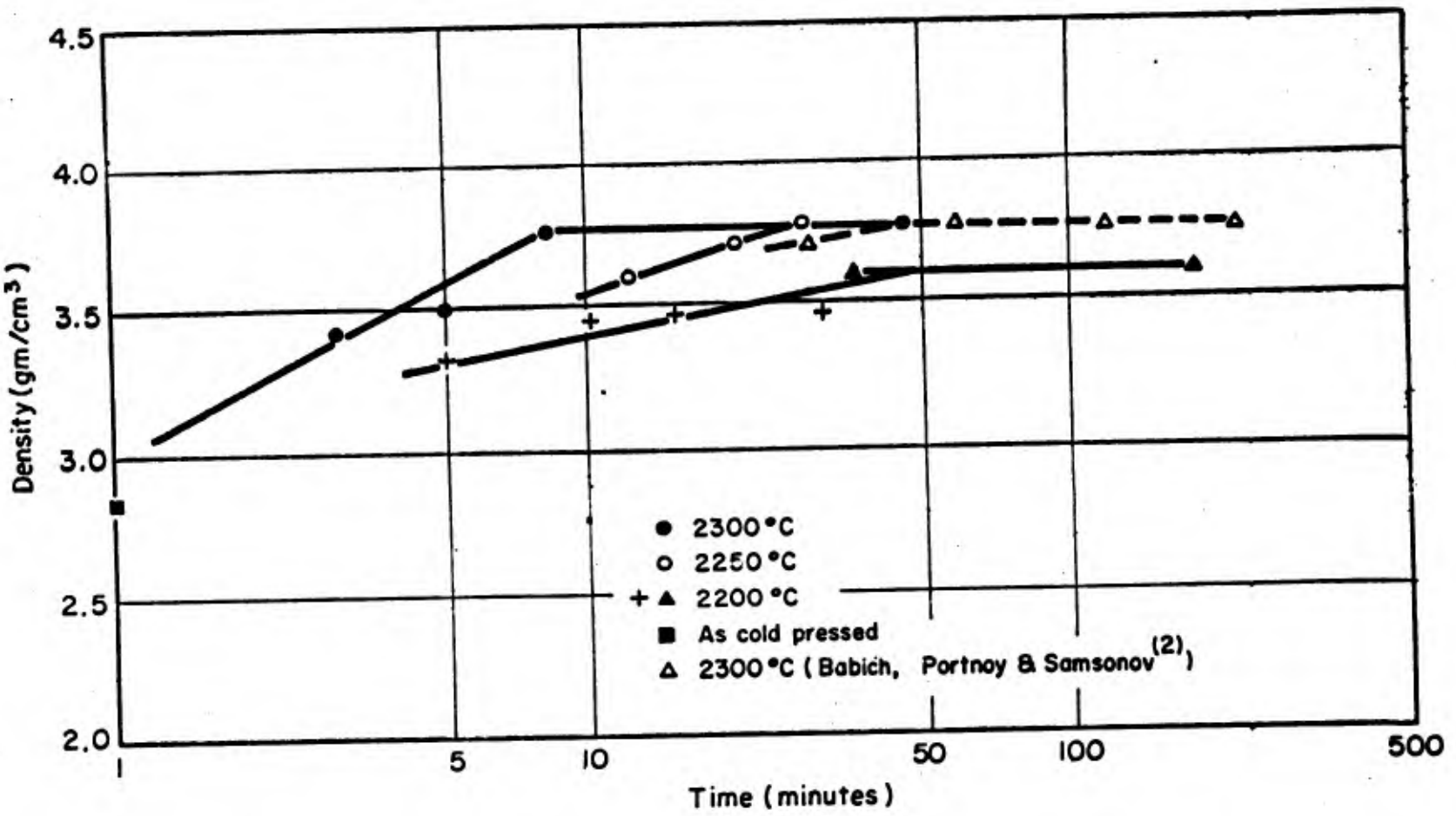

Fig. 38 - Density of FEM TiB_2 pressed at 144,000 vs. Time at 2200, 2250, and 2300°C (Density by Mercury Displacement)

Table 28

Weight Loss of TiB_2 Specimens Fired at 2200-2300°C

Sample	Temp. (°C)	Firing Time	Density (g/cm^3)	%Wt. Loss $(\frac{\Delta\omega}{\omega_o})$ 100
A) Pressed at 42,000 psi				
A-FEM	2200	15 min.	3.38	4.05
1A-FEM	2200	30 min.	3.39	4.85
3-FEM	2250	28 min.	3.69	5.35
2-FEM	2300	5 min.	3.49	3.52
1-FEM	2300	8 min.	3.68	5.3
3B-FEM	2300	42 min.	3.66	8.18
B) Pressed at 144,000 psi				
B-FEM	2200	5 min.	3.35	2.87
2A-FEM	2200	30 min.	3.54	4.93
7 As-Rec'd	2200	3 hrs.	3.63	5.65
9-FEM	2200	3 hrs.	3.67	6.18
8-70% AR				
30%-FEM	2200	3 hrs.	3.60	8.9
6-FEM	2250	28 min.	3.79	4.78
5-FEM	2300	5 min.	3.50	3.92
4-FEM	2300	8 min.	3.77	4.85
6B-FEM	2300	42 min.	3.77	7.30

5. Density Limits

Because the density limit appears to be primarily temperature dependent, the data from all long time runs are plotted in Fig. 39. The point at 1400°C should not be taken as a density limit because the sintered sample appeared contaminated. Data for the pure samples show a density limit that increases approximately linearly with temperature. The point at 1400°C falls above the curve extrapolated from the high temperature results. Samples with nickel and cobalt additives show a substantial increase in density at temperatures below 2100°C.

In Fig. 40, the data of Babich et al.[2] were plotted for samples of TiB_2 and $(TiCr)B_2$ sintered one hour. These samples were all prepared with a 1% Fe addition and show a linear increase in end point density at temperatures above 2100°C, and enhanced densification in the 1900-2000°C region, presumably resulting from the iron addition. The greater effectiveness of iron in their samples indicates that they had a finer particle size material than our as-received material.

D. Discussion

1. The Density Limit

The sintering behavior of TiB_2 is seen to be somewhat different from typical metals or oxide ceramics. The temperature dependent density limit is the most marked deviation in behavior. Babich[2] reports slight density decreases with prolonged sintering times; the results of this study show the same effect.

Density decreases (with time) have usually been associated with pore coalescence and growth. This occurs when a gas trapped within the pores

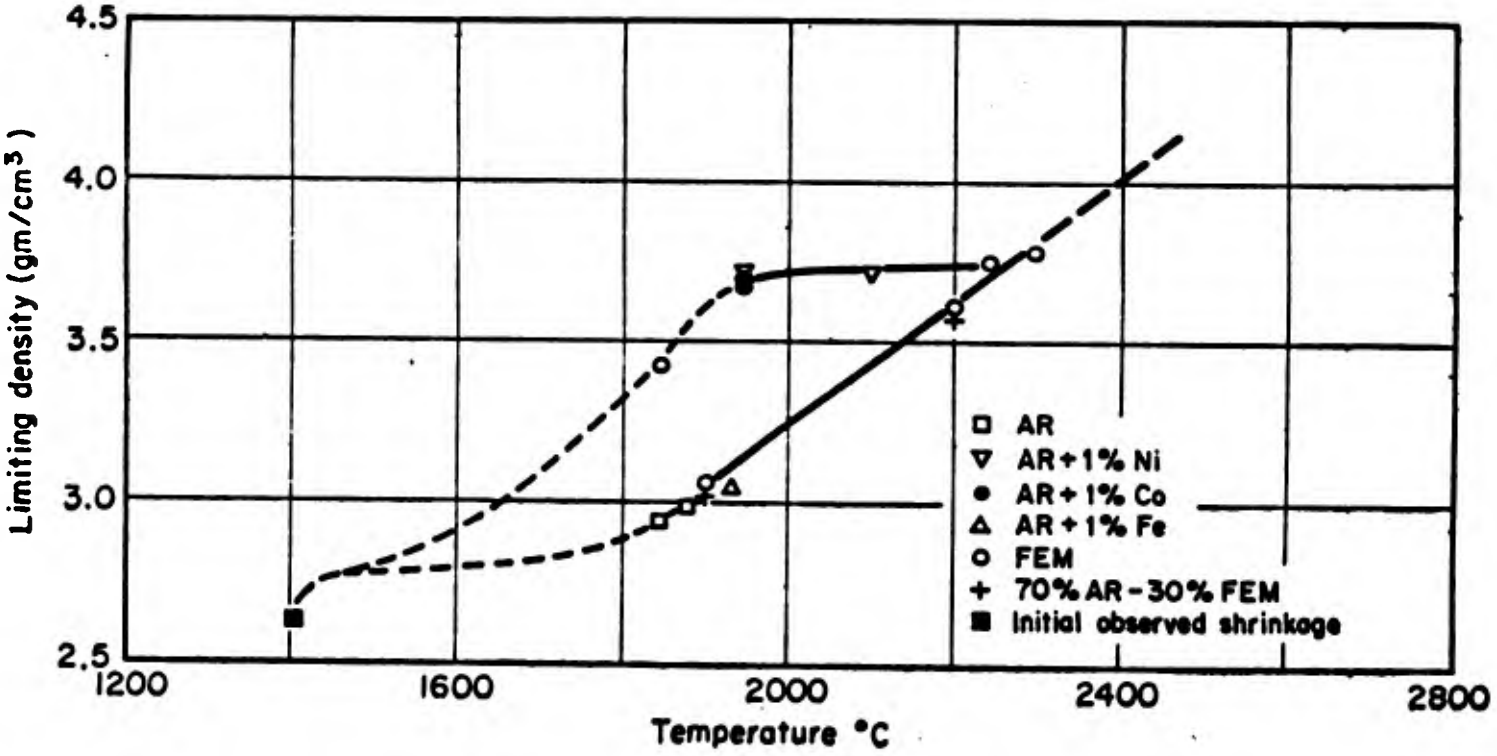

Fig. 39 - Limiting Density vs. Temperature.

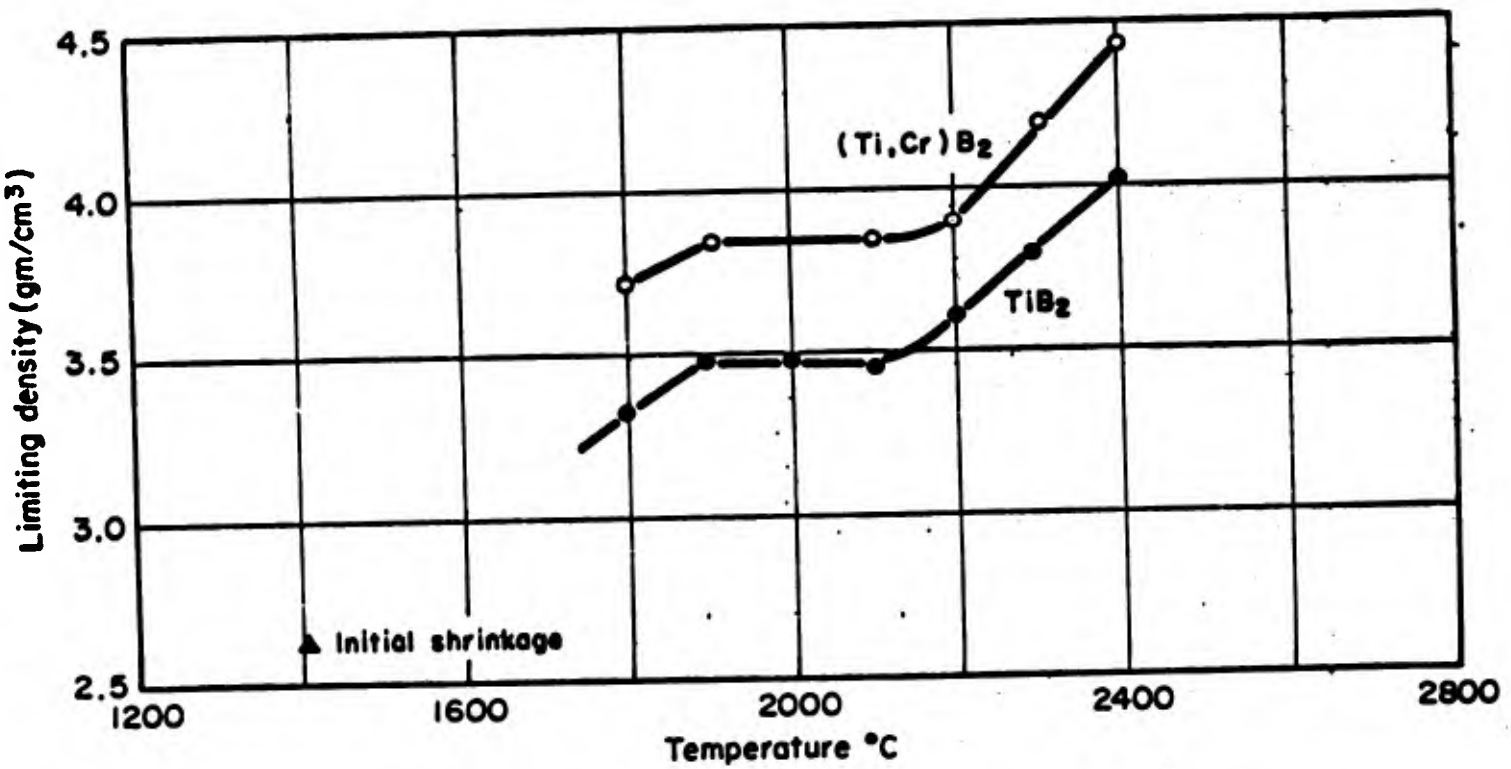

Fig. 40 - Limiting Density vs. Temperature (after Babich, Portnoy, and Samsonov[2]).

counterbalances the pressure (resulting from surface energy) which normally causes shrinkage. This effect requires that the pore phase be closed; but in TiB_2 the density decreases at 82% of theoretical density with the majority of the pores intercommunicating. The effect can also be caused by volatilization from open pores, as evidenced by the weight losses with time (Tables 27 and 28). This gives a reasonable mechanistic basis for the presence of a density limit; that is, the density limit occurs when the vaporization rate equals the densification rate. The transition from shrinkage to no shrinkage occurs as the densification rate slows down at a given temperature.

2. Microstructure

The photomicrographs reveal several features important for a mechanistic interpretation of the sintering behavior. The fact that the pores are not enclosed within grains means that discontinuous grain growth normally found in a number of oxide and metal systems is not the cause of the density limit. The measured grain sizes in the fired samples show that grain growth has occurred during sintering (the average size in the fluid energy milled powder is less than 1 micron). The contact areas between bonded grains are rather large and it appears that complete densification would have occurred if the coordination number of the particles in pressed compacts had been high enough. In alumina, it has been shown that initial densities over 35% are required for sintering to densities higher than 95%[5]. If the initial density is lower than 35%, alumina specimens develop large pores which remain open and the microstructures are similar to those observed here for TiB_2. Because the present samples were formed at densities well in excess of 35%, an additional factor is required to explain the observed behavior.

It has been shown that large pores may be stable simply because they are surrounded by an excessive number of grains such that the grain-pore interfaces between grain boundary intersections are planar. In this case, the dihedral angles formed in the pore surfaces at boundary intersections must be at equilibrium values (governed by the solid vapor and grain boundary energies). In order to reintroduce curvature which gives the driving force for shrinkage, grain growth must occur. That is, the density limit could arise because the pores are in equilibrium. The photomicrographs show that the intergranular pores are only intersected by a few grain boundaries, and if the grain boundary to surface energy ratio is normal, the pores should still have some curvature. Unfortunately, because of the small grain size, high magnifications are required and it is difficult to judge whether curvature exists on the pore surfaces. (See Figs. 31 to 33). However, the fact that some of the pores are larger than the initial particle size requires that pore growth occur by coalescence of smaller pores. Because of the observed weight loss during sintering, it seems most probable that the material transport mechanism for pore growth is evaporation-condensation. The stability of the pores may simply be attributed to their large size (microns) and to relatively small surface curvature due to boundary intersections.

3. The Sintering Mechanism in TiB_2

Both the density limit and observations of microstructure indicate that either vapor transfer or surface diffusion transfer of material takes place in TiB_2. Several systems have been described in the literature where these processes are dominant. In ice, for example[6], surface diffusion leads to pore shape change and pore growth with essentially no shrinkage. While

the other possible mechanisms of material transport; bulk diffusion, grain boundary diffusion and plastic flow can lead to densification, vapor transport and surface diffusion cannot. Therefore, if pore growth occurs without shrinkage of the sample, it seems probable that the latter mechanisms are predominant for matter transport. In NaCl, vapor transport has been shown to be the mechanism by which neck growth occurs between pairs of spheres, and NaCl powder compacts prepared from normal as-received particle sizes do not exhibit shrinkage[7]. Upon grinding to particle sizes less than one micron, NaCl compacts exhibit shrinkage of the order 10-15%. This transition can be explained in terms of the different effects of particle size on sintering rate for the respective mechanisms.[8]

For the initial stage of sintering, the rate of neck growth for an evaporation-condensation process is given by:

$$\left(\frac{x}{R}\right)^3 = \frac{3\pi\gamma p_c M^{3/2}(2\pi NkT)^{-1/2} t}{R^2 d^2 NkT} \qquad (3)$$

where x is the radius of the neck formed between spherical particles of radius R, p is the vapor pressure at temperature T, and d is the crystal density (the remaining terms are defined in Equations (1) and (2). For a lattice diffusion mechanism, the relation is:

$$\left(\frac{x}{R}\right)^5 = \frac{80\gamma DMt}{R^3 dNkT} \qquad (4)$$

Thus, the particle size dependence of the rate of normalized geometric change, i.e., $(x/R)^n$, is a function of the mass transport mechanism. The rate constant for the diffusion mechanism changes more rapidly with particle radius than

does the rate constant for the vapor process. Therefore, upon decreasing the particle size, a transition from vapor controlled transport to diffusion controlled transport can be expected if the rate constants are of the proper relative magnitudes. It is also to be noted that the transition may also occur simply as a function of time. Because of the different slopes, with $t^{1/3}$ for the vapor process and $t^{1/5}$ for diffusion, the curves cross at a point which depends on the relative magnitudes of the rate constants. For times shorter than the point of crossing, the diffusion process is predominant and shrinkage is expected. For longer times the vapor process predominates, and shrinkage is suppressed.

For practical purposes, interference between competitive mechanisms or the transition from one to the other must occur within a limited range of times and values of geometry change. If the transition occurs between x/R values from 0.01 to 0.6 and from times from ~10 seconds to ~2 hours, it will be experimentally observable. If it falls outside this range, the experimental data would lead to the conclusion that one or the other of the respective mechanisms was predominant throughout the process. Because of the different dependences of the rate constant on particle size, the transition may be shifted by changing particle size. It may also be shifted by changing temperature because the mechanisms of material transport will probably have different activation energies.

In order to determine the magnitudes of vapor pressure and diffusion coefficients for interaction between these mechanisms, a transition may be arbitrarily selected to occur at $x/R = 0.25$ at 1000 seconds. The particle size is assumed to be 2 microns, molecular weight of 50 grams, density of 5 gms/cm^3, and surface energy of 500 dynes/cm.

The vapor pressure (in Equation 3) required for an independent process is 1 dyne/cm^2 and the diffusion coefficient calculated from Equation 4 is $\sim 10^{-12}$ cm^2/sec. In units of atmospheres for vapor pressure and cm^2/sec. for diffusion coefficients, the ratio p /D is 10^6 for interaction at the specified point. In NaCl at 750°C the ratio is 7×10^4 which would make the diffusion process dominant (for 1 micron particle size). Experimental work on powder compacts with particle sizes at ~1 micron has revealed that shrinkage occurs, indicative that a diffusion process is operating, while measurements on 130 micron spheres show that the vapor process is dominant.

The vapor pressure of titanium and boron over TiB_2 at 2300°C are 5.6×10^{-6} and 5×10^{-5} atmospheres, respectively (Fig. 41). For stoichiometric evaporation an intermediate pressure of 1.5×10^{-5} atmosphere is assumed. The diffusion coefficient calculated from the sintering data using Equation (1) with a grain size at 1 micron is 4.6×10^{-10} cm^2/sec. The radio p /D is 3×10^4 (atm sec^2/cm). Because of the competition between mechanisms, the D value calculated from sintering would be low, and the p /D value would be high. Therefore, the ratio at 3×10^4 compared to 10^6 (for interaction) overestimates the contribution by diffusion than would be judged from direct diffusion measurements. We conclude that early sintering is controlled by diffusion because shrinkage occurs. Later the process is controlled by vapor transport. It is to be noted that the agreement between the ratios of p/D estimated from the models for interaction between mechanisms and those for NaCl and TiB_2 are better than would be expected in view of the uncertainties in the various necessary sources of data.

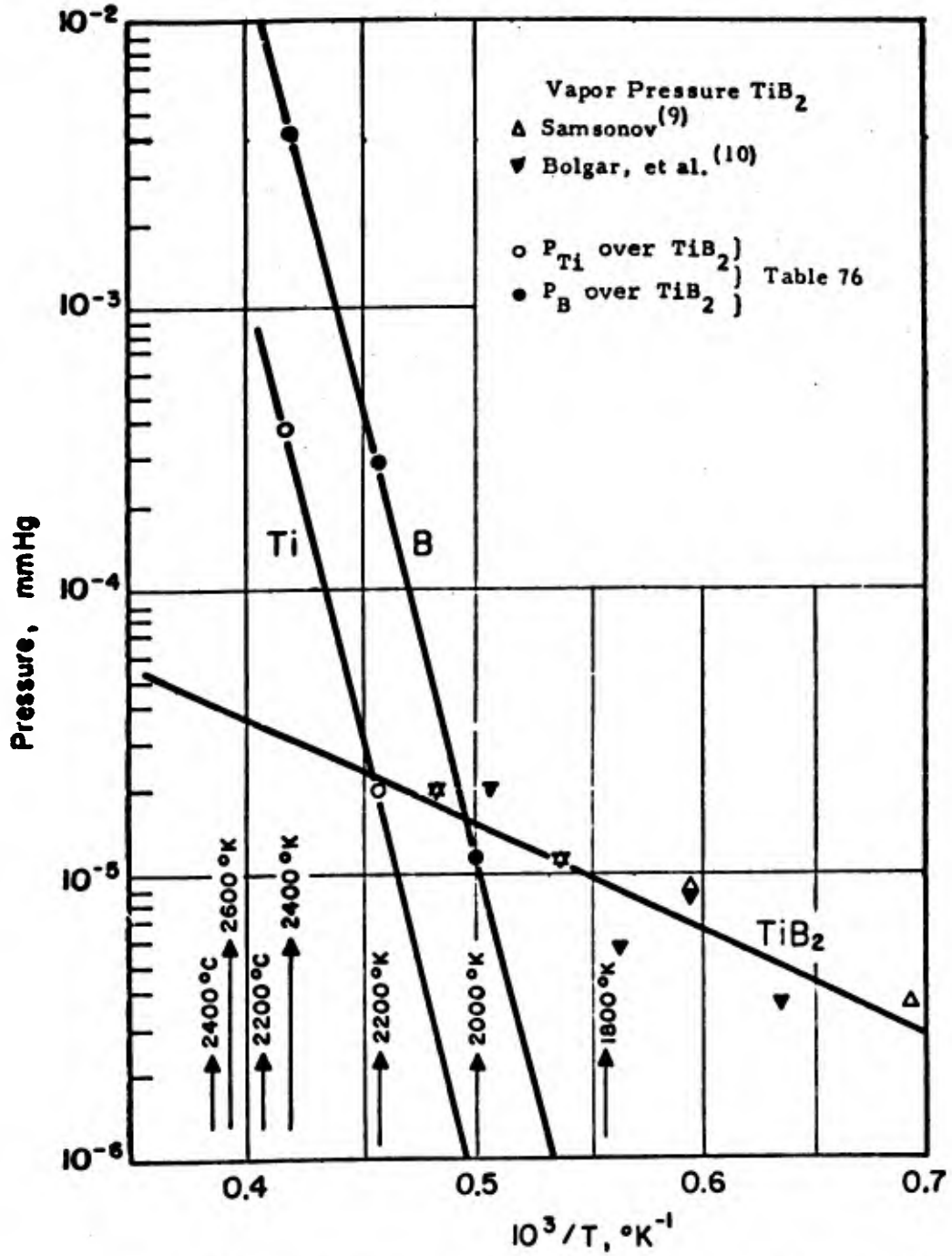

Fig. 41 - Vapor Pressure of TiB_2 as a Function of Temperature.

TiB_2 is apparently an intermediate case where neither the mechanisms which produce shrinkage nor the vapor transport mechanism is dominant. That vapor transport is operative in TiB_2 may be judged from the fact that the samples lose 2-5% of the initial weight during sintering (Tables 27 and 28).

The temperature dependence of the density limit results from the different activation energies for the vapor and diffusion transport mechanisms. The activation energies calculated from the vapor pressures of the components of TiB_2 are 110 kcal/mole for Ti and 142 kcal/mole for boron. The activation energy for sintering was found to be above 150 kcal/mole. Therefore, with increasing temperatures the diffusion transport process is increasing faster than vapor transport, and higher limiting densities can be achieved. Upon re-firing a sample of FEM TiB_2 to 2400°C which had been equilibrated at 2250°C with a density 3.79 gm/cm^3, it was found that the density did not increase. This qualitatively supports the argument that the pores attain a stable size as temperature-dependent densification occurs.

This interpretation is supported by the coincidence of the density limit observed at 2300°C for our data and for Babich's data[2]. The increased density limit with additives at low temperatures may also be interpreted as an increase in sintering rate (probably by the introduction of material transport through a liquid film formed during sintering without affecting the vapor pressure at that temperature).

4. Achieving High Densities

On the basis of the results of the sintering studies performed on this contract and the interpretation of the sintering mechanism, it is clear that sintered densities above 90% of theoretical density can be achieved for TiB_2 by

sintering at temperatures above 2400°C. In contrast to most other systems the starting particle size and sintering time are relatively unimportant. Sintering in a helium or argon atmosphere to decrease the vaporization rate would probably be helpful; this was not investigated.

Additions of ten percent of nickel, cobalt, or chromium are effective sintering aids. With fluid energy milled, submicron particle size materials and a 10% chromium addition, 95% density compacts are formed at 2200°C. This was the highest density achieved on this project. Elongated grains exist in the sintered compact, with some porosity enclosed within grains characteristic of the structures formed after discontinuous grain growth.

5. Results on Niobium Diboride and Zirconium Diboride

Niobium diboride specimens were prepared at forming pressures ranging from 42,000 to 144,000 psi. The pressed densities of the fluid energy milled powder ranged from 3.51 gm/cm^3 for samples pressed at 42,000 psi to 3.89 gm/cm^3 for samples pressed at 144,000 psi. Specimens were sintered for times varying between 5 and 60 minutes at temperatures from 2000° to 2650°C. The data are tabulated in Table 29 and the densities are plotted as a function of time in Fig. 42. In contrast to titanium diboride, niobium diboride exhibits increased densities with time up to an hour for specimens fired at 2000°C. For the limited amount of data available, the density appears to vary linearly with the logarithm of time. Samples were also fired at the higher temperatures, but for shorter total times than for the samples fired at 2000°C. The sintering rates increased with increasing temperature up to 2400°C. At 2200°C, a sample fired for 45 minutes exhibited slightly smaller density than that fired for 10 minutes indicating a density limit similar to that observed with

Table 29

Sintering Data for NbB_2 and ZrB_2

Sample	Form Pressure (kpsi)	Green Density (gm/cm^3)	Fired Density (gm/cm^3)	Time (min.)	Temp (°C)	% Wt. Loss $(\frac{\Delta\omega}{\omega_o})$ 100
A. NbB_2						
II-1 FEM	144	3.89	4.97	5	2200	2.2
	144	3.89	5.30	10	2200	
N-8 FEM	60	3.55	5.27	45	2200	1.9
II-3 FEM	144	3.54	4.46	5	2000	2.4
			4.52	10	2000	2.5
			4.72	15	2000	2.6
			4.84	30	2000	2.6
			4.89	60	2000	2.6
II-4 FEM	42	3.51	4.38	5	2000	2.9
			4.47	10	2000	3.0
			4.54	15	2000	3.1
			4.72	30	2000	3.1
			4.88	60	2000	3.1
II-5 FEM	42	3.51	4.83	5	2300	2.1
			5.10	10	2300	2.1
II-6 FEM	144	3.87	5.32	2	2420	
II-7 FEM	144	3.83	6.27*	14	2420	
			5.95*	14	2420	
N-9 70% AR 30% FEM	144	3.94	5.40	14	2650	3.4
N-10 AR	144	3.90	5.14	14	2650	2.5
B. ZrB_2						
Z-1	144	4.03	4.25	10	2200	2.1
Z-2	144	4.02	5.23	45	2200	3.1
Z-3	144	4.03	4.61	10	2600	2.9

*Sample fractured--measurements made on 2 pieces of sample.

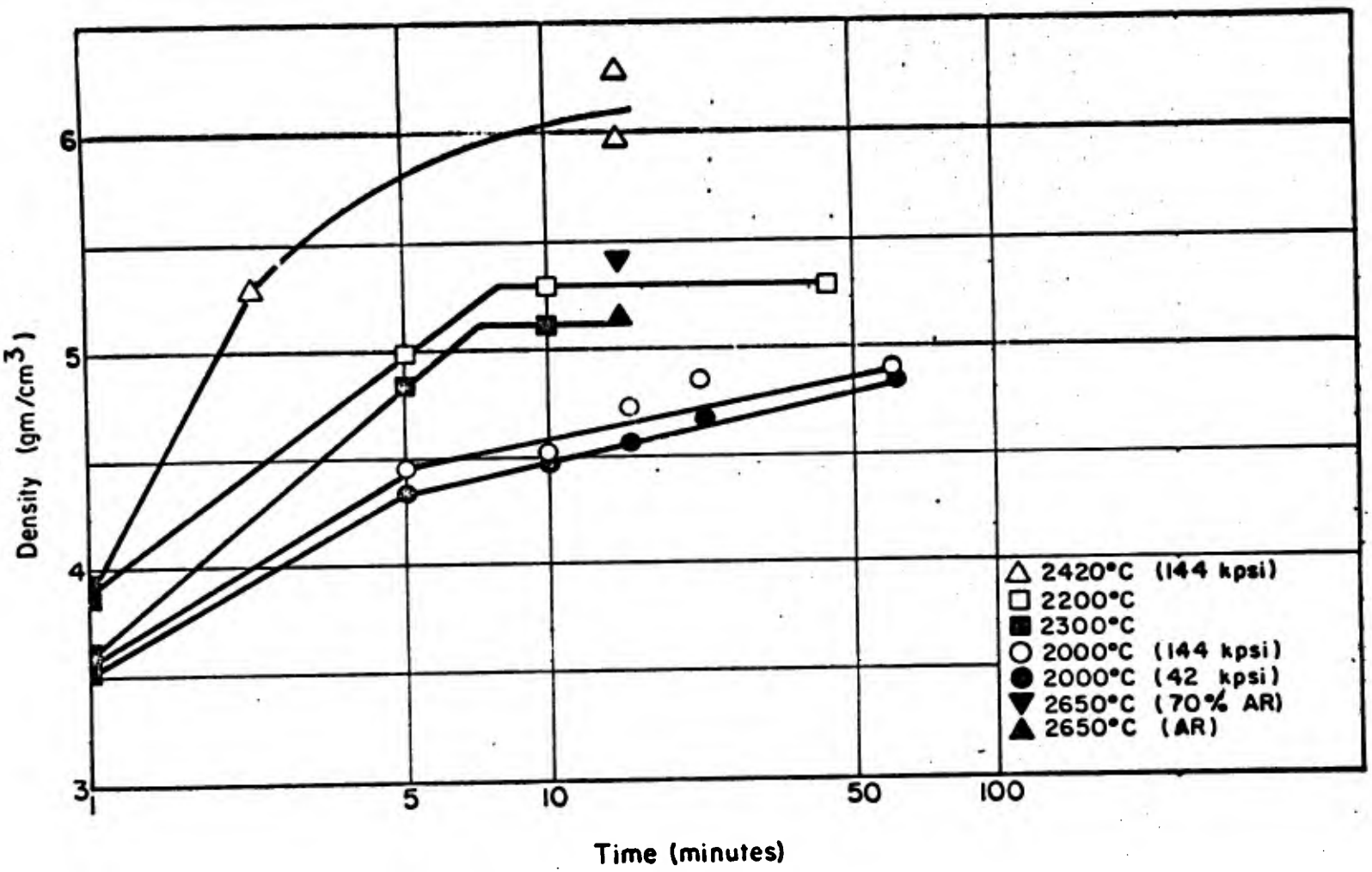

Fig. 42 - Density vs. Time for NbB_2.

TiB_2. The actual densities observed on samples fired at 2300° are less than those at 2200°C. However, they were formed at lower pressures and the density change is higher for the 2300°C specimens than for the 2200°C specimens. The highest density was observed in specimens sintered at 2420°C with a maximum value at 6.27 gm/cm^3. Samples sintered at 2650°C for 15 minutes exhibit densities averaging only 5.25 gm/cm^3. This experiment was not repeated and it is not known specifically whether the density limit for 2650°C is lower than at 2420°C. The weight loss at 2600°C (3%) is equivalent to the weight losses observed in all of the niobium diboride specimens for all temperatures of firing. Thus, the reduced density limit cannot be attributed to enhanced vaporization as judged from the weight losses.

The zirconium diboride results are presented in Table 29. The maximum density achieved is ~85% of theoretical. The results for NbB_2 and ZrB_2 are not substantiated by duplicate runs, and some of the irregularities in behavior (such as the lower density limit at 2650°C than 2420°C for NbB_2) may be due to scatter, temperature control or some other variation in procedure. It is assumed that such irregularities should be attributed to scatter until they are duplicated. Otherwise, the sintering behavior of NbB_2 appears to follow that found for TiB_2, exhibiting a density limit which is temperature dependent.

E. Conclusions

a. The sintering characteristics of TiB_2 consist of:

(1) An initial short-time density increase which is linear with log time.

(2) A temperature dependent end point density (not resulting from grain growth and pores trapped inside grains) which does not increase upon re-firing to a higher temperature.

(3) The development of pores larger than the starting pore size.

(4) Weight-loss during sintering.

(5) Near independence of end-point density and starting particle size.

b. These characteristics result from the fact that material transport by vaporization-condensation and bulk diffusion occurs at similar rates in the region where both are effective, but that the activation energy for diffusion is greater than that for vaporization.

c. Sintered densities for TiB_2 greater than 90% of theoretical density can be achieved by sintering at temperatures above 2400°C or by using Ni or Co additives which are subsequently removed by vaporization. The highest density was achieved with 10% Cr addition, 2200°C firing to yield 95% density.

d. The grain sizes are larger in the samples prepared with additives. The probable effect is therefore the enhancement of sintering by a liquid phase mechanism rather than by growth inhibition during diffusional sintering.

e. The additives are reduced during sintering by vaporization; the residual content is less than 2%.

f. Niobium diboride and zirconium diboride were not investigated as extensively as TiB_2. Density limits as a function of time and temperature also appear to exist for these materials, but are not documented.

REFERENCES

1. Kingery, W.D., "Introduction to Ceramics" pp. 369-380, John Wiley & Sons, N.Y., 1961.

2. Babich, B.N., Portnoy, K.I., Samsonov, G.V., "Pressing and Sintering of Borides: See ASD-TDR-62-873, p. 89.

3. Coble, R.L., "Sintering Crystalline Solids I," J. Appl. Phys. (1961) 32 (5) 787-92.

4. Coble, R.L., "Sintering Crystalline Solids II," J. Appl. Phys. (1961) 32 793-99.

5. Bruch, C., "Sintering Kinetics for the High Density Alumina Process," Bull. Amer. Cer. Soc., (1962) 41 (12) 799-806.

6. Kingery, W.D., "Regulation, Surface Diffusion and Ice Sintering," J. Appl. Phys., (1960) 31 (5) 833-38.

7. Kingery, W.D. and Berg, M., "Study of the Initial Stages of Sintering Solids by Viscous Flow, Evaporation-Condensation and Self Diffusion," J. Appl. Phys., (1955) 26 1205.

8. Morgan, C.S., Personal Communication.

9. Samsonov, cf ASD-TDR-62-872, p. 55.

10. Bolgar, Verkloglyadova, and Samsonov, cf ASD-TDR-62-872 p. 55.

VIII. X-RAY MEASUREMENTS OF LATTICE CONSTANTS, THERMAL EXPANSION AND DEBYE TEMPERATURES*

A. Introduction

The purpose of this section is to provide measurements of lattice constants, thermal expansion coefficients between room temperature and 1500°C and Debye temperature parameters using X-ray powder diffraction techniques. Lattice constants and thermal expansion measurements have been obtained for HfB_2, ZrB_2, NbB_2, TaB_2 and TiB_2. Debye temperature measurements at high temperature have been obtained for HfB_2 and ZrB_2 taking into account anisotropy of thermal vibrations. Entropy calculations are presented using the measured Debye temperatures and the results compared with thermodynamic measurements.

B. Experimental Apparatus

The x-ray apparatus employed in these measurements consisted of a Picker, horizontal goniometer, a bent crystal monochromator, and a high temperature specimen chamber with resistance heated filament. Detection apparatus consisted of a Norelco scintillation counter, conventional pulse height analyzer electronics and strip chart recorder. Fig. 43 is a photograph of the assembled apparatus. Fig. 44 is a photograph of the high temperature specimen chamber with vacuum cap removed and heating element displayed.

The bent crystal monochromator was designed and fabricated in this laboratory. A silicon single crystal, cut to expose a (111) face, bent to a radius of 500 mm and ground to a radius of 250 mm was mounted and oriented to focus the divergent incident beam on the specimen surface. Only a very narrow range of wavelengths centered about the $K_{\alpha_1 \alpha_2}$ doublet of the CuK_α radiation used in these measurements is diffracted by the silicon crystal. The general loss in

*H. Bernstein, ManLabs, Inc.

Fig. 43 - X-ray apparatus indicating the arrangement of goniometer, monochromator, specimen chamber and detector.

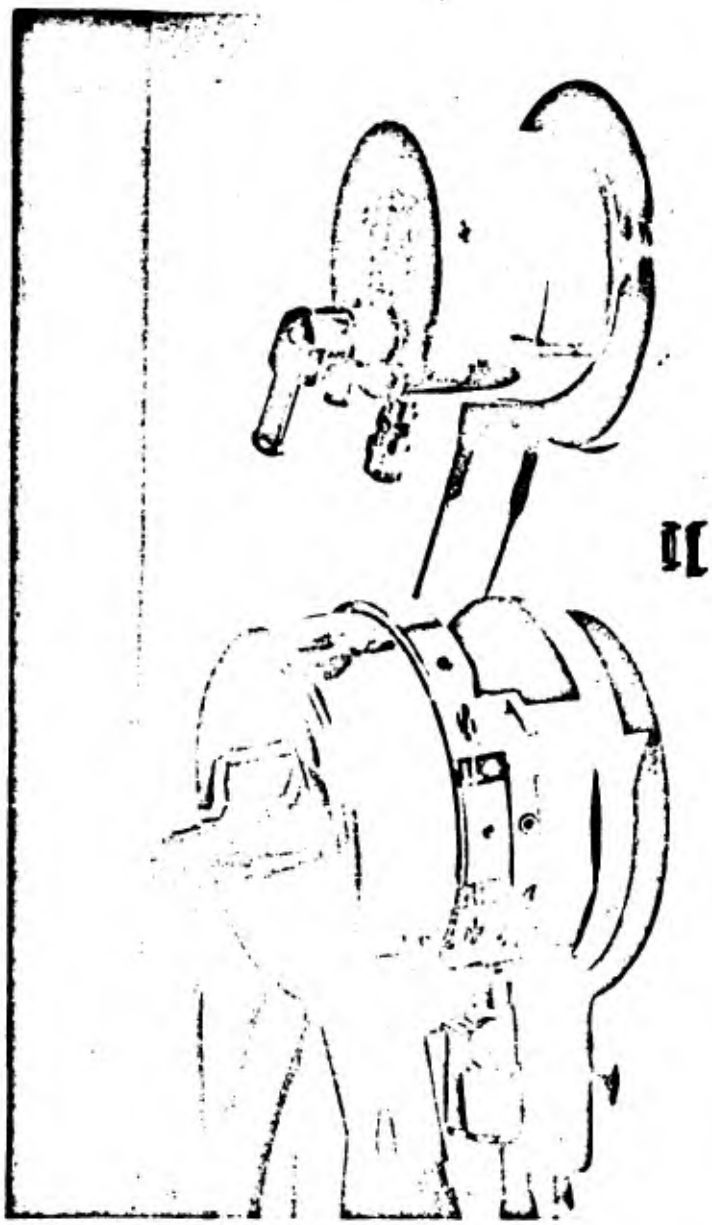

Fig. 44 - High temperature specimen chamber.

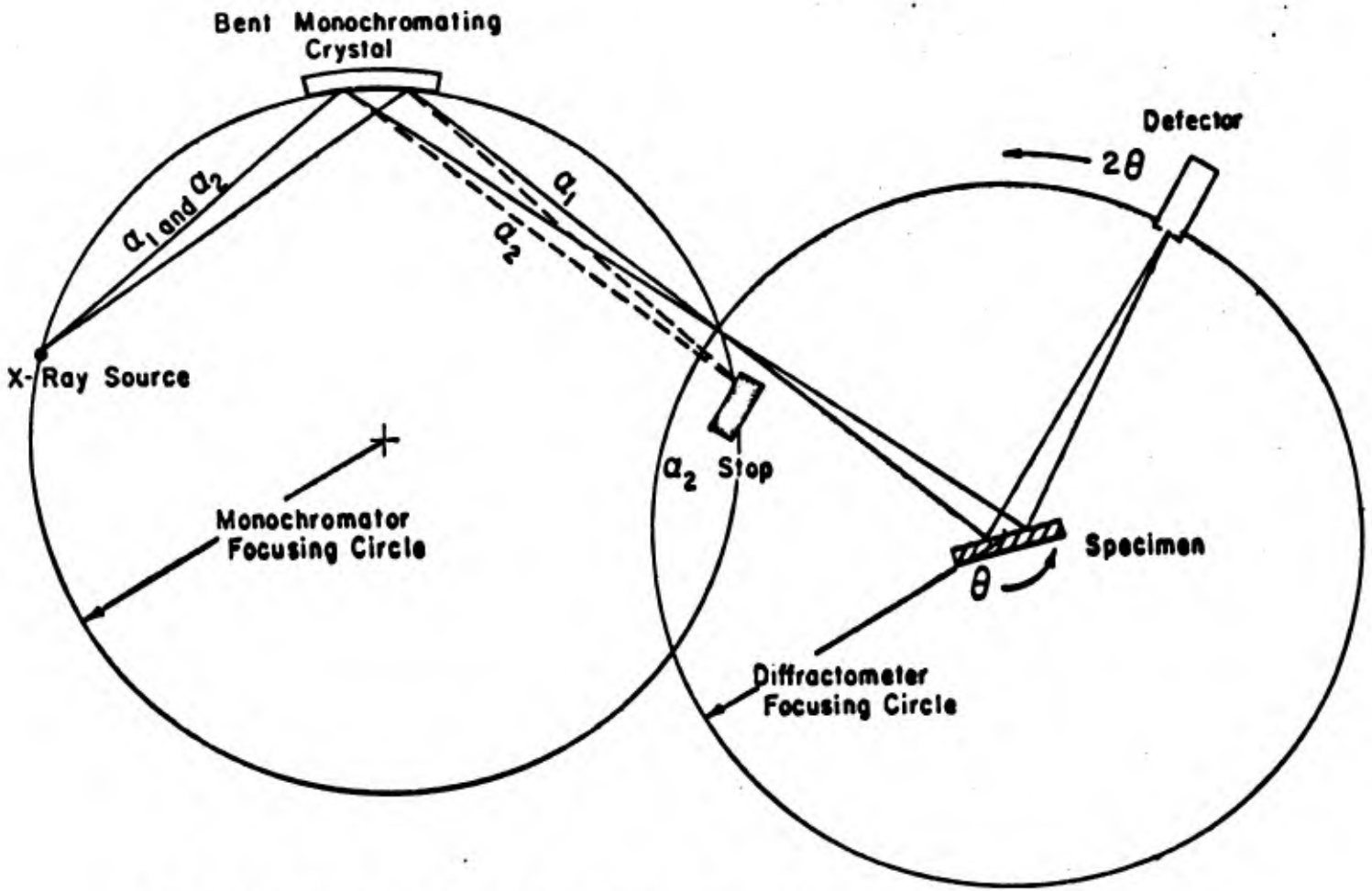

Fig. 45 - X-Ray optics for the bent crystal monochromator.

incident beam intensity, however, is compensated by the improved peak to background definition of high angle reflections. High angle reflections provide the most accurate measurements of peak position shift and intensity variation with temperature. A sketch of the X-ray optics of the bent crystal monochromator is seen in Fig. 45.

The high temperature specimen chamber, obtained from M.R.C. Corporation, is provided with external micrometer drives for specimen eccentricity and tilt adjustments at temperature, a beryllium X-ray window, vacuum feed-throughs for thermocouple use, quartz window for pyrometer viewing,and vacuum port. Water cooling to protect the X-ray window also cools the current terminals and establishes the filament reference temperature at about 3°C. Power to the heating strip is obtained from a high current power supply stabilized through an isolation transformer. Because the thermal time constant of the filament is small, temperature changes and equilibrium are attained very quickly. The tantalum filaments are sufficiently uniform to permit temperature calibration with measured current input. A portable vacuum system was fabricated which permitted the specimen chamber to rotate through the full 2θ range and maintain working pressures of $2 - 3 \times 10^{-5}$ mm of Hg.

Lattice constants at room temperature were measured on as-received powder and selected zone refined specimens in air. Thermal expansion and intensity-temperature measurements were made under vacuum after first annealing the powder specimens and tantalum filaments at about 1500°C for one hour. The heat treatment generally caused the tantalum filament to recrystallize and generate a strong X-ray peak visible through the powder pattern. The powder was deposited directly onto the filament surface from an acetone suspension and consequently remained

as a relatively thin layer. The tantalum peak, however, was used to advantage as an expansion standard.

Temperatures above 800°C were recorded with a calibrated optical pyrometer by viewing the center of the powder surface through a quartz window and pyrex prism. Uncertainties in temperature in the range of 1500°C were estimated at ± 10°C. Temperatures below 800°C were measured by a thermocouple in contact with the back of the heater filament. The contact between the thermocouple bend and filament, however, created a "cold" spot which made temperature determinations at the low end difficult. Most measurements of thermal expansion and Debye temperatures were consequently restricted to temperatures above 800°C.

C. Lattice Parameter Measurements

The room temperature lattice constants of all presently available boride powders and some zone refined crystals have been measured to at least four significant figures. Systematic errors in observed Bragg angle arising from absorption and specimen eccentricity effects can be expressed[1] as:

$$\frac{\Delta d}{d} = K f[\theta] \text{ where } f[\theta] = \frac{1}{2}\left(\frac{\cos^2\theta}{\sin\theta} + \frac{\cos^2\theta}{\theta}\right) \qquad (1)$$

$f[\theta]$ is called the extrapolation function and $\frac{\Delta d}{d} = \cot\theta\,\Delta\theta$ is the relative uncertainty in d-spacing associated with the shift in angle $\Delta\theta$ from the true Bragg angle θ. $f[\theta]$ goes to zero as θ approaches 90°, an 2θ approaches 180°. Consequently the error in calculated d-spacing is minimized by observing high angle reflections. The usual procedure is to plot the apparent lattice constants, given by:

$$c^* = \frac{\lambda l}{2\sin\theta_{(00l)}} \quad \text{and} \quad a^* = \lambda\left(\frac{h^2+hk+k^2}{3}\right)^{1/2}\frac{1}{\sin\theta_{(hk0)}} \qquad (2)$$

as a function of the extrapolation function $f[\theta]$ from the observed angles $\theta_{(ool)}$ and $\theta_{(hko)}$. The curve is then extrapolated to $f[90^\circ] = 0$ to yield the true constants c_o and a_o. A representative extrapolation plot is shown for HfB_2 in Fig. 46. for which the extrapolated lattice parameters are $a_o = 3.1410 \pm .0001$Å and $c_o = 3.4761 \pm .0001$Å. The extrapolation procedure is most accurate when high angle lines between about 70° and 90° are available. Unfortunately we are restricted to only the {hko} and {ool} series under CuK_α radiation which reduce the number of usable peaks for the borides to only a few distributed over the entire angular range. Hence, with the exception of HfB_2, the uncertainties of all other lattice parameters listed in Table 30 are between $\pm .0005$Å and $\pm .001$Å.

The slope of the curves a* and c* vs. $f[\theta]$ are a measure of the specimen eccentricity $\frac{\Delta R}{R}$, where R is the radius of the diffractometer circle and ΔR is the displacement of the specimen powder surface from the center of the focusing circle (ideally zero). For an R = 6 inches and the slopes of Fig. 46 we calculate $\Delta R \sim 2 \times 10^{-3}$ inches, indicating the sensitivity of the measurement to precise specimen centering. Once the lattice constants were determined, further measurements on a particular boride were calibrated to zero eccentricity by moving the specimen surface until the true Bragg angle calculated for the intense (100) line was attained.

The parameters of Table 30 are those for the compositions in $^a/_o$ B listed in the right hand column. These compositions are taken from the chemical analyses reported in Section III. The results are to be compared with those for the stoichiometric composition ($^a/_o$ B = 66.67) taken from the most recently reported values in the literature of Table 31 .

The measurements for NbB_2 are of special interest. According to Nowotny, et al[2] the NbB_2 phase has a wide range of homogeniety extending from

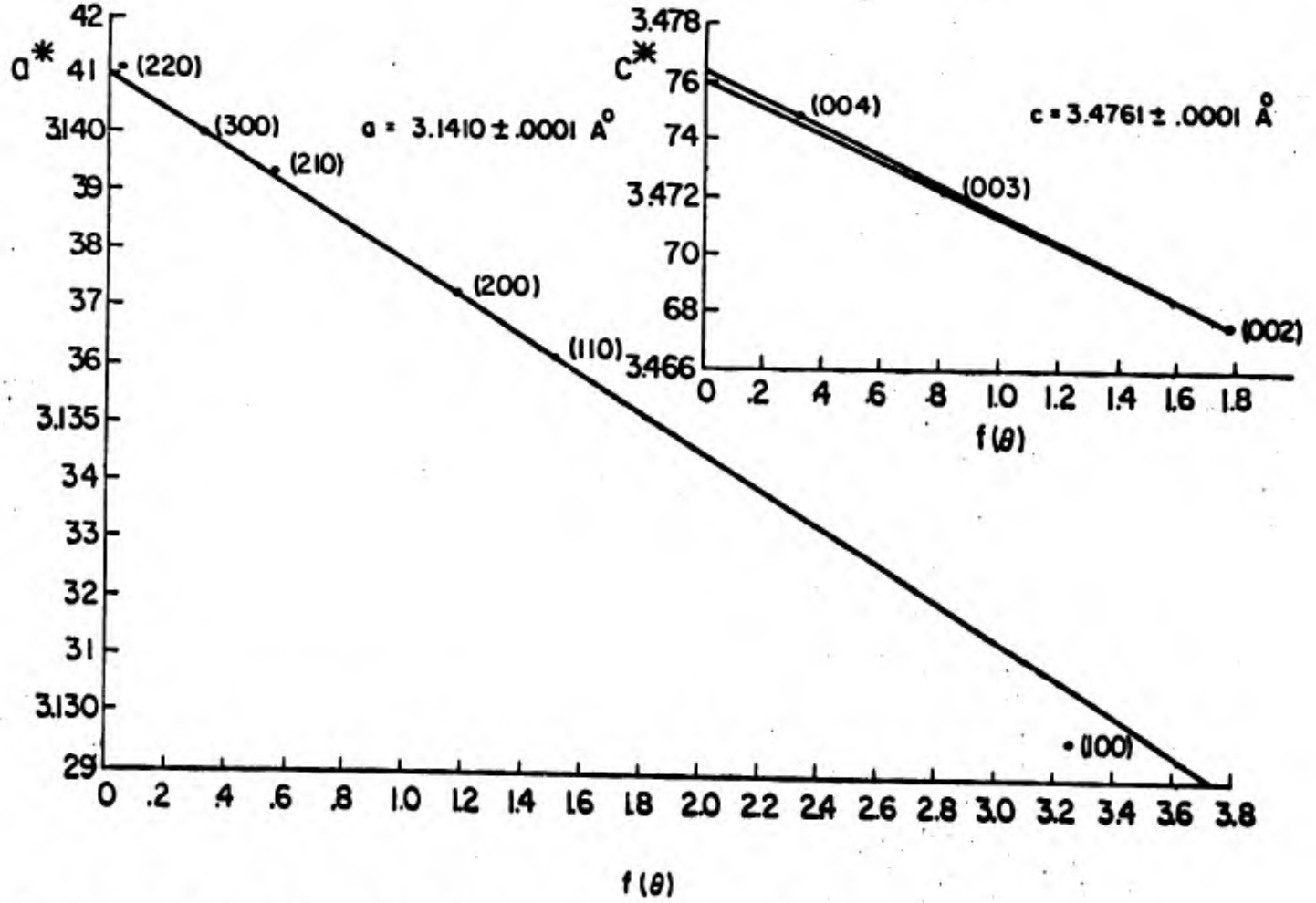

Fig. 46 - HfB_2 Lattice constant extrapolation.

65 a/o B to 70 a/o B. Over this range of composition, the lattice parameters vary significantly. a_o decreases from 3.111Å to 3.093Å while a/o B increases from 65 to 70; c_o increases linearly from 3.260Å to 3.305Å. This variation suggests the possibility of measuring departures from stoichiometry by measuring lattice parameters. Four specimens of NbB_2 having different boron concentrations according to chemical analysis were examined. Two specimens were as-received powders from U.S.B. shipments #1 and #2 and two were powdered, zone refined crystals #467 and #469 provided by G. Clay of Arthur D. Little. Unfortunately, all specimens were on the metal rich side of stoichiometry where the a_o parameter variation is small. In particular, U.S.B. #1 material contained a very definite second phase and showed lattice constants corresponding to the phase boundary. To a greater or lesser degree HfB_2, ZrB_2 and NbB_2 as-received powder patterns showed faint peaks which could be indexed as NaCl phases with lattice parameters of about 3Å. No attempt was made to identify these phases.

The measured parameters for the NbB_2 specimens were compared with Nowotny's curves and the predicted compositions compared with those obtained from chemical analyses in Table 30 . When the measured parameters a_o and c_o do not correspond to the same composition, the range of compositions between the two values is given. These results are collected in Table 32.

Zone refined single crystal boules of NbB_2 and ZrB_2 obtained from A.D.L. were examined and found to consist of a single crystal core and polycrystalline skin. The orientation determined by Laue back reflection camera techniques and diffractometer scans was found to be one in which the longitudinal axes of the boules were very closely parallel to a < 100> direction.

Table 30

Lattice Constants of the Metal Diborides

Compound	Source	a(Å)	c(Å)	a/o B(Chemical Analysis)
ZrB_2	U.S.B. #1	3.171	3.527	65.2-65.4
TiB_2	M.M. #2	3.030	3.228	66.2-66.6
TiB_2	U.S.B. #1	3.030	3.229	66.4-66.7
TaB_2	Kawecki #1	3.085	3.240	66.1
HfB_2	Wah Chang #1	3.1410	3.4761	66.3
NbB_2	U.S.B. #1	3.111	3.261	63.2-69.4
NbB_2	U.S.B. #2	3.107	3.282	66.6
NbB_2	S.C. #467 (A.D.L.)	3.1085	3.263	66.0
NbB_2	S.C. #469 (A.D.L.)	3.109	3.264	65.2

Table 31

Published Values of the Lattice Constants

Compound	a(Å)	c(Å)	Reference
ZrB_2	3.169	3.531	3
TiB_2	3.028	3.228	4
TaB_2	3.078	3.228	4
HfB_2	3.142	3.475	4
NbB_2	3.089	3.303	5

Table 32

Predicted Compositions of NbB_2 from Lattice Parameter Measurements

Compound	% B Predicted	% B Chemical Analysis
U.S.B. #1	65.0 or less	63.2-64.4
U.S.B. #2	67.6-68.0	66.6
S.C.#467	65.6-67.1	66.0
S.C. #469	66.0-67.0	65.2

D. Thermal Expansion Measurements

1. Analytical Technique

The thermal expansion of the metal diborides is characterized by two expansion coefficients parallel and perpendicular to the hexagonal axis of symmetry. When the expansion is linear with temperature in both directions, we define linear expansion coefficients α_a and α_c according to:

$$\frac{\Delta a}{a_o} = \alpha_a (t - t_o)$$

$$\frac{\Delta c}{c_o} = \alpha_c (t - t_o) \qquad (3)$$

where Δa and Δc are the changes in lattice constant accompanying an increase in temperature from t_o to t. The changes in lattice constants will cause a change in d-spacing for a particular x-ray reflection characterized by (hkl) as:

$$\frac{1}{d_o^2}\left(\frac{\Delta d}{d_o}\right) = \frac{4}{3}\frac{n^2}{a_o^2}\left(\frac{\Delta a}{a_o}\right) + \frac{l^2}{c_o^2}\left(\frac{\Delta c}{c_o}\right) \text{ where } n^2 = h^2 + hk + k^2 \qquad (4)$$

to first order in Δa and Δc. The relative change in d is now related to the observed shift in Bragg angle $\Delta\theta$ by the familiar relationship:

$$\Delta d = - d_o \cot \theta_o \, \Delta\theta \tag{5}$$

and with Bragg's law in the form:

$$d_o = \frac{\lambda}{2 \sin \theta_o} \tag{6}$$

we combine (4), (5) and (6) to obtain a relationship between the measured angular shift with temperature and the linear expansion coefficients:

$$\frac{1}{d_o^2} \left(\frac{\Delta d}{d_o} \right) = - \frac{\pi \sin \phi_o}{180 \lambda^2} \Delta\phi = \frac{4}{3} \left(\frac{n^2}{a_o^2} \alpha_a + \frac{l^2}{c_o^2} \alpha_c \right) (t - t_o) \tag{7}$$

If $\phi_o = 2\theta_o$ is the diffractometer angle, then $\Delta\phi = \Delta(2\theta) = 2\Delta\theta$ is the measured angular shift in degrees. $\Delta\phi[t]$ is necessarily a linear function of the temperature if α_a and α_c are constants. Denoting by S[hkl] the slope of the $\Delta\phi$(deg) vs. t curve, we derive expressions for α_a and α_c in terms of the measured slopes $S[h_1k_1l_1]$ and $S[h_2k_2l_2]$ for any two general peaks, namely:

$$\begin{aligned} \alpha_a &= \frac{\sigma_a}{m^2} \{ l_1^2 \sin \phi_2 \, S[h_2k_2l_2] - {}^2 \sin \phi_1 \, S[h_1k_1l_1] \} \\ \alpha_c &= \frac{\sigma_c}{m^2} \{ n_2^2 \sin \phi_1 \, S[h_1k_1l_1] - n_1^2 \sin \phi_2 \, S[h_2k_2l_2] \} \end{aligned} \tag{8}$$

The symbols in Eq. (8) are defined by:

$$\begin{aligned} \sigma_a &= \frac{\pi a_o^2}{240 \lambda^2} \; ; \quad n_1^2 = h_1^2 + h_1k_1 + k_1^2 \\ \sigma_c &= \frac{\pi c_o^2}{180 \lambda^2} \; ; \quad n_2^2 = h_2^2 + h_2k_2 + k_2^2 \end{aligned} \tag{9}$$

For the special case of an (hko) line or an (ool) line, α_a and α_c are calculated directly from:

$$\alpha_a = \left(\sigma_a \frac{\sin \phi_o}{h^2}\right) S[hko]$$

$$\alpha_c = \left(\sigma_c \frac{\sin \phi_o}{l^2}\right) S[00l] \qquad (10)$$

2. Experimental Results

The system was initially calibrated against extraneous mechanical shifts by measuring the expansion of the (321) line of pure Ta powder and comparing the resulting curve to the data of Edwards, et al[6]. If the Ta heater strip was initially heated for about one hour at temperatures between 1500°C and 1700°C, the calibration curve indicated that extraneous angular shifts were negligible and Eqs. 8 and 9 could be applied directly by feeding in the experimental numbers S[hkl]. A representative set of curves of $\Delta\phi$ vs. T for several lines of HfB_2 are shown in Fig. 47. The curves extrapolate smoothly through the origin (reference temperature $t_o = 3°C$). All the data for the borides gave linear curves within the experimental scatter between 800°C and 1500°C for points taken with either increasing or decreasing temperature. Not all of the lines extrapolated through the origin, due most probably to a shift in observed reference angle ϕ_o. When this occured, the slopes of at least three peaks were measured on the material and the computed results for α_a and α_c between pairs of peaks compared as a test of consistency. The consistency was sufficiently good to permit direct measurement of the slopes despite the shift in origin. Temperature data below 800°C with the exception of HfB_2 was finally discarded because of the perturbing effect of the thermocouple head on the heater element. Therefore, the reported coefficients

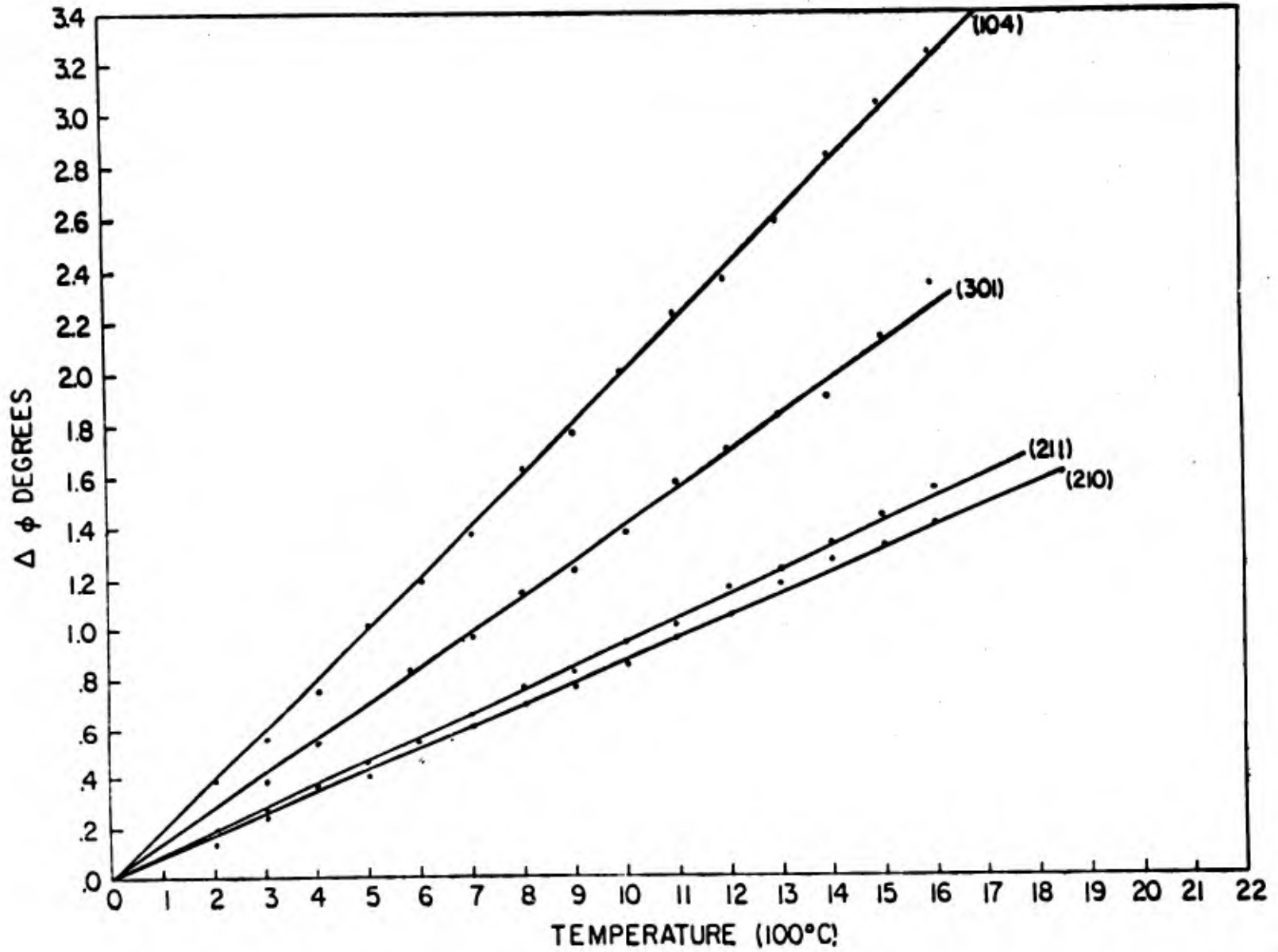

Fig. 47- Plot of angular shift of HfV_2 lines vs. temperature.

are accurate in the pyrometer range 800°C to 1500°C. The total uncertainty in the α's arising from temperature errors, uncertainties in peak position and spread in calculation between pairs of peaks is estimated at about $\pm$ .07 x 10^{-6}/°C. The results are listed in Table 33 with a crystalline average linear expansion coefficient $\alpha_L = \frac{1}{3}\alpha_c + \frac{2}{3}\alpha_a$ for comparison with polycrystalline bulk measurements. α_c is slightly larger than α_a for HfB_2 and NbB_2 but some 30 to 40% larger for TiB_2, TaB_2 and ZrB_2. Expansion anisotropy cannot be simply related to other thermophysical properties; however, it is interesting to note that the Debye temperatures associated with the "c" direction are consistently greater than those associated with the "a" direction (see Section VIII-5.3). Thus, the elastic anisotropy is the reverse of the expansion anisotropy in that the borides expand more readily in the "c" direction with temperature but vibrate with greater amplitudes in the "a" direction.

Powder X-ray determinations of thermal expansion are fundamentally different from dilatometric measurements on polycrystalline specimens. The X-ray measurements are more characteristic of single crystal behavior on an atomic scale; dilatometric measurements are more strongly effected by grain boundaries, porosity, residual stresses, etc. The X-ray thermal expansion coefficients are best compared with the linear coefficients of zone refined crystals of Section IX. Since the only orientations available for HfB_2, ZrB_2 and NbB_2 are <100> the expansion coefficients reported in Section IX on zone refined bars are effectively α_a. A comparison between the X-ray and dilatometric measurements is given in Table 34.

X-ray expansion results for ZrB_2 and TiB_2 up to 2020°C have been reported recently by Union Carbide Research Institute.[11] Their expansion coefficients α_a and α_c increase with temperature; for ZrB_2 α_a becomes greater than α_c above ~ 1100°C. In particular α_a = 6.59 to 7.54, α_c = 6.80 to 7.21 ($\times 10^{-6}$/°C) between 754°C and 1514°C for ZrB_2; and α_a = 6.02 to 7.61, α_c = 8.50 to 10.22 over the same range for TiB_2. The TiB_2 results agree with those

reported here (α_a = 7.19, α_c = 9.77) for the range 800°C to 1500°C; however the ZrB_2 results are not in good agreement (α_a = 5.92, α_c = 7.04). The reason for the discrepancy is unknown at this time; additional experimental work will be required for ZrB_2.

Table 33

X-Ray Thermal Expansion Coefficients (units of 10^{-6}/°C)
800°C to 1500°C

Compound	α_a	α_c	α_L	$\frac{\alpha_c}{\alpha_a}$
HfB_2	6.64	6.89	6.72	1.04
NbB_2	8.69	9.42	8.93	1.07
TiB_2	7.19	9.77	8.02	1.36
TaB_2	8.46	10.90	9.27	1.29
ZrB_2	5.92	7.04	6.29	1.37

Table 34

Comparison of X-Ray and Dilatometric Zone Refined Thermal Expansion Coefficients α_a

Compound	X-Ray	Dilatometric
HfB_2	6.64 x 10^{-6}/°C	7.49 x 10^{-6}/°C
ZrB_2	5.92	7.95
NbB_2	8.69	7.32

E. Debye Temperature Measurements

The calculation of the free energy of formation, vapor pressure and other thermodynamic properties of the borides requires a knowledge of the Debye temperatures of these compounds to estimate the vibrational contributions to the free energy. In the absence of specific heat data, a Debye temperature derived from X-ray intensity temperature dependence will provide a starting point for free energy estimations. When specific heat data is available, the X-ray Debye temperature can be compared with that derived from the specific heat to check the accuracy of the theoretical models. The purpose of this task has been to investigate the vibrational behavior of several borides using high temperature X-ray techniques. The investigation indicated a significant vibrational anisotropy associated with the thermal vibrations parallel and normal to the symmetry axis of the hexagonal boride structure for the two compounds investigated, HfB_2 and ZrB_2. Room temperature entropies were calculated using the "two θ" method of Section XVI for decomposing the specific heat with Debye temperatures associated with the individual metal and boron atom species. The results, after a suitable average over crystal anisotropy, were in good agreement with the entropies deduced from specific heat measurements. In addition, the X-ray Debye temperature results of Miksic[7] on TiB_2 were used to calculate the room temperature entropy of TiB_2 for comparison with specific heat data.

1. Theoretical Considerations

The integrated X-ray peak intensity for a flat powder specimen under crystal monochromated radiation has the form:

$$I[hkl, T] = K\, L[\phi, \phi']\, p[hkl]\, F[hkl, T]^2 \qquad (11)$$

where K is a constant including all factors independent of temperature T or angle ϕ, p[hkl] is the multiplicity factor for the set of Miller indices (hkl), F[hkl, T] is the generalized structure factor including the temperature dependence of the intensity and $L[\phi, \phi']$ is an angular factor appropriate to crystal monochromated radiation. $L[\phi, \phi']$ is given by[8].

$$L[\phi,\phi'] = \left(\frac{1+\cos^2 2\phi' \cos^2 2\phi}{1+\cos^2 2\phi'}\right)\left(\frac{1}{2\sin^2\phi\cos\phi}\right) \qquad (12)$$

where ϕ is the observed Bragg angle and ϕ' is the fixed Bragg angle for diffraction of the primary beam from the monochromating single crystal. In this work, the (111) reflection from single crystal silicon with CuK_{α_1} radiation was used, giving $\phi' = 14^\circ 15'$ and $\cos^2 2\phi' = .772$. $L[\phi, \phi']$ can be put into the more convenient form:

$$L[\phi,\phi'] = \text{const.}\left(\frac{1+\cos^2 2\phi}{\sin^2\phi\cos\phi}\right)\left(\frac{1+.772\cos^2 2\phi}{1+\cos^2 2\phi}\right) = L[\phi]H[\phi] \qquad (13)$$

The first factor is recognized as the familiar, tabulated, Lorentz polarization factor L[ϕ] and the second factor, H[ϕ], is a slowly varying function of ϕ ($.885 \leq H[\phi] \leq 1.00$).

The crystal structure of the metal diborides is that of the hexagonal C-32 type (AlB_2) in which the primitive unit cell contains one formula weight of MeB_2. The space group symmetry is D^1_{6h}-C6/mmm with metal atoms at (o, o, o) and boron atoms at (2/3, 1/3, 1/2), (1/3, 2/3, 1/2). Multiplicity factors for the hexagonal system are (hkl) - 24, (hhl), (ohl) & (hko) - 12, (hho) & (oko) - 6 and (ool) - 2. The equation for the generalized temperature dependent structure factor has the form:

$$F[hkl,T] = \sum_j f_j\left[\frac{\sin\phi}{\lambda}\right] e^{2\pi i(hu_j + kv_j + lw_j)} e^{-B_j[T]\frac{\sin^2\phi}{\lambda^2}} \qquad (14)$$

in which the summation over j is a summation over all atoms in the unit cell whose fractional spatial coordinates are (u_j, v_j, w_j). $f_j[\frac{\sin\phi}{\lambda}]$ is the electronic scattering factor of the jth atom and $B_j[T]$ is a temperature dependent function equal to $8\pi^2\overline{\mu_j^2[T]}$. $\overline{\mu_j^2[T]}$ is the mean square thermal displacement of the jth atom from its equilibrium lattice position in a direction normal to the diffracting plane characterized by the Miller indices (hkl). For a polyatomic cell, each atomic species in general has its own thermal amplitude.

For the C-32 structure, we have:

$$F[hkl, T] = f_{Me} \exp\left\{-B_{Me}[T]\frac{\sin^2\phi}{\lambda^2}\right\} + g[hkl]\, f_B \exp\left\{-B_B[T]\frac{\sin^2\phi}{\lambda^2}\right\} B^2$$

$$g[hkl] = 2(-1)^{h+k+1}\cos\frac{\pi}{3}(h-k) \qquad (15)$$

g[hkl] is restricted to form values ± 1, ± 2 for all (hkl). The observed intensities can now be decoupled algebraically to yield the quantities $\overline{\mu^2_{Me}}$ and $\overline{\mu^2_B}$ at fixed temperature. We define four functions F_1, F_2, F_3 and F_4 corresponding to the four values of $g = +1, -1, +2, -2$ respectively. Examples of F_1 type lines are (101), (213) etc., F_2 type lines are (100), (102) etc., and similarly for the others. Rearranging these functions we derive expressions for $\overline{\mu^2_{Me}}$ and $\overline{\mu^2_B}$ as:

$$-8\pi^2\overline{\mu^2_{Me}}\,\frac{\sin^2\phi}{\lambda^2} = \ln\left(\frac{F_1+F_2}{2f_{Me}}\right) = \ln\left(\frac{2F_1-F_3}{f_{Me}}\right) = \ln\left(\frac{2F_1+F_4}{3f_{Me}}\right) = \ln\left(\frac{2F_2+F_3}{3f_{Me}}\right)$$

$$= \ln\left(\frac{2F_2-F_4}{f_{Me}}\right) = \ln\left(\frac{F_3+F_4}{2f_{Me}}\right) \qquad (16)$$

$$-8\pi^2\overline{\mu_B^2}\ \frac{\sin^2\phi}{\lambda^2} = \ln\left(\frac{F_1 - F_2}{2f_B}\right) = \ln\left(\frac{F_3 - F_1}{f_B}\right) = \ln\left(\frac{F_1 - F_4}{3f_B}\right) = \ln\left(\frac{F_3 - F_2}{f_B}\right)$$

$$= \ln\left(\frac{F_2 - F_4}{f_B}\right) = \ln\left(\frac{F_3 - F_4}{4f_B}\right) \qquad (17)$$

Since all lines fall at different angles ϕ, the procedure is to measure the intensities $I[\phi]$ from a full powder scan; form the quantities $F = \frac{I^{1/2}}{pL}$ by normalizing the observed intensities with the appropriate angular and multiplicity factors; prepare four curves of F_1, F_2, F_3 and F_4 as a function of ϕ; form graphical sums and differences as indicated by Eqs. 16 and 17 for specific values of ϕ; and plot the logarithms of these sums and differences vs. $8\pi^2 \frac{\sin^2\phi}{\lambda^2}$. The final curves should be straight lines whose slopes have magnitudes $\overline{\mu_{Me}^2}$ and $\overline{\mu_B^2}$. An analysis of this type has been carried out for HfB_2 at room temperature. The uncertainties in the final results, however, are too large to permit published results. The uncertainties arise because the scattering power of boron is much less than that of the metal atom and because an insufficient number of lines are available with Cu radiation to permit the construction of accurate F vs. ϕ curves. The calculated spread in values of $\overline{\mu_{Me}^2}$ and $\overline{\mu_B^2}$ do, nevertheless, overlap. The indication is that the thermal amplitudes are approximately equal. We argue that the borides are high melting point compounds with strong interatomic bonding. Consequently both metal and boron atoms should experience equivalent force fields in the lattice and vibrate harmonically with equal amplitudes. Houska[9] has analyzed the refractory carbides TiC, ZrC, TiN and ZrN in the manner just indicated and was able to show accurately that the thermal amplitudes of the individual atoms up to temperatures of the order of 1700°C were approximately equal for all the

materials. Since the metal diborides are similar materials and analysis of the HfB_2 indicates equal amplitudes, we assume in the remaining analysis that the amplitudes are exactly equal. This assumption permits factoring the integrated intensity of a given peak into:

$$I[hkl, T] = e^{-16\pi^2 \overline{\mu^2[T]} \frac{\sin^2\phi}{\lambda^2}} \{\text{function of } \phi \text{ only}\} \qquad (18)$$

The subscript on $\overline{\mu^2[T]}$ in this equation has been purposely deleted. Had we been considering a monatomic, cubic lattice, the temperature dependence of the integrated intensity would have appeared identically as in Eq. 18 where $\overline{\mu^2[T]}$ would unambiguously have referred to the thermal amplitude of the single atomic species of mass m. The Debye-Waller theory immediately applies to this case and a well-defined Debye temperature θ_D is given by

$$\mu_s^2[T] = \frac{3h^2 T}{4\pi^2 m k \theta_D^2} \left\{ \underline{\Phi}(x) + \frac{x}{4} \right\} \qquad (19)$$

where

$$\underline{\Phi}(x) = \frac{1}{x} \int_0^x \frac{y\,dy}{e^y - 1}$$

and

$$x = \frac{\theta_D}{T}$$

where h and k are Planck's constant and Boltzmann's constant, T is the absolute temperature. The borides, however, present two problems for which the Debye-Waller theory is inadequate. Firstly, we are considering a diatomic lattice of very different atomic masses, which makes the assignment of m in Eq. 19

rigorously impossible. Secondly, we are dealing with a hexagonal lattice which exhibits vibrational anisotropy. Vibrational isotropy is another fundamental assumption underlying the Debye-Waller theory. We discuss the anisotropy problem below. The problem of atomic mass can be approached from the viewpoint of two physical models. If we imagine an artificial monatomic lattice of average mass $\overline{m} = \frac{1}{2}(m_{Me} + 2m_B)$ we can insert $\overline{m}$ into Eq. 19 and derive on "average" $\overline{\theta}$. If we consider that the scattered x-ray intensity is predominantly that of the metal atom we can imagine a sublattice of heavy metal atoms imbedded in a boron "continuum" and insert the metal mass m_{Me} to derive a θ_{Me}. θ_{Me} could be interpreted physically as a measure of the force field experienced by the metal atom in the compound state relative to the pure metallic state. At any rate, only these two choices appear possible if the Debye-Waller model is to be used.

The vibrational anisotropy for a hexagonal lattice containing a unique axis of symmetry, the "c" axis, can be described in the following way. Let $\overline{\mu_c^2}$ refer to the component of vibrational amplitude directed along the "c" axis, and let $\overline{\mu_a^2}$ refer to the component of vibrational amplitude anywhere in the plane normal to the symmetry axis. Since, in general, the elastic properties along the "c" direction are different from those in any of the equivalent "a" directions, we have $\overline{\mu_c^2} \neq \overline{\mu_a^2}$. For a diffracting plane whose direction normal $\overline{S}$ makes an angle α with the "c" axis, the observed amplitude $\overline{\mu_s^2[T]}$ for that peak can be expressed in a form suggested by James[10], namely:

$$\overline{\mu_s^2} = \overline{\mu_a^2} \sin\alpha^2 + \overline{\mu_c^2} \cos\alpha^2 \qquad (20)$$

The angle α is simply related to the Miller indices associated with the diffracting plane and the lattice constants for a hexagonal lattice by:

$$\cos \alpha = \left[\frac{4}{3}\left(\frac{c}{a}\right)^2 n^2 + l^2\right]^{-1/2} \qquad (21)$$

where

$$n^2 = h^2 + hk + k^2$$

Furthermore, by Bragg's law we rewrite the quantity $\frac{\sin^2\phi}{\lambda^2}$ in the form:

$$\frac{\sin^2\phi}{\lambda^2} = \frac{1}{4d^2[hkl]} = \frac{\frac{4}{3}\left(\frac{c}{a}\right)^2 n^2 + l^2}{4c^2} \qquad (22)$$

Combining (21) and (22) with the intensity formula (18) we have:

$$\ln\left(\frac{I[\phi, T]}{G[\phi]}\right) = -2B[T, \alpha]\ \frac{\sin^2\phi}{\lambda^2} = -\frac{16\pi^2}{3a^2} n^2\ \overline{\mu_a^2[T]} - \frac{4\pi^2}{c^2} l^2\ \overline{\mu_c^2[T]} \qquad (23)$$

where $G[\phi]$ is the total normalization factor including polarization factors, electronic scattering factors, etc. It should be possible to measure $\mu_a[T]$ and $\mu_c[T]$ directly by plotting the log of the normalized intensity vs. n^2 for the set of peaks {hko} or l^2 for the set of peaks {ool} at a fixed temperature. However, the powders examined exhibited a sufficient degree of preferred orientation to render the use of the fixed temperature intensity plots impossible.

The technique used was the conventional one of measuring the intensity change of selected high angle peaks as a function of temperature between room temperature T_o and temperature T up to about 1500°C. For a given peak, the intensity change with temperature is simply:

$$\ln\left(\frac{I[\phi, T_1]}{I[\phi, T_2]}\right) = \frac{16\pi^2}{3a^2} n^2\left(\overline{\mu_a^2[T_2]} - \overline{\mu_a^2[T_1]}\right) + \frac{4\pi^2}{c^2} l^2\left(\overline{\mu_c^2[T_2]} - \overline{\mu_c^2[T_1]}\right) \qquad (24)$$

We now introduce "pseudo" Debye temperatures θ_a and θ_c associated with principal crystallographic directions by assuming, without theoretical basis, that

the individual $\overline{\mu^2}$ are given by Debye-Waller functions of the form of Eq. 19.

i.e.,

$$\overline{\mu_a^2[T]} = \frac{3h^2T}{4\pi^2 m k \theta_a^2}\left\{\underline{\Phi}[x_a] + \frac{x_a}{4}\right\}, \quad x_a = \frac{\theta_a}{T} \qquad (25)$$

$$\overline{\mu_c^2[T]} = \frac{3h^2T}{4\pi^2 m k \theta_c^2}\left\{\underline{\Phi}[x_c] + \frac{x_c}{4}\right\}, \quad x_c = \frac{\theta_c}{T} \qquad (26)$$

Inserting these expressions into (24) and invoking the additional relationship $m = \frac{N_o}{M}$, where N_o is Avogadro's number and M is the molecular weight in $\frac{\text{gms.}}{\text{gm. at.}}$, we arrive at a compact form of Eq. 24:

$$\ln\left(\frac{I_o}{I_T}\right) = \frac{n^2}{\rho_a} f[\gamma, x_o^a] + \frac{l^2}{\rho_c} f[\gamma, x_o^c] \qquad (27)$$

where

$$\rho_a = \frac{a_o^2 M T_o}{4\beta} \qquad x_o^a = \frac{\theta_a}{T_o}$$

$$\rho_c = \frac{c_o^2 M T_o}{3\beta} \qquad x_o^c = \frac{\theta_c}{T_o} \qquad (28)$$

$$\beta = \frac{h^2 N_o}{k} = 1.91 \times 10^{-13} \ \frac{\text{gm cm}^2\ {}^oK}{\text{mole}}$$

and the dimensionless function $f[\gamma, x_o]$ is defined as:

$$f[\gamma, x_o] = \left\{\frac{1}{x_o}\ \frac{\underline{\Phi}[\gamma, x_o]}{\gamma x_o} - \frac{\underline{\Phi}[x_o]}{x_o}\right\} \qquad (29)$$

$$\underline{\Phi}[x] = \frac{1}{x}\int_o^x \frac{y\,dy}{e^y - 1}, \qquad \gamma = \frac{T_o}{T} < 1$$

$f[\gamma, x_o]$ is a monatomically decreasing function of x_o with γ as a parameter.

The asymptotic forms are given by:

$$f[\gamma, x_o] = \frac{1}{x_o^2}\left[\frac{\gamma-1}{\gamma}\right] - \frac{\gamma-1}{36} \quad , \quad \gamma x_o < .5 \qquad (30)$$

$$f[\gamma, x_o] = \frac{\pi^2}{6}\left[\frac{\gamma^2-1}{\gamma^2}\right]\frac{1}{x_o^3} \quad , \quad x_o > 5$$

$f[\gamma, x_o]$ vs. x_o is plotted in Fig. 48 for x_o in the range 1.0 to 2.4.

$\overline{\mu_a^2[T]}$ and $\overline{\mu_c^2[T]}$ can be calculated directly once θ_a and θ_c are determined. Eqs. 25 and 26 in compact form become:

$$\overline{\mu_a^2[T]} = \frac{\beta'}{MT} h[x_a] \qquad (31)$$

$$\overline{\mu_c^2[T]} = \frac{\beta'}{MT} h[x_c] \qquad (32)$$

where $\beta' = \frac{3\beta}{4\pi^2} = 1.45 \times 10^{-14}$ cm^{2}gm ^oK/gm.at. and $h[x] = \frac{1}{x^2}\left\{\underline{\Phi}[x] + \frac{1}{4}\right\}$

A minimum of two lines for each material must be examined as a function of temperature to determine θ_a and θ_c. Signifying two lines by the symbols 1 and 2 we use Eq. 27 and derive expressions for $f[\gamma, x_o^a]$ and $f[\gamma, x_o^c]$ in the form:

$$f[\gamma, x_o^a] = \frac{\rho_a}{m^2}\left\{l_2^2 \ln\left[\frac{I_{10}}{I_1}\right] - l_1^2 \ln\left[\frac{I_{20}}{I_2}\right]\right\} \qquad (33)$$

$$f[\gamma, x_o^c] = \frac{\rho_c}{m^2}\left\{n_1^2 \ln\left[\frac{I_{20}}{I_2}\right] - n_2^2 \ln\left[\frac{I_{10}}{I_1}\right]\right\} \qquad (34)$$

$$m^2 = n_1^2 l_2^2 - n_2^2 l_1^2$$

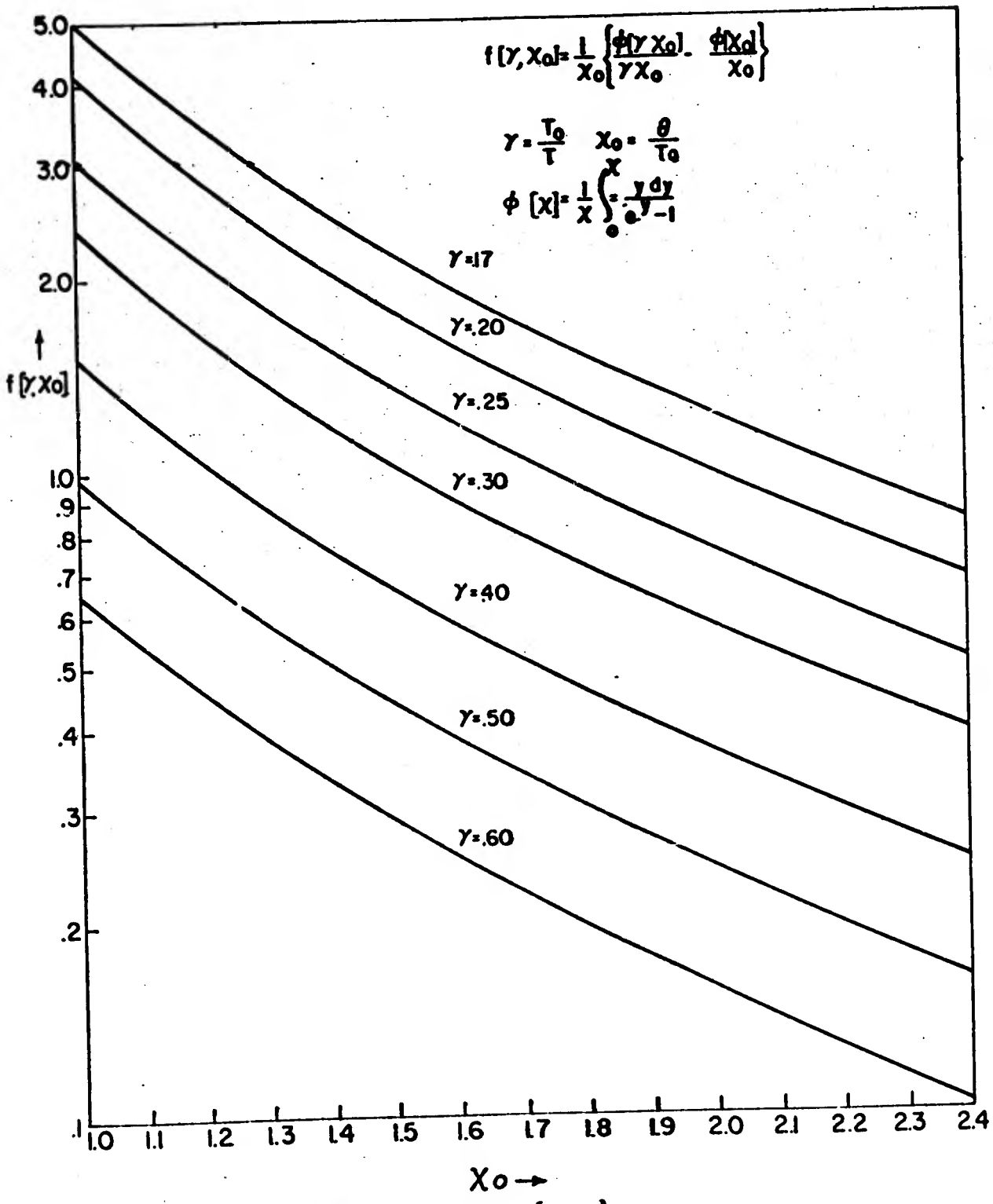

Fig. 48 - The function $f(\gamma, x_o)$.

These equations relate the functions $f[\gamma, x_o]$ directly to the measured intensity ratio data. With the use of the tabulated function $f[\gamma, x_o]$ (Fig. 48), θ_c and θ_a are obtained directly at each temperature step in the measurement.

2. Experimental Results

The peaks examined in the measurements on HfB_2 were the (211) and (104) lines. For HfB_2, $a_o = 3.141\text{Å}$, $c_o = 3.471\text{Å}$, $T_o = 276^\circ K(3^\circ C)$, $\overline{M} = 66.71 \frac{gm.}{gm.at.}$, $M_{Hf} = 178.6 \frac{gm.}{gm.at.}$. Thus, for $M = \overline{M}$, $\rho_a = 23.8$, $\rho_c = 38.7$ and for $M = M_{Hf}$, $\rho_a = 64.6$, $\rho_c = 103.3$. Five temperatures were used, namely $1350^\circ C$ ($\gamma = .17$) $1107^\circ C$ ($\gamma = .20$), $830^\circ C$ ($\gamma = .25$), $647^\circ C$ ($\gamma = .30$) and $417^\circ C$($\gamma = .40$) relative to a reference temperature of $3^\circ C$. $n_1^2 = 7$, $l_1^2 = 1$, $n_2^2 = 1$, $l_2^2 = 16$ and $m^2 = 111$ for line 1→(211) and line 2→(104). When these numbers are fed into Eqs. 33 and 34 for the two cases $M = \overline{M}$ and $M = M_{Hf}$ and the intensity ratios relative to $3^\circ C$ are measured from the average of three scans per peak at each temperature, we derive parameters θ_a and θ_c appropriate to those temperatures. The final results are tabulated in Table 35 with values of the r.m.s. thermal amplitudes $(\overline{\mu_a^2})^{1/2}$ and $(\overline{\mu_c^2})^{1/2}$ computed from Eqs. 31 and 32. Either value of M and its corresponding θ's will give the same results for the thermal amplitudes.

The calculated θ's have uncertainties of about $\pm 40^\circ K$ for θ_c and $\pm 20^\circ K$ for θ_a. The larger uncertainties for the θ_c values arise from the uncertainty in estimating the background intensity for the (104) intensity peak. The <104> direction makes an angle of $17^\circ 45'$ with the symmetry axis <001>; therefore the intensity-temperature variation of the (104) peak reflects the thermal amplitude predominantly along the "c" direction. θ_c is consistently higher than θ_a, indicating that the lattice is elastically stiffer in the "c" direction than in the "a" direction. This same feature is reflected by the consistently larger r.m.s.

Table 35

Debye Temperatures and Thermal Amplitudes for HfB_2

	M_{Hf}		$M = \overline{M}$			
T(°K)	θ_a(°K)	θ_c(°K)	θ_a(°K)	θ_c(°K)	μ_a^{RMS}(Å)	μ_c^{RMS}(Å)
690	345	439	552	695	.0706	.0564
920	342	431	552	706	.0815	.0631
1103	353	425	569	681	.0865	.0729
1380	301	381	486	619	.102	.0885
1623	284	356	464	500	.128	.119

Table 36

Debye Temperatures and Thermal Amplitudes for ZrB_2

	$M = M_{Hf}$		$M = \overline{M}$			
T(°K)	θ_a(°K)	θ_c(°K)	θ_a(°K)	θ_a(°K)	μ_a^{RMS}(Å)	μ_c^{RMS}(Å)
1103	442	524	682	793	.0964	.0815
1380	431	560	672	858	.109	.0863
1623	463	546	720	844	.112	.0944

values of μ_a compared with μ_c. The ratio of $\frac{\mu_a^{RMS}}{\mu_c^{RMS}}$ decreases, however, from 1.25 at 690°K to 1.08 to 1628°K, suggesting that as the temperature increases, the HfB_2 lattice becomes increasingly more elastically isotropic.

The results for ZrB_2 are listed in Table 36 . The fixed temperature-relative intensity analysis was not attempted for this material due to texture effects in the powder. Because of its similarity to HfB_2, however, the same assumption of equal atomic thermal amplitudes was made. The peaks examined were the (104) and (220), the latter peak measuring θ_a directly. Only three temperatures were used in this case: 830°C, 1107°C and 1350°C with a reference temperature of 22°C. Lower temperature measurements were not made because the Debye θ's from the three higher temperatures were essentially constant. For ZrB_2, $a_o = 3.171Å$, $c_o = 3.471Å$, $T_o = 295°K$, $\overline{M} = 37.62 \frac{gm.}{gm.at.}$ and $M_{Zr} = 91.22 \frac{gm.}{gm.at.}$. Thus, $\rho_a = 14.6$, $\rho_c = 24.1$ for $M = \overline{M}$ and $\rho_a = 35.4$, $\rho_c = 58.5$ for $M = M_{Zr}$. $n_1^2 = 1$, $l_1^2 = 16$, $n_2^2 = 12$, $l_2^2 = 0$, and $m^2 = 192$ for 1→(104) and 2→(220).

The uncertainties in the θ's of Table 36 are approximately ± 30°K, arising from the variation of integrated intensity from scan to scan at the higher temperatures. Again $\theta_c > \theta_a$ for either mass and $\mu_c^{RMS} < \mu_a^{RMS}$ at all temperatures considered. The remarks concerning the vibrational anisotropy of HfB_2 are similarly appropriate to ZrB_2.

The decrease in θ with temperature in the case of HfB_2 is shown in Fig. 49. This temperature dependence is larger than would be expected from the volume dependence of the Gruneisen relation:

$$\frac{d(\ln\theta)}{d(\ln V)} = -\gamma \qquad (35)$$

where γ is the Gruneisen constant and V the atomic volume. Integrating this equation and relating the change in volume to thermal expansion, we obtained a linear temperature dependence of the Debye temperature as:

$$\theta = \theta_o \{1 - \alpha_v \gamma (T - T_o)\} \qquad (36)$$

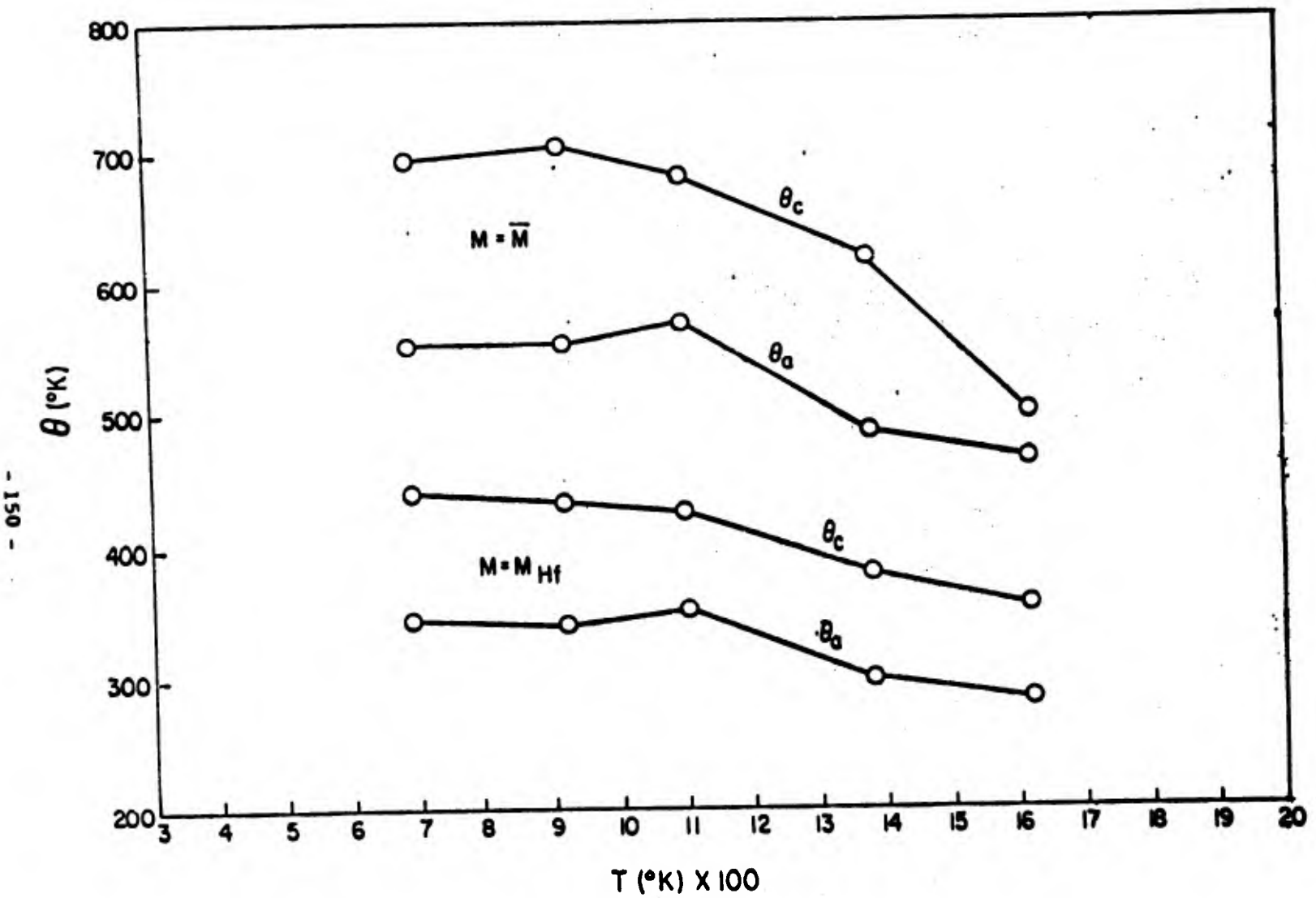

Fig. 49 - Temperature dependence of HfB_2 Debye temperatures.

where α_v is the volume coefficient of thermal expansion. The constant γ lies between about 2 and 3 for most metallic substances. α_v for HfB_2 is $20.2 \times 10^{-6}/^{\circ}K$. Considering now the curve $\theta_c[T]$ for $M = M_{Hf}$, for example, and letting $\gamma = 2.5$, we would calculate that if $\theta_c^{\circ} = 439^{\circ}K$ at a temperature of $417^{\circ}C$, θ_c should fall linearly to only about $420^{\circ}K$ at a temperature of $1350^{\circ}C$ whereas, in fact, it becomes $356^{\circ}K$. Similarly, the $\theta[T]$ curves for the other cases fall too rapidly. Several explanations are possible. The observed peak intensity at the higher temperatures may be reduced by oxidation effects or reactions with the heating element. At the higher temperatures nonharmonic oscillations may become important, although the very low values of $\overline{\mu[T]^2}$ would seem to indicate otherwise. Temperature diffuse scattering corrections which have been ignored throughout the analysis can become more important at the higher temperatures. All of these effects would tend to make the θ's too low at the higher temperatures. Fortunately, the θ's for HfB_2 are essentially constant within experimental error for the first three temperatures- $690^{\circ}K$, $920^{\circ}K$ and $1103^{\circ}K$. Similarly, the θ's for ZrB_2 are essentially constant over the temperature interval $1103^{\circ}K$ to $1623^{\circ}K$. We then calculate the averages of the θ's for these temperatures and assume they are appropriate for calculating the room temperature entropies of HfB_2 and ZrB_2.

F. Comparison of X-Ray Data and Specific Heat

1. HfB_2 and ZrB_2

The entropy at room temperature can be computed by using the method described in Section XVI employing the average θ, derived from the average mass, or from the "two θ" method using individual θ's associated with each atomic species. The latter approach utilizes the θ_{Me} derived from the X-ray measurements with the metal atom mass and a θ_B for the boron atom which is related to

θ_{Me} by $\theta_B = \left(\frac{M_{Me}}{M_B}\right)^{1/2} \theta_{Me}$. This relationship is suggested by the equality of the thermal amplitudes, which if written as Debye-Waller forms, gives:

$$M_{Me}\,\theta_{Me}^{\,2} = M_B\,\theta_B^{\,2} \qquad (37)$$

The "average θ" and "two θ" methods are expressed analytically in terms of Debye functions $S[\frac{\phi}{T}]$ as:

$$S[298] = S_D[\frac{\bar{\theta}}{298}] \qquad (38)$$

$$S[298] = \frac{1}{3} S_D[\frac{\theta_{Me}}{298}] + \frac{2}{3} S_D[\frac{\theta_B}{298}] \qquad (39)$$

The vibrational anisotropy introduces the problem of how to perform the best average over θ_a and θ_c. Since at high temperature, one associates a molar specific heat R, the gas constant, with each degree of freedom in a three dimensional solid to get a total of 3R, the classical DuLong-Petit value, it seems appropriate in our case to associate two equivalent specific heats with the "a" directions and a third different, specific heat with the "c" direction, i.e. within the Debye approximation:

$$C_v = \frac{2}{3} C_v[\frac{\theta_a}{T}] + \frac{1}{3} C_v[\frac{\theta_c}{T}] \qquad (40)$$

Translated into entropy terms, the "average θ" and "two θ" method become:

$$S[298] = \frac{2}{3} S_D[\frac{\bar{\theta}_a}{T}] + \frac{1}{3} S_D[\frac{\bar{\theta}_c}{T}] \qquad (41)$$

$$S[298] = \frac{1}{3}\left(\frac{2}{3} S_D[\frac{\theta^{Me}_a}{T}] + \frac{1}{3} S_D[\frac{\theta^{Me}_c}{T}]\right) + \frac{2}{3}\left(\frac{2}{3} S_D[\frac{\theta^{B}_a}{T}] + \frac{1}{3} S_D[\frac{\theta^{B}_c}{T}]\right) \qquad (42)$$

The room temperature entropy has been calculated by both methods in Table 37 with θ's appropriate to both choices of $\bar{M}$ and M_{Me} and the results compared

experimental entropies deduced from the measured specific heat data of Section XV. The "two θ" method gives apparently better results for S[298] compared with the experimental value, especially in the case of HfB_2.

2. $\underline{TiB_2}$

Miksic[7] has determined the Debye temperatures of TiB_2. Using spherical, single crystal specimens with MoK_α radiation, he was able to measure RMS values of μ_a^{Ti}, μ_a^B, μ_c^{Ti} and μ_c^B directly at room temperature (300°K) by the relative intensity analysis previously described. By a differential temperature measurement between 130°C and 300°C, he derived individual θ's for the Ti and B atoms along the "a" and "c" directions after assigning Debye-Waller functions to each atom with appropriate atomic masses. His results are given in Table 38 . Previously we estimated θ_B knowing θ_{Me} and using the relationship $\theta_B = \frac{M_{Me}}{M_B}^{1/2} \theta_{Me}$. For TiB_2 $(M_{Ti}/M_B)^{1/2}$ is 2.10. Miksic's θ's, however, have been measured directly. We compute his ratios θ_a^B/θ_a^{Ti} and θ_c^B/θ_c^{Ti} and get 2.06 and 1.93 respectively, which agrees very well with the mass ratio estimate. The ratio of the RMS amplitude for boron to that of titanium in the "c" direction is 1.23 while the same ratio in the "a" direction is 1.16. The assumption of equal amplitudes is therefore only approximately valid here. S[298] is now calculated according to the "two θ" method with the anisotropy average being taken according to Eq. 42. The calculated result is 1.99 $\frac{cal}{g.\ at.\ ^oK}$. The value of S[298] deduced from the specific heat measurements of Section XV is 2.27 cal/g.at.°K. This agreement is consistent with other results on the borides predicted by the "two θ" model decomposition of the specific heat.

Table 37

Room Temperature Entropies (cal/g.at.^{o}K) of HfB_2 and ZrB_2

	$\bar{\theta}_a$ (^{o}K)	$\bar{\theta}_c$ (^{o}K)	θ_a^{Me} (^{o}K)	θ_c^{Me} (^{o}K)	θ_a^{B} (^{o}K)	θ_c^{B} (^{o}K)	Avg. θ S[298]	Two θ S[298]	S(meas).
HfB_2	558	692	347	432	1350	1680	4.42	2.98	3.42
ZrB_2	691	832	444	543	1320	1620	3.39	2.59	2.93

Table 38

Debye 0's and RMS Thermal Amplitudes (Å) for TiB_2

(Miksic[7])

θ_a^{Ti}	μ_a^{Ti}	θ_a^{B}	μ_a^{B}	θ_c^{Ti}	μ_c^{Ti}	θ_c^{B}	μ_c^{B}
665^{o}K	.050 Å	1370 ^{o}K	.058 Å	740^{o}K	.044 Å	1420^{o}K	.054 Å

uncertainties in θ are $\pm$ 3^{o}K

uncertainties in μ^{RMS} are $\pm$ .001Å

REFERENCES

1. Klug, H. and Alexander, L.E., "X-Ray Diffraction Procedures," John Wiley and Sons, Inc., (New York) 1954, pg. 464.

2. Nowotny, H., et al., Z. Metallkunde, (1959), 50, 258.

3. Leitnaker, J., "Thermodynamic Properties of Refractory Borides" LASLR #LA-2402, 13 April, 1960.

4. Pearson, W.B., Handbooks of Lattice Spacings, Pergammon Press, 1958.

5. Krupka, M.C., "High Temperature Vaporization Behavior and Thermodynamic Properties of HfB_2," LASLR #LA-2611, 16 April, 1962.

6. Edwards, J. W., et al., J.A.P., (1950), 22, 424.

7. Miksic, M.G., "Thermal Vibrations and Bonding Effects in TiB_2," Tech. Rep. No. 5, NR032-414, Polytechnic Institute of Brooklyn.

8. Cullity, B.D., Elements of X-Ray Diffraction, Addison-Wesley Co., 1956, pg. 172.

9. Houska, C.R., "Thermal Expansion and Atomic Vibration Amplitudes for TiC, TiN, ZrC, ZrN and W," Tech. Rep. No. C-17, Union Carbide Research Institute, Aug. 1963.

10. James, R.W., The Optical Principles of the Diffraction of X-Rays, G. Bell & Sons (London), 1958, pg. 228.

11. Quarterly Progress Report "Research on Physical and Chemical Principles Affecting High Temperature Materials for Rocket Nozzles" Union Carbide Research Institute, Contract No. DA-30-069-ORD-2787, Sept. 30, 1963, pg. III 51.

IX. COEFFICIENT OF LINEAR THERMAL EXPANSION*

A. Introduction

The purpose of this subtask is to measure the coefficient of thermal expansion from room temperature to 1500°C. Initially, it was anticipated that these measurements would be performed primarily on single crystal material from the zone-refining procedure. High pressure hot pressing was used to complement the supply of zone-refined material. The expansion measurements were completed for the range from 25° to 1000°C. on high pressure hot pressed samples of TiB_2, HfB_2, and TaB_2 and on zone-refined samples of ZrB_2, NbB_2 and HfB_2.

A knowledge of the thermal expansion of refractory materials is required for the design and calibration of apparatus employed in high temperature investigations. Such knowledge is also necessary for the design of structural materials for high temperature applications. Thermal expansion properties also play a role in the semi-quantitative description of thermal shock as described in Section XII.

Linear expansion measurements in the range below 1500°C are usually based on the method of the interferometer or the differential dilatometer, or the measurement can be made by direct observation with a micrometer telescope. Thermal expansion data of crystal parameters can be determined by X-ray methods as discussed in Section VIII. The interferometer method is the most precise, but methods based on the differential dilatometer are more practical. The latter method was chosen for this study because this technique can be applied to measurements in the higher temperature regions where

---

*R. L. Pober and E. V. Clougherty, ManLabs, Inc.

future thermal expansion measurements will be performed to provide data for selected materials of proven oxidation resistance.

Thermal expansion measurements are discussed in a high temperature monograph[1]; thermal expansion data on high temperature reference materials are presented as an appendix to a well documented book[2] on experimental procedures for high temperature investigations.

Since X-ray orientation studies on the single crystal material prepared in this program indicate that the end faces of these rods are approximately the (100) planes of the hexagonal crystal, the measured length changes afford an expansion coefficient which will approximate the quantity $\frac{\Delta_a}{a_o \Delta t}$; the latter is obtained directly from the high temperature x-ray measurements. Expansion data on fully dense polycrystalline samples produced from the high pressure hot pressing subtask provide a measure of the linear expansion coefficient $\alpha_L = \Delta L / L_o \Delta t$.

B. Experimental

1. Apparatus

Thermal expansion data were obtained with a differential dilatometer. The dilatometer is composed of an alumina base and sapphire rods that allow it an upper temperature limit above 1500°C. The dilatometer is shown schematically in Fig. 50. The boride samples used were cylinders ranging from 1/4 inch to 3/8 inch diameter and 3/4 inch to 1 inch long. The ends of the samples were machined to provide proper inserts for the pointed end of the dilatometer rod and of the lower supporting rod. The dilatometer was suspended in a closed end, vertical, tube furnace. The furnace was heated by a resistance wire winding and the temperature was maintained by a conventional

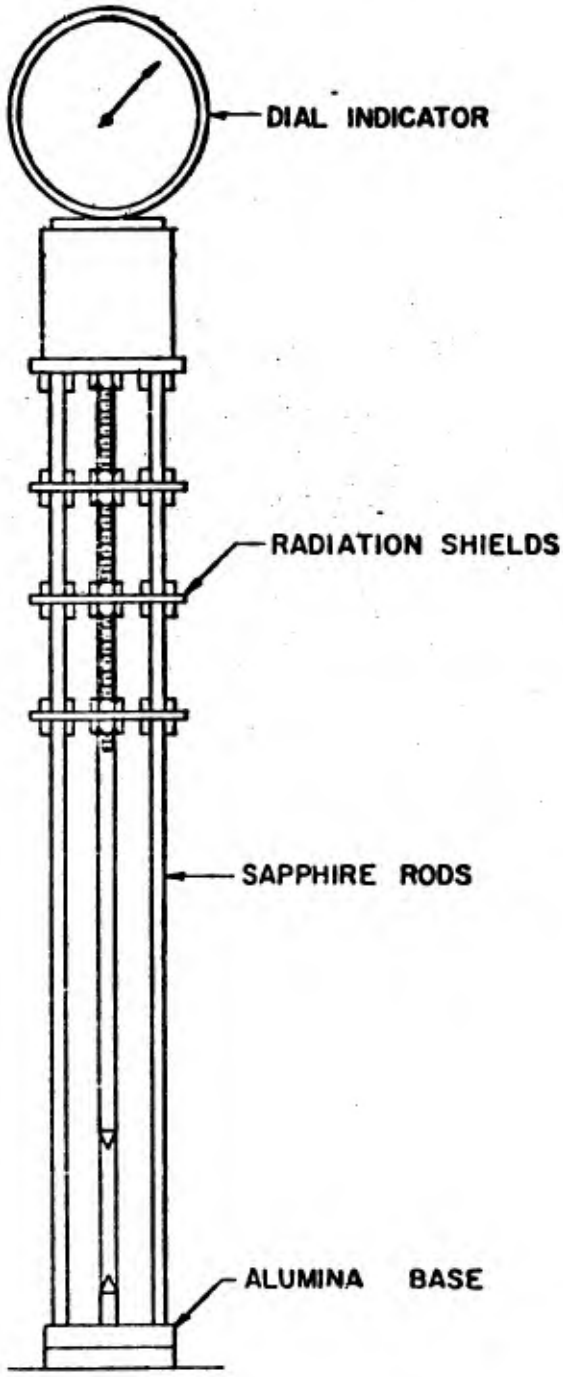

Fig. 50 - Differential Dilatometer for Linear Expansion Measurement

controller. A flowing argon atmosphere protected the samples from oxidation.

2. Technique of Measurement

The mean linear coefficient of thermal expansion between temperatures 25° and t°C is defined as:

$$\alpha = \frac{l - l_o}{L_o(t - t_o)} = \frac{\Delta l}{l_o \Delta t} \qquad (1)$$

where l_o and l are the lengths at the temperatures 25° and t°C.

The results obtained with a differential dilatometer are actually

$$l[t, \text{measured}] = l[t, \text{sample}] - l[t, \text{dilatometer}] \qquad (2)$$

Thus,

$$\alpha(\text{measured}) = \alpha(\text{sample}) - \alpha(\text{dilatometer}) \qquad (3)$$

The quantity α(dilatometer) was obtained experimentally by calibrating the dilatometer apparatus from 25°C to 1000°C with fused silica.

The expansion measurements were made at 1000°C with a reference temperature of 25°C. It was assumed that the measured expansion is linear between these limits.

C. Results

The results obtained from these measurements are collected in Table 39 with other available expansion data on diborides. The expansion coefficients obtained from the dilatometer measurements are considered to have a precision of ± 5%. The observed scatter in the comparison of the linear coefficients obtained by X-ray methods versus those obtained from the dilatometer measurements preclude the possibility of a systematic error in the latter measurements. It should be noted that the X-ray method may have some experimental advantages in the determination of the expansion properties of pure materials but the technique is not feasible for composite structures. The measurement of length

Table 39

Thermal Expansion Data for Refractory Metal Diborides

Material	Fabrication Process**	% of Theoretical Density	Mean Expansion Coefficient* $(^{\circ}C^{-1}) \times 10^{6}$	Reference
TiB_2	H.P.H.P.	95	$\alpha_L = 8.32$	Section IX
	H.P.	95	$\alpha_L = 9.7$	3
	H.P.	-	$\alpha_L = 6.8$	4
	Powder	-	$\alpha_L = 8.02$	Section VIII
	Powder	-	$\alpha_L = 7.79$	5
ZrB_2	Z.R.	100	$\alpha_a = 7.95$	Section IX
	H.P.	-	$\alpha_L = 8.2$	4
	Powder	-	$\alpha_L = 6.29$	Section VIII
			$\alpha_a = 5.92$	Section VIII
	Powder		$\alpha_L = 7.12$	5
			$\alpha_a = 7.07$	5
HfB_2	Z.R.	99	$\alpha_a = 7.49$	Section IX
	H.P.H.P.	86	$\alpha_L = 7.69$	Section IX
	H.P.	-	$\alpha_L = 5.3$	4
	Powder	-	$\alpha_L = 6.72$	Section VIII
			$\alpha_a = 6.64$	Section VIII
NbB_2	Z.R.	95	$\alpha_a = 7.32$	Section IX
	Powder	-	$\alpha_L = 8.93$	Section VIII
			$\alpha_a = 8.69$	Section VIII
TaB_2	H.P.H.P.	84	$\alpha_L = 7.88$	Section IX
	H.P.	-	$\alpha_L = 5.1$	4
	Powder	-	$\alpha_L = 9.27$	Section VIII

---

*The tabulated quantities are linear expansion coefficients. These values were obtained between 25° and 1000°C in the dilatometer measurements and between 25° and 1500°C in the X-ray measurements.

**The fabrication processes are identified as H.P.H.P., high pressure hot pressing; H.P., conventional hot pressing; and Z.R., zone-refining. The X-ray measurements were performed on powder samples.

changes by the conventional expansion techniques in fabricated sample material is the only logical way to obtain the expansion coefficients for such materials.

REFERENCES

1. Campbell, I.E., High Temperature Technology, John Wiley and Sons, Inc., New York, (1956).

2. Bockris, J. O'M., White, J.L., and Mackenzie, J.D., Physiochemical Measurements at High Temperature, Academic Press, Inc., New York, (1959).

3. Mandorf, V., Hartwig, J., and Seldin, E.J., Technical Memorandum, TMC-49, "High Temperature Properties of Titanium Diboride," Fostoria Development Laboratory, National Carbon Company, Fostoria, Ohio.

4. Samsonov, G.V., Visnyk Akademii Nauk, Ukrains koi S.S.R. (1959) No. 6, 27-37.

5. Quarterly Progress Report, "Research on Physical and Chemical Principles Affecting High Temperature Materials for Rocket Nozzles," Union Carbide Research Institute, September 30, 1963.

X. THERMAL CONDUCTIVITY

The purpose of this task is to measure the thermal conductivity of the diborides in the region 1000° to 2000°C. Sample material has been supplied from available zone-refined material i.e. ZrB_2 and HfB_2; the remaining diborides samples have been fabricated by high pressure hot pressing.

These measurements have been initiated by Professor Michael Hoch of the Materials Science Department at the University of Cincinnati. In the procedure to be used cylindrical samples of the diborides are placed in a vacuum system and brought to temperature by high frequency induction heating. When the sample reaches equilibrium, by radiating to its surroundings, its temperature is measured at selected points. This procedure is repeated for a sample with a different length to diameter ratio. Utilizing the measured temperature distributions and the solution for 2-dimensional heat flow in a cylinder of finite length, it is possible to obtain the radial and axial thermal conductivity of the sample. The emissivity will also be measured. Values which are reported for the diborides at 200°C are given below.[1,2]

DIBORIDE	K cal/cm. sec. °C
TiB_2	0.062
ZrB_2	0.055
HfB_2	-
NbB_2	0.040
TaB_2	0.026

Southern Research Institute[3] has measured the thermal conductivity of TiB_2, ZrB_2, and HfB_2 on samples containing 3-10% impurities from 25°C to 2200°C. The conductivity of TiB_2 increases to a value of 0.128 cal/cm. sec. °C at 2200°C, whereas the conductivity of ZrB_2 is virtually invariant with temperature over this range[3]. The SRI results for HfB_2 indicate a constant

value of 0.138 cal/cm. sec. ^{o}C up to 1600^{o}C followed by a rapid increase to 0.310 at 2000^{o}C. This increase may be due to some change in the nature of the specimen. Mandorf[4] found a constant thermal conductivity of 0.096 cal/cm. sec^{o}C for sintered TiB_2 in the range 1000^{o} to 1400^{o}C.

Multiplication of the K values (cal/cm. sec. ^{o}C) by a factor of 2903 yields the value of conductivity in units of BTU in/ft.^{2} hr. ^{o}F.

REFERENCES

1. Schwartzkopf, P. and Kieffer, R., Refractory Hard Metals, The MacMillan Co., N.Y., N.Y. (1953).

2. Samsonov, G.V., Visnyk Academii Nauk Ukrains koi SSR (1959) No. 6, 27-37.

3. Southern Research Institute - Technical Documentary Report No. ASD-TDR-62-765 August 1962.

4. Mandorf, V., Hartwig, J., and Seldin, E.J., Technical Memorandum, TMC-49, "High Temperature Properties of Titanium Diboride" Fostoria Development Laboratory, National Carbon Co., Fostoria, Ohio, 5 April 61.

XI. ELECTRICAL RESISTIVITY*

A. Introduction

The electrical resistivity of a fabricated diboride or other metal-like compound is dependent upon the physical state of aggregation, i.e., porosity, grain boundary precipitates, cracks, etc. The temperature coefficient of resistivity should be less sensitive to these parameters and more characteristic of the pure compound because the variation of resistivity with temperature depends primarily on thermal vibrations and thus should be related to a property characteristic of the pure compound. One such property is the Debye temperature.

A recent survey[1] of the properties of electrically conductive materials at elevated temperatures demonstrates the small amount of published electrical resistivity data, especially resistivity as a function of temperature, for metallic compounds relative to pure metals and metallic alloys. The principal objective for research in the field of high temperature high conductivity materials is to find a substitute for platinum base alloys. Among the metallic compounds, the diborides of the metals of Group IVa and Va appear to be the most promising materials for this application.

Meaningful and accurate measurements of the resistivity of any material depend on the availability of pure, well-characterized samples with well defined geometries. In the present investigation sample material has been supplied from the zone-refining and the high pressure hot pressing procedures. In order to obtain reliable electrical resistance measurements, four independent leads must be physically attached to the specimen with a minimum of contact resistance. The latter requirement is particularly important for metallic compounds such as the borides,

---

*E. V. Clougherty, ManLabs, Inc., Cambridge, Mass.

carbides, and nitrides of the metals of Group IVa and Va. In this study resistivity measurements were performed from room temperature to 1050°C with four molybdenum leads attached to the sample. Lower temperature data, i.e., 700° to 800°C, were also obtained with platinum leads. Experimental difficulties involving an apparent low melting phase composed of platinum, zirconium, and boron, caused failures for this technique above the region 700° to 800°C.

B. Experimental

Three techniques were designed to attach the required current and potential leads to the diboride sample. Initially, an attempt was made to attach a variety of both high and low melting metallic lead materials directly to the sample by discharge welding procedures. Higher melting metals such as tungsten, molybdenum, nickel, and platinum provided good wetting action but the thermal shock caused the sample to shatter in the region of the weld. Copper showed good wetting action without shattering the sample but the weld had poor mechanical strength. Nichrome and Kanthal A-1 showed poor wetting action. Tin and solder (60 Sn-40 Pb) showed no wetting action.

In order to circumvent the thermal shock problem common to the higher melting metals, and to provide lead material for measurements up to 1500°C, an alternate procedure was used to prepare the resistance specimen. Four 0.060 in. holes were positioned in a 1.00 in. sample to accommodate the two potential leads (0.50 in. separation) and the two current leads (1.00 in. separation). The holes were effectively placed without shattering the specimen with the aid of a spark cutting machine. Platinum was melted in each hole, then platinum wires were attached to the cast platinum by discharge welding. Initially, a single crystal sample of NbB_2 was prepared in this way. Although some experimental difficulties prevented the use of four independent leads, the measurements were completed in

order to check the mechanical strength of the leads and the measuring circuitry. The sample was heated in argon in a resistance type furnace up to 800°C. No further experimental difficulties were experienced with this material. In attempts to apply this technique to ZrB_2, reproducible data could be obtained from room temperature to the region of 750°C; above this temperature the platinum leads appeared to melt at the point of contact with the cast platinum.

Since it was known that the resistivity at room temperature was a sensitive measure of porosity, a simple convenient method for measuring resistance at room temperature was designed and assembled. Current leads were attached to the ends of the sample by pressure contact from brass cylinders; potential leads, by pressure contact at a fixed distance of separation by pressure point contact from brass screws. The brass components were assembled in a bakelite housing. The device was similar to the later developed molybdenum lead attachment apparatus shown in Fig. 51. The brass lead attachment device was adequate for room temperature applications. The failure of the platinum lead device above 750°C for ZrB_2 necessitated the development of the apparatus shown in Fig. 51. In this device, molybdenum is used for current and potential leads; pressure contacts were made by tightening the adjustment nuts against the boron nitride housing. Reproducible data have been obtained with this apparatus from room temperature to 1050°C in an argon atmosphere for the available diboride materials.

The schematic diagram of the circuit used to measure the resistance is also shown in Fig. 51. The potential was measured with a Keithley 150A Microvolt-Ammeter. The zero adjustment for this instrument eliminates the thermal e.m.f. from the measured potential; thermal e.m.f.'s were generally about five

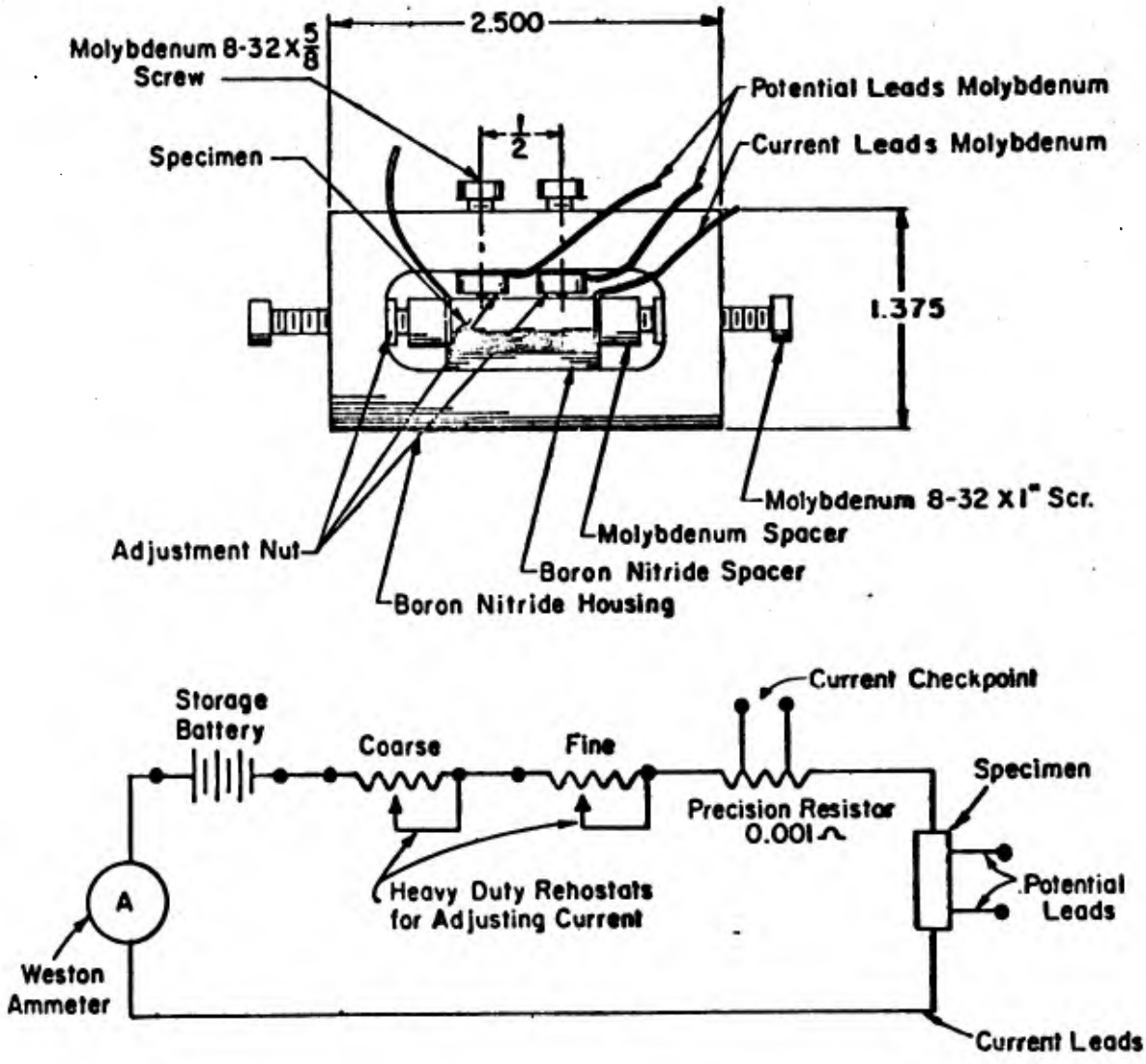

Fig. 51 - Resistivity Apparatus: Sample Holder and Measuring Circuit.

percent of the measured potential signal. The sample was heated in an argon atmosphere in a resistance wound furnace. Resistance measurements were made when the heating current was off to avoid an induced e.m.f. from the furnace windings.

C. Results

Resistivity results at room temperature are collected in Table 40. Pertinent data from the literature are also tabulated. The results of the resistivity measurements as a function of temperature are presented in Figs. 52 to 55.

The results show that fully dense, crack-free diborides of Ti, Zr, and Hf have very low resistivity values at room temperature. The previously reported values for TaB_2 and NbB_2 were substantially higher than those reported for the Group IVa diborides but the measured resistivities of TaB_2 and NbB_2 for relatively low density (80-90% of theoretical) material indicate these compounds should also have low resistivities in agreement with the extrapolated values suggested by Juretschke and Steinetz[2]. The results for the measurements of the resistivity as a function of temperature showed linear behavior over the investigated range. The measured resistivities were used to obtain the average coefficient of resistivity as defined in Eq. 1.

$$\alpha = \frac{\rho\,[t^{\circ}C] - \rho\,[25^{\circ}C]}{(t^{\circ}C - 25)\,\rho\,[25^{\circ}C]} \qquad {}^{\circ}C^{-1} \qquad (1)$$

The data for the single crystal ZrB_2 provide a comparison of the Pt lead and Mo lead techniques; the agreement is well within experimental error. Although the room temperature resistivity of the high pressure hot pressed NbB_2 was lower than that of the zone refined material, purity considerations favored the choice of the latter for the temperature dependent study. Contamination of the NbB_2 at the lead contact points prevented the measurement of meaningful data above 500°C. The relatively low density of the available TaB_2 samples precluded the use of this material for high temperature measurements at this time.

Table 40

Electrical Resistivity† of Refractory Metal Diborides at 25°C

(units: μΩcm)

Material Fabrication	TiB_2	ZrB_2	HfB_2	NbB_2	TaB_2	Reference
Extrapolated	9	7	15 or 18	12	14	2.
Hot Pressed	26.5	14	12	32	68	3.
						4.
Flame Fusion Zone Refined*	6.9 -	5.7	13.5	68	154	Section XI
High Pressure** Hot Pressed	R-46(96%) 11.9 R-71(96.4%) 13.4 R-72(96.4%) 13.2 R-73(95.4%) 11.6	R-1(98.9%) 10.2 R-2(92.9%) 20.2 R-3(92.4%) 12.4 R-12(98.2%) 10.3	R-2(94.5%) 10.3 R-6(85.5%) 18.3	R-3(90.8%) 28.2 R-9(91%) 20.5	R-1(85.1%) 63.4 R-12(83.5%) 49.4	Section XI Section XI Section XI Section XI

† Results obtained by the various techniques described in subsection B were in agreement within experimental error.

* Zone refined material from Arthur D. Little described in Section V; ZrB_2, NbB_2 and HfB_2 are single crystals, TaB_2 is polycrystalline and badly cracked.

** For the high pressure hot pressed material the tabulated results are identified by an experimental run number, e.g. R-46, followed by the percentage of the theoretical density, then the measured resistivity.

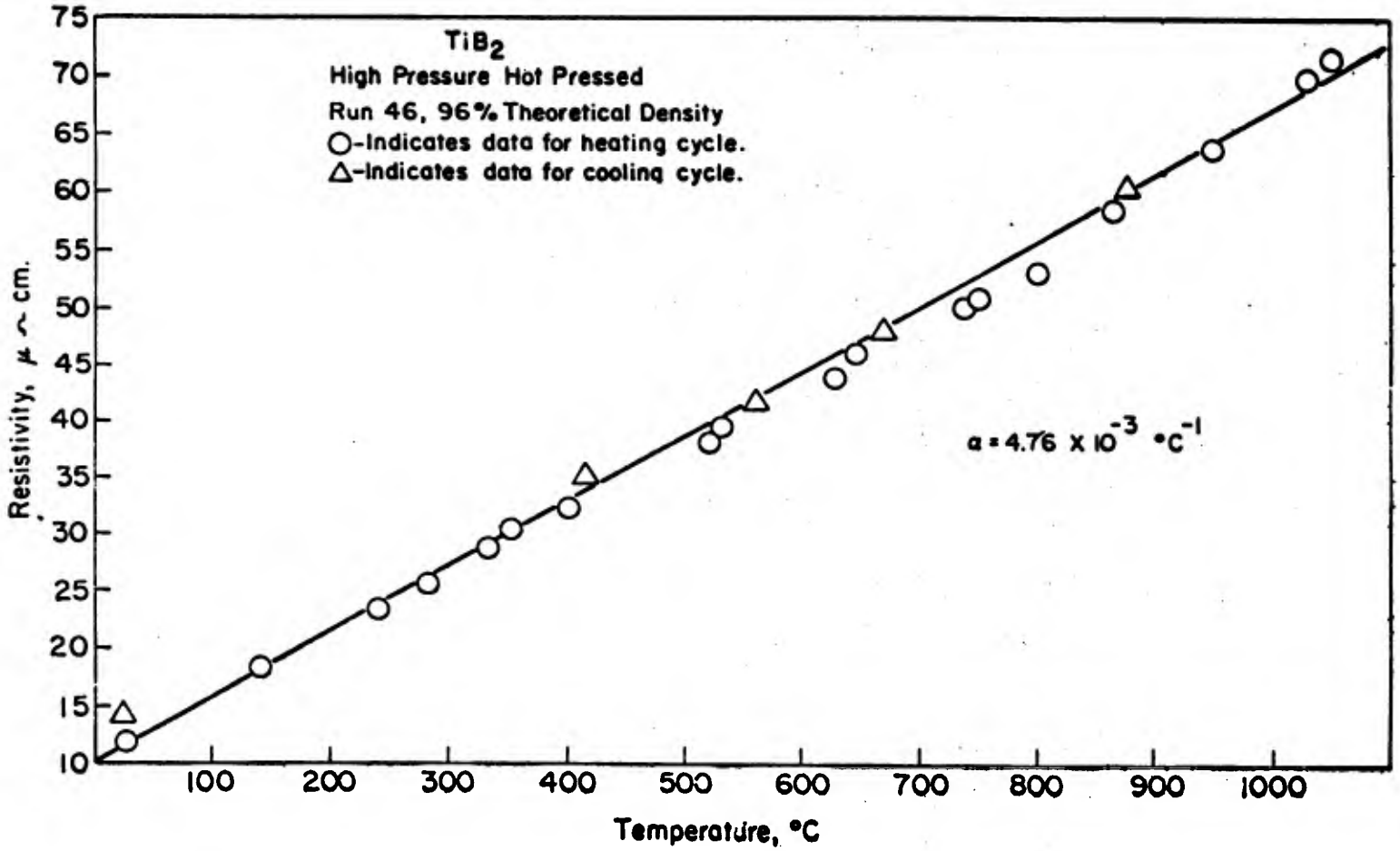

Fig. 52 - Temperature Dependence of the Resistivity of TiB_2.

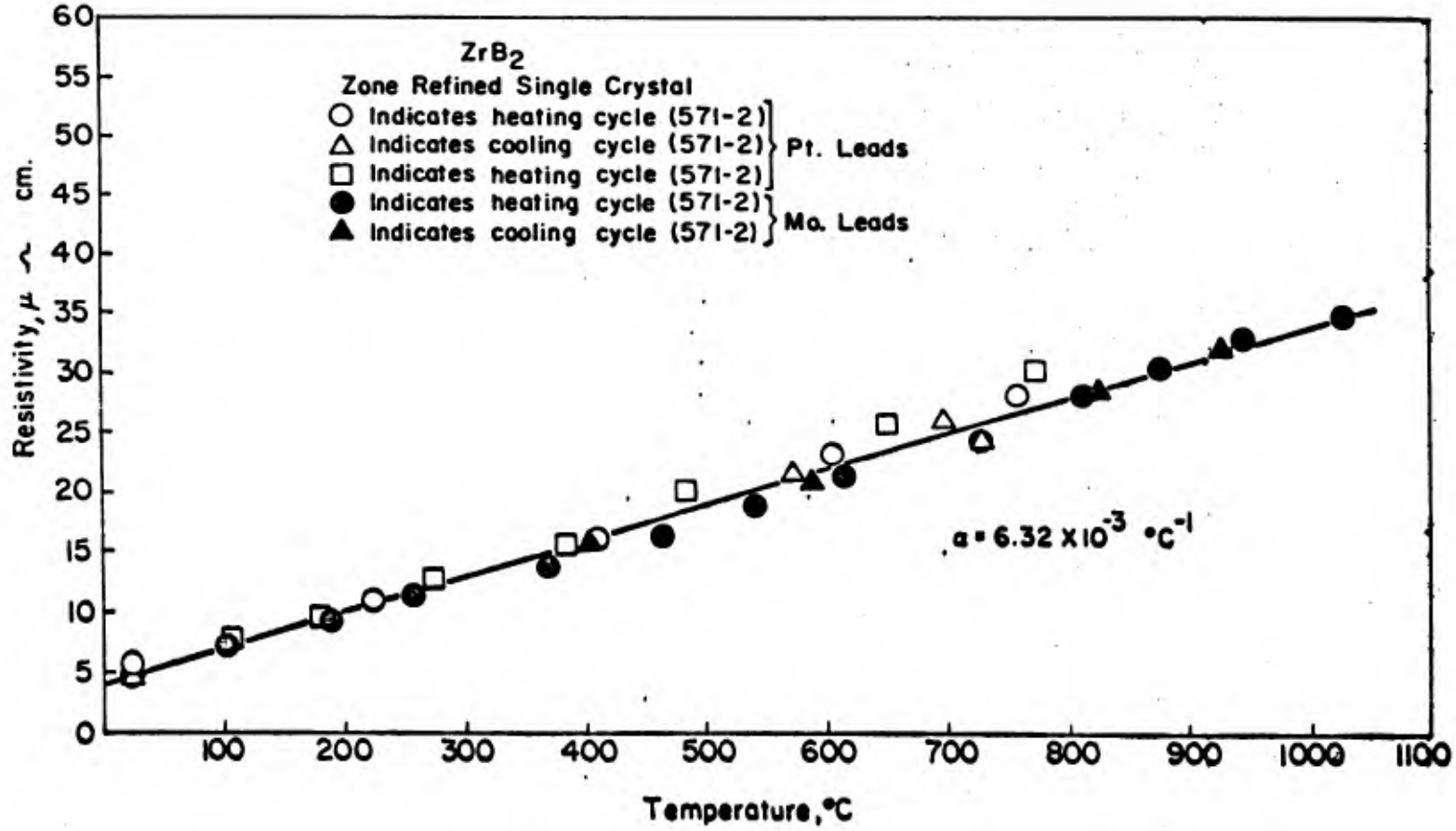

Fig. 53 - Temperature Dependence of the Resistivity of ZrB_2.

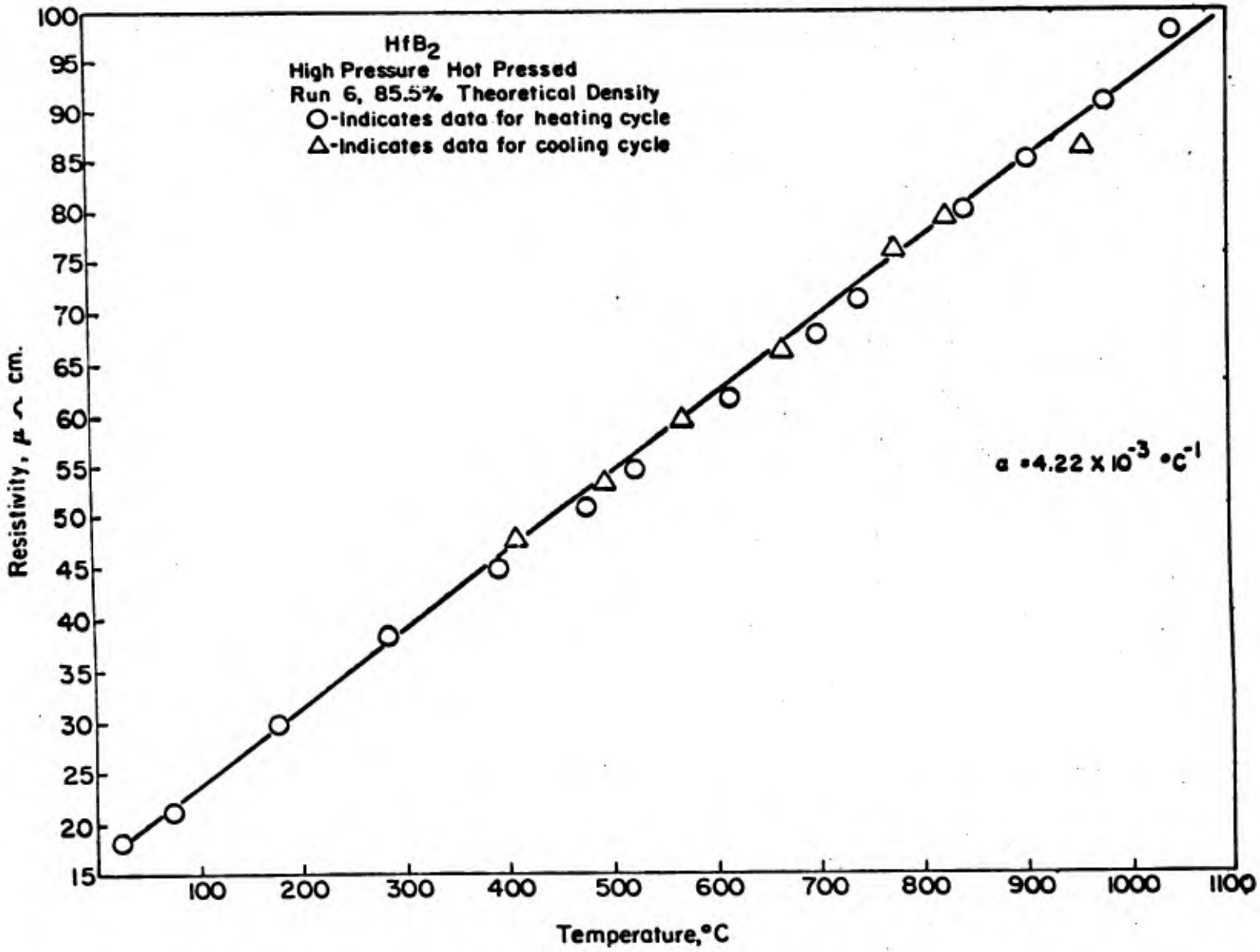

Fig. 54 - Temperature Dependence of the Resistivity of HfB_2.

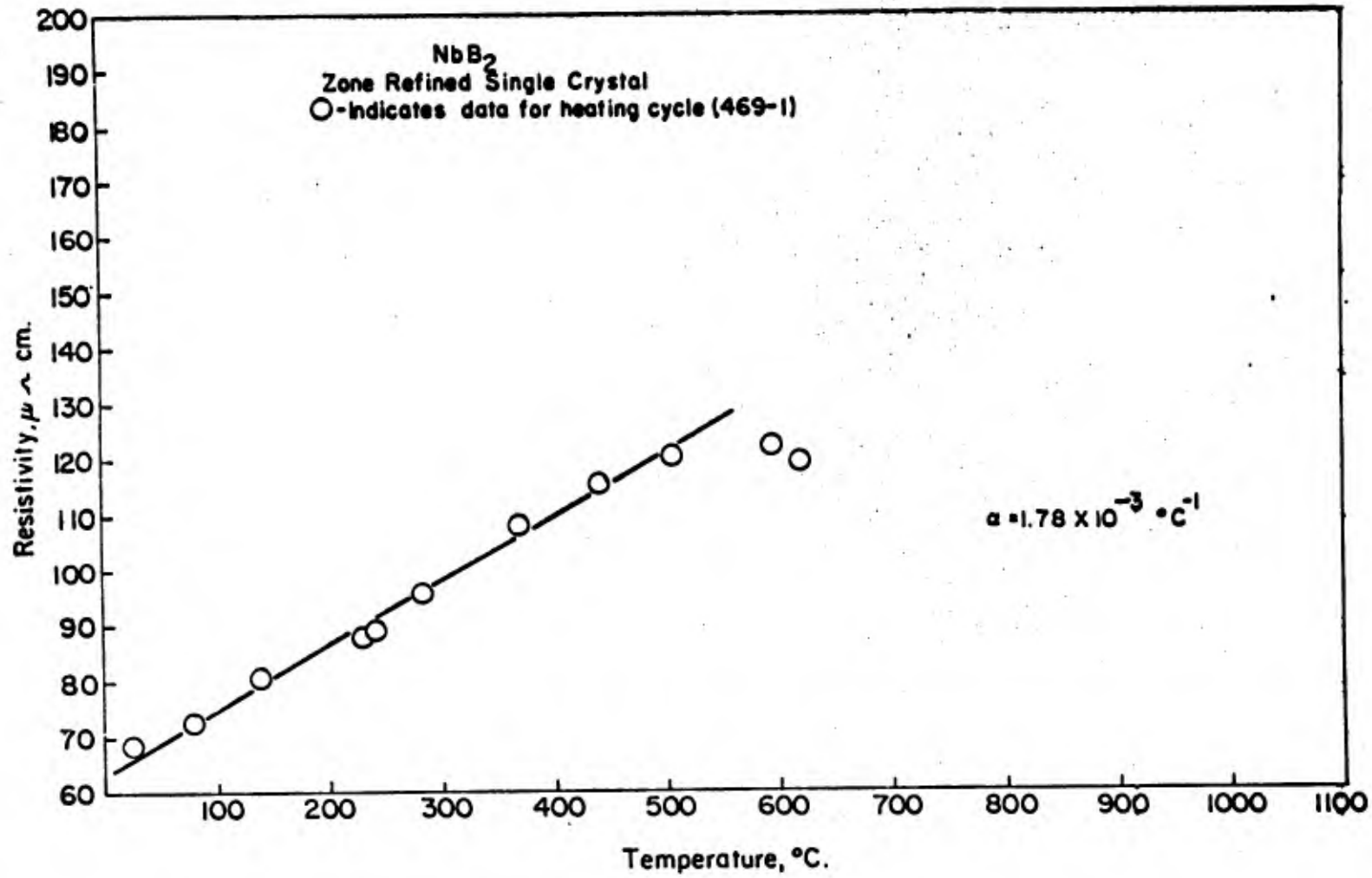

Fig. 55 - Temperature Dependence of the Resistivity of NbB_2.

Results for comparable materials measured over a significant range of temperature are generally not available but recent data[5] on TiB_2 (10 $\mu\Omega$ cm. at 25°C) and HfB_2 (15 $\mu\Omega$ cm. at 25°C) afford α (TiB_2) = 4.5×10^{-3} $^oC^{-1}$ and α (HfB_2) = 3.0×10^{-3} $^oC^{-1}$. The results obtained in the present investigation gave α (TiB_2) = 4.76×10^{-3} $^oC^{-1}$ and α (HfB_2) = 4.22×10^{-3} ^oC.

The values of the coefficients of resistivities of the diborides of Ti, Zr, Hf, and Nb do not appear to be simply related to the Debye temperatures obtained from specific data (see Table 55). Such correlations must await the completion of measurements on additional materials. The apparent low coefficient, $\alpha = 1.78 \times 10^{-3}$ $^oC^{-1}$, for NbB_2 will be checked when material of higher density becomes available.

REFERENCES

1. Fuschillo, N., and Lindberg, R.A., "Electrical Conductors at Elevated Temperatures," ASD-TDR-62-481, Contract No. AF33(616)-8386, Melpar, Inc., Falls Church, Virginia, January 1963.

2. Juretschke, H. J., and Steinetz, R., J. Phys. and Chem. Solids, (1958) 4 118-127.

3. Samsonov, G.V., Visnyk Akademii Nauk Ukrains koi SSR, (1959) No. 6 27-37.

4. Williams, W.S. and Dolloff, R.T., Bull. Am. Phys. Soc., (1959) 4 No. 4, 228.

5. Pears, C.D. and Oglesby, S., "The Thermal Properties of Twenty-Six Solid Materials to 5000°F or Their Destruction Temperatures," ASD-TDR-62-765, Southern Research Institute, April (1962).

XII. MECHANICAL PROPERTIES*

The original purpose of this task included the determination of the rupture strength and the modulus of bending over the temperature range from 25° to 1500°C. It was planned to use these results in conjunction with elastic moduli data and other thermal and physical property data to characterize the thermal shock resistance of the diborides. Unfortunately the experimental difficulties in obtaining crack-free specimens from the zone-refining subtask precluded the performance of the strength measurements. It is conceivable that high pressure hot pressing could be used to supply appropriate samples of polycrystalline material, but the performance of these measurements will be restricted to materials which display superior oxidation resistance properties.

A. Strength and Modulus

Values for the modulus and rupture strength reported in the literature are admittedly spotty because of variable porosity and impurity levels present in materials subjected to testing. For example, the rupture strength of ZrB_2 increases from 8,000 to 25,000 psi as the density increased from 87 to 95.5% of theoretical density[1]. The variation of the flexural strength of TiB_2[2] with grain size and porosity was discussed in Section VI. It was pointed out that grain size plays a more significant role in determining the flexural strength. The extrapolated flexural strength of high density TiB_2 with a 10μ average grain size was 80,000 psi.

Samsonov[3] has suggested the following values for the modulus of elasticity, TiB_2 - 76×10^6 psi, ZrB_2 - 50×10^6 psi, TaB_2 - 37×10^6 psi. Mandorf[2]

---

*R. L. Pober and E. V. Clougherty, ManLabs, Inc.

reports a variation of the modulus of elasticity of TiB_2 with porosity and temperature. At room temperature, material of 89.8% and 92.9% theoretical density showed moduli of 53×10^6 psi and 62×10^6 psi. The moduli were essentially independent of temperature up to 900°C. From 900° to 2000°C, the moduli dropped linearly. The rate of decrease of the modulus with temperature was larger for the material of lower density.

Gilman and Roberts[4] have performed measurements of the elastic constants of single crystal TiB_2 and reported the following values (in 10^{12} dynes/cm^2) C_{11}-6.9, C_{33}-4.4, C_{44}-2.5, C_{12} - 4.1, C_{13}- 3.2 (estimated). These values indicate that the anisotropy in the elastic constants of TiB_2 is about one half that of zinc and about two orders of magnitude less than that of pyrolytic graphite.

B. Thermal Shock Resistance

Thermal shock resistance is dependent, for the most part, on three properties: thermal conductivity, thermal expansion, and strain at fracture. For purposes of calculation and comparison, it is convenient to approximate the strain at fracture as the fracture stress divided by the modulus. Since most materials which are subject to thermal shock show little plastic deformation at fracture, this is a fairly good approximation. Good thermal shock resistance is exhibited by materials having relatively high conductivity and high strength, and low expansion coupled with low modulus. The relative thermal shock resistance of a material can be expressed as, $\frac{k\sigma(1-\mu)}{\alpha E}$. The problem in calculating this parameter lies in obtaining reliable values for

μ Poisson's ratio;

k Thermal conductivity;

α Coefficient of thermal expansion;

σ Tensile breaking stress;

E Modulus of elasticity.

For materials such as the borides, which are difficult to fabricate, reported properties vary depending on density, grain size, and other material variables. The largest variations in reported data are present in values for σ and E. In the interests of good thermal shock resistance, the ratio σ/E should be maximized for a given k, α, and μ. The most convenient way to reduce E is to add a second phase of lower modulus to the matrix material. In the ideal situation, this second phase should improve the oxidation resistance of the pure matrix material. Voids can function as effective second phase material. In this case, the strength decreases faster than the modulus so that σ/E decreases. If the second phase is a material of low modulus, the modulus can decrease more rapidly than the strength and σ/E will increase. The difficulty with this approach is the selection of a second phase which is compatible with the matrix and which will actually increase σ/E.

There is also the possibility of increasing σ. For polycrystalline materials of the boride type the strength is inversely proportional to the grain size. Mandorf[2] indicates the flexural strength of TiB_2 as 43,000 psi for a grain size of about 20μ. ManLabs has produced high pressure hot pressed TiB_2 with grain sizes of 10 microns and less. For a grain size of 10 microns, the extrapolated strength is of the order of 80,000 psi. Thus, it is conceivable that the low grain size material which presumably will have very high strengths might very well also have improved thermal shock resistance properties.

REFERENCES

1. Schwartzkopf, P. and Kieffer, R., Refractory Hard Metals, The MacMillan Co., New York, N.Y. (1953).

2. Mandorf, V., Hartwig, J., and Seldin, E.J., Technical Memorandum, TMC-49, "High Temperature Properties of Titanium Diboride" Fostoria Development Laboratory, National Carbon Company, Fostoria, Ohio.

3. Samsonov, G.V., Visnyk Academii Nauk Ukrains koi SSR, (1959) No. 6, 27-37.

4. Gilman, J.J. and Roberts, B.W., J. App. Phys., (1961) 32 1405.

XIII. HOT HARDNESS*

A. Introduction

The purpose of this task is to obtain data on the variation of the microhardness of the pertinent refractory metal diborides as a function of temperature. Specimens for these measurements were selected from the available zone-refined crystals; additional samples were supplied from the high pressure, hot pressed material. Considerable experimental data were collected at room temperature in order to adequately define the variation of hardness with load and crystal orientation prior to the measurements at high temperatures. The latter were performed with a Hot Hardness Tester designed and built at ManLabs, Inc. The measurements were made in vacuo (5×10^{-5} torr) from room temperature to 1000°C.

The usefulness of hot hardness data was discussed in a symposium entitled "Mechanical Properties of Intermetallic Compounds"[1]. The general features of several instruments and some comments on the relationship of hot hardness data to other temperature dependent mechanical properties were presented in a monograph by Domagala[2]. In general, hot hardness data are related to the temperature dependence of strength properties, to general high temperature load-carrying abilities and to resistance to high temperature erosion. Knowledge of the variation of hardness with temperature may be used in the design of stress-rupture and creep tests. Accordingly, stress-rupture tests should be performed in the temperature range where the hot hardness data indicate minor plastic deformation; creep tests should be designed in the higher temperature range where the hot hardness data indicate significant plastic deformation. The knowledge of the temperature region where plastic deformation is small is also required for the proper evaluation of the thermal shock resistance

*E. V. Clougherty and R. L. Pober, ManLabs, Inc., Cambridge, Mass.

parameter as described in subtask XII. When the variation of hardness with temperature is plotted in the form "log Hardness" versus "Temperature", a linear relation is generally observed. A change of slope in the Hardness vs. Temperature curve suggests a change in plastic behavior.

Thibault and Nyquist[3] presented detailed results of an investigation of the factors affecting the measurement of the Knoop hardness of hard brittle materials but the interpretation of other microhardness data in the literature for metal-like compounds is generally limited by experimental uncertainties and incompletely reported results. The specification of indenter configuration and descriptions of the physical characteristics of the impressions are generally lacking. The relationship between indenter load and hardness number is not defined. The effects of cracking on the observed sizes of impressions are often not considered. Although the Knoop configuration was designed to minimize stress-induced cracking in brittle materials, hardness data for these materials are frequently obtained with a Vickers diamond. Data on single crystal material has not been generally available but H. B. Probst at N.A.S.A., Cleveland has received some single crystal boride material from Arthur D. Little for hot hardness measurements. The measurements reported herein have established the relationship between hardness and load for the Knoop configuration for available single crystal and polycrystalline material; the former material showed an orientation effect. These variables were considered in the design of the high temperature measurements in order to provide meaningful data.

B. Experimental

1. Apparatus

An apparatus for measuring microhardness in the temperature range from 25° to 1000°C in vacuo and in inert atmospheres has been designed and built at ManLabs, Inc. A schematic diagram of the unit is shown in Fig. 56;

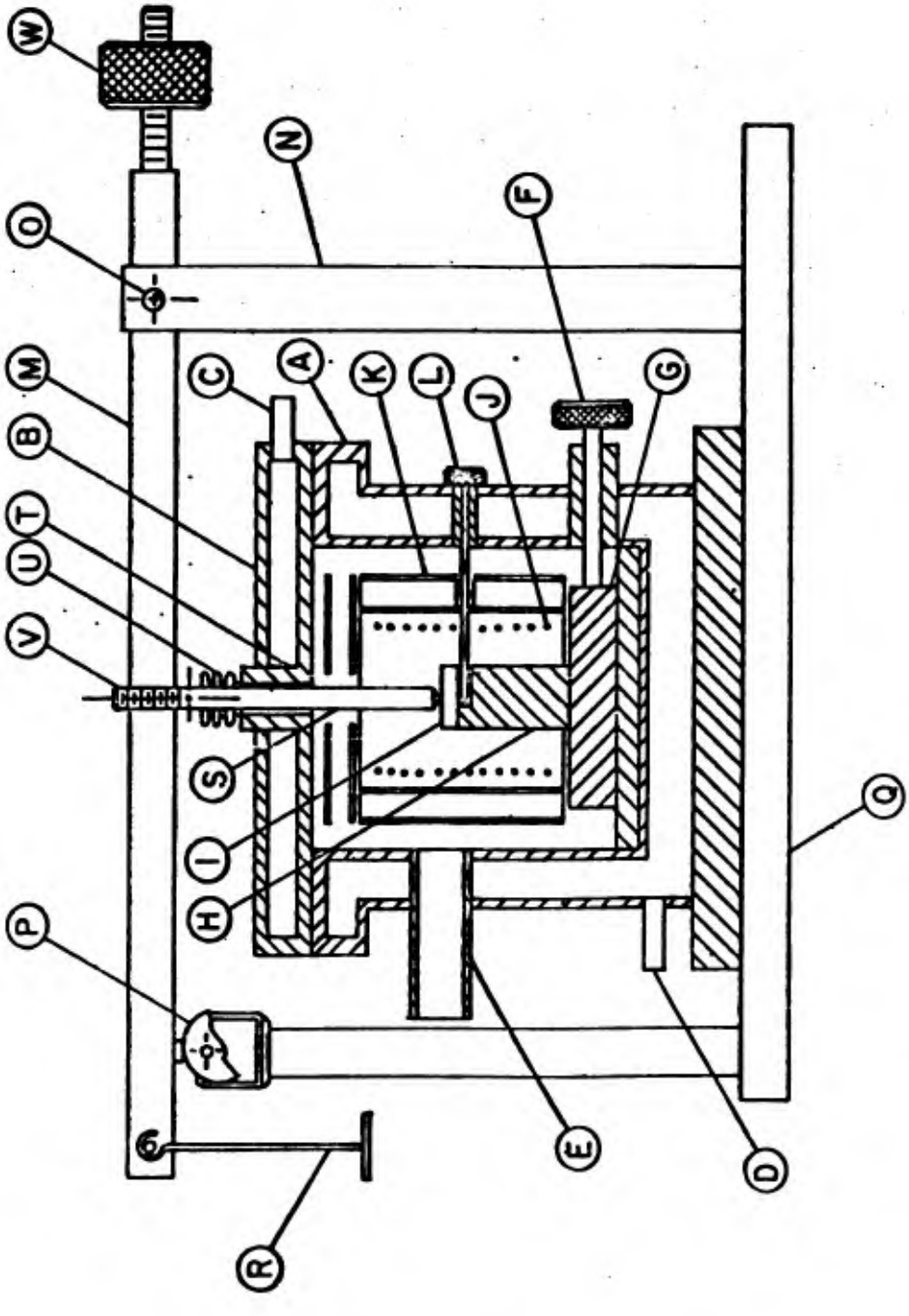

Fig. 56 - Schematic diagram of ManLabs' hot hardness tester. (The parts of the apparatus, identified by the letters, A, B, etc. are described on page 182.

a description of the parts is given below. A photograph of the apparatus is shown in Fig. 57. The hardness tester has three parts: a test chamber, an indenter loading mechanism, and accessories including a vacuum system and a power supply.

1.1 Test Chamber (Capital letters refer to parts of apparatus in Fig. 56.)

A double-walled, water cooled, stainless steel cylinder, A, and a water-cooled, brass top cover, B, comprise the vacuum tight working chamber. The working chamber is connected to the vacuum system through the manifold, E. The specimen, I, located on the molybdenum pedestal, H, which in turn, is attached to the moveable molybdenum block, G is accurately positioned by the micrometer type drive, F. The coreless, self-supporting, thoriated tungsten filament, J, is wound in the form of a spiral and surrounded by two sets of tantalum radiation shields, K. This design provides temperatures up to 1000°C. The temperature of the specimen is measured by a Pt vs. Pt 10 Rh thermocouple L, enclosed in an alumina insulating sleeve and located underneath the specimen.

1.2 Indenter Loading Mechanism

The kinematic principle underlying the indenter loading mechanism allows one degree of freedom. This design requires that the beam, M, be supported on one end by the column, N, at the pivoting point, O. The other end rests on the cam, P. The cam is driven by a synchronous motor (1/20 r.p.s.) and has the following motion profile: a) Fall, 180 degrees; b) Dwell (externally controlled by time-delay relay), c) Rise, 180 degrees. The entire framework of the loading mechanism is rigidly mounted on the base plate, Q. Loads from 50 to 500 grams in increments of 50, 100, and 200 grams

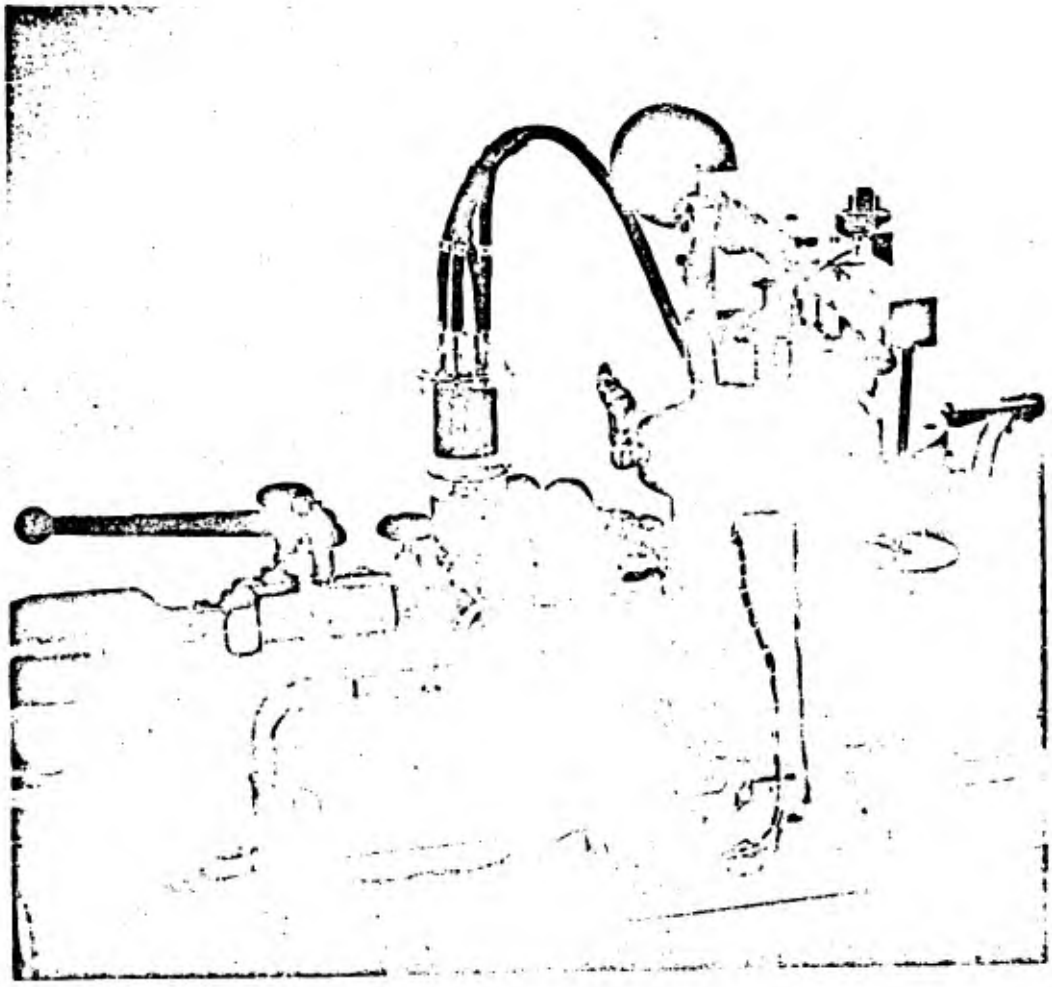

Fig. 57 - ManLabs' hot hardness tester.

can be placed on the loading tray, R. The remaining parts of the indenter assembly are: the molybdenum shaft, S, with a sapphire or diamond indenter mounted on the bottom; a water-cooled bushing, T; a miniature low spring constant bellows, U, which is used as an axial vacuum seal for the indenter shaft. The counterweight, W, is used to balance the system.

1.3 Accessories

The 220 volt, A.C., 4 kilovoltampere power supply coupled with the design of the heater unit can produce sufficient wattage to heat the sample to 1000°C in one hour. Temperature control is provided by conventional methods.

The vacuum system is capable of providing pressures of 5×10^{-5} torr in the test chamber in relatively short times.

2. Indenter Material

The indenter materials which could be used for hot hardness measurements are sapphire, diamond, and titanium diboride. Each of these materials have shortcomings. Although titanium diboride has a high hardness and high temperature stability, and is oxidation resistant, the fabricated material has proven extremely difficult to shape into desired configurations. This material tends to powderize during machining. Sapphire can be machined to the proper configuration; it has good oxidation resistance and is stable to the melting point (2040°C). The limitation for sapphire is the hardness. Diamond can be ground to the proper configuration and has excellent hardness properties. Diamond is reported[2] to be metastable to 1500°C, but results in this work indicate extensive graphitization above 1050°C. The oxidation resistance properties of diamond are inferior to titanium diboride and sapphire, but this problem is circumvented by performing the measurements in vacuum.

Sapphire indenters were originally made in this laboratory for hot hardness measurements on intermetallic compounds. For the present program diamond indenters were used to obtain the hardness data. The diamonds were fabricated to the Knoop configuration. The Knoop configuration was chosen over the Vickers configuration because the former appears to minimize errors arising from cracks due to stress concentrations in brittle materials. Elastic recovery errors are also reduced with a Knoop impression.

3. Sample Requirements

The sensitivity of the microhardness test necessitates the procurement of well characterized and uniform material in order to obtain meaningful results. For single crystal material, the specimen should have a crystal of sufficient area so that the impressions can be made with the same orientation and can be located well within the bounds of the crystal. For polycrystalline material, the specimen should be fine grained so that the impression will span a number of grains and thus give an average result. Grain boundary precipitates should be avoided and the sample should have a minimum number of voids. If an impression is made partially within a surface void, that particular data point can be discarded. Impressions made on a surface just above a void which is not visible will show experimental scatter. Accordingly the density of polycrystalline material should approach the theoretical maximum to minimize errors caused by the presence of voids. The surface of the sample should be perpendicular to the axis of the indenter in order to obtain a symmetrical impression; unsymmetrical impressions yield low hardness results.

3.1 Sample Material

Single crystal specimens for hot hardness measurements were obtained from zone-refined ZrB_2 and HfB_2; polycrystalline specimens, from high

pressure hot pressed TiB_2, ZrB_2, and HfB_2. The presence of excessive cracks and the reduced crystal size of the zone-refined single crystals of NbB_2 prohibited the use of this material for hot hardness measurements; this material was, however, useful for room temperature measurements with the Leitz instrument.

Samples for the hardness measurements were discs cut from cylinders of available material. Both diamond cut-off wheels and electrolytic discharge cutting procedures were employed. The resulting samples varied from 0.25 to 0.38 in. diameter and from 0.010 to 0.020 in. thickness.

4. Method of Measurement

The hardness values were determined in the following manner. The sample was polished and cleaned, then placed in the hot hardness tester. The chamber was then evacuated to a pressure of approximately 5×10^{-5} torr. Next, the sample was heated by thermal radiation to various temperatures. At each temperature, five or more hardness impressions were made. After the series of temperatures were completed, the sample was cooled and removed from the apparatus. The sample was then inspected and the impressions were measured. This process was repeated 3 times to yield about 20 data points for the hardness value at each temperature.

5. Accuracy

The design of the apparatus causes the load on the indenter to vary as the temperature of the sample changes. A room temperature load of 160 grams becomes an effective load of 190 grams at high temperature. The uncertainty in the measurement of the compressive force of the bellows leads to an error of less than $\pm$ 2% in calculation of the load at any given temperature. Thermal etching and slight oxidation of the sample surface at the higher temperature produces an uncertainty in the measurement of the long diagonal of the Knoop impression

of less than ± 3 microns; the uncertainties in the hardness number from these sources of error are ± 2% and ± 8% respectively. The total uncertainty in the Knoop hardness number is ± 10%.

C. Results and Discussion

1. Variation of Hardness with Crystal Orientation

Considerable scatter in experimental results was encountered in the initial investigation of the variation of hardness with temperature for zone-refined, large grain material. These experiments were performed without considering the possibility of significant variations of hardness with crystal orientation. The latter behavior was carefully investigated with the Leitz Microhardness Tester at room temperature. The results showed a pronounced change in hardness at a constant load for a series of measurements taken across a grain boundary as well as within a given large grain. Since each grain showed the same crystallographic plane, it was assumed that this difference was the result of directional anisotropy within the plane. A check of the available single crystal material indicated that the hardness was dependent on crystallographic direction. For impressions made on a $\{10\bar{1}0\}$ face of zone-refined HfB_2, the direction parallel to the c-axis, the $<0001>$, as measured by the long diagonal of the Knoop impression is soft relative to the direction perpendicular to the c-axis, $<11\bar{2}0>$. Accordingly, the data for the hardness vs. temperature plots for each single crystal sample were taken in a constant crystallographic direction. This procedure provided consistent results from which the shape of the hardness vs. temperature plot was obtained. The shape of the curve for other directions is unknown. The series of impressions shown in Fig. 58 clearly demonstrate the variation of hardness with crystal orientation. Specific orientations were only obtained for one sample of HfB_2 because an extensive study of hardness variation with crystal orientation is not within the scope of this investigation.

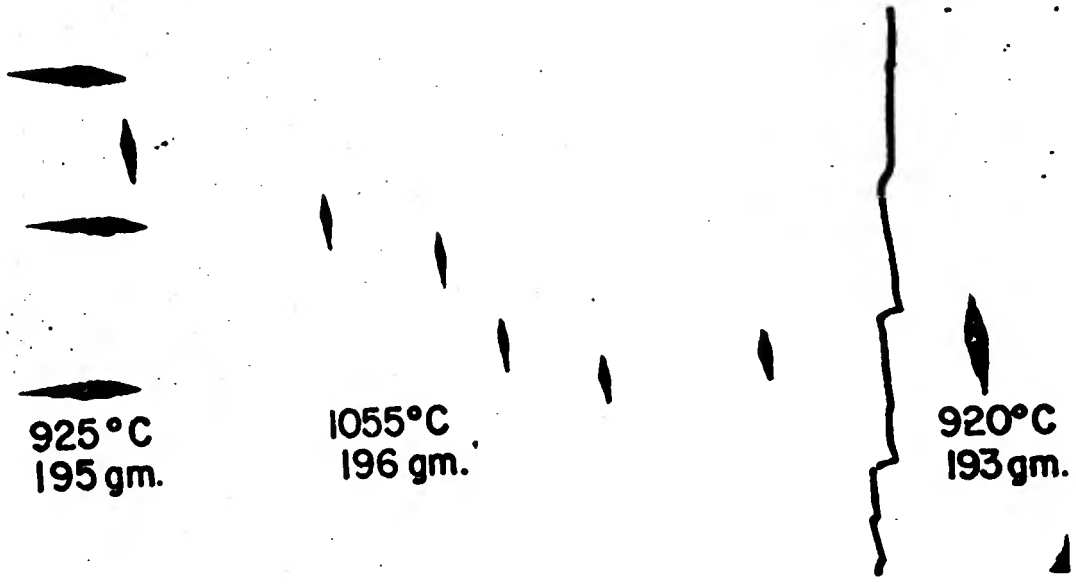

Fig. 58 - Knoop hardness impressions on $\{10\bar{1}0\}$ face of zone refined ZrB_2. (note increase in size of impressions within the same crystal with 90° change in orientation for a decrease in temperature. Also note difference in size of impressions between two grains for same indenter position relative to the sample. The noted variation in load with temperature is brought about by the expansion of the sample holder and the consequent change in the compressive force of the bellows).

2. Variation of Hardness with Applied Load

The definition of Hardness Number can be expressed as

$$H = H_o \frac{\text{LOAD}}{\text{AREA}} \tag{1}$$

where H_o is a constant which is fixed by the geometry and the hardness of the indenter. From this simple description a Vickers Hardness Number would be larger than a Knoop Hardness Number as elastic recovery errors would be more significant for Vickers impressions.

According to Samsonov[4] an expression for the variation of hardness with load for a Vickers type of indenter can be derived as follows: The size of the hardness impression, S, is determined by the plastic deformation under the action of the applied load and by the elastic recovery after the load is removed. If the elastic deformation is directly proportional to the stress and consequently, to the applied load, and the plastic deformation is proportional to the square of the stress, and consequently, to the square of the applied load, then the size of the impression is

$$S = AP^2 - BP + C \tag{2}$$

where A, B, and C are constants characteristic of the material and P is the applied load. The microhardness number is

$$H_M = \frac{P}{S} = \frac{P}{AP^2 - BP + C} \tag{3}$$

Samsonov's[4] results for transition metal borides are shown in Fig. 59. Analogous results were reported for other metal-like compounds and the analytical function for Eq. 3 corresponds fairly well with the experimental curves. The rising part of the function $H_M = f(P)$ which is shown as a dashed line in Fig. 59 cannot be realized because large errors arise from uncertainties in the measurement of the small impressions. A more sophisticated derivation would provide a functional

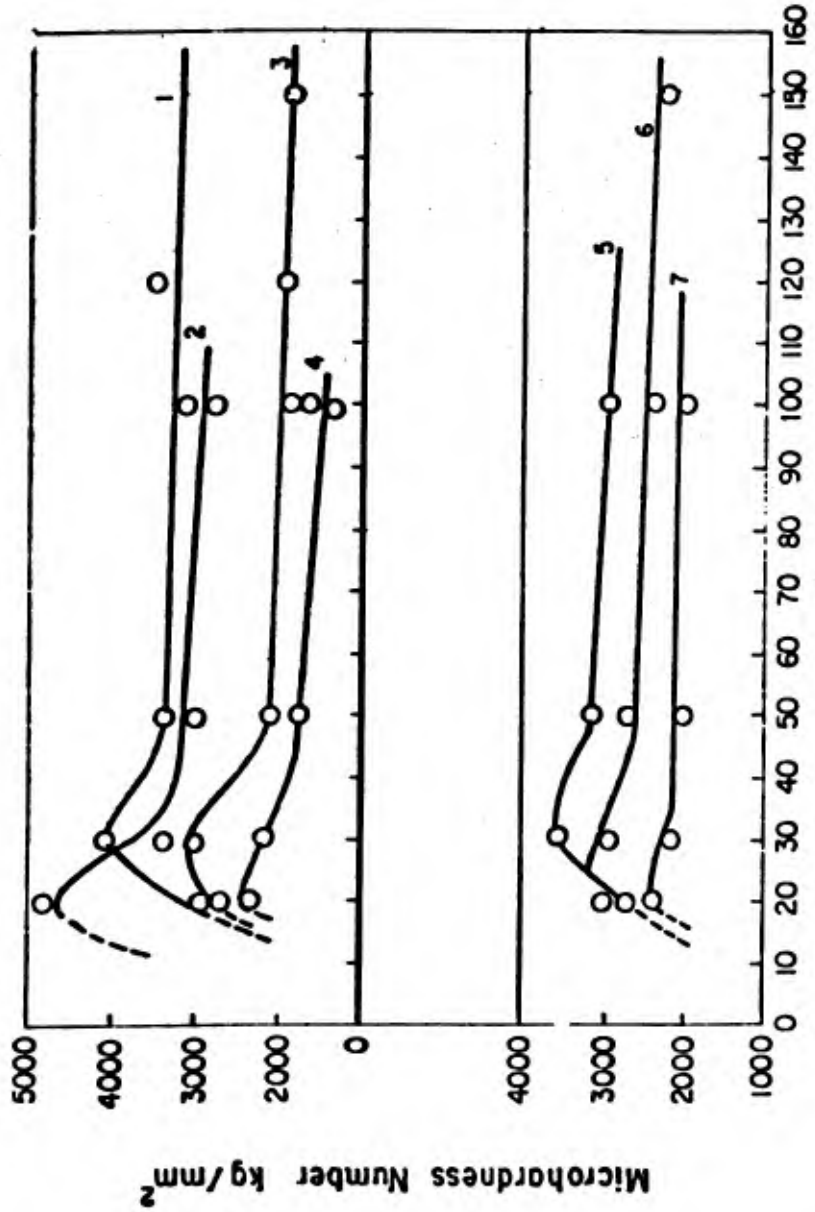

Fig. 59 - Variation of Vickers Microhardness of Borides with Applied Load (after Samsonov[5])
1-TiB_2; 2-NbB_2; 3-TaB_2; 4-ZrB_2; 5-Mo_2B_5; 6-W_2B_5; 7-CrB_2.

relationship between A, B, and C and the applied load, P. For the Knoop impressions the elastic term, BP would vanish and since in reality $C \rightarrow O$ as $P \rightarrow O$, the Knoop Hardness Number would be represented as

$$H_K = \frac{1}{AP} \tag{4}$$

The results obtained for the variation of Knoop hardness with load are collected in Fig. 60. These data are based on an average of at least seven crack-free impressions for each load. The analytical form of these curves agrees with the form predicted by Eq. 4. Appropriate steps were taken to obtain meaningful data for the polycrystalline material and the single crystal material as explained in detail in the foregoing discussion. All data on the variation of hardness with load were obtained with the Leitz Microhardness instrument.

A tentative relationship between the measured geometric properties of Knoop impressions at various applied loads and the elastic properties of a material can be derived by assuming that the elastic stress, σ_E, can be represented by

$$\sigma_E = \frac{P}{\alpha_E} \tag{5}$$

where α_E is the projected area of the Knoop impression arising from elastic deformation, and the elastic strain, ϵ_E, can be represented by

$$\epsilon_E = \frac{\Delta L}{L(exp) + \Delta L} \tag{6}$$

where L(exp) is the experimentally measured short diagonal of the impression and ΔL is the reduction in the original short diagonal caused by elastic recovery.

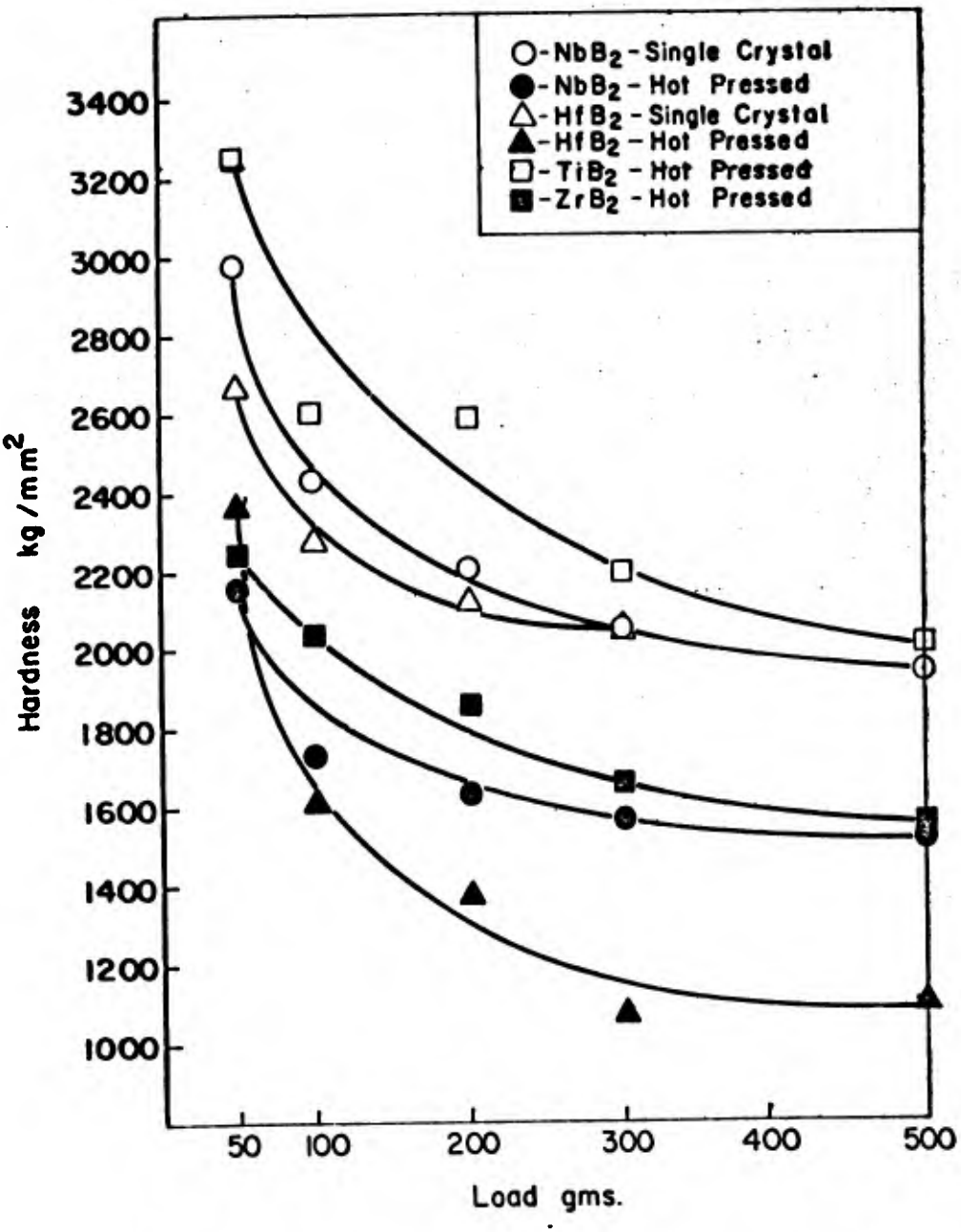

Fig. 60 - Variation of Knoop Microhardness of Diborides with Applied Load for Zone Melted Single Crystal and High Pressure Hot Pressed Specimens. Single crystals were 100% dense; high pressure hot pressed NbB_2 was 90.0%, ZrB_2 97.9%, and HfB_2 86.8% dense.

then the elastic modulus is approximated as

$$\sigma_E = E \epsilon_E \tag{7}$$

The geometry of the Knoop indenter fixes the ratio of the long diagonal to the short diagonal as

$$\frac{\ell_o}{L_o} = 7.15 \tag{8}$$

Since elastic recovery errors are assumed to be absent in the long diagonal,

$$\ell_o = \ell \text{ (exp)} \tag{9}$$

but elastic recovery errors will reduce the experimentally observed short diagonal. Thus,

$$L_o > L \text{ (exp)} \tag{10}$$

The measured long diagonal and Eq. 7 afford a calculated short diagonal,

$$L^1(\text{exp}) = \frac{\ell \text{ (exp)}}{\ell_o / L_o} \tag{11}$$

Accordingly, ΔL in Eq. 6 is calculated as

$$\Delta L = L^1(\text{exp}) - L \text{ (exp)} \tag{12}$$

The quantity $\Delta L + L(\text{exp})$ is the short diagonal corrected for elastic recovery. The quantity α_E in Eq. 5 is obtained from appropriate area calculations. The moduli calculated in this way were of the appropriate order of magnitude, that is, 37×10^6 p.s.i. for NbB_2 compared to a reported value[5] of 76×10^6 p.s.i. for TiB_2; 50×10^6 p.s.i., for ZrB_2; and 37×10^6 p.s.i. for TaB_2. Considerable experimental work will be required in order to demonstrate the usefulness of this procedure. The expenditure of such effort on this task was not within the scope of this contract.

3. Variation of Hardness with Temperature

The results obtained for the variation of Knoop hardness with temperature up to 1000°C are collected in Figs. 61-65. The data are plotted as Hardness (log scale) vs Temperature (linear scale) in accordance with suggested procedures[1,2]. All the compounds display an apparent anomaly at high temperatures. Smooth curves were drawn through the data points to demonstrate the decrease in slope with increasing temperature. Although the averaged data points for the indicated temperatures were taken at different loads, it is significant to note that the higher loads at the higher temperatures would lead to lower hardness values. The observed anomalous results are characterized by higher hardness values at the higher temperatures. These results suggest additional work in the area of high temperature mechanical property measurements to attempt to provide appropriate data necessary for a complete understanding of the variation of hardness with temperature for these materials.

All data on the variation of hardness with temperature were obtained with the ManLabs Hot Hardness instrument. The applied load was 160 grams at room temperature. The aforementioned change in applied load (which can be calculated to $\pm$ 2%) with temperature produced an effective load of 190 grams at 1000°C. Since the hardness vs. load curve (Fig. 60) was only determined at room temperature, no correction was made for the effect of temperature on this curve. Such corrections are presently assumed to be small and will be quantitatively evaluated at a later date.

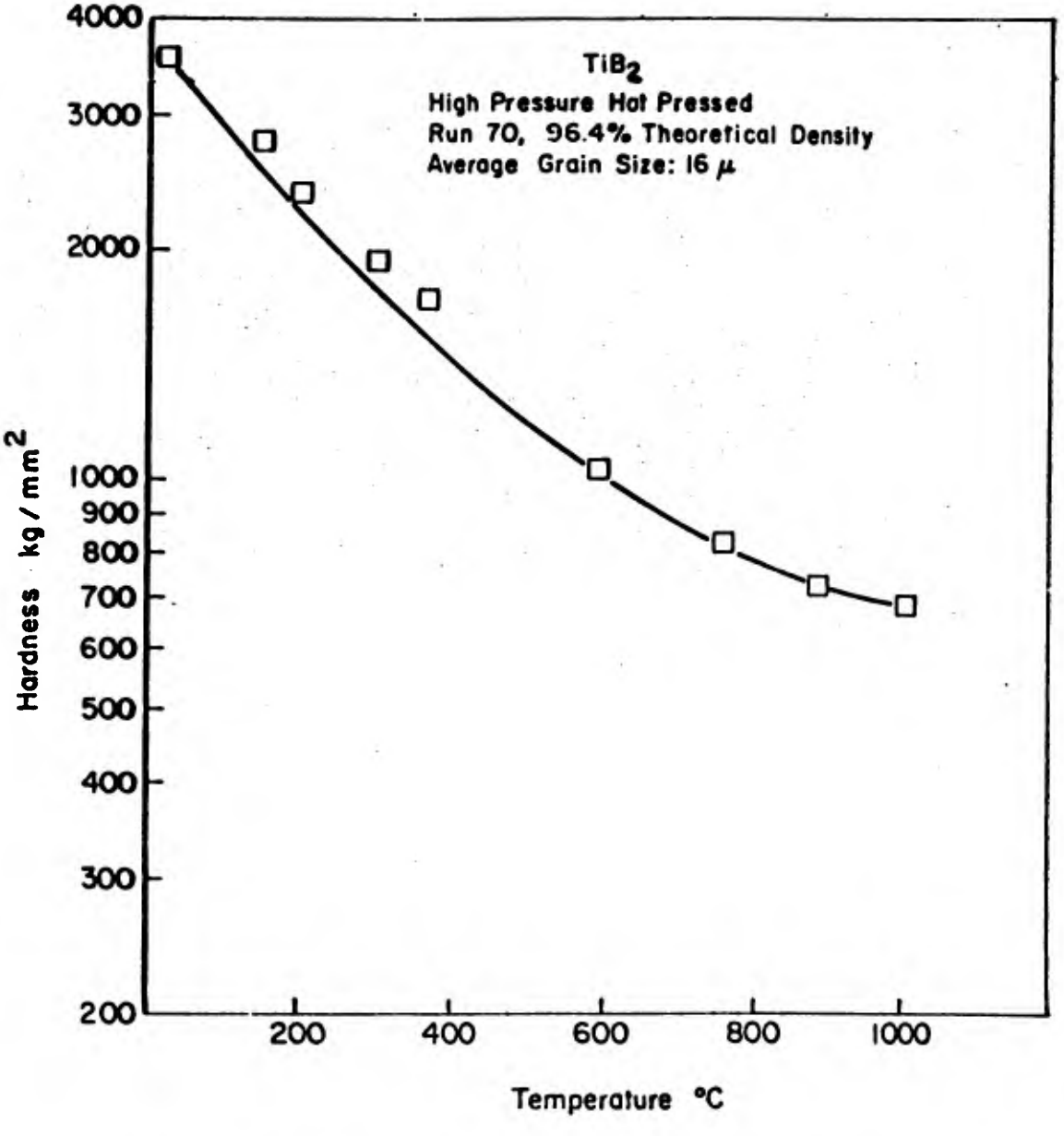

Fig. 61 - Variation of Knoop Hardness with Temperature for High Pressure Hot Pressed TiB_2. (Indenter Load: 160 grams at 25°C, 190 grams at 1000°C.)

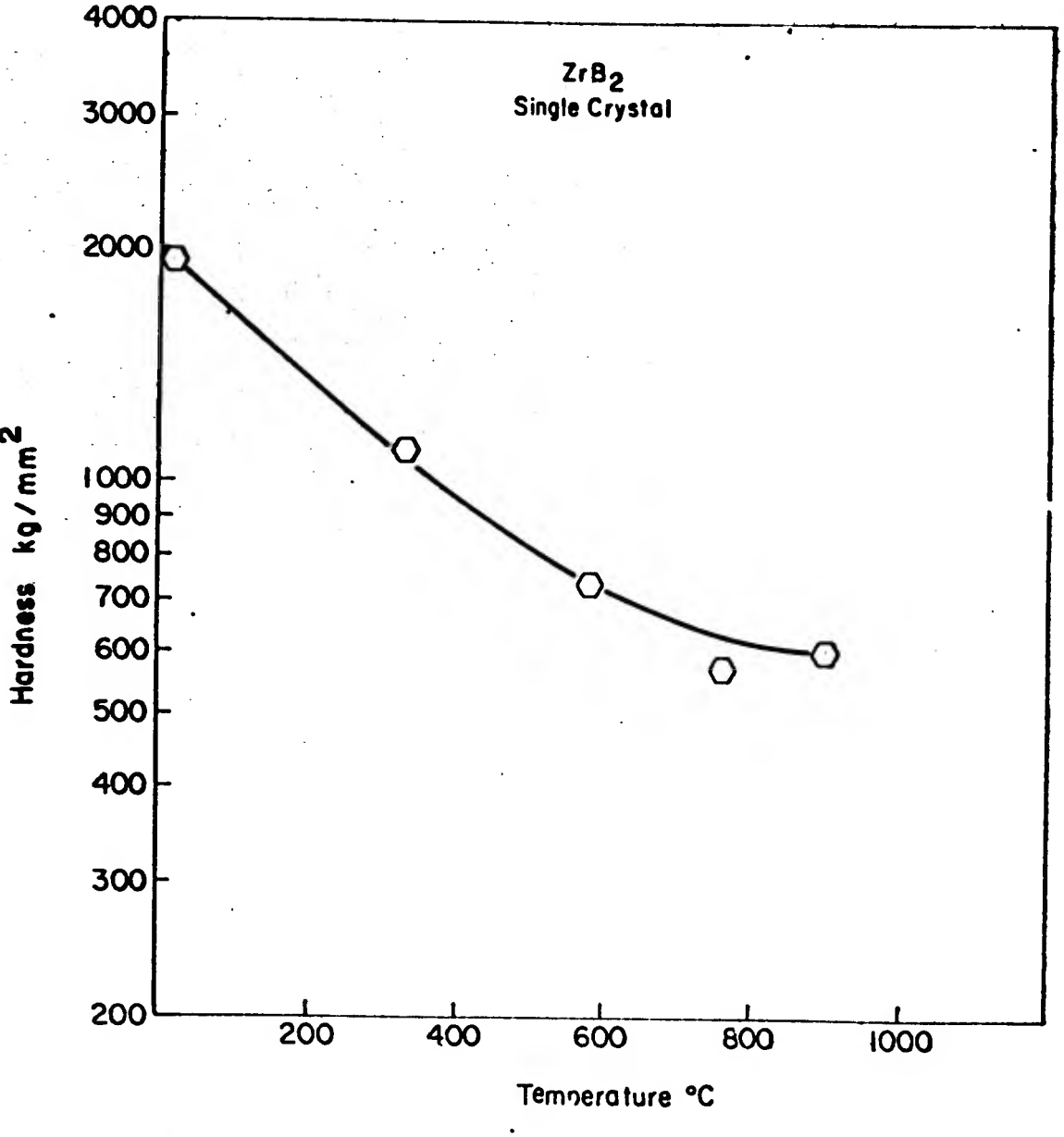

Fig. 62 - Variation of Knoop Hardness with Temperature for Zone-Refined Single Crystal ZrB_2. (Indenter Load: 160 grams at 25°C, 190 grams at 1000°C.)

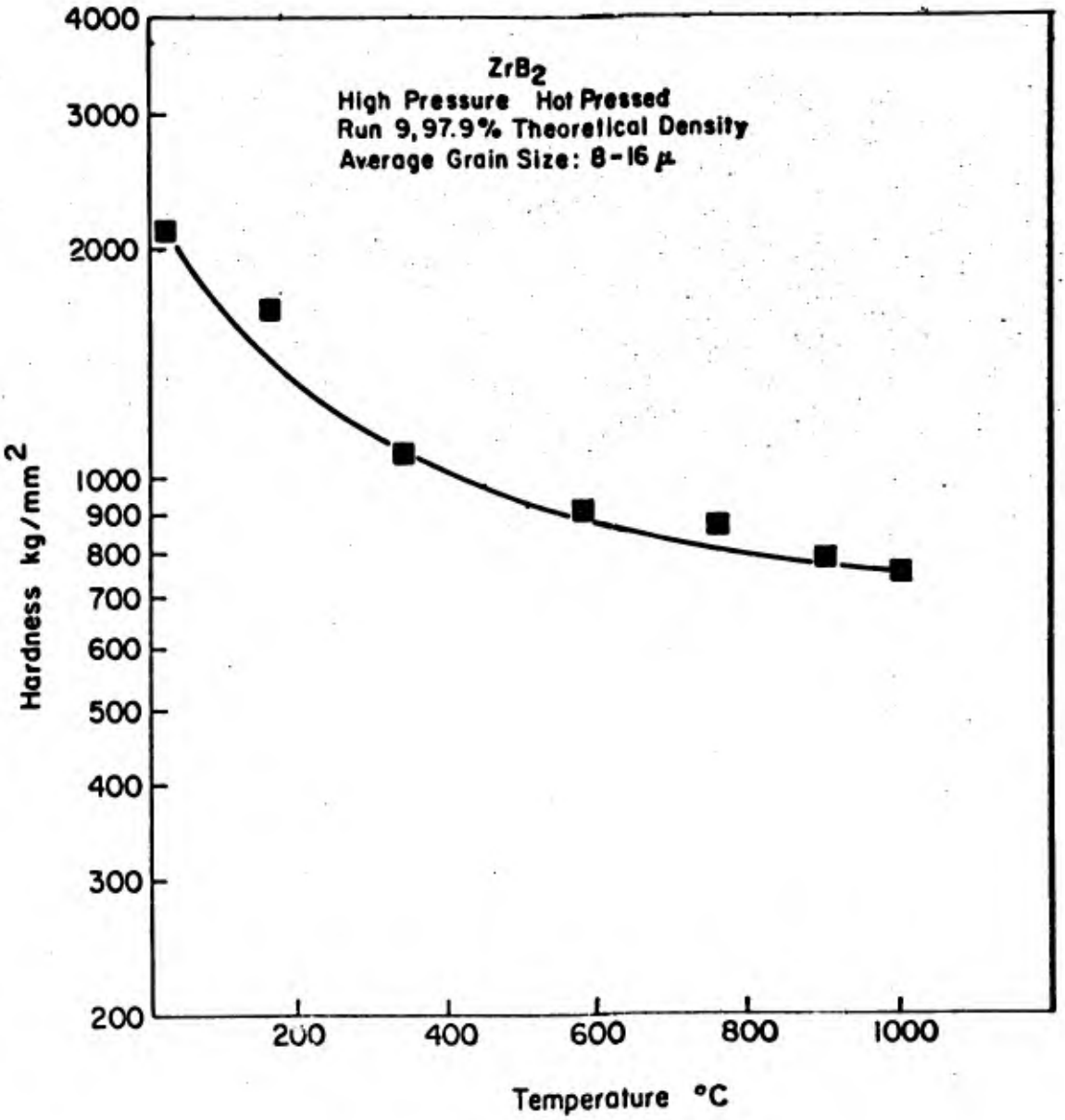

Fig. 63 - Variation of Knoop Hardness with Temperature for High Pressure Hot Pressed ZrB_2. (Indenter Load: 160 grams at 25°C, 190 grams at 1000°C.)

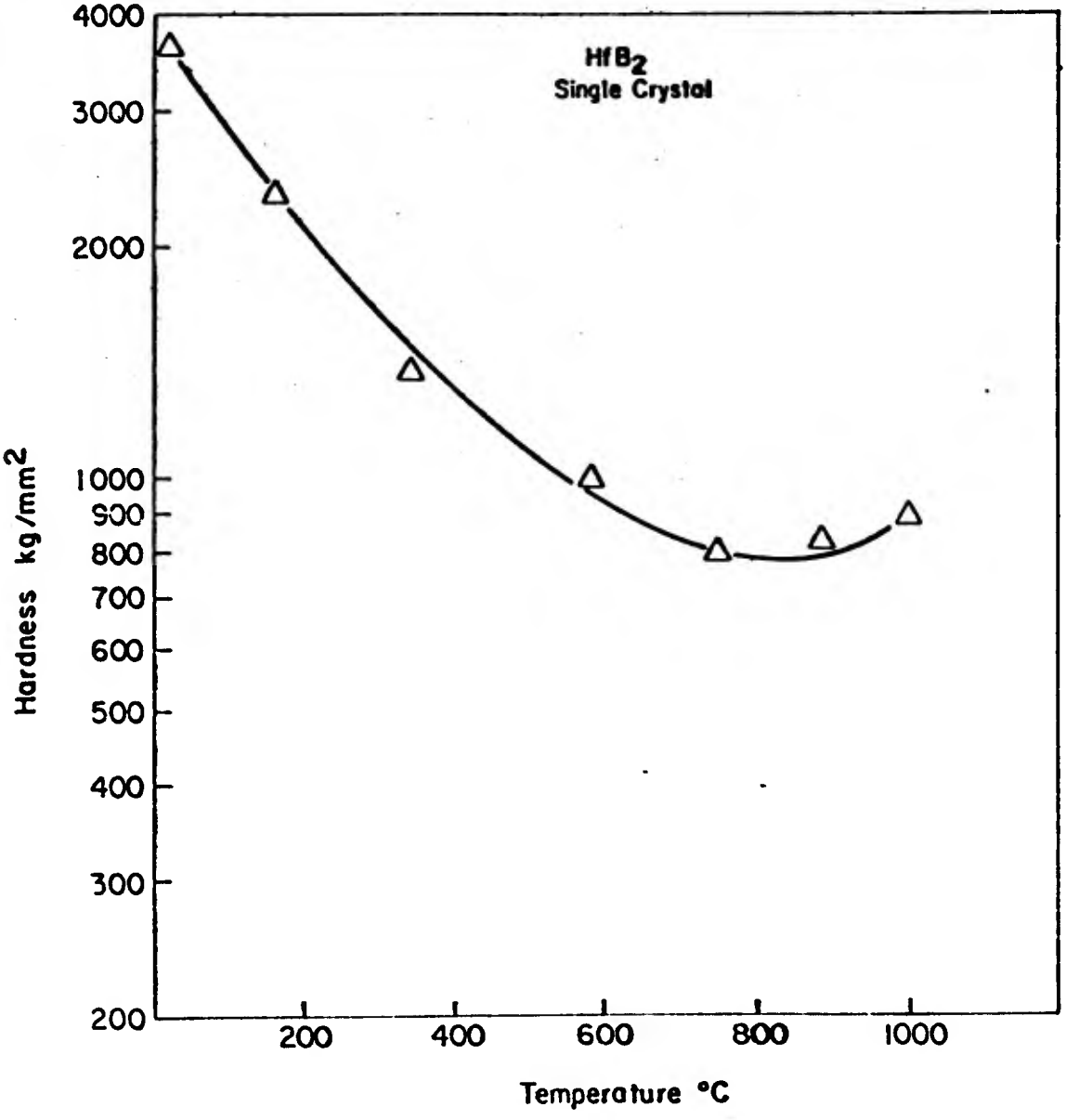

Fig. 64 - Variation of Knoop Hardness with Temperature for Zone-refined Single Crystal HfB_2. (Indenter Load: 160 grams at 25°C, 190 grams at 1000°C.)

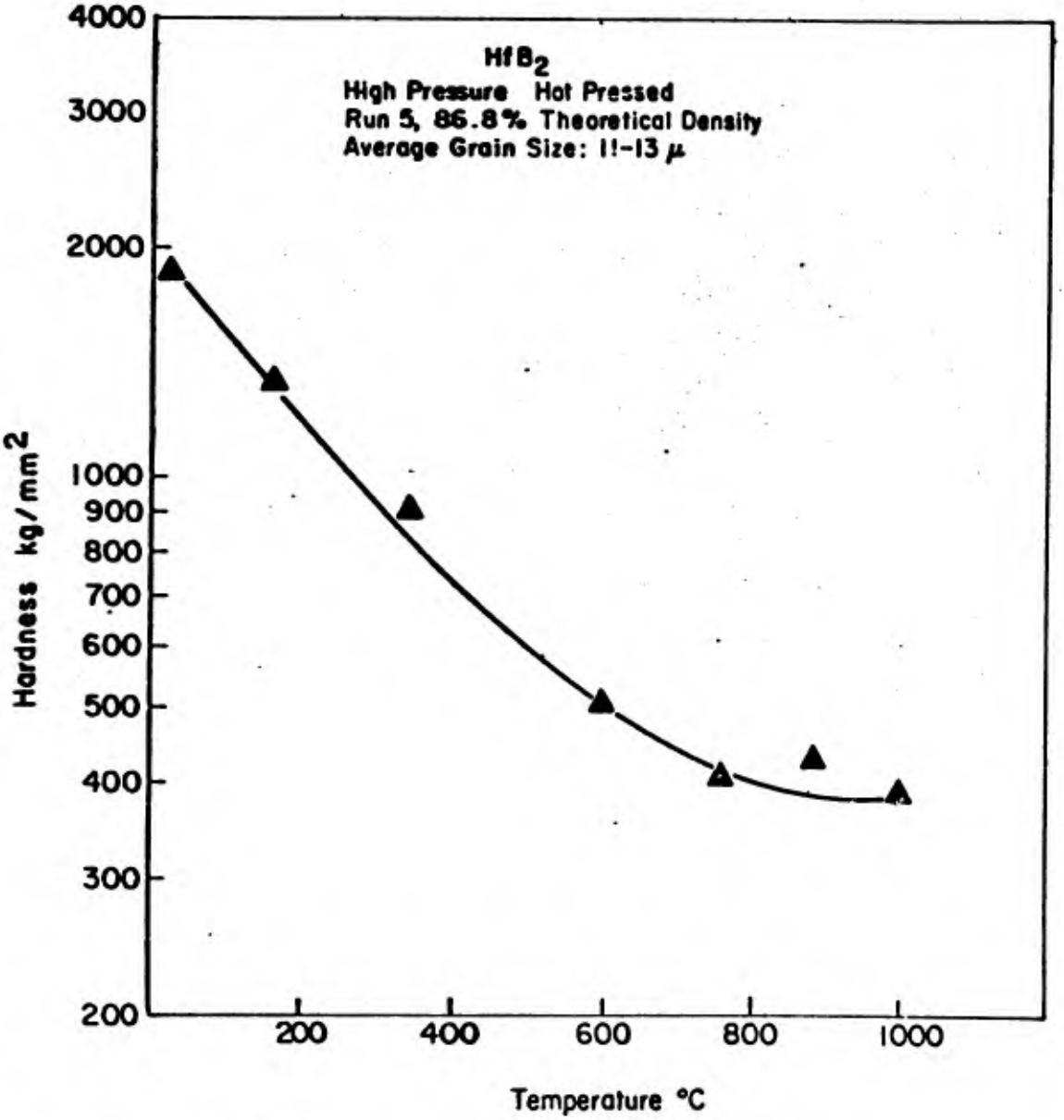

Fig. 65 - Variation of Knoop Hardness with Temperature for High Pressure Hot Pressed HfB_2 (Indenter Load: 160 grams at 25°C, 190 grams at 1000°C.)

REFERENCES

1. Westbrook, J.H., Mechanical Properties of Intermetallic Compounds, John Wiley and Sons, Inc., New York, (1959).

2. Domagala, R.F., High Temperature Technology, Campbell, I.E., Edit., John Wiley and Sons, Inc., New York, (1956).

3. Thibault, N.W., and Nyquist, H.L., Trans. ASM (1947) 38 271.

4. Samsonov, G.V., Neshpor, V.S., and Khrenova, L.M., Fiz. Metal. metalloved., (1959) 8 No. 4, 137-144.

5. Samsonov, G.V., Visnyk Academii Nauk Ukrains koi, SSR, (1959) No. 6, 27-37.

XIV. OXIDATION*

A. Introduction

The purpose of this task is to determine the mechanism of oxide growth on diborides of metals of Groups IV-A and V-A of the periodic table in the temperature range 1200-2200°C under various environmental conditions. The background literature is discussed briefly in Section B. In Section C, the experimental results obtained during the contract period on the Group IV-A diborides, TiB_2, ZrB_2, and HfB_2, and the Group V-A compounds NbB_2 and TaB_2 are summarized. (VB_2 is of no interest to the present program). In Section D, the results on the diborides are compared; in Section E, the oxidation behavior of HfB_2, the most promising of the refractory diborides, is related to the oxidation behavior of other promising high temperature materials. Finally, the direction of future effort is considered in Section F.

B. Literature Survey on the Oxidation of Diborides of Groups IV-A and V-A of the Periodic Table

1. Titanium Diboride

The oxidation of vapor deposited films of TiB_2 in pure oxygen at one atmosphere in the temperature range 700-1100°C was studied by Münster and Schlamp [1]. The reaction appeared to follow a parabolic rate law with an activation energy of 51 ± 6 in the range 700-850°C, and an activation energy of 21 ± 2 kcal/mole in the 950-1100°C range. The energies were computed from least squares analysis of the data and differ from the values given in the original paper. The oxide film was shown by X-ray, chemical and metallographic analysis to contain TiO_2 (rutile) and B_2O_3(c). Between 700 and 800°C, the rutile

*J. B. Berkowitz-Mattuck, Arthur D. Little, Inc., Cambridge, Mass.

was finely dispersed in an amorphous B_2O_3(c) matrix. Above 800°C, phase separation occurred with TiO_2 at the oxide alloy interface separated from the ambient atmosphere by a layer of B_2O_3(*l*). At 1050°C, a comparison of net weight change with total oxygen consumption provided evidence for the loss of boron as B_2O_3(g). A platinum marker experiment at 1000°C suggested that TiO_2(rut) grows by inward diffusion of oxygen. The growth mode of the B_2O_3(*l*) could not be determined by the marker Technique.

Neshpor and Samsonov[2] studied the oxidation of TiB_2 in dry air at 800°C. They, too, fit their data to a parabolic rate equation, but their calculated rate constant, 6.5×10^{-5} mg^2/cm^4-sec, is a factor of 5.5 lower than found by Münster and Schlamp at the same temperature in pure oxygen. The difference may reflect either a pressure dependence of the oxidation rate, or differences in the initial TiB_2 sample.

Meyerson, et al. worked with hot pressed specimens that were contaminated with about 1% of both carbon and iron[3]. Münster and Schlamp, on the other hand, dealt with rather thin films plated on an Al_2O_3 substrate. Meyerson, et al. measured the weight change as a function of time, and his low apparent rate may be due to volatilization of the carbon impurity as CO_2 combined with oxidation of TiB_2 to TiO_2 and B_2O_3.

In 1955, Meyerson et al.[3] assumed, checked and confirmed that Ti and Zr do not form borates. By metallographic examination of the oxide scale on TiB_2 they concluded, in agreement with Münster and Schlamp, that a mechanical mixture of TiO_2 and B_2O_3 is the first product of oxidation. As time progressed, a layered scale structure was observed, and the B_2O_3 content in the outer scale declined since the rate of vaporization of B_2O_3(g) was somewhat larger than the rate of growth of condensed B_2O_3(c,*l*). Subsequent publica-

tions[2,4,5] indicated that the oxide consists of vitreous salts of pyroboric acid of the form $Ti(B_4O_7)_2$.

A third study of the oxidation of TiB_2 was made by F. H. Brown, Jr.[6] on porous compacts of the diboride. He worked in the temperature range 482-1315°C and compared results in an ambient atmosphere, in well-dried air, and in pure oxygen. Due to the porous nature of Brown's materials, his surface areas are unknown, and his results cannot be compared quantitatively with the previously reported data. Brown measured the weight change of his samples after successive times at temperature. Brown's results differ in two significant respects from those of other workers. First, he did not observe a parabolic rate law, but rather a sharp drop in oxidation rate with time. Second, he found that the net extent of oxidation was less at 788°C than at 482°C. It seems very likely that sintering is occurring simultaneously with oxidation in these experiments, and that the surface area is therefore continuously changing. This makes interpretation of the results extremely difficult. Brown did make two interesting and significant observations, however. He found that oxidation rates in undried air were very much higher than in dried air, and that the rates in pure, dried oxygen were somewhat higher than the rates in dried air. As discussed below, the volatility of boron oxide is greatly enhanced in the presence of water vapor, and therefore small amounts of moisture should have considerable effect on the oxidation behavior of diborides. His second observation provides further evidence that the oxidation of TiB_2 is pressure dependent.

McDonald and Ransley[7] studied the oxidation of TiB_2 in the 300-1000°C range, and found a linear oxidation rate at 450°C, where the major oxidation product was TiO_2 in the anatase modification. At higher temperatures, these workers confirm the parabolic oxidation reported in references (1-5).

2. Zirconium Diboride

F. H. Brown, Jr. investigated the oxidation of ZrB_2 in pure oxygen between 649 and 1315°C in much the same way as he did TiB_2. Although his data show an apparent minimum in oxidation rate around 1000°C, it is suggested that these results are questionable due to uncertainties in surface area. With ZrB_2, as with TiB_2, an accelerated oxidation rate was observed in pure oxygen compared to dry air, and a much higher rate was observed in moist air than in dried air.

Meyerson[3] examined the oxide scale formed on ZrB_2 at 1000°C and concluded that ZrO(s) exists at the alloy-oxide interface. He postulated that in the first 2 hours in oxygen at 1000°C, a film of ZrO covered by fluid B_2O_3 (possibly with dissolved ZrO in it) forms on the surface of the ZrB_2. As oxidation proceeds over the next 10-20 hours, oxygen diffuses through the oxide and reacts with ZrO to form ZrO_2. In the meantime, B_2O_3 gradually evaporates. A depth of corrosion of 0.45 mm after 150 hours in air at 1000°C was observed.

3. Hafnium Diboride

The high cost of hafnium is perhaps responsible for the paucity of oxidation data on HfB_2. No quantitative information could be found at all, but Paderno[8] reports intensive oxidation in air above 600-700°C, and disintegrative oxidation at 1000-1200°C.

4. Niobium Diboride

The oxidation of niobium diboride has been studied only by the Samsonov group in the Soviet Union. Neshpor and Samsonov[2] found that at 800°C in air, the oxidation of hot pressed NbB_2 is parabolic for the first two hours, with a rate constant of 1.3×10^{-8} g^2/cm^4-min. In the same paper,[2] the weight gains, Δp, of NbB_2 samples in one hour at a number of temperatures

between 450 and 1000°C are reported. Assuming parabolic behavior over the entire temperature range, we have computed parabolic rate constants k_p in mg^2/cm^4-sec from each experimental point. The activation energy for the overall oxidation process, from the least squares' slope of the log k_p vs 1/T plot is 31.7 ± 2.0 kcal/mole. If the probable errors in the data are taken into account, Samsonov and Neshpor's fitting of the points to two straight lines, with a change in slope at 750°C seems unjustified. The Russian group[9] reports quantitative data on the oxidation of niobium borides as a function of boron composition. Alloys containing less than 40 atom % boron (Nb_3B_2) oxidize completely in 5 hours at 900°C, while alloys with more boron, NbB, Nb_3B_4, and NbB_2, are more resistive to oxidation.

5. Tantalum Diboride

Samsonov[9] remarks that the stability of Ta-B alloys to oxidation is low, with samples suffering intensive oxidation at temperatures of 900°C.

Thus, at the inception of the present program, no quantitative data at all was available on the oxidation of HfB_2 or TaB_2, and very little was known about the oxidation of any of the diborides above 1200°C.

C. Summary of Experimental Results on the Oxidation of Diborides of Groups IV-A and V-A of the Periodic Table

The experimental program was aimed at filling in the important gaps in the published literature. Since work in the field of oxidation of refractory alloys has hitherto been severely hampered by lack of availability of dense well-characterized samples, the oxidation program followed closely the materials' preparation program.

Continuous measurements were made of total oxygen consumption vs time by inductively heated sample pellets in a flowing stream of helium and oxygen. Samples were machined in the form of cylinders approximately 0.6 cm in diameter and 0.3 cm thick. They were mounted by three point contact with platinum or platinum-rhodium thermocouple wire, were placed in a quarts system, surrounded by a silver plated copper concentrate and were heated with a 5 kw Sylvania induction furnace. Temperatures, measured with an optical pyrometer through a calibrated flat window, were uniform across the top surface of the pellet to $\pm$ 5°C. The oxygen consumption measurements were made by using a thermal conductivity cell of the type familiar in vapor phase chromatography to compare the oxygen concentration in the helium stream before and after removal of some of the oxygen by reaction with the sample.

1. Titanium Diboride

Due to the unforeseen difficulties discussed in Section V in preparing pure dense bodies of TiB_2 by zone-refining, this material was supplied late in the program by high pressure hot pressing as discussed in Section VI. Two experimental measurements were made at an oxygen partial pressure of 39.1 torr in helium, one at 1551°K, a second at 1761°K. The data are summarized in Table 41.

The first column is a notebook designation of the run. The initial weights in the second column are weights taken after degassing the sample pellets in pure dry helium at 1995°K for 20 minutes. The weight loss during the degassing period was 0.0056 g for pellet XV-35, and 0.0042 g for pellet XV-31, and was probably due to vaporization of boron, since the evolution of permanent gases as monitored with the thermal conductivity apparatus[10] was negligibly

small and a cloud of black smoke was evolved that condensed on the cool walls of the apparatus.

The sample surface areas (A) were calculated from the gross physical dimensions of the specimens. The densities (ρ) were obtained from initial sample weights after degassing and geometric sample volumes. The theoretical X-ray density of TiB_2 is 4.52 g/cm^3. The temperatures (T, °K) are observed pyrometer temperatures corrected for sample emissivity (assumed equal to 0.6) and for transmission of the optical window. The oxygen pressures, p_{O_2}, are partial pressures in helium, the total pressure in every case was 760 torr. The carrier gas flow rate of 95 cm^3/min corresponds to a linear flow velocity in the neighborhood of the sample pellet of about 3 cm/sec. The exposure time indicates the duration of each oxidation experiment. The net weight changes were calculated as difference in weight of each pellet before and after oxidation divided by initial surface area A. The total oxygen consumed during time t was calculated from the area under the thermal conductivity curve and represents the amount of oxygen in all of the titanium and boron oxides formed.

Table 41

Oxidation Data for TiB_2*

Pellet	Initial wt., g	A, cm^2	ρ, g/cm^3	T, °K	p_{O_2}, torr	Flow, cm^3/min	Exposure time, min	Net wt. change, g/cm^2	Total oxygen consumed, g/cm^2	k_{pp}, g^2/cm^4-min
XV-35	0.5728	1.654	4.24	1551	39.1	95	126	0.0032	0.0112	6.9×10^{-7}
XV-31	0.6069	1.729	4.23	1761	39.1	95	92	-	0.220	2.1×10^{-4}

*High pressure hot pressed, Run-64, pycnometric density 4.33 g/cm^3, 95.4 % theoretical.

Some difficulty was experienced in both runs in maintaining the sample at constant temperature. Fig. 66 is a plot of total oxygen consumption squared vs time for the first 70 minutes' oxidation of pellet XV-35. Over the next 50 minutes the temperature rose 30° and resulted in a gradual increase in oxidation rate, which is not easily interpreted. Similar behavior was observed with pellet XV-31 and only the data for the first hour are plotted in Fig. 67. Over the next 30 minutes, the average temperature was increased by 25°K and spots as much as 130° higher began to appear on the surface of the heavily oxidized pellet. The oxidation of TiB_2 between 1551 and 1761°K at an oxygen pressure of 39.1 torr seems to obey a parabolic rate law, at least for the first hour of exposure. The parabolic rate constants derived from the slopes of the lines drawn in Figs. 66 and 67 are given in the last column of Table 41.

X-ray analysis of pellet XV-31 after oxidation revealed 7 lines for TiO_2(rutile). X-ray analysis of pellet XV-35 failed to identify the surface oxide unambiguously, but suggested the presence of both B_2O_3(c) and TiO_2(rut).

The results reported here were obtained at higher temperatures than previous quantitative results from other laboratories[1,2]. Furthermore, previous measurements were of net weight change; the present ones are of oxygen consumption. Due to the unknown vaporization rate of B_2O_3 in an oxidation experiment, comparisons are difficult to make. At 1373°K, in pure oxygen at 760 torr, Münster and Schlamp[1] report a parabolic rate constant based on net weight change of 1.8×10^{-7} g^2/cm^4-min. At 1473°K, in air, Samsonov[2] finds a parabolic rate constant of 10.9×10^{-7} g^2/cm^4-min, also based on net weight change. At 1551°K, the present results indicate a parabolic rate constant based on total oxygen consumption of 6.9×10^{-7} g^2/cm^4-min.

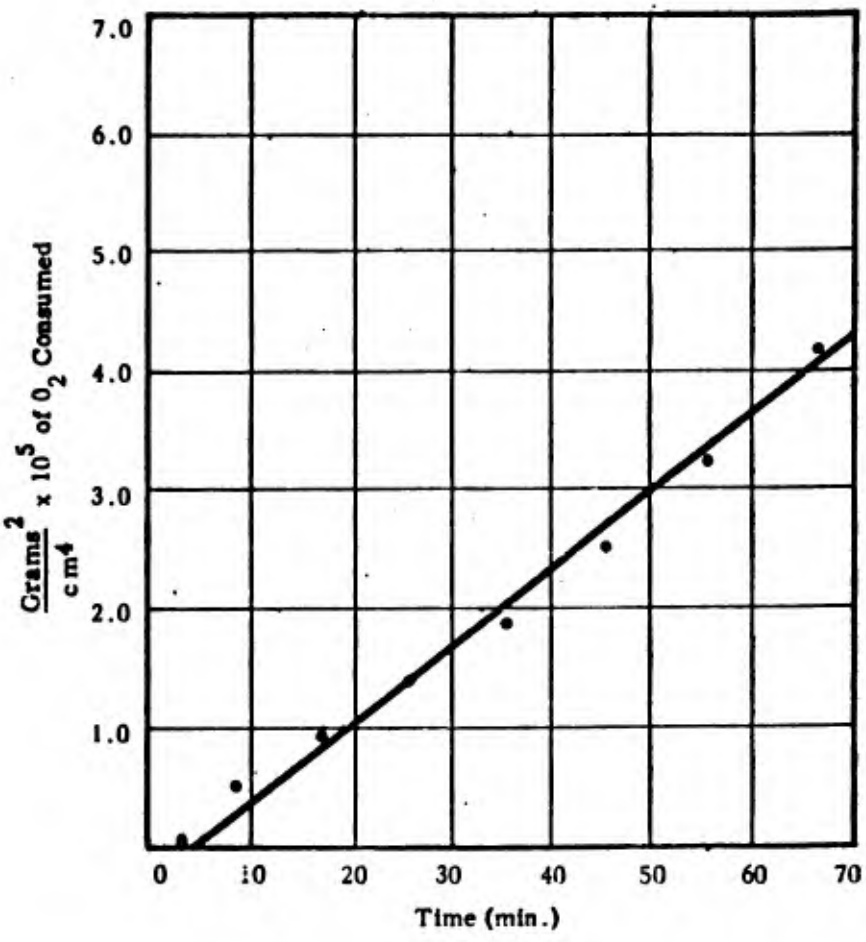

Fig. 66 - Oxidation of TiB_2, XV-35, T = 1551°K p_{O_2} = 39.1 Torr. r.

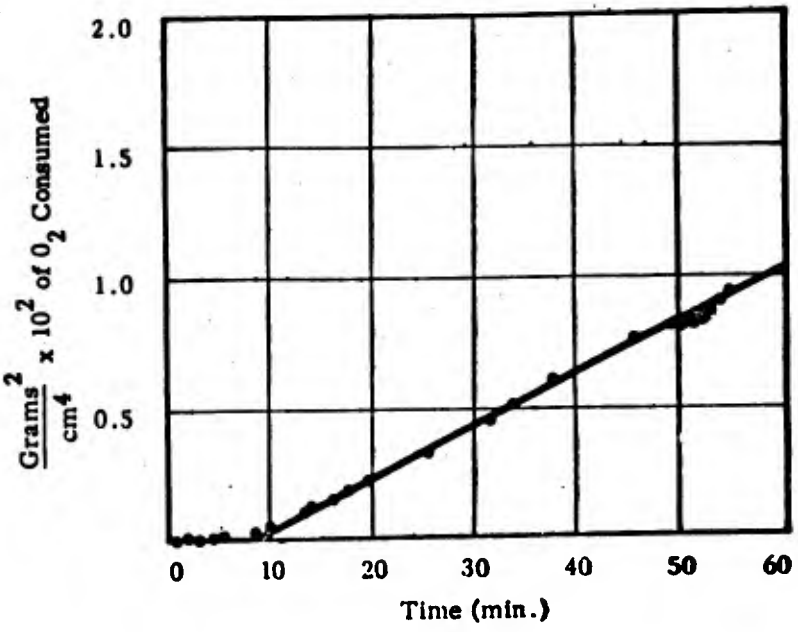

Fig. 67 - Oxidation of TiB_2, XV-31, T = 1761°K, P_{O_2} = 39.1 Torr.

Net weight change differs numerically from total oxygen consumption by the amount of oxide vaporized. The results are therefore at least in qualitative agreement.

2. Zirconium Diboride

The oxidation of ZrB_2 at temperatures of 1217-1805°K and oxygen pressures between 10 and 40 torr has been studied by Berkowitz-Mattuck[11] under AF33(616)-7472 by an oxygen consumption method. After an initial period of about 40 minutes, the oxygen consumption vs time data could be fitted to a parabolic rate equation. Parabolic rate constants k_p were calculated from final slopes of plots of $(w_{O_2}/A)^2$ vs t, where w_{O_2} is the weight of oxygen picked up by the sample in time t and A is the initial surface area of the sample. From the Arrhenius plot shown in Fig. 68 of log k_p vs 1/T, an activation energy of 77 $\pm$ 5 kcal/mole was calculated for the over-all oxidation process above 1400°K. In the low temperature range the activation energy is smaller. The large standard deviation of the experimental points from the least squares straight line through them is due (1) to the high absolute value of the activation energy, i.e. at 1200°C, an error or fluctuation of 10° in experimental temperature will be reflected in a 15% error in k_p, and (2) to cracks in the as-prepared samples; metallographic examination showed that oxide growth proceeds at the surface of a crack just as it does on the external surface; thus an error is introduced by using surface areas based on gross physical dimensions. S evidence was found for pressure dependence of the oxidation rate, but [redacted] tive results were masked by temperature fluctuations during a single r

Since cracks do not fill in during oxidation, the solid [redacted] must form at least in part by inward diffusion of oxygen. Since the oxide g

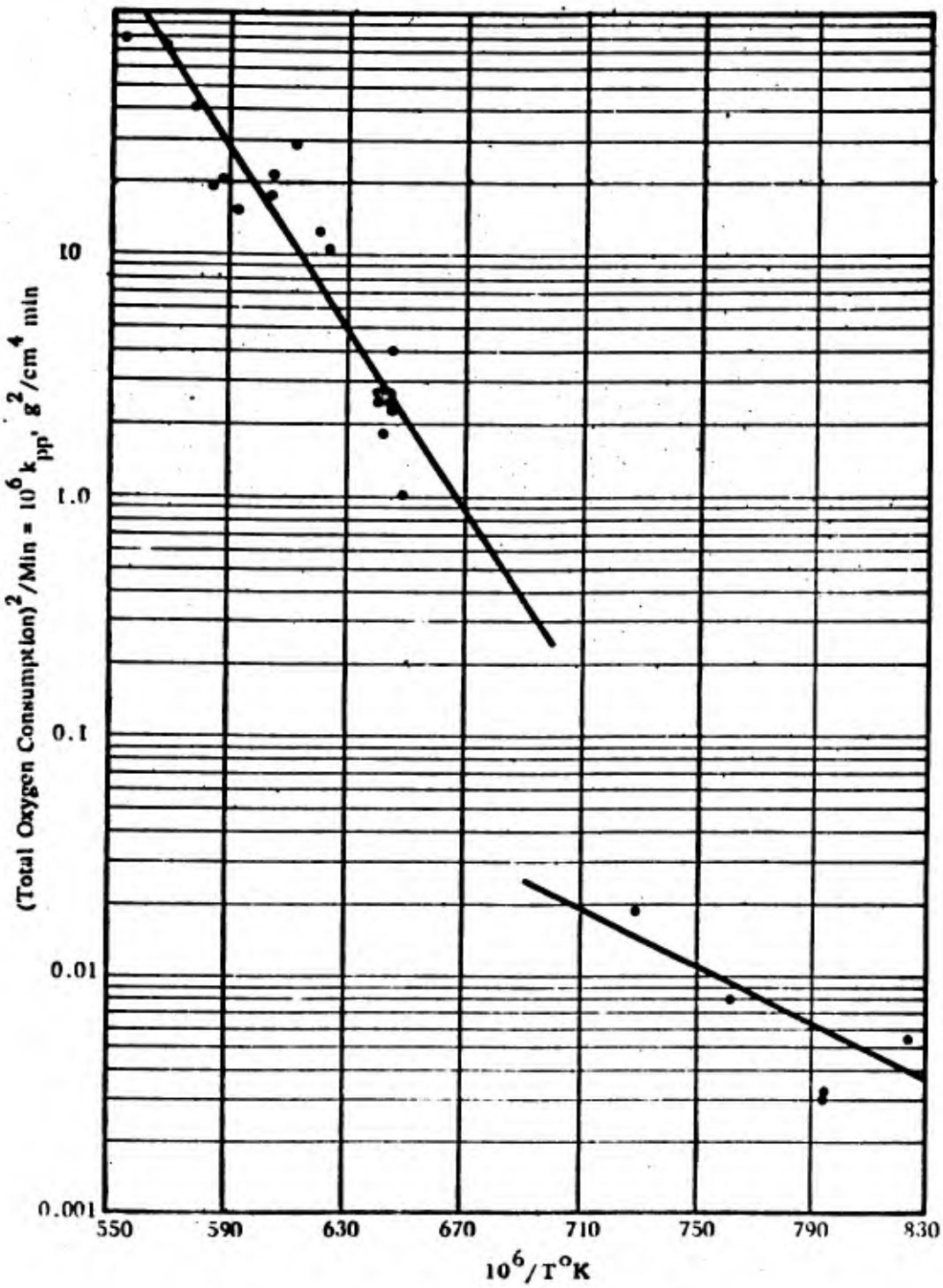

Fig. 68 - Arrhenius Plot for Oxidation of ZrB_2; (Total Oxygen Consumption) 2/min. vs. $1/T^\circ K$.

X-ray lines for monoclinic ZrO_2, which is believed to be an anion deficit semiconductor, oxide growth by inward diffusion of oxygen anions it is not unreasonable. However, the small amount of data available suggests an activation energy for anion diffusion of less than 40 kcal/mole, compared to an observed activation energy for oxidation of 77 $\pm$ 5 kcal/mole. It is thus not entirely clear that a simple Wagner mechanism can be used to explain the results. The oxidation of pure zirconium metal in dry oxygen at 1 atm follows a cubic rate law over the temperature range 575-950°C. The pure metal has not been studied at the temperatures used here, and therefore results cannot be compared, but on the basis of extrapolated data, the diboride shows greater oxidation resistance.

In the range 1200-1500°K at oxygen partial pressures between 100 and 760 torr, net weight change measurements were recently made by Kuriakose and Margrave. The parabolic rate constants based on net weight change are shown in Fig. 69[11], and give an activation energy of 19 $\pm$ 1 kcal/mole. The results from the two laboratories can be brought into fair agreement by taking into account the vaporization of $B_2O_3(g)$ as described below, and converting both sets of data to an alloy consumption basis.

3. Hafnium Diboride

The oxidation of zone melted HfB_2 was also studied by Berkowitz-Mattuck under AF33(616)-7472 at temperatures between 1488 and 1999°K and oxygen partial pressures of 8.5 and 19.9 torr. The parabolic rate constants observed are given in an Arrhenius plot in Fig. 70[12].

A sample of HfB_2 prepared at ManLabs by high pressure hot pressing was exposed at 2024 and 1982°K at an oxygen partial pressure of 18.5 torr. Data for the run are given in Table 42.

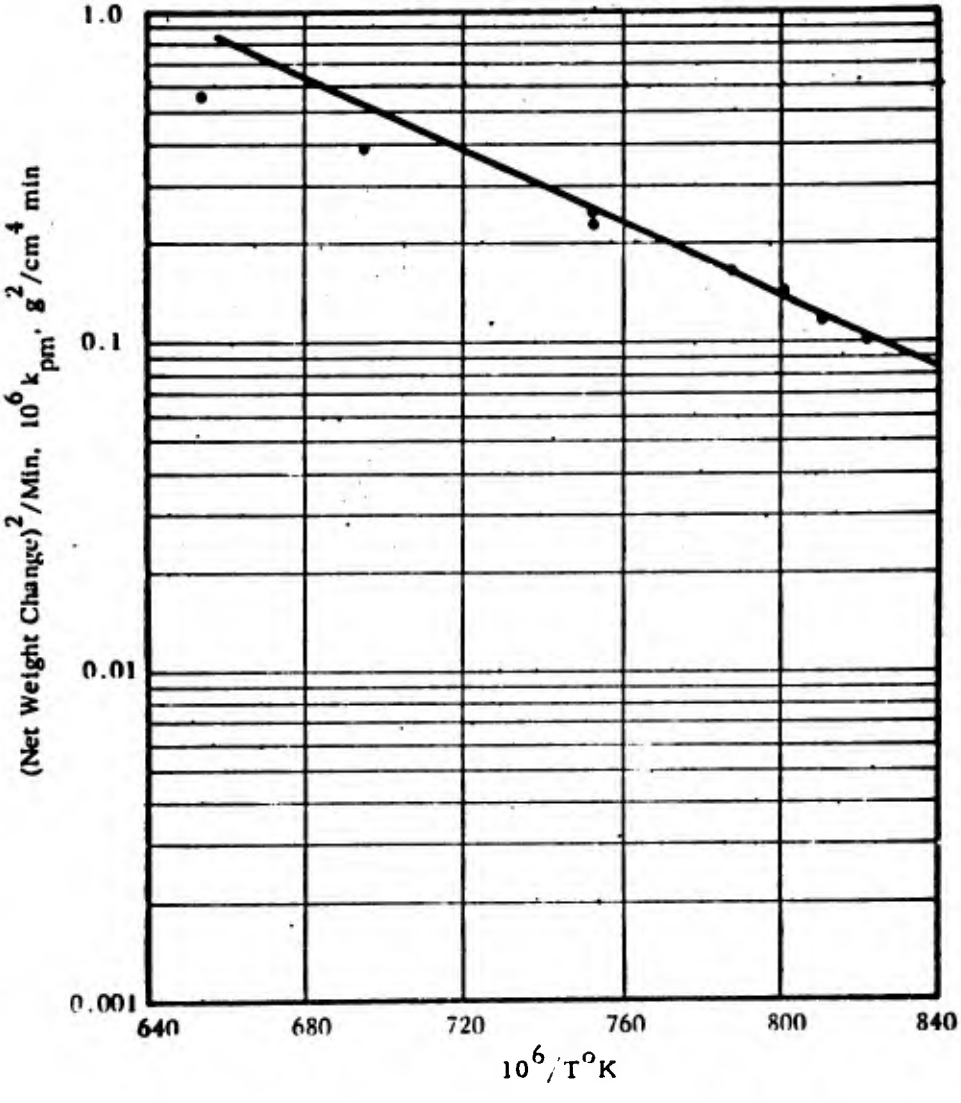

Fig. 69 - Arrhenius Plot for ZrB_2 (Net Weight Change) 2/min. vs. $1/T^oK$

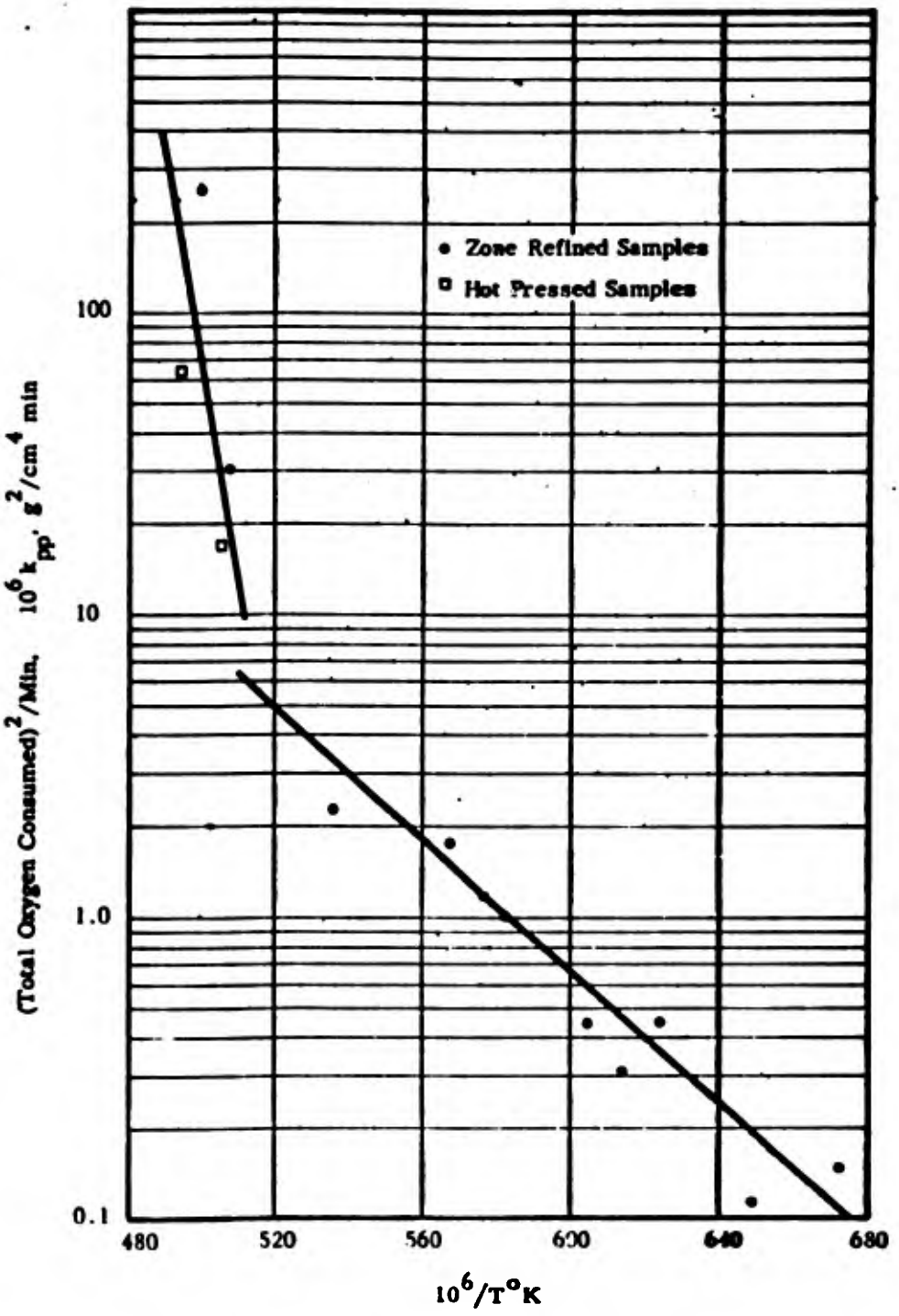

Fig. 70 - Arrhenius Plot for the Oxidation of HfB_2 (Total Oxygen Consumption) 2/min. vs. 1/°T.

Table 42

Oxidation of Man Labs HfB_2*

Pellet XVI-4

Initial weight after degassing	1.4820 g
Surface area	1.737 cm^2
Density	10.3 g/cm^3
Temperature	2024°K for 30 minutes; 1982°K for 20 minutes
Oxygen partial pressure	18.5 torr
Carrier gas flow rate	119 cm^3/min
Exposure time	120 min
Total oxygen consumed	0.1175 g
Parabolic rate constants, k_{pp}	6.4×10^{-5} g^2/cm^4-min at 2024°K 1.7×10^{-5} g^2/cm^4-min at 1982°K

*High pressure hot pressed, Run -1, pycnometric density 10.74 g/cm^3, 97.9% theoretical.

Prior to oxidation the pellet was degassed at 2150°K for one hour. The weight loss during this time was 0.0106 g, compared to 0.0004 g for zone melted material under comparable conditions. During the oxidation run, which was started at maximum r.f. power, the pellet temperature declined almost continuously. A plot of total oxygen consumption squared vs time is given in Fig. 71. Parabolic rate constants were calculated from the slopes of the lines shown, taken over periods for which the temperature remained constant within $\pm$ 5°K. Three points are plotted in between during a time when the temperature was changing rapidly. The results are included in the Arrhenius plot of Fig. 70, and are seen to be in good agreement with previous data.

4. Niobium Diboride

Results on the oxidation of niobium diboride at temperatures of 1319-2061°K and oxygen pressures of 19.9 and 38.8 torr are summarized in

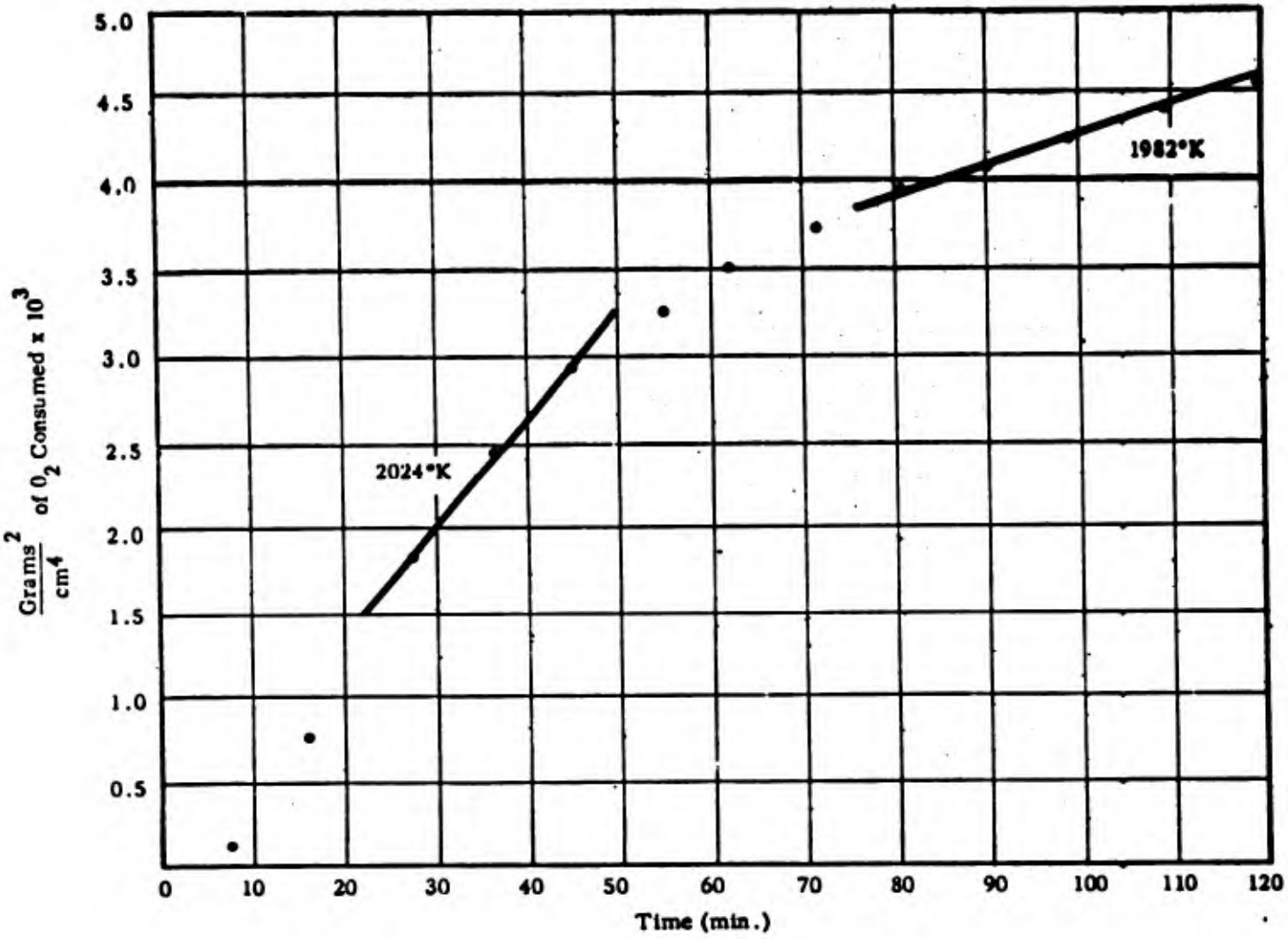

Fig. 71 - Oxidation of HfB_2, XVI-4, p_{O_2} = 18.5 Torr.

Table 43. For the runs made at higher temperature, oxidation was so extensive, and the product oxide showed so little adherence to the substrate that accurate net weight change could not be obtained.

Data for pellets XIII-35, XIII-38, XIV-37, and XIII-33 all run at an oxygen partial pressure of 19.9 torr are plotted in Fig. 72. For the first three samples, the rate of oxidation is initially high, diminishes with time for a brief period, then increases abruptly and remains linear. The final linear rates are given in column 12 of Table 43. The increase in temperature from 1320 to 1560°K results in about a ten-fold increase in oxidation rate after breakaway. For pellet XIII-33, the rate of oxygen consumption was inversely proportional to the square root of time after an induction period of 10 minutes. The parabolic rate constant was found to be 4.94×10^{-4} g^2/cm^4-min. It is conceivable, however, that the transition from protective to linear oxidation, "breakaway," would have occurred at a later time. Pellet XV-34 was run at a temperature of 2061°K in an attempt to determine whether the oxidation of NbB_2 actually becomes parabolic above 1700°K. Unfortunately, the rate of oxidation in this experiment was equal to the rate of arrival of oxygen and it was only possible to determine a minimum oxidation rate.

Data for pellet XIV-25 which was exposed at two different temperatures within a single run at an oxygen pressure of 38.8 torr are plotted in Fig. 73. At the lower temperature, 1559°K, an initial protection period is followed by a period of linear oxidation; when the temperature is raised to 1657°K, the linear rate increases by about a factor of ten. Since both linear rates are higher than those found for pellets XIII-38 and XIV-32 at comparable temperatures and a lower pressure, the oxidation of NbB_2 may be pressure dependent.

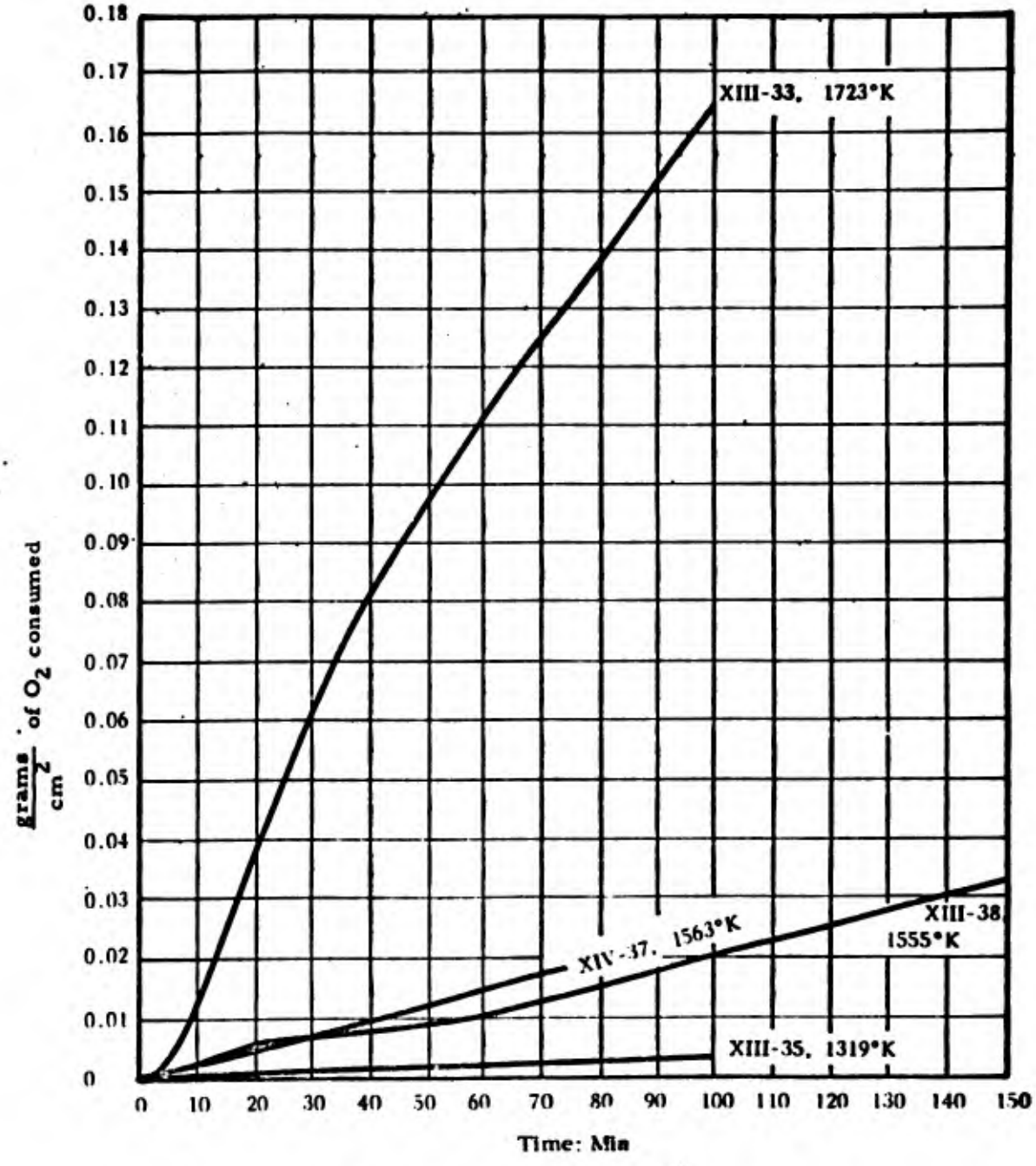

Fig. 72 - Oxidation of NbB_2, p_{O_2} = 19.9 Torr.

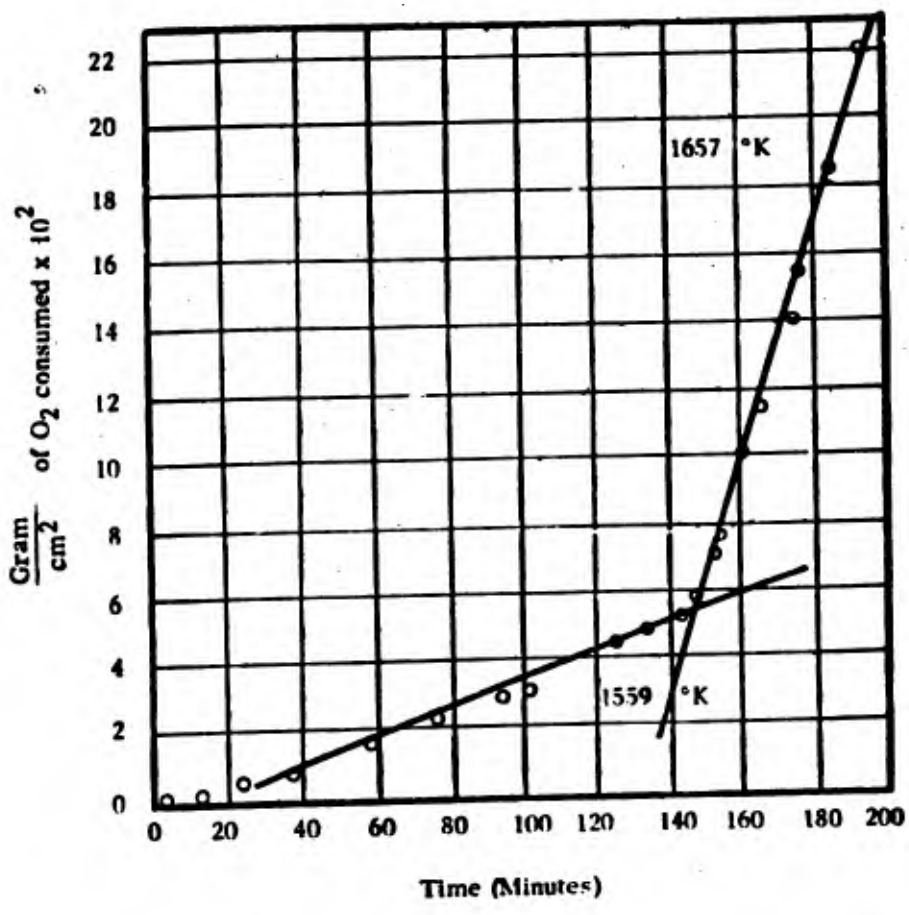

Fig. 73 - Oxidation of NbB_2, XIV-25, p_{O_2} = 38.8 Torr.

Table 43

Summary of Experimental Data on NbB_2

Pellet	Initial wt., g	A, cm^2	ρ, g/cc	T, °K	P_{O_2}, torr	Flow, cc/min	Exposure time, min	Net weight change, c/cm^2	Total oxygen consumed, g/cm^2	g/cm^2-min, final	g/cm^2-min	Oxides
XIII-35	0.4730	1.021	6.54	1319	19.9	95	100	0.0026	0.0039	3.35×10^{-5}		Nb_2O_5
XIII-38	0.4892	1.040	6.59	1555	19.9	95	149	0.0257	0.0342	2.59×10^{-4}		Nb_2O_5
XIV-37	0.4140	0.9056	6.56	1563	19.9	95	71	-	0.0148	2.54×10^{-4}		
XIV-32	0.6202	1.2320	6.70	1662	38.8	95	123	-	0.2694	-	1.66×10^{-3} 2.52×10^{-3}	NbO_2, Nb_2O_5
XIII-33	0.5247	1.061	6.49	1723	19.9	95	87	-	0.1568	Parabolic oxidation $k_p=4.9\times10^{-4}g^2/cm^4$-min.		NbO_2+unidentified lines
XIV-25	0.6282	1.2324	6.76	1559	38.8	95	135	-	0.0645	4.11×10^{-4}		
XIV-25	0.6282	1.2324	6.76	1657	38.8	95	150	-	0.2101	3.58×10^{-3}		
XV-34	0.6763	1.350	6.49	2061	39.1	95				$>4.73\times10^{-3}$		

*Characterized as $NbB_{1.96}$ in Section V.

Data for pellet XIV-32, run at 1662°K and an oxygen partial pressure of 38.8 torr are plotted in Fig. 74. The characteristic pattern is again in evidence - the rate diminishes with time for about 20 minutes, then increases linearly. In this case, however, a second break occurs after about 90 minutes, when the oxidation rate increases once more to a higher linear value. Both linear rates are given in column 13 of Table 43 and are lower, but of the same order of magnitude, as the final linear rate found for pellet XIV-25 at a slightly lower temperature, 1657°K and the same pressure, 38.8 torr.

The oxidation products identified by X-ray analysis of the pellets after reaction are listed in Table 43. The results are ambiguous, because all of the niobium oxides have many X-ray lines of low intensity over the entire angular range. Furthermore, the observed intensities, as is frequently the case, did not correspond to those given by ASTM for standard samples. The reason is that the surface oxide frequently grows in some epitaxial relationship to the substrate, and therefore often does not have precisely the same crystal structure as the bulk material.

Since the oxide was flaky and very poorly adherent to the alloy, it was not possible to prepare high quality metallographic specimens. The micrographs that were finally obtained showed two distinct layers in the oxide, a narrow dark layer adjacent to the substrate (NbO_2?) and a light structureless oxide (Nb_2O_5?).

The weight gains for pure niobium metal are approximately a factor of ten higher than the oxygen consumption results reported here for NbB_2 when runs have been made in a comparable temperature - pressure range

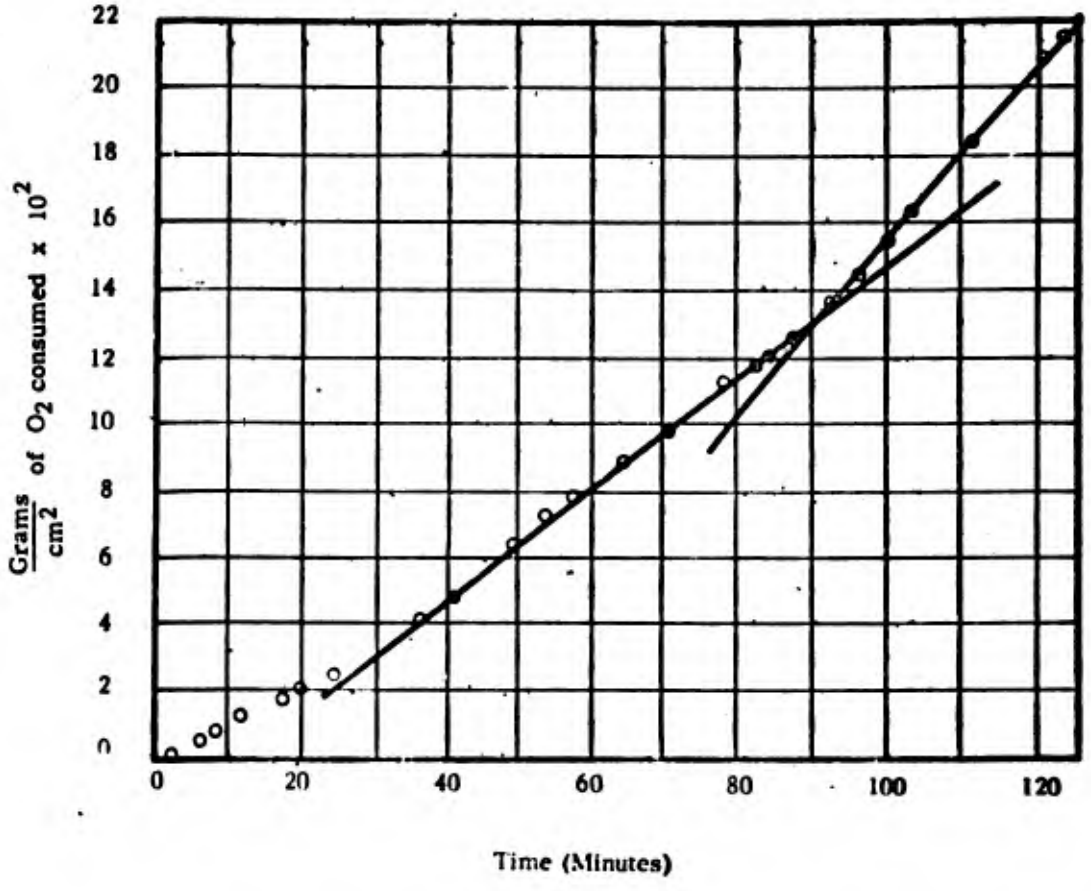

Fig. 74 - Oxidation of NbB_2, XIV-32, T = 1662°K, P_{O_2} = 38.8 Torr.

(1300-1500°K and 10-100 torr). Thus, on the basis of depth of corrosion in a given time, the diboride does have some advantage over the pure metal. However, the result may be due merely to the lowered niobium activity in the alloy. The general form of the oxidation vs time curves is quite similar for both metal and diboride. There is a tendency toward parabolic behavior at short times, and a distinct transition to linear behavior at later times. For both materials the data is poorly reproducible and the time to transition is variable. Parabolic behavior is roughly correlated with the formation of NbO_2, and the transition to a linear rate law may be associated with nucleation and growth of Nb_2O_5.

At 1273°K, Samsonov reports a net weight change in 100 min. of 0.0042 g/cm^2 for NbB_2, compared to a total oxygen consumption measurement of 0.0039 g/cm^2 at 1319°K in our experiments.

5. Tantalum Diboride

The experimental observations made on zone melted samples of TaB_2 are summarized in Table 44.

Table 44

Oxidation of TaB_2*

Pellet	Initial wt., g	A, cm^2	ρ, g/cm^3	T, °K	P_{O_2}, torr	Flow, cm^3/min	Exposure time, min	Total oxygen consumed, g/cm^2	k_{pp}, g^2/cm^4-min
XV-25	1.2692	1.489	10.7	1320	39.1	95	116	0.0024	5.0×10^{-8}
XV-20	1.3153	1.490	11.1	1545	39.1	95	120	-	6.4×10^{-7}
				1666	39.1	95	125	0.1329	2.9×10^{-5}

*Characterized as $TaB_{2.11}$ in Section V.

Oxidation results are plotted as g^2/cm^4 of oxygen consumed vs time in Fig. 75. After the first few minutes of oxidation the data can be fitted to a parabolic rate equation over the time periods studied. At the termination of both runs, X-ray analysis of the oxide film indicated the presence of α- and β-Ta_2O_5.

D. Comparison of the Oxidation Resistance of the Group IV-A and V-A Diborides

1. Interpretation of Oxygen Consumption Data

The experimental measure of extent of oxidation reported above is rate of total oxygen consumption as a function of time. With binary alloys at high temperatures such results must be interpreted with care. The total weight of oxygen consumed in an oxidation experiment is the sum of the amounts of oxygen in each of the reaction products. Unambiguous interpretation of the results thus requires knowledge of the reaction stoichiometry.

As a first approximation, it may be assumed that the oxidation of a diboride, MeB_2, will yield the oxides of the metal and boron, MeO_y and B_2O_3. Boron oxide is a liquid above 723°K, and has an appreciable vapor pressure, ranging from 2.3×10^{-6} atm at 1400°K to 5.4×10^{-2} atm at 2000°K.[13] In this section, the over-all oxidation reaction is considered in terms of two non-elementary steps.

$$MeB_2(c) + \frac{3+y}{2} O_2 \rightarrow MeO_y(c) + B_2O_3(\ell) \qquad (1)$$

$$B_2O_3(\ell) \rightarrow B_2O_3(g) \qquad (2)$$

It is thus assumed that the composition of the boride is not changed during oxidation. The total oxygen consumed, Δp up to some time t, may be written as

$$\Delta p = \frac{y[O]}{[MeO_y]} m_{MeO_y(c)} + \frac{3[O]}{[B_2O_3]} m_{B_2O_3(\ell)} \qquad (3)$$

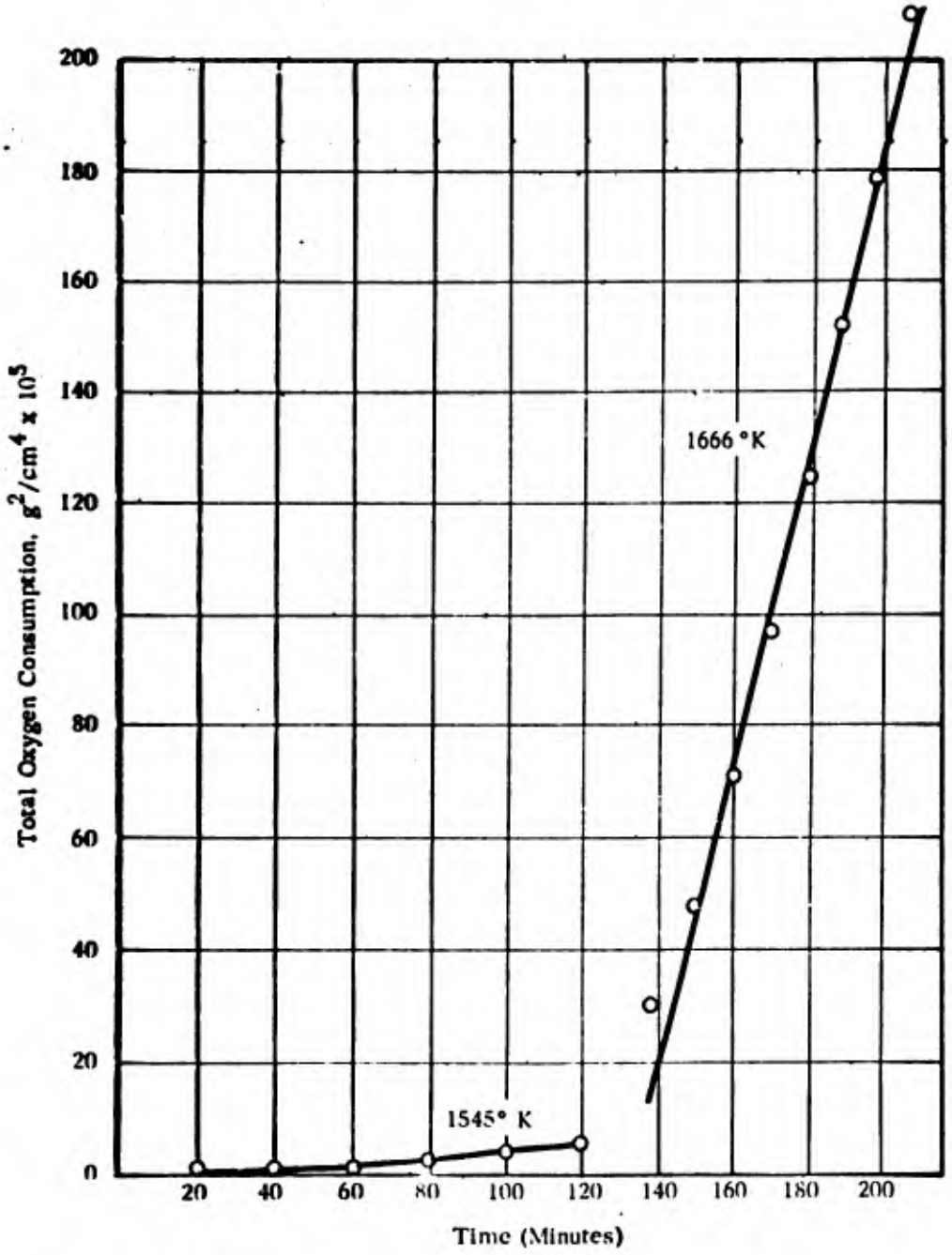

Fig. 75 - Oxidation of TaB_2, XV-20, p_{O_2} = 39.1 Torr.

where m_x is the number of grams of product X formed per unit boride surface area up to time t, and the symbols in brackets are molecular weights. Since the oxidation is supposed to be non-preferential, the number of moles of $MeO_y(c)$ formed must be equal to the number of moles of $B_2O_3(l)$ formed in the same time period; i.e.

$$\frac{m_{B_2O_3(l)}}{[B_2O_3]} = \frac{m_{MeO_y(c)}}{[MeO_y]} \tag{4}$$

Therefore:

$$\Delta p = \frac{(3+y)[O]}{[MeO_y]}\, m_{MeO_y(c)} = \frac{(3+y)[O]}{[B_2O_3]}\, m_{B_2O_3(l)} \tag{5}$$

(6)

and

$$\frac{d\Delta p}{dt} = \frac{(3+y)[O]}{[MeO_y]}\,\frac{dm_{MeO_y(c)}}{dt} = \frac{(3+y)[O]}{[B_2O_3]}\,\frac{dm_{B_2O_3(l)}}{dt}$$

For the oxidation of TiB_2, ZrB_2, HfB_2 and TaB_2 $(\Delta p)^2$ was found to increase linearly with t, as reported above; i.e.

$$(\Delta p)^2 = k_{pp}t \tag{7}$$

or

$$\frac{d\Delta p}{dt} = \frac{\sqrt{k_{pp}}}{2\sqrt{t}} \tag{8}$$

For NbB_2 after break-away, Δp varies linearly with time

$$\frac{d\Delta p}{dt} = k_l \tag{9}$$

Where the microstructure of the oxide formed on diborides had been investigated, workers have found either a dispersion of metal oxide in a B_2O_3 matrix or a two layer structure with MeO_y adjacent to the boride surface

and B_2O_3 covering the metal oxide, or simply a layer of MeO_y without a trace of B_2O_3. It is thus reasonable to assume that the rate of vaporization of B_2O_3 is constant, independent of time, as long as any $B_2O_3(\ell)$ is present. Since all of the above experimental work was done at a total pressure of one atmosphere, in a relatively slow moving stream, the rate of formation of $B_2O_3(g)$ is taken as 0.01 of the equilibrium rate of vaporization of B_2O_3, G, in vacuum[12].

$$\frac{dm_{B_2O_3(g)}}{dt} = 0.01G \qquad (10)$$

If the condensed oxides grow parabolically, then at any temperature, there will be some time t_o after which the rate of vaporization of $B_2O_3(g)$ will exactly balance the rate of formation of $B_2O_3(\ell)$. To find t_o, the two rates are equated:

$$\left.\frac{dm_{B_2O_3(g)}}{dt}\right|_{t=t_o} = \left.\frac{dm_{B_2O_3(\ell)}}{dt}\right|_{t=t_o} \qquad (11)$$

Substituting (6) into (8), and (8) and (10) into(11), one obtains the final expression for t_o:

$$t_o = [B_2O_3]^2 k_{pp}/(3+y)^2[O]^2(0.0016)G^2 \qquad (12)$$

For TiB_2, the lowest temperature run was made at 1551°K. At this temperature, B_2O_3 should vaporize as rapidly as it forms after the first 2 minutes' oxidation. Thus, to a good approximation, one may assume that the oxidation of TiB_2 under the conditions stuuied here yielded only TiO_2(rut.) and $B_2O_3(g)$.

For ZrB_2, vaporization of B_2O_3 is negligible below 1329°K over the time period of a typical experiment, while above 1439°K, essentially all of the B_2O_3 formed immediately evaporates.

For HfB_2, t_o = 5 minutes at the lowest temperature investigated, 1488°K. For all of the experiments therefore $HfO_2(c)$ should be the only condensed oxide on the boride surface.

For NbB_2, the rates of formation of both the condensed oxides and the volatile oxide are independent of time. At the lowest experimental temperature, 1319°k, $k_\ell = 3.35 \times 10^{-5}$ g/cm^2, after break-away and $G = 1.8 \times 10^{-4}$ g/cm^2-min. Therefore, assuming the condensed oxide to be $Nb_2O_5(c)$:

$$\frac{dm_{B_2O_3(\ell)}}{dt} = \frac{[B_2O_3]}{(5.5)[O]}\, k_\ell = 2.6 \times 10^{-5} \text{ g/cm}^2\text{-min} \qquad (13)$$

and

$$\frac{dm_{B_2O_3(g)}}{dt} = 1.8 \times 10^{-6} \text{ g/cm}^2\text{-min} \qquad (14)$$

At 1319°K, some $B_2O_3(\ell)$ might be present on the boride surface. At 1555°K B_2O_3 will vaporize as fast as it is formed.

For TaB_2 at 1320°K, the lowest experimental temperature, t_o = 2400 min. Therefore, essentially all of the B_2O_3 formed remains condensed on the surface. At 1545°K, the next experimental temperature, t_o = 1 min, and therefore B_2O_3 vaporizes as rapidly as it forms.

Table 45 summarizes the probable products formed in the experiments described in Section C above.

Table 45

Summary of Probable Products in the Oxidation Experiments

Alloy	Temperature	Products
TiB_2	$\geq$ 1551°K	TiO_2(rut); B_2O_3(g)
ZrB_2	$\leq$ 1329°K	ZrO_2(c); B_2O_3(c)
	$\geq$ 1439°K	ZrO_2(c); B_2O_3(g)
HfB_2	$\geq$ 1488°K	HfO_2(c); B_2O_3(g)
NbB_2	$\leq$ 1319°K	Nb_2O_5(c); B_2O_3(ℓ); B_2O_3(g)
	$\geq$ 1555°K	Nb_2O_5(c); B_2O_3(g)
TaB_2	$\leq$ 1320°K	Ta_2O_5(c); B_2O_3(ℓ)
	$\geq$ 1545°K	Ta_2O_5(c); B_2O_3(g)

2. Thermodynamics of Oxidation

Following Webb, Norton, and Wagner,[14] it is interesting to consider whether the metal oxide MeO_y(c) is thermodynamically stable in contact with the boride $Me_{1-x}B_x$ with respect to decomposition to B_2O_3(g) and the metal. If the pressure of B_2O_3(g) calculated from the equilibrium:

$$MeO_y(c) + \frac{2y}{3} B(a_B^{\eta}) \rightarrow \frac{y}{3} B_2O_3(g) + Me(a_{Me}^{\eta}) \qquad (15)$$

exceeds one atmosphere at the alloy-oxide interface, then a potentially protective metal oxide film would be ruptured by evolution of B_2O_3(g). The equilibrium pressure of B_2O_3(g) can be calculated from the equation:

$$\ln p_{B_2O_3} = 2 \ln a_B^{\eta} - \frac{3}{y} \ln a_{Me}^{\eta} - \frac{\Delta F_{f, B_2O_3(g)}}{RT} + \frac{3}{y} \frac{\Delta F_{f, MeO_y(c)}}{RT} \qquad (16)$$

The activities of boron and metal, a_B^{η} and a_{Me}^{η}, in the boride $Me_{1-x}B_x$ were calculated from the formulas in Section XX. The free energies of formation of the oxides, $\Delta F_{f,B_2O_3(g)}$ and $\Delta F_{f,MeO_y(c)}$, were taken from the JANAF Tables[13] and from Kubaschewski and Evans' "Metallurgical Thermochemistry."[15]

For the stoichiometric diborides (x = 0.666), the equilibrium pressure of B_2O_3 at the boride/oxide interface exceeds an atmosphere at 2000°K for TiO_2 on TiB_2, NbO_2 on NbB_2, and Ta_2O_5 on TaB_2. At 1500°K, NbO_2(c) and Ta_2O_5(c) are still unstable in contact with the respective diboride. At 1000°K the equilibrium B_2O_3(g) pressure exceeds one atmosphere only for NbO_2 on NbB_2. For ZrO_2 on ZrB_2 and HfO_2 on HfB_2, the equilibrium B_2O_3 pressures at 2000°K are respectively 0.38 atm, and 0.015 atm. Thus, HfB_2 might be expected to show greater oxidation resistance than ZrB_2. However, ZrB_2 should be far superior to TiB_2, NbB_2, and TaB_2.

3. Comparison of the Oxidation Resistance of Diborides on an Alloy Consumption Basis

Oxidation is frequently monitored by net weight change or oxygen consumption measurements. For most practical purposes, however, the critical parameter is alloy consumption, the recession rate of the alloy or the depth of penetration of oxide. On the basis of the assumptions made in Section D.1. above, the parabolic rate constants k_{pp} given above on the basis of total oxygen consumption can be converted to constants k_{px} based on total alloy consumption. For TiB_2, ZrB_2, and HfB_2,

$$k_{px}/k_{pp} = [XB_2]^2/25[O]^2\rho^2_{XB_2} \qquad X = Ti, Zr, Hf \qquad (17)$$

where ρ_{XB_2} is the density of the diboride. For TaB_2,

$$k_{px}/k_{pp} = \frac{[TaB_2]^2 \ (4)}{(121)\,[O]^2 \rho^2_{TaB_2}} \qquad (18)$$

Values of k_{px}, (thickness of alloy consumed)^2/min, derived from the data in Tables 41, 43, and 44 and Figs. 68, 69, and 70 are plotted against reciprocal temperature in Fig. 76. Several interesting features can be noted. First, HfB_2 is by far the most oxidation resistant of the refractory diborides above 1400°K. However, around 1700°C, where the phase transition from monoclinic to tetragonal occurs in HfO_2, there is an abrupt increase in alloy consumption rate. Second, ZrB_2 is much less oxidation resistant above 1400°K than one would predict from the above thermodynamic considerations. Below 1400°K, there is a fundamental change in mechanism of oxidation of ZrB_2, due in part to the phase transition in $ZrO_2(c)$ and in part to the existence of $B_2O_3(\ell)$ in the low temperature range. It would appear that in both ZrB_2 and HfB_2 the monoclinic oxide imparts greater oxidation resistance than the tetragonal oxide. Data on TiB_2 and TaB_2 are insufficient to establish any definite conclusions, but these materials are better relative to ZrB_2 than one might have anticipated.

Since NbB_2 undergoes break-away oxidation, while the other materials are oxidized parabolically, direct comparison is not possible. In Table 46 the depth of penetration of oxide after one hour in an oxygen containing atmosphere is given for each of the diborides at a number of temperatures.

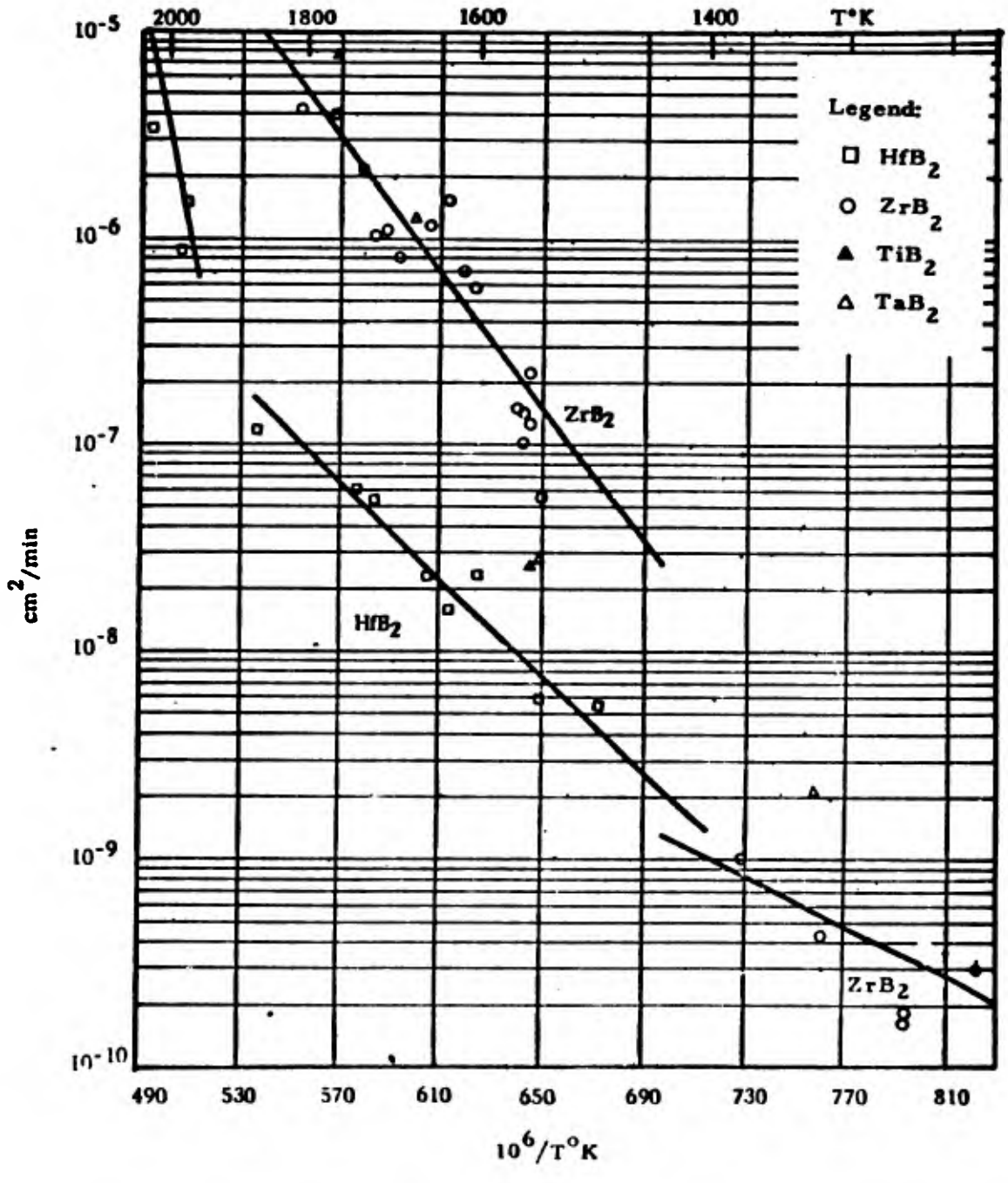

Fig. 76 - Depth of Oxide Penetration, cm^2/min. vs $1/T^{\circ}K$.

Table 46

Thickness of Alloy Consumed in the Oxidation of IV-A and V-A Diborides

Alloy	Temp., °K	Depth of penetration after one hour, cm α 10^4
HfB_2	1320	-
ZrB_2		1.8
TaB_2		3.6
NbB_2		3.9
HfB_2	1550	7.2
TiB_2		12.4
TaB_2		13.2
NbB_2		28.8
ZrB_2		31.8
HfB_2	1670	13.8
ZrB_2		80.5
TaB_2		88.0
TiB_2		-
NbB_2		413.0

Although the depth of penetration after one hour at 1550°K is less for NbB_2 than for ZrB_2, the rate curves are such that this order must be reversed at longer times.

E. Comparison of HfB_2 with other Oxidation Resistant Materials

From the foregoing discussion, the most promising of the refractory diborides from the point of view of oxidation resistance is HfB_2. It is therefore of interest to compare the oxidation behavior of HfB_2 with the behavior of other promising materials.

Carborundum Co. recently reported a ZrB_2-$MoSi_2$ formulation which is supposed to have good oxidation resistance up to 1950°C.[16] A sample of this material fabricated by conventional hot pressing techniques was supplied by R.T.D. A plot of total consumption vs. time for this material is shown in Fig. 77. Difficulty was experienced in maintaining temperature in this run, but over the last hour the temperature was constant at 1866 ± 10°K. The parabolic rate constant for this period was found to be 1.2×10^{-5} g^2/cm^4-min, compared to a value of 0.22×10^{-5} g^2/cm^4-min for HfB_2 at the same temperature. At this temperature, the commercial material has no advantage over HfB_2, although it is superior to pure ZrB_2. However, the important comparison must be made above the phase transition temperature for HfO_2.

Up to 1700°C, $MoSi_2$, which oxidizes logarithmically must eventually be superior to HfB_2 which oxidizes parabolically. Unfortunately, $MoSi_2$ oxidizes catastrophically above 1700°C. Over a period of two hours at 1917°K, the total oxygen consumption for $MoSi_2$ is 3.8×10^{-4} g/cm^2,[1] compared to 2.4×10^{-2} g/cm^2 for HfB_2.

F. Summary and Future Effort

The oxidation of TiB_2, ZrB_2, HfB_2, NbB_2, and TaB_2 has been studied in the temperature range 1300-2000°K at oxygen partial pressures of around 20 torr in helium. A parabolic rate law was observed for all of the materials except NbB_2. The latter showed the break-away behavior characteristic of pure niobium metal. The probable products of oxidation are listed in Table 45. The activation energy for oxidation of ZrB_2 is 77 ± 5 kcal/mole in the range 1540-1800°K and 25 ± 6 kcal/mole in the range 1200-1400°K. The activation energy for oxidation of HfB_2 is 46 ± 6 kcal/mole in the range 1480-1870°K. A large increase in the rate of oxidation of HfB_2 occurs at

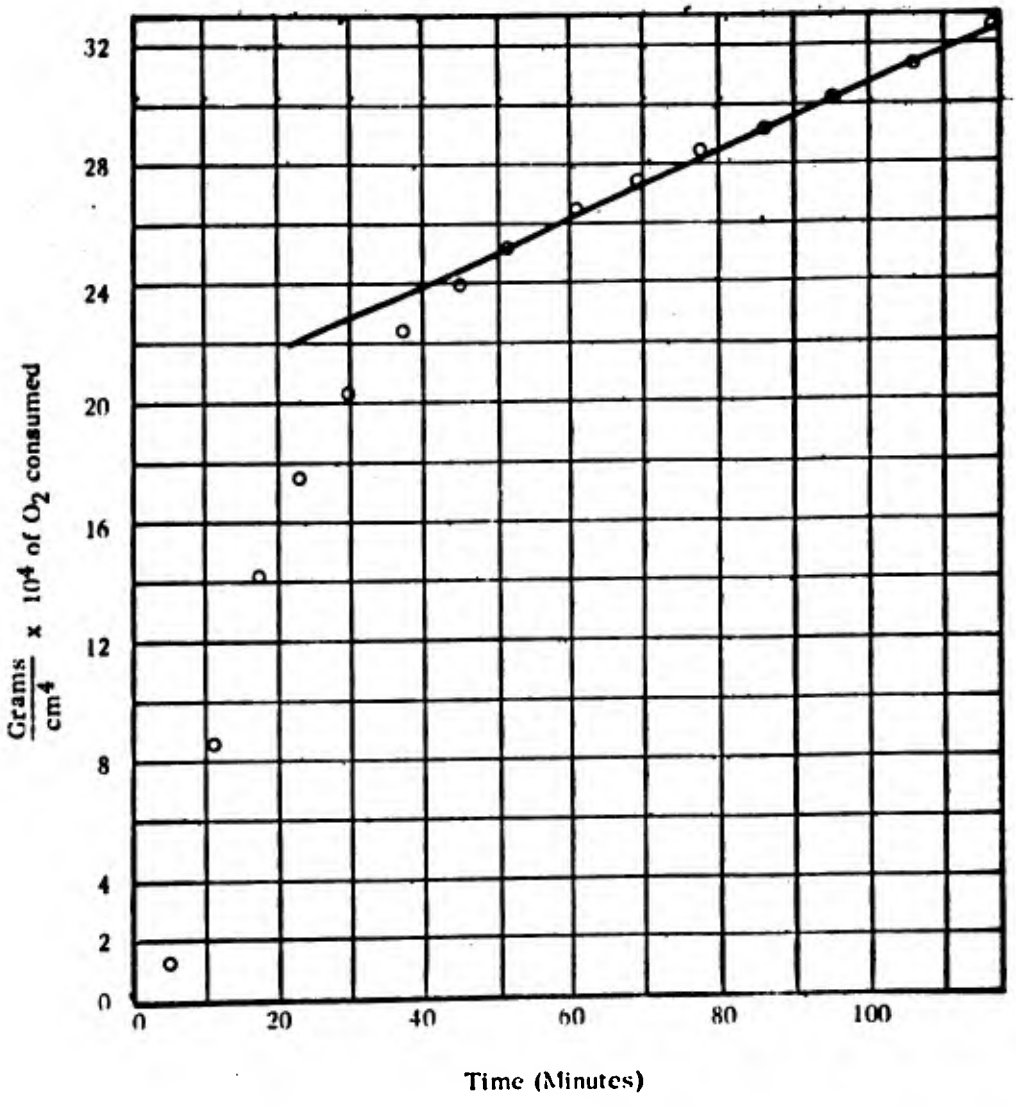

Fig. 77 - Total Oxygen Consumption vs Time for Carborundum ZrB_2-$MoSi_2$.

at 1970°K, the monoclinic→tetragonal transition temperature for HfO_2(c).

Although there is much to be learned about the oxidation of all of the refractory diborides, practical considerations suggest that future effort be concentrated on HfB_2. The first question is whether the Wagner mechanism describes the oxidation adequately. If it does, then a number of conclusions can be drawn which should be checked experimentally. These pertain to the oxygen pressure dependence of the oxidation rate, and to the effect of impurity metal atoms of valency greater than or less than 4 on the oxidation process.

The observation of F.H. Brown, Jr. that water vapor accelerates the oxidation of TiB_2 and ZrB_2 should be confirmed for HfB_2.

REFERENCES

1. Münster, A., and Schlamp, G., Zeit. Phys. Chem., (1960) 25 116.

2. Neshpor, V.S., and Samsonov, G.V., "Investigation of the Resistance to Oxidation of Alloys of Titanium and Niobium Borides," May, 1956.

3. Meyerson, G.A., Samsonov, G.V., Kotel'nikov, R.B., Voyonova, M.S., Yerterjera, I.P., and Krasnenkova, S.D., Akad. Nauk SSSR Zh. Neorganicheskoy Khimii; from Konferenskiya Po Khimii Bora I Yego Soyedineii, pp. 58-73.

4. Portnoi, K.I., Samsonov, G.V., and Frolova, K.I., Zhurnal Prikladnoi Khimii, (1960) 33 577.

5. Samsonov, G.V. and Golubeva, N.K., Zhur. Fiz. Khim, (1956) 30 1258.

6. Brown, F.H., Jr., Progress Report No. 20-252, Jet Propulsion Lab., Pasadena, California, Feb. 25, 1955.

7. Macdonald, N.F., and Ransley, C.E., Powder Metallurgy (London), (1959) No. 3 172.

8. Paderno, Ym. B., Serebryakova, T.I., and Samsonov, G.V., Tsvetnye Metally (1959) 11, pp 48-50, D.S.I. Trans. No. 614.

9. Samsonov, G.V. and Portnoi, K.I., "Alloys Based on High Melting Compounds," FTD-TT-62-430.

10. "Kinetics of Oxidation of Refractory Metals and Alloys at 1000-2000°C," ASD-TDR-62-203, Part II, Arthur D. Little, Inc., March, 1963.

11. "Thermodynamic and Kinetic Studies for a Refractory Materials Program," ASD-TDR-62-204, Part II, Arthur D. Little, Inc., May, 1963.

12. "Thermodynamic and Kinetic Studies for a Refractory Materials Program," Contract No. AF33(616)-7472, Semi-Annual Report No. 4, Arthur D. Little, Inc., June, 1963 (In Press).

13. JANAF Tables of Thermodynamic Data.

14. Webb, W.W., Norton, J.T., and Wagner, C, J. Electrochem. Soc., (1956) 103, 112.

15. Kubaschewski, O. and Evans, E. Ll., Metallurgical Thermochemistry, Pergamon Press, N.Y. (1958).

16. Shaffer, Peter T.B., Am. Ceramic Soc. Bull., (1962) 41 96.

XV. HEAT CAPACITY*

A. Introduction

A prime motivation for cryogenic thermal property measurements on boride systems is in the provision of definitive data for thermodynamic purposes. The heat capacity, besides being a sensitive and revealing parameter of the energetics of substances and one of the most powerful tools available for the study of condensed phases, provides the raw material for chemical thermodynamic functions useful in science and technology. Measurements of the heat capacity at constant pressure, C_p, of the various phases ($\alpha, \beta, \ldots, \gamma$) involved together with the enthalpy increments of such phase transitions, ΔH_i, occurring reversibly at temperatures, T_i, permits evaluation of the standard enthalpy increment of a substance by the equation:

$$(H_T^o - H_0^o) = \int_0^{T_1} C_p^{\alpha}\, dT + \Delta H^{\alpha \to \beta}[T_1] + \int_{T_1}^{T_2} C_p^{\beta}\, dT + \Delta H^{\beta \to \gamma}[T_2] + \ldots . + \int_{T_2}^{T} C_p^{\gamma}\, dT \qquad (1)$$

and the standard entropy by the related equation:

$$S_T^o = S_0^o + \int_0^{T_1} \frac{C_p^{\alpha}\, dT}{T} + \frac{\Delta H^{\alpha \to \beta}[T_1]}{T_1} + \int_{T_1}^{T_2} \frac{C_p^{\beta}\, dT}{T} + \frac{\Delta H^{\beta \to \gamma}[T_2]}{T_2} + \ldots + \int_{T_2}^{T} \frac{C_p^{\gamma}\, dT}{T} \qquad (2)$$

---

*Edgar F. Westrum, Jr., Department of Chemistry, University of Michigan.

These functions may be combined to yield the standard Gibbs energy function for the substance:

$$\left[\frac{G_T^\circ - H_0^\circ}{T}\right] = \left[\frac{H_T^\circ - H_0^\circ}{T}\right] - S_T^\circ \qquad (3)$$

Symbolizing a generalized chemical reaction as

$$\sum \nu_i S_i = 0 \qquad (4)$$

in which S_i indicates a mole of the ith substance involved and ν_i is the stoichiometric coefficient (positive for products and negative for reactants). The Gibbs energy increment of the reaction ΔG°, may be found by summation of the Gibbs energy functions and the enthalpies of formation, ΔH_f°, for the substances involved:

$$\Delta G_T^\circ = \sum \nu_i (G_T^\circ)_i = \sum \nu_i \left[\frac{G_T^\circ - H_0^\circ}{T}\right]_i - \sum \nu_i (\Delta H_f^\circ [0^\circ K])_i \qquad (5)$$

From ΔG_T° the equilibrium constant of the reaction, K, may be readily evaluated from the familiar relation:

$$\Delta G_T^\circ = -RT \ln K \qquad (6)$$

R here represents the gas constant in appropriate units.

Relatively few data exist on refractory borides because these materials are relatively difficult to prepare and to characterize well in thermodynamically defined states. The present studies on $NbB_{1.963}$, and $TaB_{2.11}$ owe much to the necessary preparative and analytical work done by Gerald Clay of Arthur D. Little, Inc.

B. Experimental

These low-temperature heat capacity determinations were made by high-precision quasi-adiabatic calorimetric techniques; the results were calculated with a high speed digital computer.

1. Cryostat and Technique of Measurement

Measurements were made in the Mark III adiabatic, vacuum cryostat schematically similar to one previously described[1], but modified and improved in several respects to give an instrument of greater compactness, mechanical rigidity, and operating convenience. The cryostat is, however, not provided with an "economizer". Constantan thermocouples monitor the difference in temperature between calorimeter and shield and between shield and ring. Three separate channels of recording electronic circuitry with proportional, rate, and reset control actions are used for shield control above 50°K. This instrumentation controls temperature to within about a millidegree over the temperature range and makes the uncertainty in the energy exchange negligible in comparison with other sources of error.

The calorimeter is surrounded by a cylindrical adiabatic shield. The top, bottom and cylindrical sections of this shield are individually controlled by separate channels of automatic regulation which provide a.c. power to the respective shield heaters. Copper-Constantan thermocouples monitor the temperature difference between calorimeter and shield and between shield and the ring used to temper the gradient in the bundle of leads. Three separate channels of recording electronic circuitry having proportional, rate, and reset control actions regulate temperature differences to within a millidegree over the range 50° to 350°K. Below 50°K manual control of the adiabatic shield is employed. Energy exchange between the calorimeter and the surroundings is so reduced that it is negligible compared with other sources of error. The adiabatic method of operation has been described[1].

2. Calorimeter

The copper calorimeter (laboratory designation W-35) with a capacity of 98 cc was specially constructed for measurement on the long rod-like,

zone-refined cylinders of the sample. It is gold plated on all exterior and interior surfaces. It is similar to one previously described[2] except that only two vanes are employed. The sample space has a diameter of 3.64 cm. and an internal length of 10.4 cm. The heat capacity of the empty calorimeter was determined in a separate series of measurements in which identical amounts of indium-tin (Cerroseal) solder for sealing the calorimeter and Apiezon-T grease for thermal contact with the heater-thermometer assembly were used. A small helium pressure was used to facilitate thermal equilibrium in the sample space.

Temperatures determined with a capsule-type, strain-free, platinum-resistance thermometer (laboratory designation A-3) contained within an entrant well in the calorimeter are considered to be in accord with the thermodynamic temperature scale within 0.03°K. Temperature increments may, of course, be determined with more precision than absolute temperatures and are probably correct to a few tenths of a millidegree after correction for quasi-adiabatic drift. A 150-ohm Constantan heater was bifilarly wound on a grooved cylindrical copper sleeve closely fitted to the resistance thermometer. Apiezon-T grease permitted the ready removal of this heater-thermometer from the calorimeter. All measurements of resistance, potential, temperature, time, and mass are referred to calibrations made by the National Bureau of Standards.

Relevant data concerning the determinations are presented in Table 47.

3. Preparation and Characterization of Sample Material

The procurement of high purity, well characterized sample material is of prime importance in the performance of thermochemical measurements. In the present investigation, the zone-refining subtask is the principal source of

Table 47

Experimental Data on Calorimetric Samples

Substance	Mass of Sample (g.)	Gram formula mass	Calorimeter (Cryostat)
$NbB_{1.963}$	182.3345	114.15	W-35, (III)
$TaB_{2.11}$	210.7972	203.78	W-35, (III)
TiB_2	202.8139	69.54	W-35, (III)

Substance	Percent of Heat Capacity from Empty Calorimeter					
	at 10	25	50	100	200	300°, K
$NbB_{1.963}$	80	70	65	35	30	25
$TaB_{2.11}$	65	68	50	49	40	35
TiB_2	55	80	75	44	23	17

sample material for heat capacity measurements. A current research program has provided heat capacity data for HfB_2[3] and ZrB_2[4]; these data were also obtained on zone-refined material.

The niobium diboride was supplied as zone-refined, single crystal, single phase material with a stoichiometry represented as $NbB_{1.963}$. The tantalum diboride was supplied as zone-refined, polycrystalline, single phase material with a stoichiometry represented as $TaB_{2.11}$. The titanium diboride was supplied as a high purity powder sample. Measurements were made directly on the powder material for this compound.

3.1 Niobium Diboride

The zone-refined product was obtained in the form of macrocrystalline rods about 6 to 8 mm. diameter, which were established to be single phase by metallographic examinations and X-ray diffractional examination of several representative samples. Chemical analysis for Nb and B gave the following results:

Sample No.	435-2	473-1	477-2	527-2	531-3
Wt. % Nb	81.51	82.01	81.41	80.93	80.51
Wt. % B	18.45	18.22	18.69	18.79	18.71
Total	99.96	100.23	100.10	99.72	99.22
B/Nb Ratio	1.945	1.909	1.973	1.995	1.997

This represents an average composition of $NbB_{1.963}$. Analyses for nonmetallic impurities indicate (in ppm): 142, C; 66, O; and 45, N. Quantitative spectrographic analyses show: 0.13% Ti, 0.001% Fe, and less than 0.001% Si by weight. Carbide, oxide, nitride, and metallic impurities are present in amounts too small to require correction of the heat capacity data.

3.2 Tantalum Diboride

The zone-refined rods were obtained in the form of polycrystalline rods about 6-8 mm. diameter. X-ray diffraction and metallographic examinations established this material as single phase tantalum diboride. Chemical analysis for Ta and B gave the following results:

Sample No.	576-5	659-3	679-2	675-3
Wt. % Ta	89.11	88.56	88.55	89.0
Wt. % B	10.92	11.56	11.48	10.9
Total	100.03	100.12	100.03	99.9
B/Ta Ratio	2.04	2.18	2.16	2.05

This represents an average composition of $TaB_{2.11}$. Averaged analyses for nonmetallic impurities indicate (in ppm): 200, C; 22, N; and 29, O. Quantitative spectrographic analyses show: Ti, Si, and Cr in the range 0.001 to 0.01 % by weight. The complete description of the preparation and the detailed results of analyses are presented in Section V. These analyses show that the impurity level is too low to require any corrections for the measured heat capacity.

3.3 Titanium Diboride

The sample material was 'as received' high purity titanium diboride powder from Millmaster Chemical Company (Shipment No. 2). The zone-refining procedure could not be successfully applied to this compound. The experimental difficulties are presented in detail in Section V. The averaged chemical analyses show (weight %): Ti, 68.85; B, 30.48; C, 0.12; N, 0.10; O, 0.11; and Fe, 0.06. The total Ti and B is 99.33; the total of the analyzed elements is 99.72. Spectrographic analyses indicate the following impurity levels (weight percent): Cr and Co, 0.1; Si and Ni, 0.01; Mg, Al, and Mo, 0.01-0.001; and all other elements 0.001 or not detected. The detailed results of these analyses and a discussion of alternate available powder samples of titanium diboride are presented

in Section III. The heat capacity data were calculated for a stoichiometry represented as TiB_2; the averaged analytical results show a stoichiometry represented as $TiB_{1.96}$. No corrections were made for impurity contributions to the measured heat capacity.

C. Results

1. Heat Capacity and Thermal Data

The experimental heat capacities are presented in chronological order at the mean temperatures of the determinations in Tables 48, 49, and 50. These data are presented in terms of the defined thermochemical calorie equal to 4.1840 abs. joules, and an ice point of 273.15°K. These data have been corrected for curvature--i.e., for the difference between the measured $\Delta H/\Delta T$ and the limit of $(\Delta H/\Delta T)$ as ΔT approaches 0. The approximate values of ΔT used in the heat capacity determinations can usually be estimated from the increments between adjacent mean temperatures shown in Tables 48, 49 and 50. These heat capacity values are considered to have a probable error decreasing from less than 5% at 5°K, to 1% at 10°K, and to less than 0.1% above 50°K, but are further subject to the purity of the sample as noted earlier.

1.1 Niobium Diboride

The thermal data on this composition are presented in Table 48 and Fig. 78.

1.2 Tantalum Diboride

The thermal data are presented in Table 49 and Fig. 78.

1.3 Titanium Diboride

The thermal data are presented in Table 50 and Fig. 78.

1.4 Zirconium Diboride

The heat capacity data are presented in Fig. 78. These results were taken from a current investigation[3].

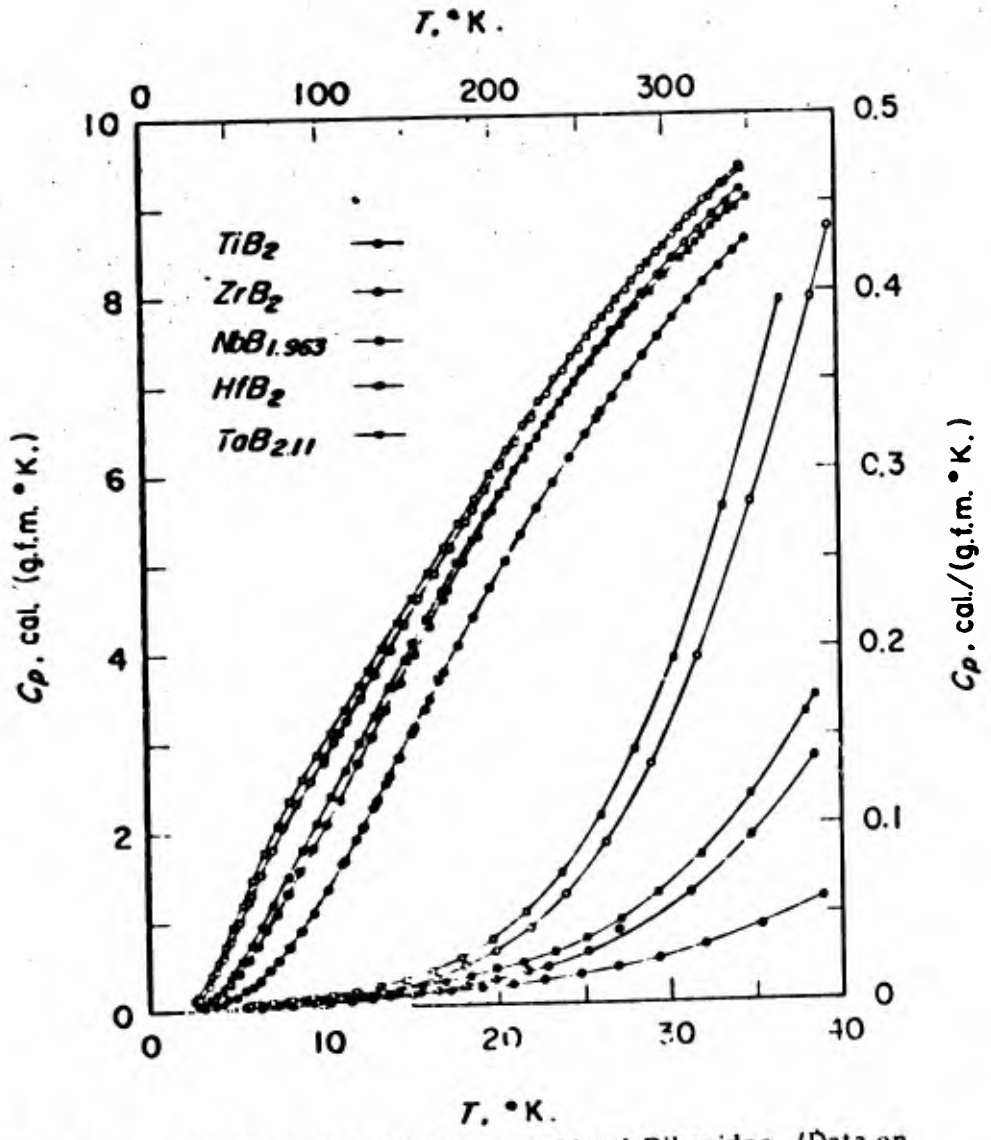

Fig. 78 - Heat Capacity of Refractory Metal Diborides. (Data on HfB_2 and ZrB_2 obtained under subcontract with Arthur D. Little[3].

1.5 Hafnium Diboride

The heat capacity data are presented in Fig. 78. These results were taken from a current investigation[3].

2. Thermodynamic Functions

Heat capacities and thermodynamic functions at selected temperatures, as presented in Tables 51-55 are obtained from the heat capacity data by a least squares-fitted curve through the experimental points (carefully compared with a large scale plot of the data) and the integration thereof. Both the fitting and the quadrature are performed by highspeed digital computer programs[5]. The thermodynamic functions are considered to have a precision indicated by a probable error of less than 0.1% above 100°K. An additional digit beyond those significant is given in Tables 51 to 55 for internal consistency and to permit interpolation and differentiation. The entropies and Gibbs energies have not been adjusted for nuclear spin and isotopic mixing contributions and are hence practical values for use in chemical thermodynamic calculations.

2.1 Niobium Diboride

Thermodynamic functions are presented in Table 51.

2.2 Tantalum Diboride

Thermodynamic functions are given in Table 52.

2.3 Titanium Diboride

Thermodynamic functions are shown in Table 53.

2.4 Zirconium Diboride

Thermodynamic functions are shown in Table 54.

2.5 Hafnium Diboride

Thermodynamic functions are shown in Table 55.

Table 48

Heat Capacity of Niobium Diboride ($NbB_{1.963}$)

Av. Temp. (°K)	Heat Capacity (cal/g.f.m.*)	Av. Temp. (°K)	Heat Capacity (cal/g.f.m.)	Av. Temp. (°K)	Heat Capacity (cal/g.f.m.)
Series I		**Series III**		**Series III (cont'd)**	
7.74	0.0057	38.46	0.2408	203.03	8.058
8.94	0.0066	42.23	0.3411	211.65	8.423
		46.81	0.4923	220.48	8.781
Series II		49.22	0.5838	229.49	9.136
		53.94	0.7805	238.23	9.469
8.64	0.0061	59.15	1.0240	247.12	9.796
10.09	0.0082	64.98	1.3184	256.05	10.103
11.74	0.0097	71.67	1.661	265.06	10.406
12.96	0.0115	79.63	2.082	273.19	10.669
14.14	0.0132	87.98	2.530	282.10	10.949
15.46	0.0157	95.92	2.929	290.82	11.211
16.85	0.0193	104.09	3.339	299.72	11.467
18.28	0.0229	112.42	3.759	309.17	11.728
19.76	0.0284	120.72	4.177	318.83	11.981
21.39	0.0335	129.29	4.607	328.42	12.221
23.19	0.0420	138.05	5.042	337.71	12.436
25.05	0.0518	147.04	5.481	346.05	12.635
27.04	0.0666	151.78	5.715		
29.25	0.0868	160.23	6.121	**Series IV**	
31.85	0.1176	169.10	6.540		
34.75	0.1637	178.07	6.954	313.40	11.832
37.92	0.2282	186.83	7.346	322.59	12.069
		195.44	7.727	331.91	12.307
				341.21	12.515
				347.74	12.652

---

*The gram formula mass of $NbB_{1.963}$ is 114.13. Conversion of the heat capacity to units of cal/gram atom is made by dividing the tabulated quantity by 2.963.

Table 49

Heat Capacity of Tantalum Diboride ($TaB_{2.11}$)

Av. Temp. (°K)	Heat Capacity (cal/g.f.m.*)	Av. Temp. (°K)	Heat Capacity (cal/g.f.m.)	Av. Temp. (°K)	Heat Capacity (cal/g.f.m.)
Series I		Series I (cont'd)		Series II (cont'd)	
126.62	5.306	299.73	11.924	23.67	0.1040
134.73	5.660	309.07	12.185	25.91	0.1478
143.67	6.050	318.35	12.431	27.97	0.2006
152.53	6.435	327.49	12.673	30.24	0.2713
161.50	6.826	336.58	12.898	33.24	0.3894
170.52	7.207	345.64	13.104	36.68	0.5525
179.67	7.590			40.35	0.7535
188.71	7.972	Series II		44.54	1.0095
197.77	8.348			49.26	1.3171
207.30	8.736	6.10	0.0038	54.43	1.658
216.98	9.125	7.01	0.0051	60.47	2.057
226.38	9.491	8.06	0.0063	67.25	2.480
235.74	9.842	9.15	0.0081	74.37	2.881
245.06	10.191	10.31	0.0100	81.55	3.276
254.17	10.497	11.67	0.0126	88.20	3.619
263.08	10.792	13.10	0.0164	96.16	3.983
271.94	11.084	14.54	0.0212	104.24	4.332
281.07	11.371	16.08	0.0276	112.58	4.696
290.40	11.656	17.80	0.0374	120.96	5.063
		19.65	0.0519		
		21.60	0.0730		

---

*The gram formula mass of $TaB_{2.11}$ is 203.76. Conversion of the heat capacity to units of cal/gram atom is made by dividing the tabulated quantity by 3.11.

Table 50

Heat Capacity of Titanium Diboride

Av. Temp. (°K)	Heat Capacity (cal/g.f.m.*)	Av. Temp. (°K)	Heat Capacity (cal/g.f.m.)	Av. Temp. (°K)	Heat Capacity (cal/g.f.m.)
Series I		17.17	0.0119	128.42	3.164
		18.96	0.0137	135.88	3.547
138.02	3.654	20.76	0.0161	143.78	3.951
143.63	3.947	22.60	0.0194	152.39	4.388
150.87	4.315	24.68	0.0235	161.33	4.841
158.58	4.703	26.88	0.0291	169.96	5.275
166.94	5.126	29.26	0.0358	178.39	5.690
		32.02	0.0456	187.32	6.122
Series II		35.27	0.0606	196.74	6.571
		38.83	0.0813	206.02	6.997
111.37	2.324	42.32	0.1078	215.15	7.414
118.25	2.661	45.95	0.1440	224.41	7.819
122.47	2.870	50.37	0.1998	233.90	8.218
130.28	3.263	55.50	0.2841	243.40	8.610
137.86	3.650	60.74	0.3944	252.62	8.977
				261.69	9.315
Series III		Series IV		259.06	9.215
				268.23	9.555
5.79	0.0016	59.74	0.3722	277.24	9.880
6.44	0.0021	63.37	0.4592	286.27	10.192
7.10	0.0026	69.02	0.6119	295.40	10.493
7.93	0.0036	74.23	0.7713	304.48	10.785
8.78	0.0054	80.02	0.9764	313.54	11.061
9.75	0.0074	86.75	1.2411	322.91	11.334
10.83	0.0083	93.87	1.533	332.18	11.586
12.12	0.0091	101.92	1.884	340.53	11.823
13.68	0.0100	110.68	2.294	347.25	12.002
15.40	0.0108	121.48	2.819		

---

*The gram formula mass of TiB_2 is 69.52. Conversion of the heat capacity to units of cal/gram atom is made by dividing the tabulated quantity by 3.00.

Table 51

Thermodynamic Properties of Niobium Diboride ($NbB_{1.963}$)

Temp. (°K)	C_p (cal/°K, g.f.m.*)	S° (cal/°K, g.f.m.)	$H^\circ - H^\circ_0$ (cal/g.f.m.)	$-(G^\circ - H^\circ_0)/T$ (cal/°K, g.f.m.)
5	0.0044	0.0011	0.004	0.0003
10	0.0024	0.0055	0.036	0.0019
15	0.0152	0.0098	0.090	0.0037
20	0.0283	0.0158	0.197	0.0060
25	0.0516	0.0243	0.390	0.0087
30	0.0950	0.0372	0.746	0.0123
35	0.1681	0.0569	1.390	0.0172
40	0.2788	0.0861	2.491	0.0239
45	0.4292	0.1273	4.244	0.0330
50	0.6145	0.1818	6.841	0.0450
60	1.066	0.3323	15.16	0.0796
70	1.578	0.5347	28.36	0.1296
80	2.104	0.7798	46.77	0.1951
90	2.624	1.0578	70.42	0.2753
100	3.135	1.3607	99.22	0.3685
110	3.640	1.683	133.11	0.4732
120	4.143	2.022	172.03	0.5881
130	4.642	2.373	215.96	0.7118
140	5.137	2.735	264.85	0.8433
150	5.626	3.106	318.68	0.9818
160	6.108	3.484	377.35	1.1263
170	6.580	3.869	440.80	1.2763
180	7.042	4.258	508.91	1.4312
190	7.492	4.651	581.59	1.5903
200	7.929	5.047	658.70	1.7533
210	8.352	5.444	740.12	1.920
220	8.762	5.842	825.70	2.089
230	9.155	6.240	915.30	2.261
240	9.533	6.638	1008.8	2.435
250	9.894	7.034	1105.9	2.611

---

* The gram formula mass of $NbB_{1.963}$ is 114.13. Conversion of the thermodynamic quantities to units in gram atoms is made by dividing the tabulated quantity by 2.963.

Table 51 (Cont'd.)

Thermodynamic Properties of Niobium Diboride ($NbB_{1.963}$)

Temp. (°K)	C_p (cal/°K, g.f.m.*)	S^o (cal/°K, g.f.m.)	$H^o - H^o_0$ (cal/g.f.m.)	$-(G^o - H^o_0)/T$ (cal/°K, g.f.m.)
260	10.239	7.429	1206.6	2.788
270	10.569	7.822	1310.6	2.968
280	10.884	8.212	1417.9	3.148
290	11.186	8.597	1528.3	3.329
300	11.473	8.983	1641.6	3.511
310	11.748	9.364	1757.7	3.694
320	12.008	9.741	1876.5	3.877
330	12.256	10.113	1997.8	4.060
340	12.491	10.484	2121.6	4.244
350	12.719	10.849	2247.6	4.427
273.15	10.67	7.94	1344	3.024
298.15	11.42	8.91	1620	3.478

---

*The gram formula mass of $NbB_{1.963}$ is 114.13. Conversion of the thermodynamic quantities to units in gram atoms is made by dividing the tabulated quantity by 2.963.

Table 52

Thermodynamic Properties of Tantalum Diboride ($TaB_{2.11}$)

Temp. (°K)	C_P (cal/°K, g.f.m.*)	S° (cal/°K, g.f.m.)	$H^\circ - H^\circ_0$ (cal/g.f.m.)	$-(G^\circ - H^\circ_0)/T$ (cal/°K, g.f.m.)
5	0.0027	0.0009	0.003	0.0002
10	0.0096	0.0047	0.033	0.0014
15	0.0232	0.0108	0.110	0.0035
20	0.0550	0.0212	0.294	0.0065
25	0.1283	0.0403	0.730	0.0111
30	0.2641	0.0747	1.682	0.0186
35	0.4688	0.1299	3.487	0.0303
40	0.7332	0.2092	6.470	0.0474
45	1.0390	0.3129	10.887	0.0709
50	1.3660	0.4392	16.90	0.1013
60	2.026	0.7468	33.87	0.1823
70	2.642	1.1062	57.26	0.2882
80	3.195	1.4958	86.50	0.4145
90	3.692	1.9013	120.97	0.5571
100	4.152	2.3143	160.2	0.7121
110	4.591	2.7308	203.9	0.8767
120	5.023	3.1488	252.0	1.0486
130	5.454	3.5679	304.4	1.2263
140	5.887	3.9879	361.1	1.4085
150	6.322	4.409	422.2	1.594
160	6.756	4.831	487.5	1.784
170	7.187	5.253	557.3	1.975
180	7.613	5.676	631.3	2.169
190	8.032	6.099	709.5	2.365
200	8.443	6.522	791.9	2.562
210	8.846	6.943	878.3	2.761
220	9.240	7.364	968.8	2.960
230	9.623	7.783	1063.1	3.161
240	9.994	8.200	1161.2	3.362
250	10.352	8.616	1262.9	3.564

---

*The gram formula mass of $TaB_{2.11}$ is 203.76. Conversion of the thermodynamic quantities to units in gram atoms is made by dividing the tabulated quantity by 3.11.

Table 52 (Cont'd.)

Thermodynamic Properties of Tantalum Diboride ($TaB_{2.11}$)

Temp. (°K)	C_p (cal/°K, g.f.m.*)	S^o (cal/°K, g.f.m.)	$H^o - H^o_0$ (cal/g.f.m.)	$-(G^o - H^o_0)/T$ (cal/°K, g.f.m.)
260	10.696	9.029	1368.2	3.766
270	11.024	9.438	1476.8	3.969
280	11.339	9.845	1588.6	4.172
290	11.640	10.248	1703.5	4.374
300	11.929	10.648	1821.4	4.576
310	12.209	11.044	1942.1	4.779
320	12.478	11.435	2065.5	4.981
330	12.736	11.823	2191.6	5.182
340	12.977	12.207	2320.2	5.383
350	13.196	12.587	2451.1	5.584
273.15	11.12	9.57	1512	4.033
298.15	11.88	10.57	1799	4.539

---

*The gram formula mass of $TaB_{2.11}$ is 203.76. Conversion of the thermodynamic quantities to units in gram atoms is made by dividing the tabulated quantity by 3.11.

Table 53

Thermodynamic Functions of Titanium Diboride (TiB_2)

Temp. (°K)	C_p (cal/°K, g.f.m.*)	S° (cal/°K, g.f.m.)	$H^\circ - H^\circ_0$ (cal/g.f.m.)	$-(G^\circ - H^\circ_0)/T$ (cal/°K, g.f.m.)
5	0.0015	0.0004	0.002	0.0001
10	0.0039	0.0021	0.014	0.0007
15	0.0084	0.0044	0.044	0.0015
20	0.0151	0.0077	0.102	0.0026
25	0.0244	0.0120	0.199	0.0041
30	0.0380	0.0176	0.353	0.0058
35	0.0587	0.0249	0.591	0.0080
40	0.0896	0.0346	0.956	0.0107
45	0.1341	0.0476	1.509	0.0140
50	0.1954	0.0647	2.325	0.0182
60	0.3770	0.1152	5.119	0.0298
70	0.6408	0.1921	10.142	0.0472
80	0.9766	0.2988	18.18	0.0716
90	1.3668	0.4359	29.86	0.1042
100	1.798	0.6019	45.65	0.1455
110	2.260	0.7948	65.92	0.1955
120	2.746	1.0121	90.93	0.2544
130	3.248	1.2517	120.89	0.3217
140	3.757	1.511	155.9	0.3973
150	4.268	1.788	196.0	0.4807
160	4.776	2.079	241.3	0.5714
170	5.278	2.384	291.5	0.6690
180	5.770	2.700	346.8	0.7730
190	6.252	3.025	406.9	0.8829
200	6.722	3.357	471.8	0.9983
210	7.180	3.696	541.3	1.1187
220	7.623	4.041	615.3	1.2437
230	8.053	4.389	693.7	1.3728
240	8.469	4.741	776.4	1.506
250	8.869	5.094	863.1	1.642

---

*The gram formula mass of TiB_2 is 69.52. Conversion of the thermodynamic quantities to units in gram atoms is made by dividing the tabulated quantity by 3.00.

Table 53 (Cont'd)

Thermodynamic Functions of Titanium Diboride (TiB_2)

Temp. (°K)	C_p (cal/°K, g.f.m.*)	S° (cal/°K, g.f.m.)	$H^\circ - H^\circ_0$ (cal/g.f.m.)	$-(G^\circ - H^\circ_0)/T$ (cal/°K, g.f.m.)
260	9.254	5.450	953.7	1.782
270	9.624	5.806	1048.1	1.924
280	9.979	6.163	1146.1	2.069
290	10.318	6.519	1247.6	2.217
300	10.641	6.874	1352.4	2.366
310	10.950	7.228	1460.4	2.517
320	11.246	7.580	1571.4	2.670
330	11.531	7.931	1685.3	2.824
340	11.807	8.279	1802.0	2.979
350	12.079	8.625	1921.4	3.136
273.15	9.738	5.918	1079	1.970
298.15	10.583	6.808	1333	2.338

*The gram formula mass of TiB_2 is 69.52. Conversion of the thermodynamic quantities to units in gram atoms is made by dividing the tabulated quantity by 3.00.

Table 54

Thermodynamic Functions of Zirconium Diboride (ZrB_2)

Temp. (°K)	C_p (cal/°K, g.f.m.*)	S° (cal/°K, g.f.m.)	$H^\circ - H^\circ_0$ (cal/g.f.m.)	$-(G^\circ - H^\circ_0)/T$ (cal/°K, g.f.m.)
5	0.001	0.0003	0.001	0.0001
10	0.0037	0.0018	0.012	0.0005
15	0.0094	0.0042	0.043	0.0013
20	0.0206	0.0083	0.116	0.0025
25	0.0408	0.0148	0.264	0.0043
30	0.0762	0.0251	0.549	0.0068
35	0.1354	0.0409	1.066	0.0105
40	0.2250	0.0645	1.953	0.0157
45	0.3456	0.0977	3.368	0.0228
50	0.5026	0.1419	5.474	0.0324
60	0.8986	0.2672	12.404	0.0604
70	1.363	0.4100	23.67	0.1018
80	1.858	0.6541	39.76	0.1570
90	2.363	0.9021	60.87	0.2258
100	2.870	1.1773	87.03	0.3070
110	3.375	1.4745	118.26	0.3994
120	3.881	1.790	154.54	0.5021
130	4.390	2.121	195.9	0.6137
140	4.900	2.465	242.3	0.7336
150	5.410	2.820	293.9	0.8608
160	5.917	3.185	350.5	0.9946
170	6.416	3.559	412.2	1.1134
180	6.904	3.940	478.8	1.2787
190	7.7379	4.326	550.2	1.4298
200	7.840	4.716	626.3	1.584
210	8.286	5.109	707.0	1.743
220	8.717	5.505	792.9	1.905
230	9.134	5.902	881.3	2.070
240	9.534	6.299	974.6	2.238
250	9.919	6.696	1071.9	2.408
260	10.285	7.092	1172.9	2.581
270	10.635	7.487	1277.6	2.755
280	10.967	7.880	1385.6	2.931
290	11.285	8.270	1496.8	3.109
300	11.589	8.658	1611.2	3.287

*The gram formula mass of ZrB_2 is 112.86. Conversion of the thermodynamic quantities to units in gram atoms is made by dividing the tabulated quantity by 3.00.

Table 54 (Cont'd)

Thermodynamic Functions of Zirconium Diboride (ZrB_2)

Temp. (°K)	C_p (cal/°K, g.f.m.*)	S° (cal/°K, g.f.m.)	$H^\circ - H^\circ_0$ (cal/g.f.m.)	$-(G^\circ - H^\circ_0)/T$ (cal/°K, g.f.m.)
310	11.879	9.043	1728.6	3.467
320	12.155	9.424	1848.8	3.647
330	12.412	9.802	1971.6	3.828
340	12.648	10.176	2096.9	4.009
350	12.878	10.546	2224.6	4.190
273.15	10.74	7.611	1311.	2.811
298.15	11.53	8.586	1590.	3.254

---

*The gram formula mass of ZrB_2 is 112.86. Conversion of the thermodynamic quantities to units in gram atoms is made by dividing the tabulated quantity by 3.00.

Table 55

Thermodynamic Functions of Hafnium Diboride (HfB_2)

Temp. (°K)	C_p (cal/°K, g.f.m.*)	S° (cal/°K, g.f.m.)	$H^\circ - H^\circ_0$ (cal/g.f.m.)	$-(G^\circ - H^\circ_0)/T$ (cal/°K, g.f.m.)
5	0.0016	0.0006	0.002	0.0001
10	0.0055	0.0027	0.018	0.0008
15	0.0172	0.0068	0.071	0.0020
20	0.0440	0.0148	0.214	0.0041
25	0.1045	0.0303	0.567	0.0076
30	0.2196	0.0586	1.351	0.0136
35	0.3984	0.1051	2.870	0.0231
40	0.6348	0.1731	5.432	0.373
45	0.9148	0.2637	9.291	0.573
50	1.221	0.3758	14.623	0.0833
60	1.852	0.6541	29.98	0.1544
70	2.457	0.9856	51.56	0.2489
80	3.004	1.3500	78.92	0.3635
90	3.497	1.7327	111.46	0.4943
100	3.953	2.1250	148.73	0.6377
110	4.390	2.522	190.45	0.7909
120	4.823	2.923	236.52	0.9519
130	5.258	3.326	286.92	1.119
140	5.699	3.732	341.70	1.291
150	6.143	4.140	400.90	1.467
160	6.588	4.551	464.56	1.647
170	7.031	4.964	532.65	1.830
180	7.469	5.378	605.16	2.016
190	7.901	5.793	682.02	2.204
200	8.326	6.209	763.16	2.394
210	8.743	6.626	848.52	2.585
220	9.150	7.042	937.99	2.778
230	9.547	7.457	1031.5	2.973
240	9.932	7.872	1128.9	3.168
250	10.304	8.285	1230.1	3.365
260	10.661	8.696	1334.9	3.562
270	11.003	9.105	1443.2	3.760
280	11.331	9.511	1554.9	3.958
290	11.645	9.914	1669.8	4.156
300	11.948	10.314	1787.8	4.355

*The gram formula mass of HfB_2 is 200.11. Conversion of the thermodynamic quantities to units in gram atoms is made by dividing the tabulated quantity by 3.00.

Table 55 (Cont'd)

Thermodynamic Functions of Hafnium Diboride (HfB_2)

Temp. (°K)	C_p (cal/°K, g.f.m.*)	S° (cal/°K, g.f.m.)	$H^\circ - H^\circ_0$ (cal/g.f.m.)	$-(G^\circ - H^\circ_0)/T$ (cal/°K, g.f.m.)
310	12.238	10.711	1908.7	4.553
320	12.516	11.104	2032.5	4.752
330	12.779	11.493	2159.0	4.950
340	13.029	11.878	2288.1	5.148
350	13.275	12.259	2419.6	5.346
273.15	11.11	9.23	1478.	3.822
298.15	11.89	10.24	1766.	4.318

*The gram formula mass of HfB_2 is 200.11. Conversion of the thermodynamic quantities to units in gram atoms is made by dividing the tabulated quantity by 3.00.

REFERENCES

1. Westrum, E.F., Jr., Hatcher, J.B., Osborne, D.W., J. Chem. Phys., (1953) 21 419.
2. Osborne, D.W., Westrum, E.F., Jr., J. Chem. Phys., (1953) 21 1884.
3. McClaine, L.A., "Thermodynamic and Kinetic Studies for a Refractory Materials Program" Contract No. AF33(616)-7472 by Arthur D. Little, Inc.
4. Justice, B.H., U. S. At. Energy Comm. Rept. TID-6216, June 1960; Ph. D. Dissertation, University of Michigan, 1961.

XVI. CALCULATION OF Δ fef FOR DIBORIDES*

A. Introduction

In order to define the thermodynamic stability of the diborides at high temperatures, it is necessary to specify the free energy of the stoichiometric diboride (i.e., x = atomic fraction of boron = 2/3) as a function of temperature. Thus, $F^{\eta}[2/3, T]$, the free energy of the η (diboride) phase must be specified†. Definition of F^{η} (dropping the argument) in units of cal/g.at., where one g.at. contains Avogadro's number of atoms, is given by equation (1).

$$F^{\eta} = H^{\eta}[0^{\circ}K] + \int_{o}^{T} Cp^{\eta} dT - T \int_{o}^{T} T^{-1} Cp^{\eta} dT \quad \text{cal/g.at.} \qquad (1)$$

where $H^{\eta}[0^{\circ}K]$ is the enthalpy of the (stoichiometric) η phase at $0^{\circ}K$ and $Cp^{\eta} = Cp^{\eta}[T]$ is the specific heat of the η phase.

Similar expressions can be written for the free energies of pure boron, F^{o}_{B}, and the pure metal component of η, F^{o}_{Me}. In the cases of the pure components, solid phase transformations, and melting must be represented by additional free energy contributions.

The free energy of formation of the diboride, ΔF^{η}, is defined as

$$\Delta F^{\eta} = F^{\eta} - \frac{1}{3} F^{o}_{Me} - \frac{2}{3} F^{o}_{B} = \Delta H^{\eta}[0^{\circ}K] + \Delta E^{\eta}_{T}[T] \quad \text{cal/g.at.} \qquad (2)$$

where $\Delta H^{\eta}[0^{\circ}K]$ is the enthalpy of formation of the diboride at $0^{\circ}K$ and $\Delta E^{\eta}_{T}[T]$ is the temperature dependent part of the free energy of formation.

---

*L. Kaufman, ManLabs, Inc.

† Square brackets will be used exclusively to denote functional relations.

The latter term includes differences in specific heat between the η phase and the pure components (i.e., $C_p^{\eta} - 1/3\, C_{p_{Me}}^{o} - 2/3\, C_{p_B}^{o}$) in addition to free energy increments due to phase changes. The quantity $\Delta F_T^{\eta}[T]$ as defined as

$$\Delta F_T^{\eta}[T] = -T(\text{times})\, \Delta \text{fef cal/g.at.} \qquad (3)$$

when Δ fef is the difference between fef for a g.at. of η and the sum of 1/3 fef for metal and 2/3 fef for boron.

Since calculation of the individual fef's require a great deal of experimental data on specific heat, heats of melting and transformation etc., most of which is currently not available, a simple method for predicting and estimating such data is required. The method used for this purpose[1-3] is detailed in the following sections.

B. Boron

Boron exists in several crystallographic forms[4], the α rhombohedral form being stable below 1100°C and the β rhombohedral form stable above 1500°C. The exact temperature of the α-β transition has not been clearly fixed nor has the identity of other possible polymorphs of pure boron been established. The range of uncertainity in transition temperature, and other possible polymorphs, indicates that the free energy and entropy differences between the polymorphs of boron are small.

In line with the methods used earlier[1-3] for describing the specific heat of metals, alloys, and compounds, the specific heat of boron is approximated as follows

$$Cp = Cv\left[\frac{\theta}{T}\right](1 + 10^{-4}T) + \gamma T \text{ cal/g.at.}^{\circ}K \qquad (4)$$

where θ is the Debye temperature, $C_v[\frac{\theta}{T}]$ is the Debye specific heat function[5, 6], γ is the electronic specific heat coefficient, and $10^{-4} T C_v[\frac{\theta}{T}]$ is an approximation to the C_p-C_v correction[1-3]. Assuming $\theta_B \simeq 1270^\circ K$ and $\gamma \simeq 0$ the specific heat and entropy of boron can be computed as shown in Fig. 79. Comparison of the calculations with measurements[7,8] of Cp vs T shown in Fig. 79 yield excellent agreement. Thus, these parameters which are tabulated in Table 56 can be used to represent the specific heat of solid boron. It should be noted, that the experimental data (as well as the calculation) do not show discontinuities corresponding to phase transformations.

The melting point of boron, T_B, is generally taken to be $2300^\circ K$. With an estimated entropy of melting of 2.3 cal/g.at.$^\circ K$, the difference in free energy between solid and liquid boron is estimated as

$$\Delta F_B^{\beta \to L} = 2.3(2300^\circ K - T) \text{ cal/g.at.} \qquad (5)$$

C. Titanium

The thermodynamic properties of titanium can be described as follows[1]: $0^\alpha = 365^\circ K$, $\gamma^\alpha = 8.25 \times 10^{-4}$ cal/g.at.$^\circ K^2$. This electronic specific heat coefficient appears appropriate for low and high temperature calculations. Above $1155^\circ K$ the α, h.c.p., form transforms to a b.c.c., β, form. The difference in free energies between these forms has been tabulated[1] and can be represented for the present purposes by Eq. 6,

$$\Delta F_{Ti}^{\alpha \to \beta} = 0.91(1155^\circ K - T) \text{ cal/g.at.} \qquad (6)$$

B.C.C. titanium melts at $1941^\circ K = T_{Ti}$, and $\Delta E_{Ti}^{\beta \to L}$ is estimated as

$$\Delta F_{Ti}^{\beta \to L} = 2.1(1941^\circ K - T) \text{ cal/g.at.} \qquad (7)$$

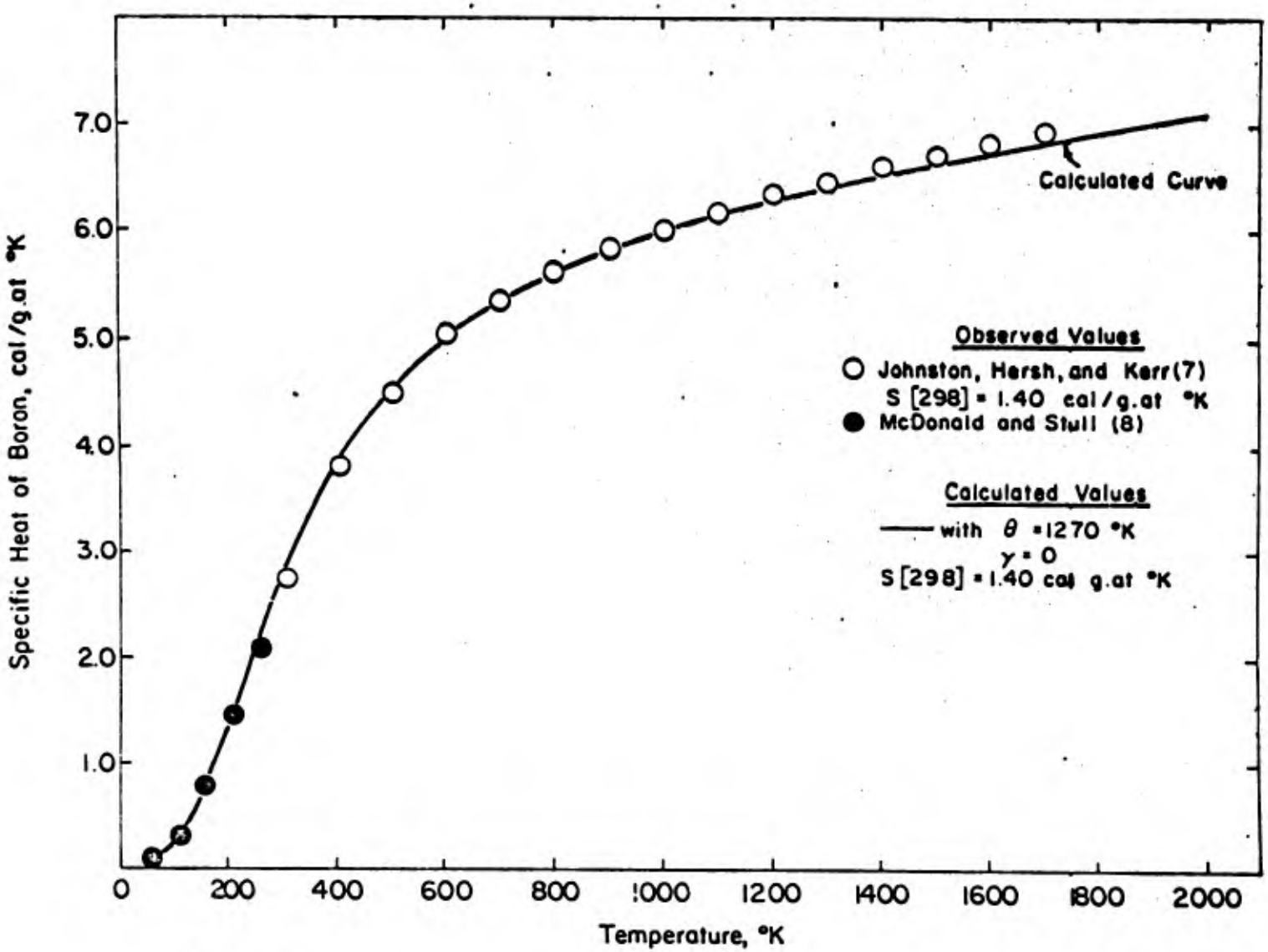

Fig. 79 - Comparison of Calculated and Observed Specific Heat of Boron.

Table 56

Thermodynamic Properties of the Pure Elements Required for ΔF_T^η Calculations

Element	θ	γ	$T_o^{\alpha\rightarrow\beta}$	$\Delta S^{\alpha\rightarrow\beta}$	T	ΔS (fusion)
	^oK	cal/g.at.$^oK^2$	^oK	cal/g.at.^oK	^oK	cal/g.at.^oK
B	1270	0	——	——	2300	2.3
Ti	365	8.25×10^{-4}	1155	0.91	1941	2.1
Zr	260	7.1×10^{-4}	1143	0.91	2125	2.1
Hf	200	6.3×10^{-4}	2033	0.9	2495	2.1
Nb	235	6.0×10^{-4}	——	——	2770	2.3
Ta	230	6.0×10^{-4}	——	——	3270	2.3

Non-Vibration, Temperature-Dependent Free Energy Terms for the Pure Elements ϕ_T^o (kcal/g.at.)

T^oK	B	Ti	Zr	Hf	Nb	Ta
1400	0.0	-1.0	-1.0	-0.6	-0.6	-0.6
1600	0.0	-1.5	-1.4	-0.8	-0.8	-0.8
1800	0.0	-1.9	-1.7	-1.0	-1.0	-1.0
2000	0.0	-2.5	-2.1	-1.3	-1.2	-1.2
2200	0.0	-3.4	-2.7	-1.7	-1.5	-1.5
2400	-0.2	-4.4	-3.6	-2.1	-1.7	-1.7
2600	-0.7	-5.4	-4.5	-2.8	-2.0	-2.0
2800	-1.2	-6.5	-5.4	-3.7	-2.4	-2.4
3000	-1.5	-7.5	-6.4	-4.7	-3.2	-2.7
3200	-2.0	-8.5	-7.4	-5.7	-4.0	-3.1

D. Zirconium

The Debye temperature of hcp zirconium[1] is 260°K with $\gamma^{\alpha} = 7.1 \times 10^{-4}$ cal/g.at.°K^2. This electronic specific heat coefficient appears appropriate for low and high temperature calculations. Zirconium undergoes an $\alpha \rightarrow \beta$ transition at $T_o^{\alpha \rightarrow \beta} = 1143$°K for which $\Delta F_{Zr}^{\alpha \rightarrow \beta}$ has been tabulated[1]. For present purposes this difference can be approximated by

$$\Delta F_{Zr}^{\alpha \rightarrow \beta} = 0.91(1143^{\circ}K - T) \text{ cal/g.at.} \qquad (8)$$

$\overline{T} = 2125$°K for Zr and $\Delta F_{Zr}^{\beta \rightarrow L}$ is estimated as

$$\Delta F_{Zr}^{\beta \rightarrow L} = 2.1\ (2125^{\circ}K - T) \text{ cal/g.at.} \qquad (9)$$

E. Hafnium

Specific heat measurements on h.c.p., α, hafnium (5°K-350°K) have been performed by Walcott[9] who found $\theta_{Hf}^{\alpha} = 200$°K and $\gamma^{\alpha} = 6.3 \times 10^{-4}$ cal/g.at.°K^2 the latter value is consistent with the high temperature measurements (500-1800°K) of Fieldhouse and Lang[10]. $T_o^{\alpha \rightarrow \beta}$ for hafnium is 2033°K[11,12], and in the absence of experimental enthalpy of transformation data, $\Delta S_{Hf}^{\alpha \rightarrow \beta}$ is estimated by choosing a value similar to the corresponding values for Ti and Zr. Thus,

$$\Delta F_{Hf}^{\alpha \rightarrow \beta} = 0.9\ (2033^{\circ}K - T) \text{ cal/g.at.} \qquad (10)$$

With $\overline{T}_{Hf} = 2495$°K[13], the free energy of fusion is estimated as

$$\Delta F_{Hf}^{\beta \rightarrow L} = 2.1(2495^{\circ}K - T) \text{ cal/g.at.} \qquad (11)$$

F. Niobium

Low temperature specific heat data for b.c.c., β, Nb (1-4°K) yields a very high value[6], $\gamma = 19.5 \times 10^{-4}$ cal/g.at.°K^2, for the electronic specific

heat coefficient. By comparison, the high temperature γ^{β} values for Ti and Zr[1] are 5.7×10^{-4} and 4.4×10^{-4} cal/g.at.$^{\circ}K^2$ respectively. High temperature measurements of Cp[14,15] covering the range 500-2000°K (i.e. for $T >> \theta$) indicate a value $\gamma^{\beta}_{Nb} \sim 6 \times 10^{-4}$ cal/g.at.$^{\circ}K^2$. The latter value is adopted and when coupled with the entropy of Nb at 298°K[16] yields $\theta^{\beta}_{Nb} = 285^{\circ}K$. Niobium is stable in the b.c.c. form up to $\overline{T} = 2770^{\circ}K$[16]. The free energy of fusion is estimated[16] as

$$\Delta F^{\beta \rightarrow L}_{Nb} = 2.3(2770^{\circ}K - T) \text{ cal/g.at.} \qquad (12)$$

G. Tantalum

Low temperature specific heat data[6] for b.c.c., β, tantalum (1-4°K) yield $\gamma = 13.5 \times 10^{-4}$ cal/g.at.$^{\circ}K^2$. However, the results of Sterrett and Wallace[17] (12-550°K) and Taylor and Finch[18] (950-3250°K) suggest $\gamma^{\beta}_{Ta} = 6 \times 10^{-4}$ cal/g.at.$^{\circ}K^2$ as being more appropriate for the high temperature ($T > \theta$) range. The former study[17] indicates $\theta^{\beta} = 230^{\circ}K$. Tantalum remains b.c.c. up to $\overline{T} = 3270^{\circ}K$[16]. Consequently, the free energy of fusion is estimated[16] as

$$\Delta F^{\beta \rightarrow L}_{Ta} = 2.3(3270^{\circ}K - T) \text{ cal/g.at.} \qquad (13)$$

H. Electronic Specific Heat Coefficients for Diborides

Westrum has measured the specific heats of ZrB_2[19], HfB_2[20], TiB_2, $NbB_{1.963}$, and $TaB_{2.11}$ over the range 5-350°K. The data for all of the compounds appear in Section XV of this report. Plotting Westrum's data as Cp/T vs T^2 in the range 5-20°K, where the T^3 law should hold for vibrational terms, yield Fig. 80 . These data indicate values of γ^{η} for TiB_2, ZrB_2, and HfB_2 less than 1×10^{-4} cal/g.at.$^{\circ}K^2$. The γ^{η} for NbB_2 and TaB_2 on the other hand lie closer to 2×10^{-4} cal/g.at.$^{\circ}K^2$. For purposes of the following calculations, the γ^{η} values

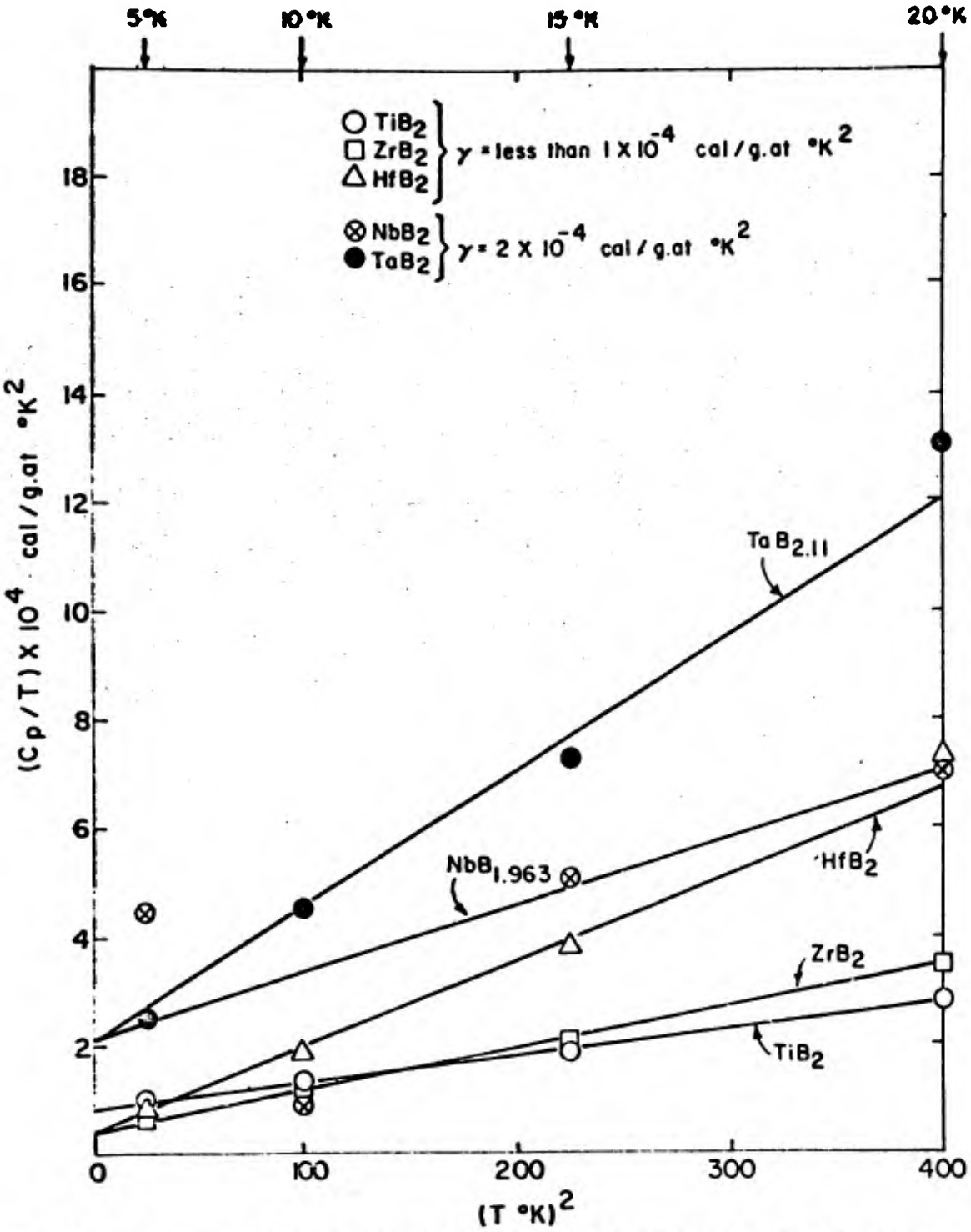

Fig. 80 - Estimation of the Electronic Specific Heat Coefficients of the Diborides.

for TiB_2, ZrB_2, and HfB_2 will be neglected. It should be noted that similar measurements by Westrum[21] on ZrC yields γ less than 1×10^{-4} cal/g.at. $^oK^2$.

I. Vibrational Specific Heat of Diborides

In order to analyze or predict the specific heat of the diborides, an equation similar to Eq. 4 will be used.

In order to compute $Cp^\eta[T]$, the specific heat is represented by

$$Cp^\eta[T] = \left\{1/3\,Cv[\frac{\theta^\eta_{Me}}{T}] + 2/3\,Cv[\frac{\theta^\eta_B}{T}]\right\}(1+10^{-4}T) + \gamma T \text{ cal/g.at.}^oK \quad (14)$$

where

$$(\theta^\eta_{Me})^2 M_{Me} = (\theta^\eta_B)^2 M_B \quad (15)$$

Eq. 15 implies that the applitudes of vibration of both atoms are equal. Similariy, the entropy is defined as

$$S = 1/3(S[\theta^\eta_{Me}/T] + 10^{-4}U[\theta^\eta_{Me}/T]) + 2/3(S[\theta^\eta_B/T] + 10^{-4}U[\theta^\eta_B/T]) + \gamma T \text{ cal/g.at.}^oK \quad (16)$$

where $S[\frac{\theta}{T}]$ is the Debye entropy function[6] and $U[\frac{\theta}{T}]$ is the Debye energy function[5,6]. The $10^{-4}\,U[\frac{\theta}{T}]$ terms arise from the Cp-Cv correction. Since Eq. 15 specifies θ^η_{Me} in terms of θ^η_B, knowledge of S[298] for the diborides fixes θ^η_{Me} and θ^η_B (since γ^η has been fixed). The data given by Westrum for S[298], which are shown in Table 55 were used to evaluate θ^η_{Me} and θ^η_B. These values were then substituted into eq. 14 to compute $C^\eta_p[T]$. The results are shown in Table 57 and in Figs. 81 through 85.

The Debye temperatures of the metal atoms and boron atoms for each of the compounds can be interrelated by means of a "Lindemann type formula" as indicated in reference (2).

$$\theta_{Me} = 130\, V^{-1/3}(T^\eta)^{1/2}(M_{Me})^{-1/2} \quad (17)$$

Table 57

Summary Comparison of Experimental and Calculated Low Temperature Specific Heat Data (cal/g.at.°K)

$$(\theta^{\eta}_{Me}/\theta^{\eta}_{B}) = (M_B/M_{Me})^{1/2}$$

	TiB_2		ZrB_2		HfB_2	
T°K	Obs.	Calc.	Obs.	Calc.	Obs.	Calc.
25	0.008	0.012	0.014	0.031	0.046	0.081
50	0.065	0.099	0.168	0.214	0.324	0.473
100	0.599	0.641	0.976	1.04	1.155	0.804
150	1.42	1.43	1.80	1.84	1.78	1.47
200	2.24	2.22	2.61	2.56	2.78	2.70
250	2.96	2.93	3.31	3.20	3.44	3.29
300	3.55	3.53	3.86	3.74	3.98	3.80
350	4.03	4.01	4.29	4.19	4.43	4.23
S[298]	2.27	2.27	2.93	2.93	3.42	3.44

$\theta^{\eta}_{Ti} = 620°K$, $\theta^{\eta}_{B} = 1302°K$ $\quad$ $\theta^{\eta}_{Zr} = 440°K$, $\theta^{\eta}_{B} = 1277°K$ $\quad$ $\theta^{\eta}_{Hf} = 320$ $\quad$ $\theta^{\eta}_{B} = 1299°K$

$\gamma^{\eta} = 0$ cal/g. at. $°K^2$ $\quad$ $\gamma^{\eta} = 0$ cal/g. at. $°K^2$ $\quad$ $\gamma^{\eta} = 0$ cal/g. at. $°K^2$

	$NbB_{1.963}$		$TaB_{2.11}$	
T°K	Obs.	Calc.	Obs.	Calc.
25	0.017	0.034	0.041	0.073
50	0.207	0.259	0.439	0.465
100	1.056	1.117	1.33	1.38
150	1.90	1.92	2.03	2.05
200	2.67	2.68	2.71	2.68
250	3.33	3.32	3.32	3.27
300	3.87	3.89	3.83	3.79
350	4.29	4.35	4.24	4.23
S[298]	3.01	3.05	3.40	3.43

$\theta^{\eta}_{Nb} = 425°K$, $\theta^{\eta}_{B} = 1245°K$ $\quad$ $\theta^{\eta}_{Ta} = 320$, $\theta^{\eta}_{B} = 1309°K$

$\gamma = 2 \times 10^{-4}$ cal/g. at. $°K^2$ $\quad$ $\gamma = 2 \times 10^{-4}$ cal/g. at. $°K^2$

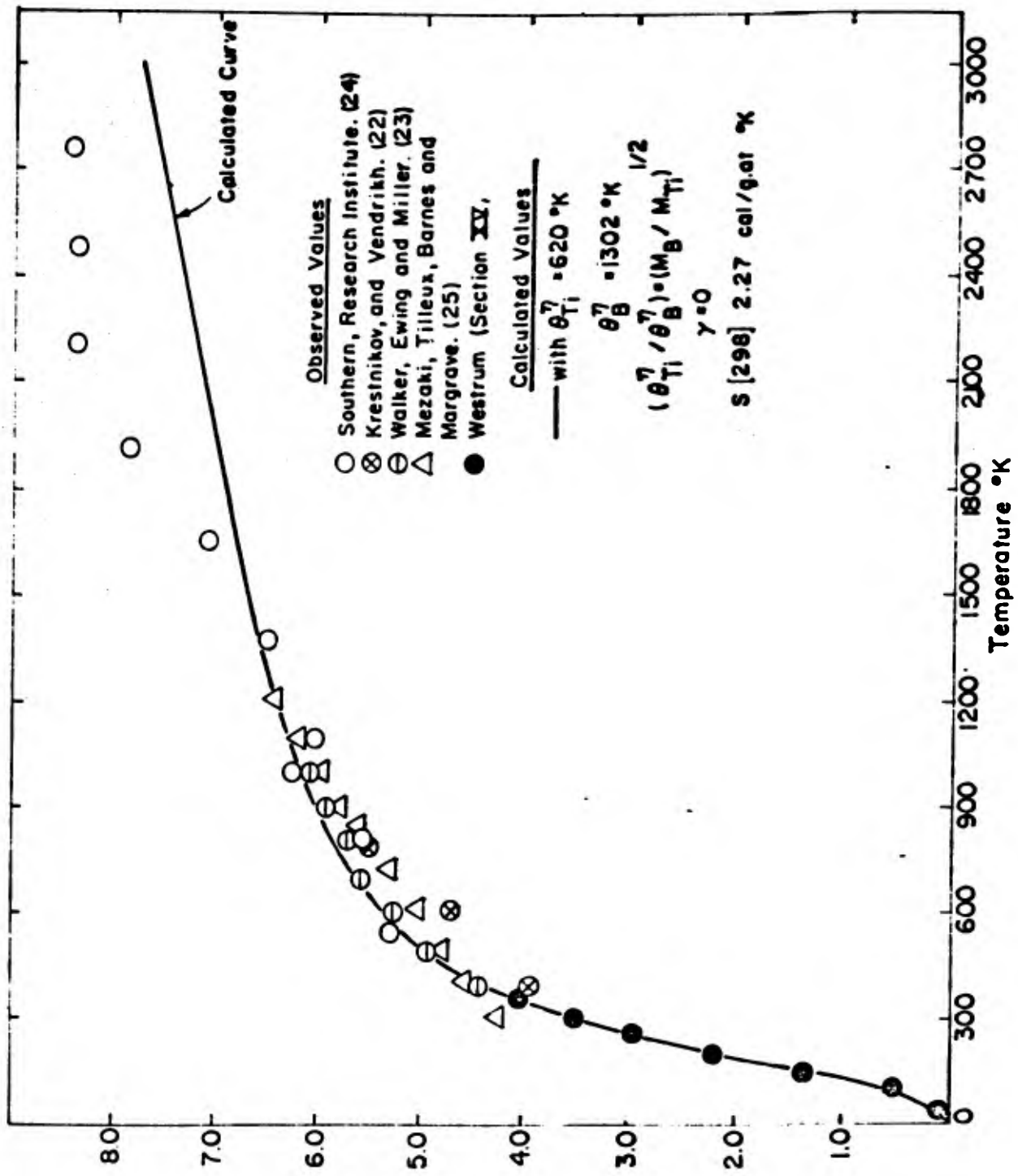

Fig. 81 - Comparison of Calculated and Observed Specific Heat of TiB_2.

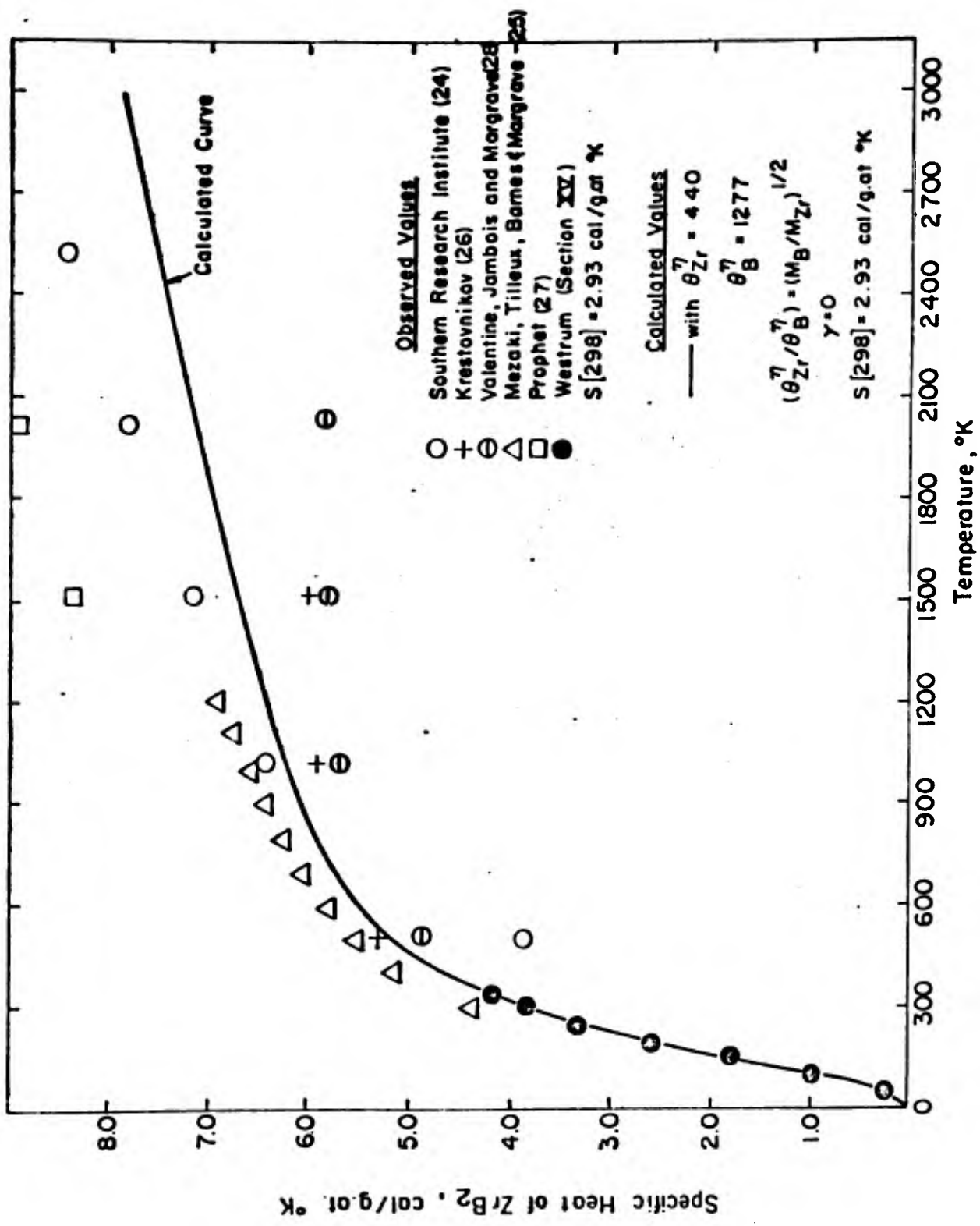

Fig. 82 - Comparison of Calculated and Observed Specific Heat of ZrB_2.

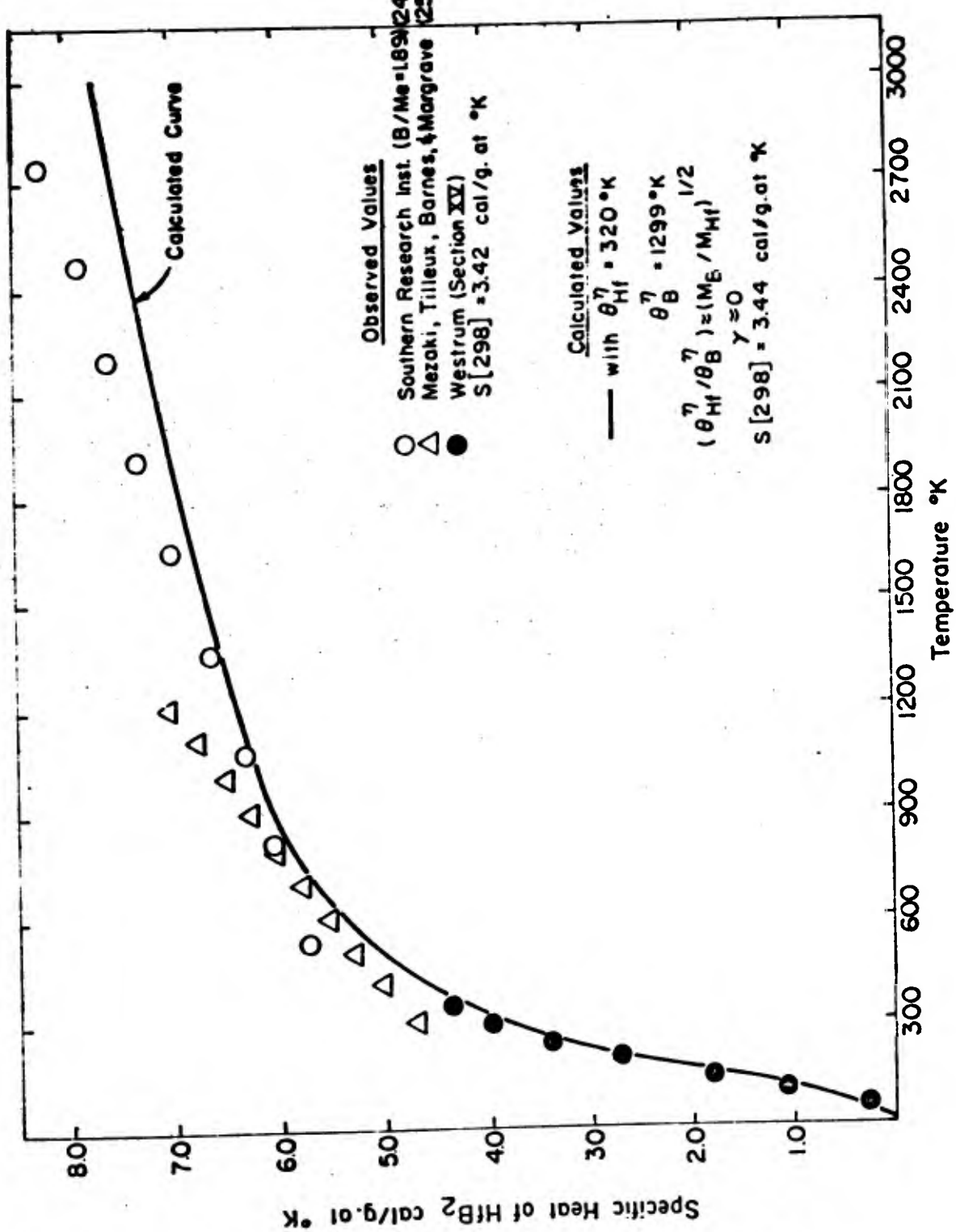

Fig. 83 - Comparison of Calculated and Observed Specific Heat of HfB_2.

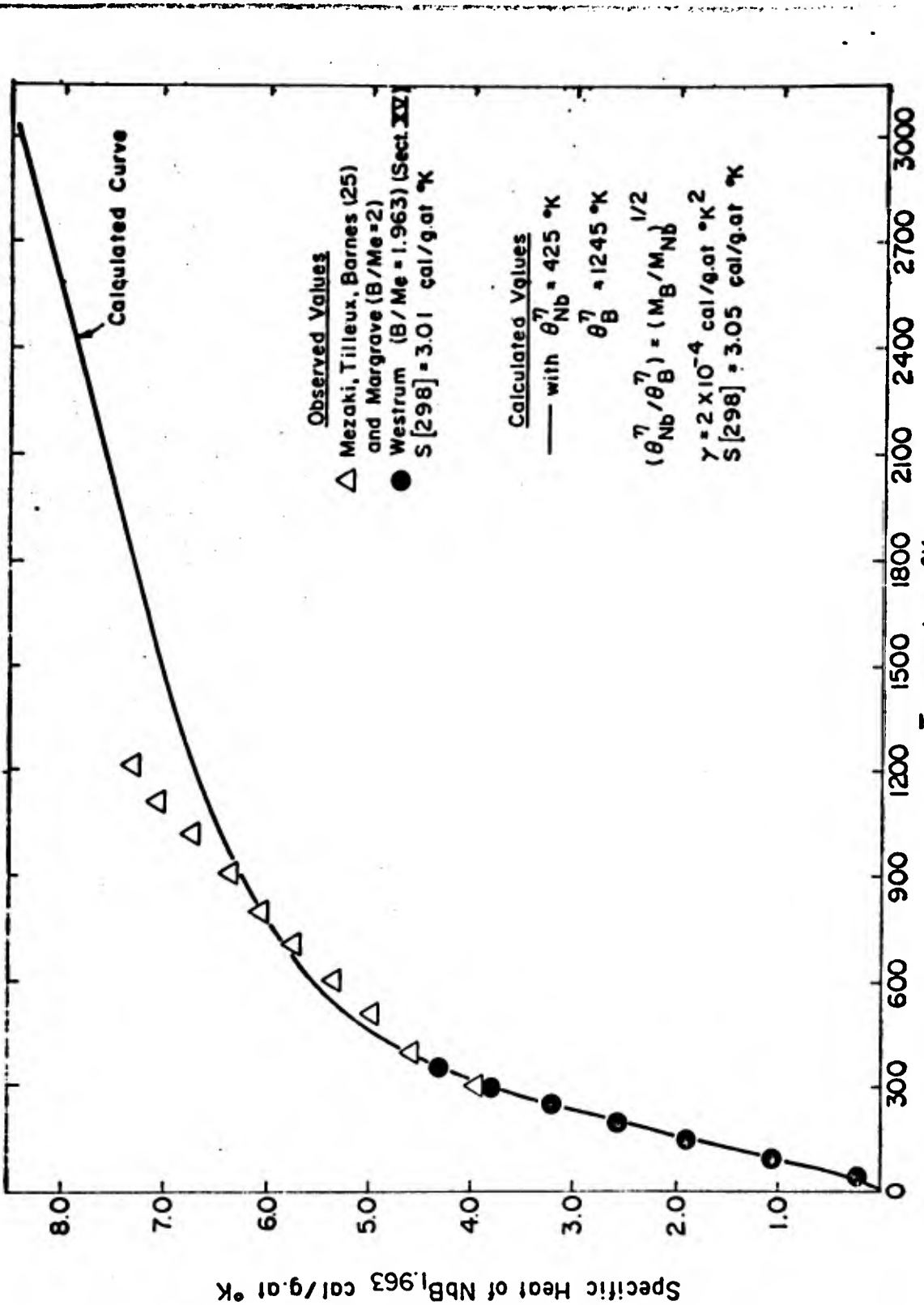

Fig. 84 - Comparison of Calculated and Observed Specific Heat of $NbB_{1.963}$.

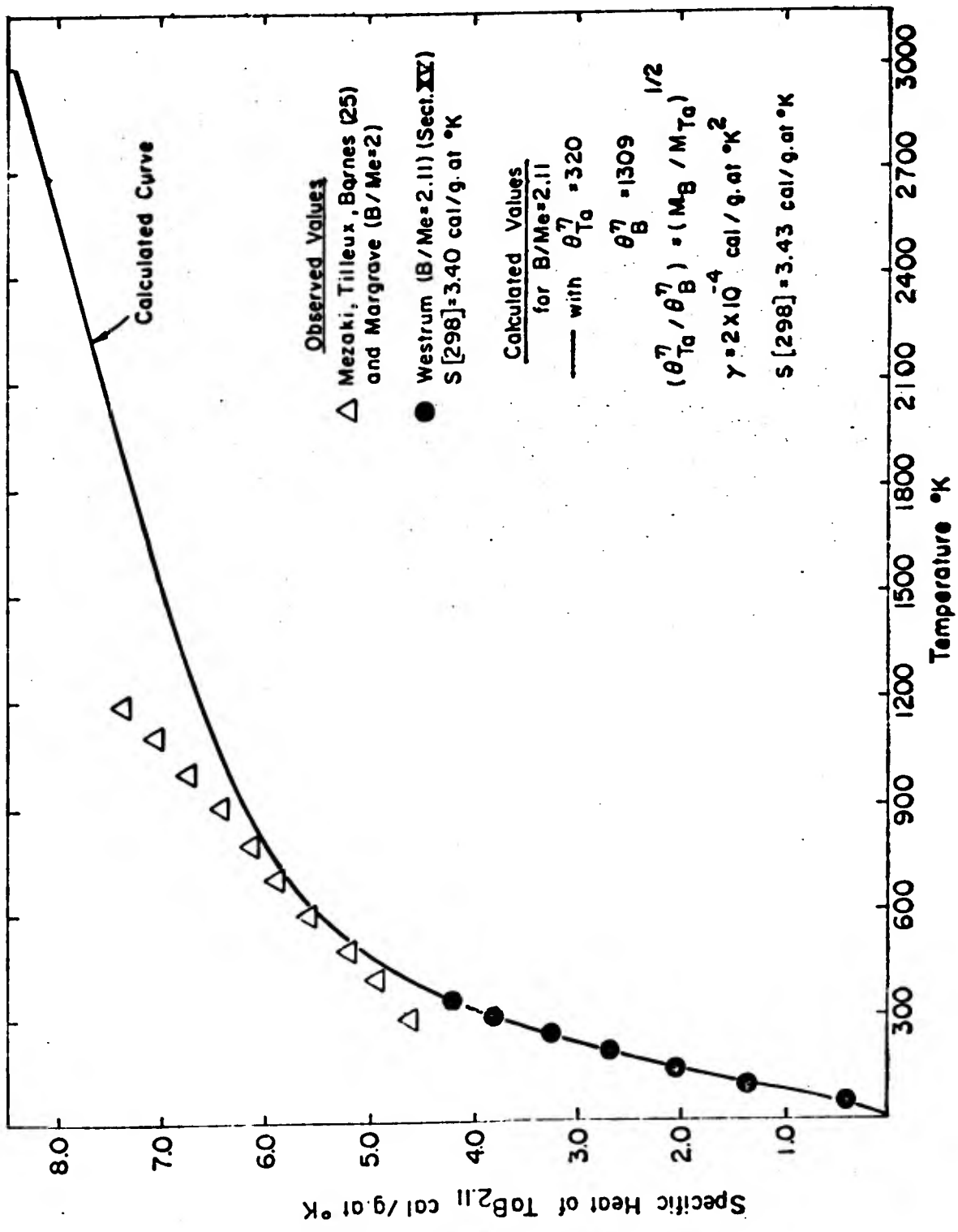

Fig. 85 - Comparison of Calculated and Observed Specific Heat of $TaB_{2.11}$.

where V is the volume per gm atom in cm^3 (Table 60), T° is the melting point (Table 58) and M_{Me} is the atomic weight of the metal. The calculated θ_{Me} values for TiB_2, ZrB_2, HfB_2, NbB_2, and TaB_2 are 619, 429, 319, 438 and 321°K respectively. These values compare favorably with the experimental values given in Table 57. Thus, combination of Eqs. (15) and (17) can be used to adequately describe the vibrational specific heats of the diborides.

J. Comparison of Observed and Calculated Low Temperature(5-350°K) Specific Heat Data

Table 55 shows the comparison of the low temperature specific heat data. In view of the fact that the calculated values were obtained on the basis of a one parameter evaluation (plus Eq. 15), the agreement is quite satisfactory Moreover, because of the "force fit" of the 298°K entropy, the θ values tabulated should be accurate for the free energy calculations performed below.

K. Comparison of Observed and Calculated High Temperature Specific Heat Data

Figs. 81 through 85 compare experimental data and calculations for TiB_2[22-25], ZrB_2[24-28], HfB_2[24, 25], NbB_2[25], and TaB_2[25]. While the data reflect results obtained on a wide range of materials varying considerably in impurity content, stoichiometry, etc., the differences between different investigation are quite large. Much larger in fact than can be attributed to chemical effects. ZrB_2 is a good case in point where the experimental values vary from 6 to 9 cal/g.at.°K at 2000°K. In the opinion of the present author, this indicates that the high temperature specific heat measurements are in need of improvements! Under these circumstances, the high temperature comparison between calculated and observed specific heat seems quite satisfactory.

L. Calculation of $\Delta F_T[T]$ and the Free Energy of Formation Function

With the foregoing background, it is now possible to perform the numerical calculations of $\Delta F_T^{\eta}[T]$ indicated by Eqs. 2 and 3. For purposes of illustration, it is convenient to consider the TiB_2 case in detail. Reference to Tables 54 and 55 suggest that $\theta_{Ti}^{\eta} = 620^{\circ}K$, $\theta_B^{\eta} = 1302^{\circ}K$, $\theta_B = 1270^{\circ}K$, and $\theta_{Ti} = 365^{\circ}K$. Consequently, the vibrational contribution to $\Delta F_T^{\eta}[T]$ is

$$\frac{1}{3}\left(F\left[\frac{620}{T}\right] - F\left[\frac{365}{T}\right]\right) + \frac{2}{3}\left(F\left[\frac{1302}{T}\right] - F\left[\frac{1270}{T}\right]\right) \text{ cal/g.at.}^{\circ}K$$

where $F\left[\frac{\theta}{T}\right]$ is the Debye Free Energy[1,6]. At high temperatures, this difference can be approximated by

$$RT \ln \theta_{Me}^{\eta}\, \theta_{Me}^{-1}\, (\theta_B^{\eta})^2 (\theta_B)^{-2} \text{ cal/g.at.} \qquad (18)$$

Eq. 18 must be supplemented by several terms in order to complete the $\Delta F_T^{\eta}[T]$ function. The first term arises from the electronic specific heat coefficients, i.e.,

$$-0.5T^2(\gamma^{\eta} - 1/3\,\gamma_{Me} - 2/3\,\gamma_B) \text{ cal/g.at.} \qquad (19)$$

The sum of 17 or 18, and 19 would accurately represent $\Delta F_T^{\eta}[T]$ if there were no phase transformations in the metal or in boron. For $1155^{\circ}K \leq T \leq 1941$ a term equal to $-1/3(0.9(1155^{\circ}K - T)$ to account for the $\alpha \rightarrow \beta$ transition in Ti must be added. Between $1941^{\circ}K$ and $2300^{\circ}K$, this additional term becomes $-1/3(0.9(1155^{\circ}K-T)+2.1(1941-T))$. For $T > 2300^{\circ}K$, the additional term is equal to $-1/3(0.9(1155^{\circ}K-T) + 2.1(1941-T)) - 2/3(2.3(2300-T))$.

In order to simplify representation of the computations, it is convenient to define ϕ_T° as the non-vibrational temperature-dependent free energy terms for the pure elements ϕ_T° values are shown in Table 54 . For the case of boron ϕ_T°

Table 58

Temperature Dependent Component of the Free Energy of Formation of the Diborides

$$\Delta F_T^\eta = T\left(\frac{\Delta F^\eta[T] - \Delta H^\eta[0^\circ K]}{T}\right) = -T(\text{times})\Delta \text{f. e. f.}$$

(kcal/g.at.)

$T^\circ K$	TiB_2	ZrB_2	HfB_2	NbB_2	TaB_2
1400	+1.9	+1.7	+1.5	+0.9	+1.0
1600	2.3	2.1	1.8	1.0	1.1
1800	2.6	2.4	2.1	1.1	1.3
2000	3.0	2.8	2.4	1.3	1.5
2200	3.6	3.1	2.7	1.4	1.6
2400	4.3	3.8	3.2	1.7	1.9
2600	5.1	4.6	3.9	2.1	2.3
2800	6.0	5.4	4.7	2.5	2.7
3000	6.9	6.2	5.6	3.1	3.3
3200	7.8	7.0	6.5	3.6	3.9

at high temperatures

$$\Delta F_T^\eta = RT \ln \theta_{Me}^\eta \theta_{Me}^{-1} (\theta_B^\eta)^2 \theta_B^{-2} - 1/2\,\gamma^\eta T^2 - 1/3\,\phi_{Me}^\circ - 2/3\phi_B^\circ$$

$\overline{T}^{\eta\circ}K$	3250	3330	3520	3270	3370

is zero below 2300°K since $\gamma = 0$ and the free energy differences between polymorphs are neglected. Above 2300°K, boron melts. On this basis,

$$\Delta F_T^{\eta} = RT \ln 0_{Me}^{\eta} \, 0_{Me}^{-1} (\theta_B^{\eta})^2 (\theta_B)^{-2} - 0.5T^2 \gamma^{\eta} - 1/3 o_{Me}^{o} - 2/3 \phi_B^{o} \text{ cal/g.at.} \qquad (20)$$

Table 56 shows the values of $\Delta F_T^{\eta}[T]$ which is equal to -T times Δf.e.f. Clearly these values are very significant. Hence, the free energy of formation and the enthalpy of formation are not equal.

M. Comparison of X-Ray and Specific Heat Debye Temperatures

The X-ray measurements of Debye temperatures which are reported in Section VIII yield values of S[298°K] of 3.0 cal/g.at.°K for HfB_2 and 2.5 cal/g.at.°K for ZrB_2. These values are within 10% of the measured values of 3.42 cal/g.at.°K for HfB_2 and 2.93 for ZrB_2 (see Table 55). The X-ray values were computed by summing the vibrational components in the "a" and "c" direction and utilizing equation 16.

REFERENCES

1. Kaufman, L., Acta. Met., (1959) 7 575.
2. Kaufman, L., Tr. A.I.M.E., (1962) 224 1006.
3. Kaufman, L., Clougherty, E.V., and Weiss, R.J., Acta Met. (1963) 11 323.
4. Hoard, J.L., and Newkirk, A.E., J. Am. Chem. Soc. (1960) 82 70.
5. Beattie, J.: J. Math. Phys. (1926) 6 1, M.I.T., Cambridge, Mass.
6. American Institute of Physics Handbook, McGraw Hill Book Co., New York, N.Y. pp. (4-42 to 4-48).
7. Johnston, H.L., Hersh, H.N., and Kerr, E.C., J. Am. Chem. Soc. (1951) 73 1112.
8. McDonald, R.A., and Stull, D.R., J. Chemical and Engineering Data (1962) 7 84.
9. Walcott, N.M., Phil. Mag. (1957) Ser. 8, 2 1246.
10. Fieldhouse, I.B., and Lang, J., "Measurement of Thermal Properties of Hafnium," Armour Research Foundation WADD TR-60-904, July 1961.
11. Deardorf, D.K. and Kato, H., "The Transformation Temperature of Hafnium, USBM-U-426 (8 April 1958).
12. Thomas, D.E. and Hayes, E.T., "The Metallurgy of Hafnium, U.S. A.E.C. (1960).
13. Deardorf, D.K., and Hayes, E.T., Tr., A.I.M.E. (1956) 206 509.
14. Fieldhouse, I.B., Hedge, J.C. and Lang, J.I., Armour Research Foundation WADC TR-58-274, AD206892 (1958).
15. Gel'd, P.V. and Kusenko, F.G., Izv. Akad, Nauk. SSSR OTN Met i Top (1960).
16. Stull, D.R. and Sinke, G.C., Thermodynamic Properties of the Elements, No. 18 of the Advances in Chemistry Series, Am. Chem. Soc., Washington, D.C. (1956).
17. Sterrett, K. F. and Wallace, W.E., J. Am. Chem. Soc. (1958) 80 3176.
18. Taylor, R.E. and Finch, R.A., "The Specific Heat of Mo, Ta, and Re From Low to High Temperatures" Atomics International Report NAA-SR-6034 (1961).

19. Westrum, E.F., "Thermodynamic and Kinetic Studies for a Refractory Materials Program" ASD-TR-62-204, Part 1 April 1962 prepared under Contract No. 33(616)-7472 by L. A. Mclaine of Arthur D. Little, Inc.

20. Westrum, E.F., Ibid, report of December 1962.

21. Westrum, E.F., Ibid, report of August 1963.

22. Krestovnikov, A.N., and Vendrikh, M.S., Izv. Vuz, Tsvet. Metall. (1959) #2 pp 54-57 Brutcher Tr. #4673 (TiB_2).

23. Walker, B.E., Ewing, C.T. and Miller, R.R., J. Phys. Chem. (1957) 61 1682 (TiB_2).

24. Southern Research Institute A.S.C. Technical Rpt. 62-675, August 1962 (TiB_2, HfB_2, ZrB_2).

25. Mezaki, R., Tilleux, E.W., Barnes, D.W., and Margrave, J.L., Paper No. SM-26/48 International Conference on Thermodynamics of Nuclear Materials held in Vienna, Austria, May 1962) by the International Atomic Energy Agency, Vienna, Austria, Proceeding to be published (TiB_2, ZrB_2, HfB_2, NbB_2 and TaB_2).

26. Krestovnikov, A.N., et al. Izvest. Vyeshikh. Ucheh. Zavedenii, Rasvedoch Tsvetnoya. Met. (1958) No. 173-75 also Chem. Abst. (1959) 19552c 53 (ZrB_2).

27. Prophet, H., Dow Chemical Co., Midland, Michigan. Unpublished work cited in JANAF chemical tables Dow Chemical Co., Midland, Michigan (ZrB_2).

28. Valentine, R.H., Jambois, T.F., and Margrave. J.L., Dept. of Chemistry, University of Wisconsin, Madison, Wisconsin. Work on A.S.D. contract with Arthur D. Little, San Francisco contract AF33(616)-7472 (ZrB_2).

XVII. HEAT OF FORMATION*

A. Introduction

The purpose of this subtask is to perform measurements of the enthalpy of formation, $\Delta H^{\eta}[298]$, of the diborides, by means of combustion or fluorine bomb calorimetry. Specimens of suitable diborides have been sent to W. Hubbard of Argonne National Laboratory and E. Huber of Los Alamos National Laboratory for this purpose. A tabulation of materials sent for measurement is given below. Since $\Delta H^{\eta}[298]$ is required in the evaluation of $\Delta F^{\eta}[T]$ (see Eq. (1) of Section XVI and note that the difference between $\Delta H^{\eta}[298]$ and $\Delta F^{\eta}[0^{\circ}K]$ is relatively small) a method of estimating $\Delta H^{\eta}[298]$ for diborides where reliable data is absent has been developed. Subsequent portions of this section contain a discussion of this procedure, the present values for $\Delta H^{\eta}[298]$, the compositional dependence of $\Delta H^{\eta}[298]$, and the free energy of formation of the diborides.

B. Summary of Materials Provided for Fluorine Bomb and Combustion Calorimetry

The following materials were sent to Dr. Ward N. Hubbard, for the determination of the heat of formation by fluorine bomb calorimetric techniques:

Material	Supplier	Quantity (Grams)	Physical State	Reference
TiB_2 (#1)	U.S. Borax	100	Powder	Sec. III Table I
TiB_2 (#2)	Millmaster	100	Powder	Sec. III Table I
HfB_2 (#1)	Wah Chang	50	Powder	Sec. III Table I
NbB_2 (#2)	U.S. Borax	100	Powder	Sec. III Table I
$NbB_{1.97}$	Arthur D. Little	20	Zone-refined Rods	Sec. IV B.
TaB_2 (#1)	Kawecki	100	Powder	Sec. III Table I
$TaB_{2.11}$	Arthur D. Little	20	Zone-refined Rods	Sec. IVE

* L. Kaufman, ManLabs, Inc.

The following materials were sent to Dr. Elmer Huber, Jr. for the determination of the heat of formation by combustion bomb calorimetric techniques:

Material	Supplier	Quantity (Grams)	Physical State	Reference
TiB_2 (#1)	U.S. Borax	100	Powder	Sec. III Table I
HfB_2 (#1)	Wah Chang	100	Powder	Sec. III Table I
TaB_2 (#1)	Kawecki	100	Powder	Sec. III Table I

C. Consideration of the Presently Available Data on the Heat of Formation of the Diborides

Table 57 summarizes the values reported for the heats of formation of the diborides of titanium, zirconium, hafnium, niobium, and tantalum through 1962. The values are given in kcal/mol rather than kcal/g.at. to avoid introducing additional confusion on this subject. As indicated in Sec. XVI and Sec. XX, a gram atom basis will be used in all of the thermodynamic considerations in this study. However, in view of the wide disparity in results (see Table 59) it seems most prudent at present to quote values in units of kcal/mol which is the general practice.

Reference to Table 59 shows that a variety of "measured" and "estimated" values have been suggested for several of the diborides. Brewer and Haraldson have estimated limits for ΔH^{η} by considering phase equilibria and competing boride-carbide reactions[1]. Samsonov[4] has estimated ΔH^{η} values by employing a method similar to the calculation of Kubaschewski[10]. In Kubaschewski's method, which has been successfully applied in correlating the enthalpy of formation at 298°K of NaCl and CsCl type oxides, nitrides and carbides, the heat of formation is considered to be a function of the percentage of a corrected volume change, $\Delta V'\%$.

Table 59

Heats of Formation Suggested for the Diborides (1962)

$-\Delta H^{\circ}[298]$ in kcal/mol = $-3\Delta H^{\circ}[298]$ in kcal/g.at.

	Measured Values (kcal/mol)				Estimated Values (kcal/mol)	
TiB_2	52[f]	50 ± 5[g]	32[e]	70[b]	72[a]	73[d]
ZrB_2	76.7[h] ± 1.5		63.1[d]	58[i]	> 78[a]	65[d]
HfB_2	74.2[c]					
NbB_2					> 36[a]	59[d]
TaB_2					> 52[a]	63[d]

Notes

a. Ref. 1 Estimated from Phase Equilibria.
b. Ref. 2 Determined from vapor pressure measurements.
c. Ref. 3 Determined from vapor pressure measurements.
d. Ref. 4 Calculated from gram-atomic volume of formation by Kubaschewski's method.
e. Ref. 5 Mass spectrometric measurements.
f. Ref. 6 Mass spectrometric measurements.
g. Ref. 7 High temperature calorimetric measurements.
h. Measurement of the heat of combustion, E.J. Huber, Jr., E.L. Head, and C. Holley: unpublished research (see ref. 8).
i. Ref. 9 Mass spectrometric measurements.

Where

$$\Delta V'\% = 100\ (e\ V - \Sigma V')/\Sigma V') \qquad (1)$$

In this equation, V is the volume per gram atom of the compound and e is a numerical factor which converts V to an equivalent volume which the compound would have if it were in the f.c.c. form. In addition $\Sigma V'$ is the sum of the atom fraction of metal times the atomic volume of metal and the atom fraction of boron times the atomic volume of boron where both atomic volumes are computed on the basis of a coordination number of twelve. Samsonov[4] does not indicate the values of e and the atomic volume of C.N. 12 boron which were used in his computation[4].

Table 60 shows the quantity

$$\Delta V^{o}\% = 100(V^{\eta} - \Sigma V^{o})/\Sigma V^{o} \qquad (2)$$

where V^{η} is the volume per gram atom of the diboride and V^{o} is the volume per gram atom of boron and metal at 298°K. The calculation of this simple volume change does not allow for the conversion of all of the structures to the close packed state. However, it suggests that the TiB_2, ZrB_2, HfB_2 group should have heats of formation which are larger in magnitude than NbB_2 and TaB_2. As was mentioned previously, Samsonov's estimates[4] are difficult to reproduce since he does not state the numerical values of the coordination transformation factors used in his computations.

The measured values of ΔH^{η} fall into three catagories, direct determinations of ΔH^{η} by calorimetric techniques (i.e. yielding -50 ± 5 and -76.7 ± 1.5 kcal/mol for TiB_2 and ZrB_2 respectively), evaluation of ΔH^{η} from high temperature mass spectrometric vapor pressure measurements (i.e. yielding -32 and -52 kcal/mol for TiB_2 and -58 kcal/mol for ZrB_2) and calculation of ΔH^{η} from

Table 60

Simple Computation of the Volume Change Attending The Formation of the Diborides (298°K)

Element	Volume $cm^3/g.at.$	Diboride Volume $cm^3/g.at.$	ΔV^o%
B	4.60	----	------
Ti	10.64	5.15	-22.1
Zr	14.02	6.17	-21.2
Hf	13.45	5.97	-20.9
Nb	10.83	5.48	-18.0
Ta	10.86	5.32	-17.4

analysis of vapor pressure-temperature curves which has been performed by Samsonov and co-workers (i.e. -70, -63, and -74 kcal/mol for TiB_2, ZrB_2 and HfB_2 respectively). It should be pointed out that the "Heat of Formation" values determined on the basis of high temperature vapor pressure measurements are incorrect because of the assumption that ΔC_p and $\Delta F_T[T]$ are zero (see Table 58).

D. Evaluation of Literature Data and Estimation of the Enthalpy of Formation of Diborides

Recently, Margrave and Hubbard[11] have reported a value of $\Delta H^\eta[298] = -72$ kcal/mole $= -24$ kcal/g.at. for ZrB_2. This value was obtained by fluorine bomb calorimetry using well characterized specimens of high purity. At about the same time, Goldstein and Trulson[12] have reported a mass spectrometer vapor pressure value of $\Delta F^\eta[2400°K] = -58$ kcal/mole or -19.3 kcal/g.at. According to the formalism developed in section XVI

$$\Delta F^\eta[2400] = \Delta H^\eta[0°K] + \Delta F_T^\eta[2400] \text{ cal/g.at.} \qquad (3)$$

*This value was originally[12] reported as a "ΔH" i.e. assuming $\Delta C_p = 0$.

Substitution of $\Delta F^{\eta}[2400] = -19.3$[12] kcal/g.at., and $\Delta F_T^{\eta}[2400] = +3.8$ kcal/g.at. from Table 56 of section XVI, yields,

$$\Delta H^{\eta}[0^{\circ}K] = -23.1 \text{ kcal/g.at.} = -69.3 \text{ kcal/mole} \qquad (4)$$

for ZrB_2 derived from the mass spectrometer study. This value is in relatively good agreement with the fluorine bomb measurement of[11]

$$\Delta H^{\eta}[298] = -24 \text{ kcal/g.at.} = -72 \text{ kcal/mole} \qquad (5)$$

for ZrB_2, because the difference between $\Delta H^{\eta}[298]$ and $\Delta H^{\eta}[0^{\circ}K]$ is only 300 cal/mol or 100 cal/g.at.

Applying the same procedure to the mass spectrometric measurement of $\Delta F^{\eta}[2300^{\circ}K] = -52$ kcal/mol $= -17.3$ kcal/g.at. on TiB_2* obtained by Schissel and Trulson[6] yields (6)

$$\Delta F^{\eta}[2400] = -17.3 \text{ kcal/g.at.} = \Delta H^{\eta}[0^{\circ}K] + 3.9 \text{ kcal/g.at.}$$

or

$$\Delta H^{\eta}[0^{\circ}K] = -21.2 \text{ kcal/g.at.} = -63.6 \text{ kcal/mol} \qquad (7)$$

for TiB_2.

On the basis of the correlation between the volume change on formation of a compound and the enthalpy of formation, it is useful to consider the approximation

$$\Delta H^{\eta}[0^{\circ}K] \simeq C\Delta V^{o}\% \qquad (8)$$

where $\Delta V^{o}\%$ values are those tabulated in Table 60, and C is a constant. On the basis of Eq.8.

$$\Delta F^{\eta}[T] \simeq C\Delta V^{o}\% + \Delta F_T^{\eta}[T] \qquad (9)$$

Substitution of the abovementioned values for TiB_2 and ZrB_2 into Eq.(9) yields the following equations.

*This value was originally reported as a "ΔH" assuming $\Delta C_p = 0$.

for TiB_2 $-17.3 = C(-22.1) + 3.9$ kcal/.gat. (10)

for ZrB_2 $-19.3 = C(-21.2) + 3.8$ kcal/g.at. (11)

and $-24 = C(-21.2)$ kcal/g.at. (12)

Eqs. 10-12 yield three values of C corresponding to 0.96, 1.09, and 1.13 kcal/g.at. respectively. Averaging yields a value

$C = 1.1$ kcal/g.at. or 1100 cal/g.at. (13)

This quantity can be used to estimate $\Delta H^{\eta}[0^{o}K]$ for HfB_2, NbB_2, and TaB_2 until measurements (see section B) become available. Table 61 shows $\Delta H^{\eta}[0^{o}K]$, and $\Delta F^{\eta}[T]$ for the diborides.

E Consideration of the Compositional Variation of the Heat of Formation

The thermodynamic expressions derived for the compositional and temperature dependence of the free energy of the diborides, $F^{\eta}[x,T]$, developed in section XX can be used to represent the compositional dependence of the heat of formation. Applying the relation

$$H = F - T\,\partial F/\partial T \qquad (14)$$

to these equations yields

$$\Delta H^{\eta}[x,T] - \Delta H^{\eta}[2/3,T] = (y-1)\Delta H^{\eta}[2/3,T] + (y/3+x-1)H^{\eta}_{Me+} + (2y/3-x)H^{\eta}_{B+} \quad (15)$$

when α and $d\alpha/dT$ are small.

In this equation $\Delta H^{\eta}[x,T]$ is the enthalpy of formation for a variable composition, $\Delta H^{\eta}[2/3,T]$ is the enthalpy of formation of the stoichiometric diboride, H^{η}_{B+} and H^{η}_{Me+} are the enthalpies of formation of boron and metal sublattice vacancies, y is the ratio of lattice sites to atoms, and α is the vacancy concentration parameter. (See section XX for complete definitions). When $x < 2/3$, $y = 3(1-x)$ thus

$$H^{\eta}_{B+} = (\Delta H^{\eta}[x] - 3(1-x)\Delta H^{\eta}[2/3])(2-3x)^{-1} \qquad (16)$$

Table 61

The Free Energy and Enthalpy of Formation of Diborides in k cal/g.at.

(to convert to k.cal/mole, multiply by three)

$\Delta H^{\eta}[\ O^{\circ}K]$

TiB_2	ZrB_2	HfB_2	NbB_2	TaB_2
-21.2	-23.3	-23.0	-19.8	-19.1

$\Delta F^{\eta}[T]$

$T^{\circ}K$	TiB_2	ZrB_2	HfB_2	NbB_2	TaB_2
1400	-19.3	-21.6	-21.5	-18.9	-18.1
1600	-18.9	-21.2	-21.2	-18.8	-18.0
1800	-18.6	-20.9	-20.9	-18.7	-17.8
2000	-18.2	-20.5	-20.6	-18.5	-17.6
2200	-17.6	-20.2	-20.3	-18.4	-17.5
2400	-16.9	-19.5	-19.8	-18.1	-17.2
2600	-16.1	-18.7	-19.1	-17.7	-16.8
2800	-15.2	-17.9	-18.3	-17.3	-16.4
3000	-14.3	-17.1	-17.4	-16.7	-15.8
3200	-13.4	-16.3	-16.5	-16.2	-15.2

When $x > 2/3$, $y = 3/2x$, hence

$$H^{\eta}_{Me+} = (\Delta H^{\eta}[x] - (3x/2)\Delta H^{\eta}[2/3])(3x/2 - 1)^{-1} \quad (17)$$

since Section XX indicates

$$H_{Me+} = +26,000 - 2.5\Delta H^{\eta}[2/3, 0^{\circ}K] \text{ cal/g.at.} \quad (18)$$

and

$$H_{B+} = -13,000 - 2.5\Delta H^{\eta}[2/3, 0^{\circ}K] \text{ cal/g.at.} \quad (19)$$

substitution of Eq.(19)into (16) yields

$$\Delta H^{\eta}[x] - \Delta H^{\eta}[2/3] = -(2-3x)(1.5\Delta H^{\eta}[2/3] + 13,000) \text{ cal/g.at.} \quad (20)$$

for $x < 2/3$, while substitution of (18) into (17) yields

$$\Delta H^{\eta}[x] - \Delta H^{\eta}[2/3] = (1.5x - 1)(26,000 - 1.5\ \Delta H^{\eta}[2/3]) \text{ cal/g.at.} \quad (21)$$

for $x > 2/3$.

These equations can be used to estimate the change in the enthalpy of formation with deviation from stoichiometry. As expected, Eqs.(20) and (21) indicate increases in the enthalpy of formation (i.e. the enthalpy of formation becomes more positive, or less negative) as the composition departs from $x = 2/3$.

REFERENCES

1. Brewer, L. and Haraldsen, H.: J. Electrochem. Soc. (1955) 102 399.

2. Samsonov, G.V.: Zh. Prikl. Khimii (1955) 28 919.

3. Paderno, Yu. B., Serebryakova, T.I., and Samsonov, G.V. Tsvetnye Metally. (1959) 11 48.

4. Samsonov, G.V.: Zh. Fizicheskoy, Khim (1956) Vol. XXX No. 9, 2057.

5. Schissel, P.O. and Williams, W.S.: Bull, Am. Phys. Soc. (1959) Ser. II, No. 3.

6. Schissel, P.O. and Trulson, O.C., J. Phys. Chem. (1962) 66 1492.

7. Lowell, C.E. and Williams, W.S.: Rev. Sci. Inst. (In Press).

8. Lietnaker, J. "Thermodynamic Properties of Refractory Borides" Los Alamos Scientific Laboratory Report #LA-2402, 13 April 1960 (also, J. Chem. Phys. (1962) 36 350.

9. Trulson, O.C. and Goldstein, H.W., Union Carbide Research Institute, Reported at International Symposium on "Condensation and Evaporation of Solids" Dayton, Ohio, 14 September 1962. (Proceedings to be published).

10. Kubaschewski, O. and Evans, E. Ll. "Metallurgical Thermochemistry." Butterworth-Springer, London (1951).

11. Margrave, J. and Hubbard, W.: Research on Materials For a Refractory Metals Program Contract AF33(616)-7472 with ASD, Dayton, Ohio directed by Arthur D. Little, Inc., San Francisco, California.

12. Goldstein, H.W. and Trulson, O.C., Union Carbide Research Institute Quarterly Progress Report on Contract DA-30-069-ORD-2787 with ARPA and Army Missile Command 31 December 1962.

XVIII. PHASE BOUNDARIES*

A. Introduction

Accurate descriptions of the compositional limits of the diboride phases are essential to the ultimate utilization of these materials in various environments and to the application of the thermodynamic models proposed for these systems. A comparison of the available information for the five systems of interest indicates that the diborides of titanium, niobium, and tantalum are stable over a significant range of composition while the diborides of zirconium and hafnium are stable in a very narrow region near stoichiometric MeB_2. Nevertheless, significant changes in thermodynamic properties are predicted for even the narrow regions of homogeneity and these changes can markedly influence the vaporization and the oxidation properties of these materials.

From a more general viewpoint the accurate description of the entire phase diagram for each system of interest is required for many technological applications and theoretical studies.

The determination of the compositional range of stability of the diboride phases requires the use of several different techniques. The choice of a particular technique is governed by the range of temperature for a given experiment and the compositional region of interest; that is, metal rich, or boron rich, relative to the composition of the diboride phase. The experimental procedures originally planned for this subtask were: (1) a study of diffusion couples between the zone refined diboride and metal, or boron, and (2) a study of "off-stoichiometric" alloys in the two-phase regions on both sides of the diboride phase. Vapor pressure measurements in Section XIX were considered as a complementary technique for providing data on the compositional variation of the diboride phases.

---

*E. V. Clougherty, L. D. Blackburn, ManLabs, Inc., Cambridge, Mass.

In addition, extreme compositional limits were calculated for the equilibria between metal and diboride and between boron and diboride. These calculations yielded extreme compositional limits because the presence of intermediate phases was neglected.

Experimental difficulties stemming from the physical characteristics of the available zone refined material, the absence of well defined phase diagrams, and the high vapor pressure of elemental boron in the temperature regions of interest have hampered the performance of the planned experiments using diffusion couples. Since the zone refining procedure could only supply ZrB_2 and HfB_2 as useful material for this subtask, the use of high purity metal and boron was attempted for diffusion couple experiments. At the outset it was thought that the latter experiments would circumvent the experimental problems associated with the availability and the feasibility of the zone refined diboride material and would supply ancillary information on the phase diagrams. In practice, the presupposed advantages of the metal/boron diffusion couples were not realized. Successful diffusion couples were prepared for Zr/ZrB_2 in the temperature range from 1000° to 1500°C. An apparently incorrect designation of the metal - diboride eutectic temperature in this system caused experimental failures for attempted diffusion couples above 1650°C. Additional experiments included equilibration of a two phase alloy, boron rich ZrB_2 + a second phase at 1770° and 1850°C. Vapor pressure measurements for NbB_2 as a function of composition at temperatures above 2000°K were used to define the high temperature phase field of NbB_2.

In the course of the present investigation it became apparent that very little experimental information was available for the five metal-boron phase diagrams of interest. A careful examination of the summary presented

in the monograph by Samsonov and Portnoy[1] revealed the absence of any original phase diagram work for these systems by these authors. In general, no references to experimental work for these systems have appeared in the recent literature. Accordingly, it was considered appropriate to present the available information on these diagrams as part of this final report.

B. Phase Diagrams

1. General Considerations

A review of the literature on transition metal-boron phase diagrams indicates that serious experimental problems can interfere with the determination of an accurate equilibrium diagram. Three important factors which complicate the experimental work are:

a. Very high melting temperatures

b. Slow solid-state reaction rates

c. Boron vaporization

The very high liquidus temperatures in transition metal-boron systems prohibits the use of conventional thermal analysis, which is the basic technique for determining this portion of a diagram in lower melting point systems. Sample container material can be a source of specimen contamination leading to false results. Consequently, there is little experimental data available for the very high temperature regions of the phase diagrams.

Extremely slow reaction rates in the solid state make it very difficult to achieve equilibrium and can lead to considerable superheating and supercooling of the various intermediate phases. The true temperature range of stability of an intermediate phase may be difficult to assess, either because an invariant reaction (i.e. eutectoid or peritectoid reaction) escapes detection

entirely, or because the determination of the range of temperature for a detectable reaction is subject to considerable error. These problems of solid-state equilibria are so serious, that apparently much of the reported work is based on the interpretation of non-equilibrium structures. For example, investigators often find three or even four metal-boron phases present in samples annealed at several different temperatures, but under equilibrium conditions three phases can coexist only at an invariant temperature, while four phases can never coexist at equilibrium in a binary system.

Finally, boron losses from the surface can produce composition gradients within a specimen and thus lead to erroneous conclusions regarding equilibrium. For example, in addition to introducing an error in the average composition, boron vaporization may lead to the appearance of new phases on the surface. This surface phase can have equilibrium properties which are not characteristic of the homogeneous sample of the average composition. Under these circumstances, the construction of an accurate phase diagram depends largely on the skill of the investigator in designing experiments and interpreting the results.

Much of the published work does not contain sufficient detail of the experimental procedures and the results to determine how the investigators handle these various factors. Therefore, a critical evaluation of the various metal-boron phase diagrams is not possible. In general, it appears that the intermediate phases which can occur are well established, while the exact details of the diagram, i.e. the invariant reactions, may or may not be correct. The following summary of phase diagrams of interest in this program is a collection of the diagrams as reported by the various authors.

2. Titanium-Boron System

The phase diagram determined by Palty, Margolin, and Nielsen[2] is shown in Fig. 86. Although equilibrium could only be achieved at low boron contents, the authors were able to construct the higher boron (up to TiB_2) portion of the diagram by an analysis of cast and heat-treated structures.* Except for some uncertainty in the temperatures of invariant reactions, this diagram appears to be essentially correct.

The structures of the intermediate phases in the titanium-boron system are summarized in Table 62. Although several authors reported a face-centered cubic structure for TiB, the work of Decker and Kasper[3] has established that this phase has an orthorhombic (B27) structure.

3. Zirconium-Boron System

The phase diagram reported by Glaser and Post[4] is shown in Fig. 87. Schedler[5] has proposed a different temperature range for the ZrB phase. The alternate diagram is shown in Fig. 88. With the available information, it is not possible to judge which of these diagrams is more accurate.

Experiments conducted in the present program show that the reported eutectic temperature is too high. Our results indicate that the eutectic lies below 1650°C. Further, the eutectoid decomposition temperature of ZrB_{12} is higher than 1730°C. The results of diffusion couple experiments at 1000° and 1400°C are in accord with the phase diagram proposed by Schedler[5].

*It is interesting to note that the cast structures proved quite helpful in classifying several of the invariant reactions (i.e. eutectic, peritectic, etc.). This technique might also be used with success in further studies of the other metal-boron diagrams.

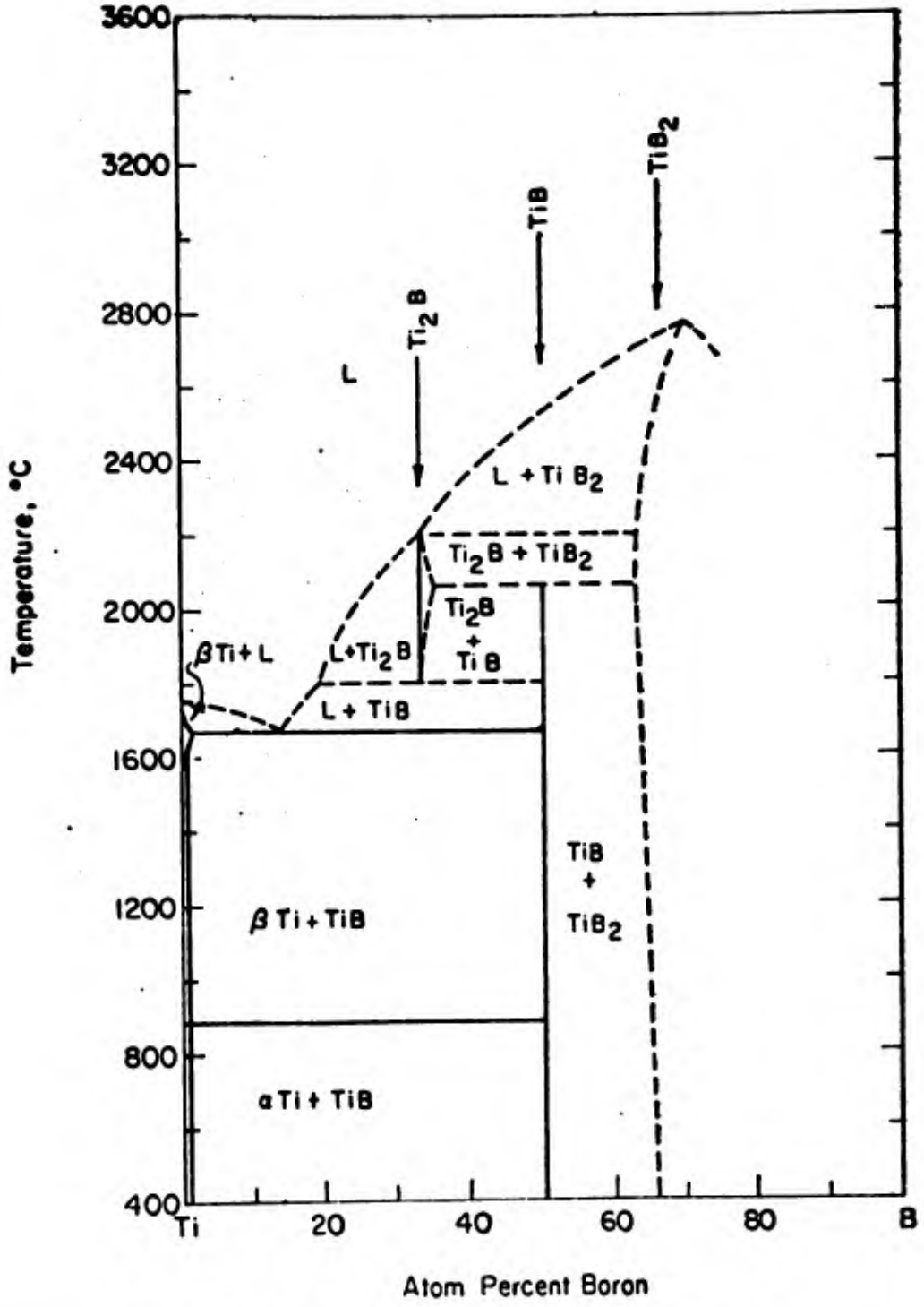

Fig. 86 - Titanium-Boron System (Palty, et al., Ref. 2).

Table 62

Intermediate Phases in the Titanium-Boron System

Phase	Structure	Parameters(Å)	Reference
Ti_2B	Tetragonal		10
	Tetragonal	a = 6.10 c = 4.53	2
		or a = 5.24 c = 7.602	
TiB	Cubic(B-1)	a = 4.26	10
	Cubic(B-3)	a = 4.20	11
	Cubic(B-1)	a = 4.26	2
	Orthorhombic(B27)	a = 6.12 b = 3.06 c = 4.56	3
TiB_2	Hexagonal(C32)		12
	Hexagonal		10
	Hexagonal(C32)	a = 3.03 c = 3.21	2
	Hexagonal(C32)	a = 3.028 c = 3.230	13
	Hexagonal(C32)*	a = 3.030 c = 3.229	
Ti_2B_5	Hexagonal($D8_h$)	a = 2.98 c = 13.98	23

---

* 66.4-66.7 a/o B, See Section VIII.

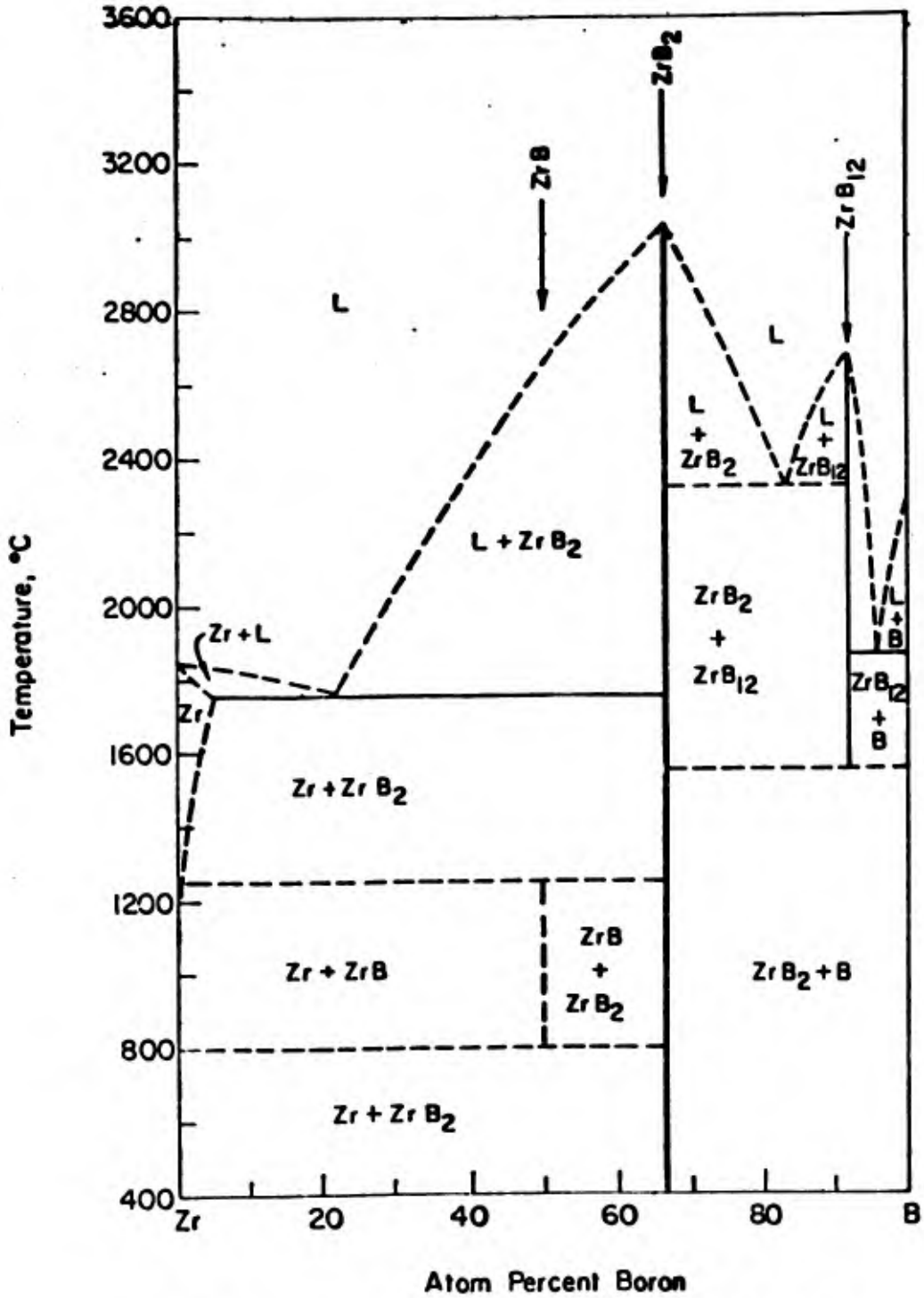

Fig. 87 - Zirconium-Boron System (Glaser and Post, Ref. 4).

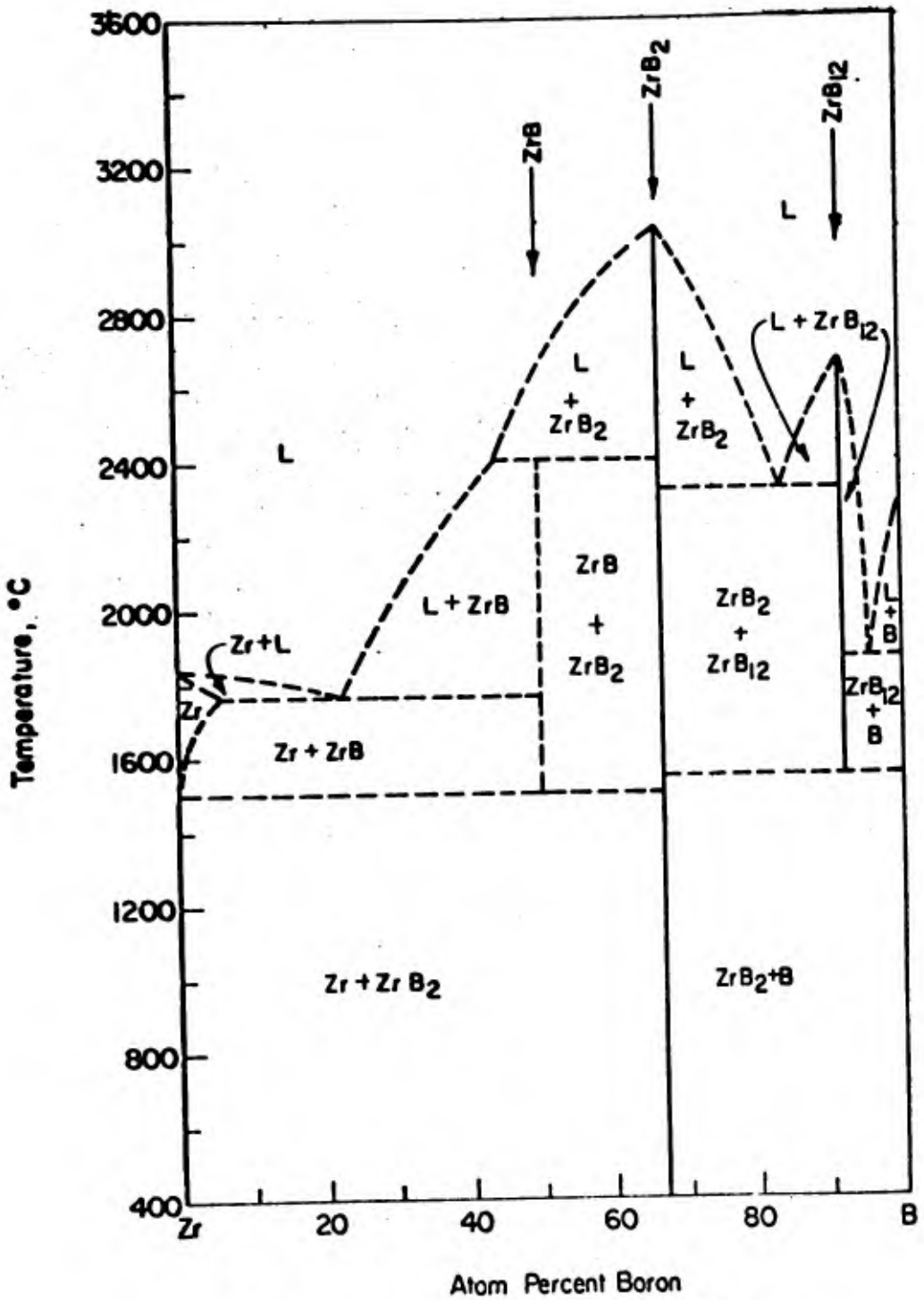

Fig. 88 - Zirconium-Boron System (Schedler, Ref. 5).

The intermediates phases in the zirconium-boron system are summarized in Table 63. The monoboride has been indexed as a face-centered cubic phase, but the establishment of the orthorhombic (B27) structure for TiB[3] and HfB[6] suggests that ZrB may also be orthorhombic[7].

4. Hafnium-Boron System

The phase diagram reported by Nowotny et al[6] is presented in Fig. 89. The structures of HfB and HfB_2 are summarized in Table 64.

5. Niobium-Boron System

Nowotny, Benesovsky, and Kieffer[8] have reported the phase diagram shown in Fig. 90. In the same paper, these authors presented a similar diagram for the tantalum-boron system (see Fig. 91). However, as discussed in the following section, Leitnaker[9] has proposed a tantalum-boron diagram which differs from that of Nowotny et al[8]. If the work of Leitnaker should prove to be correct in the tantalum-boron system, the niobium-boron diagram should be reinvestigated.

The structures of the intermediate phases in the niobium-boron system are collected in Table 65.

6. Tantalum-Boron System

The diagram proposed by Nowotny et al[8] is shown in Fig. 91. Leitnaker[9] has determined a partial diagram, shown in Fig. 92, which differs significantly from that of Nowotny and co-workers. According to Leitnaker[9] TaB has a higher melting point, Ta_2B is stable only at high temperatures, and the liquidus curves must be considerably higher than the reported values. This apparent discrepancy should be resolved.

Table 63

Intermediate Phases in the Zirconium - Boron System

Phase	Structure	Parameters(Å)	Reference
ZrB	Cubic(B1)	a = 4.65	4
	Orthorhombic(B27)	NONE REPORTED	7
ZrB_2	Hexagonal(C32)	a = 3.170 c = 3.533	12
	Hexagonal(C32)	a = 3.170 c = 3.533	4
	Hexagonal(C32)	a = 3.169 c = 3.530	14
	Hexagonal(C32)	a = 3.168 c = 3.528	13
	Hexagonal(C32)*	a = 3.171 c = 3.527	
ZrB_{12}	Cubic(B1)	a = 7.408	4
	Cubic(B1)	a = 7.408	15

---

*65.2-65.4 a/o B, See Section VIII.

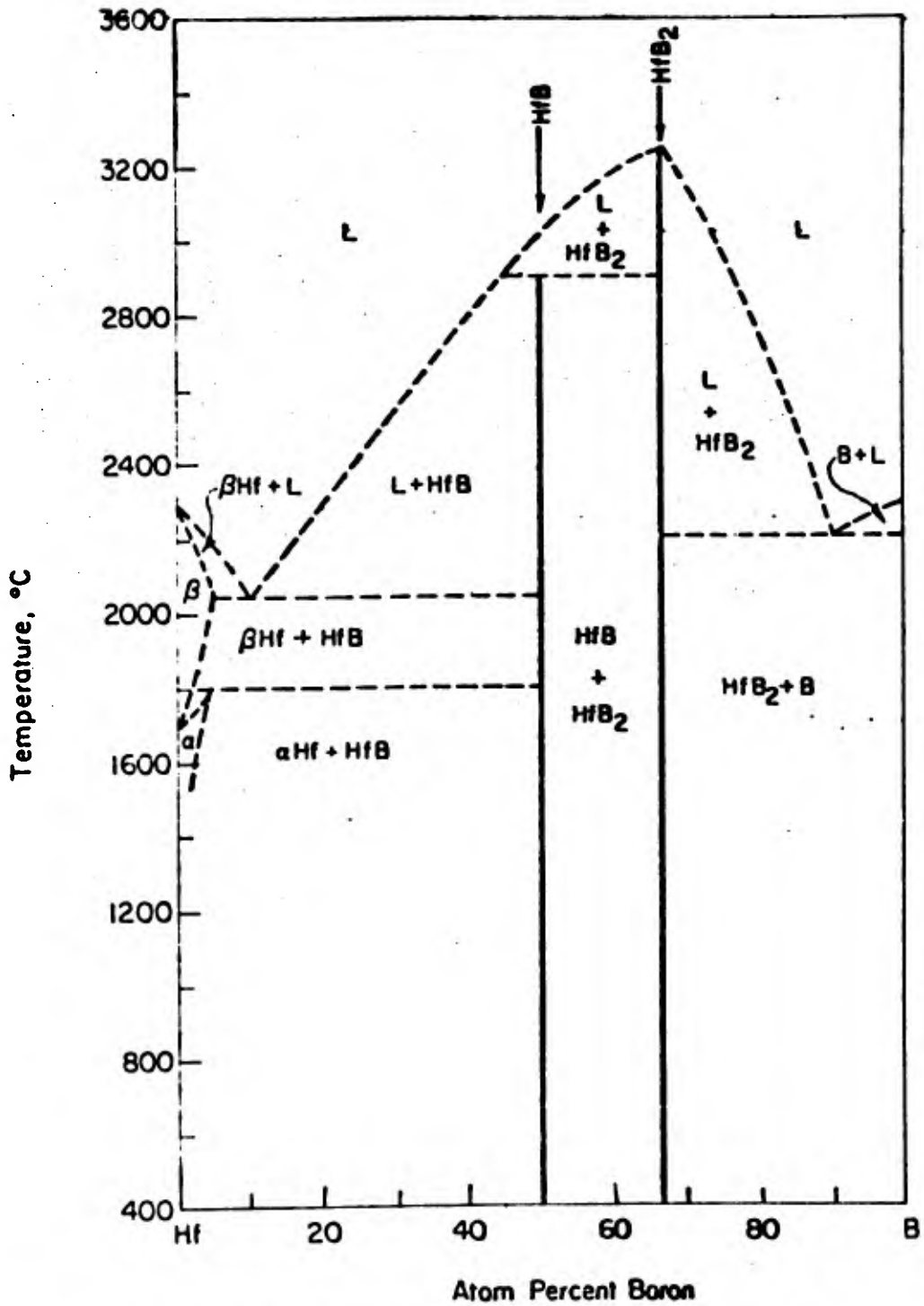

Fig. 89 - Hafnium-Boron System (Nowotny, et al., Ref. 6).

Table 64

Intermediate Phases in the Hafnium - Boron System

Phase	Structure	Parameters(Å)	Reference
HfB	Cubic(B1)	a = 4.62	16
	Orthorhombic(B27)	a = 6.50_2 b = 3.21_2 c = 4.82_9	6
HfB_2	Hexagonal(C32)	a = 3.141 c = 3.470	16
	Hexagonal(C32)		6
	Hexagonal(C32)		7
	Hexagonal(C32)*	a = 3.1410 c = 3.4761	

---

*66.3 a/o B, See Section VIII.

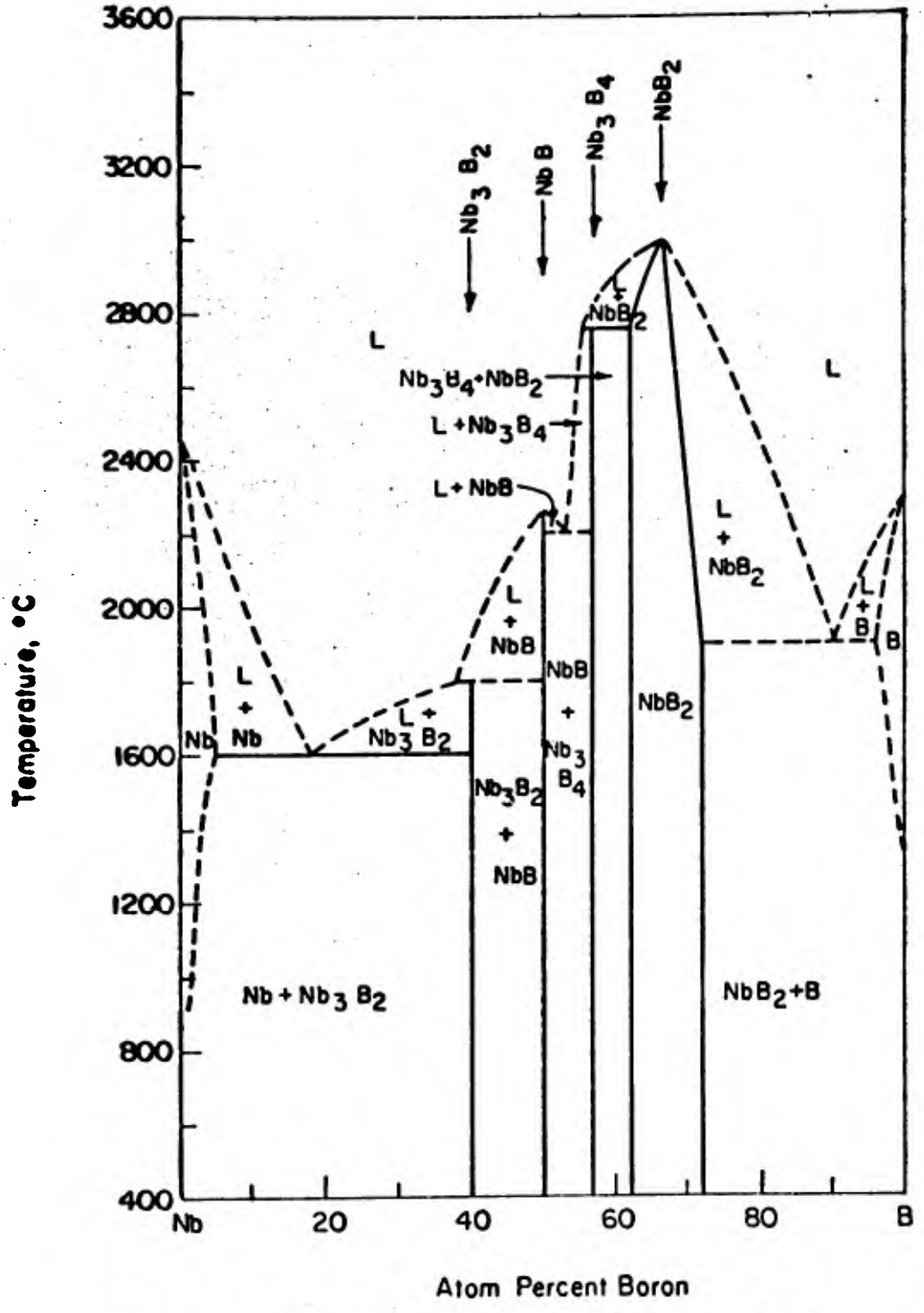

Fig. 90 - Niobium-Boron System (Nowotny, et al., Ref. 8).

Table 65

Intermediate Phases in the Niobium-Boron System

Phase	Structure	Parameters(Å)	Reference
Nb_3B_2	Tetragonal(U_3Si_2)	a = 6.173 c = 3.274	8
NbB	Orthorhombic(B27)	a = 3.292 b = 8.713 c = 3.165	13
	Orthorhombic(B27)	a = 3.298 b = 8.724 c = 3.166	17
Nb_3B_4	Orthorhombic	a = 3.30 b = 14.1 c = 3.13	13
	Orthorhombic	a = 3.305 b = 14.08 c = 3.137	17
	Orthorhombic(Mn_3B_4)	-	8
NbB_2	Hexagonal(C32)	a = 3.110 c = 3.264	13
	Hexagonal(C32)	a = 3.089 c = 3.304	17
	Hexagonal(C32)		12
	Hexagonal(C32)*	a = 3.111 c = 3.260	18
	Hexagonal(C32)**	a = 3.093 c = 3.305	18
	Hexagonal(C32)***	a = 3.107 c = 3.282	

---

*65 ^{a}/o B; **70 ^{a}/o B, See Section VIII.

***66.6 ^{a}/o B, See Section VIII.

The structures of the various intermediate phases in the tantalum-boron system are summarized in Table 66.

C. Experimental Procedures

1. Diffusion Couples

Diffusion couples are formed by placing two dissimilar metals in intimate contact with each other and allowing interdiffusion to occur until equilibrium is attained at elevated temperatures. The materials used contain only two elements and the diffusion couple will consist of layers of as many single phases as are present between the two starting compositions. In addition the total compositional ranges of the phases will be present. In the present study it was originally proposed that two couples be made for each refractory boride: 1) metal plus metal diboride, and 2) boron plus metal diboride. By analyzing the diboride from its edge to the interface in each couple with an electron microprobe it is possible to determine the compositional limits at the equilibrating temperature.

The following is the general procedure used for studying diffusion couples:

a. Wafers of the metals, the diborides, and boron are cut to approximately 0.25 inches in diameter and 0.080 inches thick.

b. The wafers are prepared as parallel metallographic surfaces, using the normal procedures.

c. After preparation, the wafers are inserted into pressure welding jigs (cf. Fig. 93) similar to those developed by E. M. Passmore[21]. The pressure welding jig operates on the principle of differential thermal expansion.

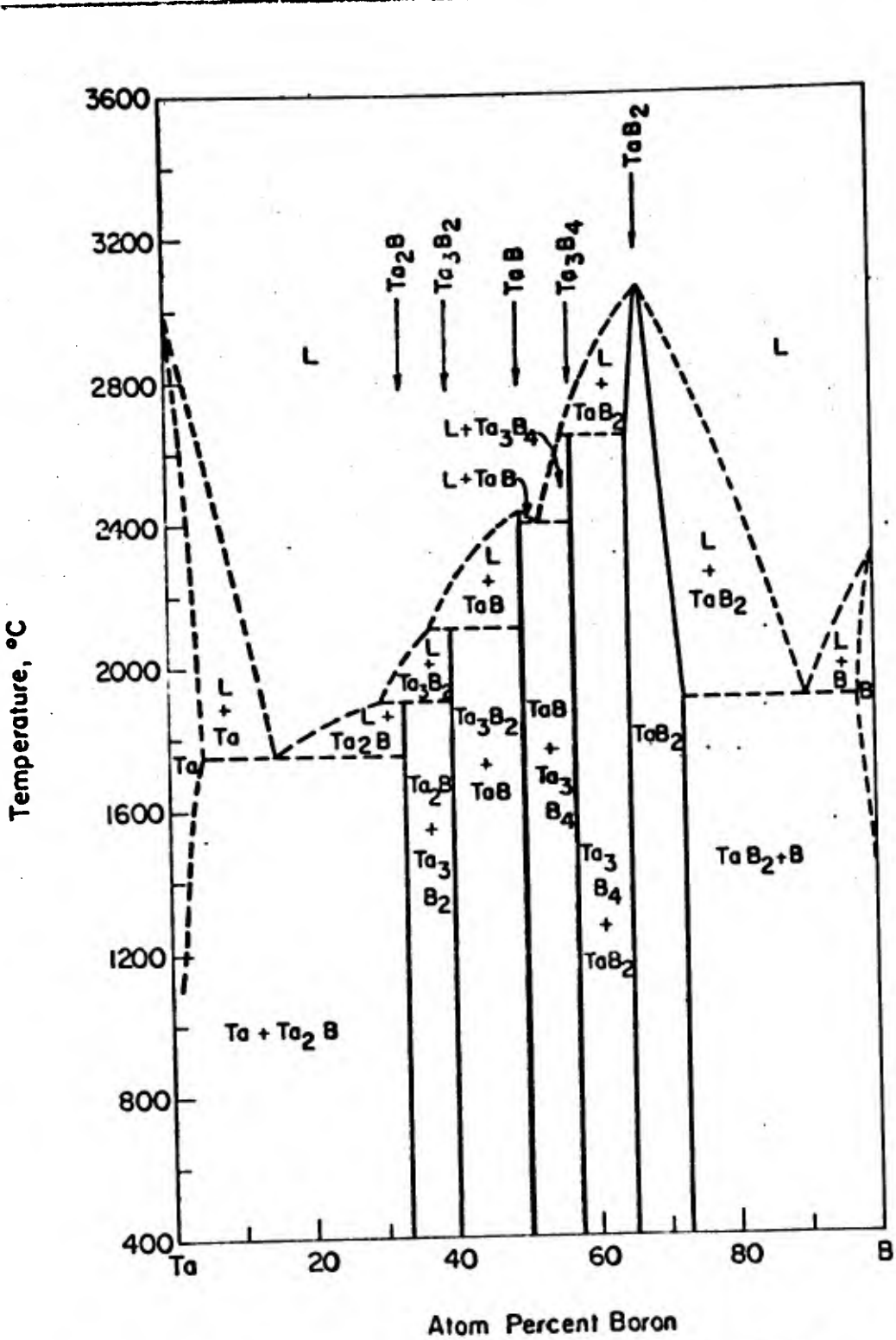

Fig. 91 - Tantalum-Boron System (Nowotny, et al., Ref. 8).

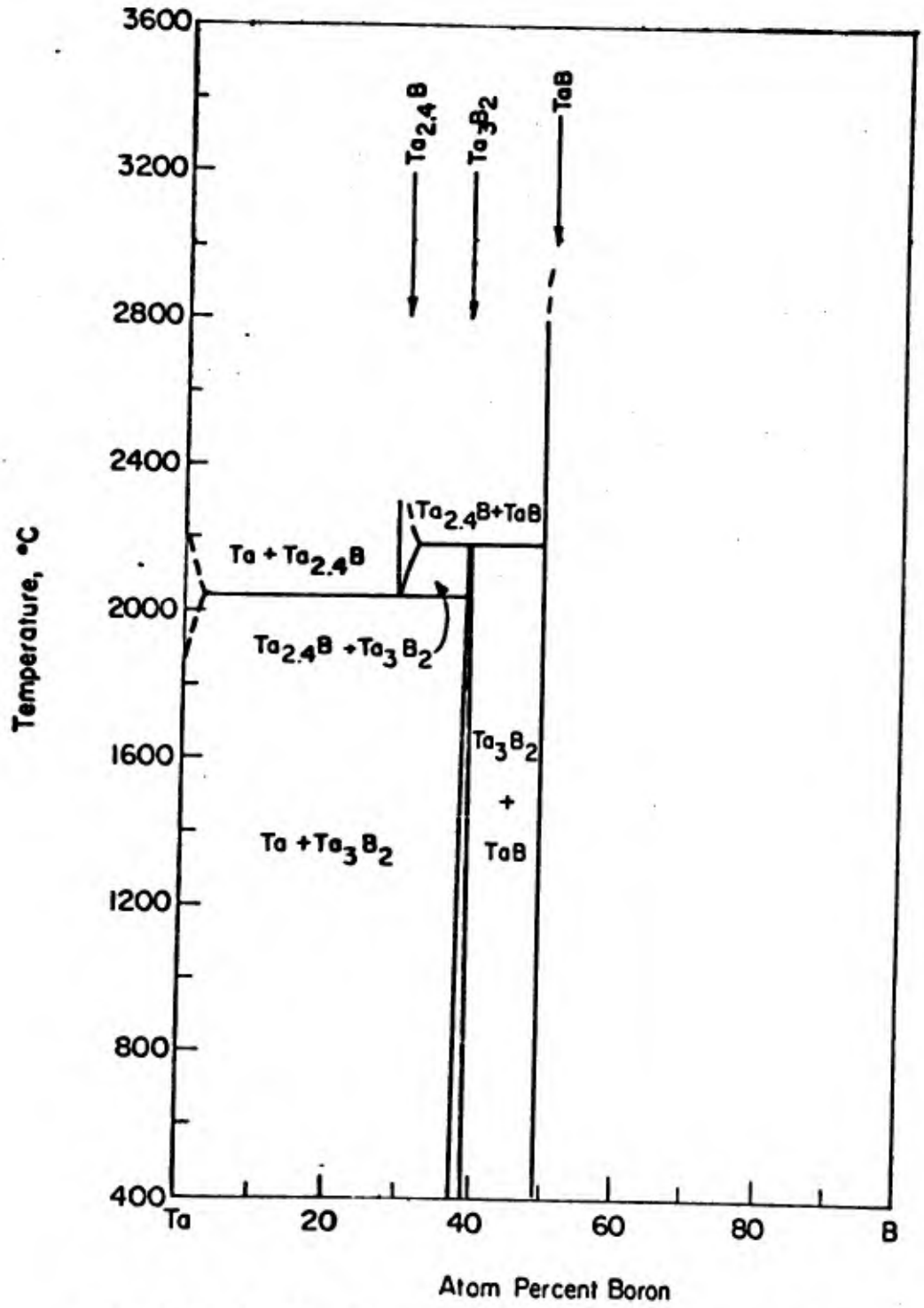

Fig. 92 - Tantalum-Boron System (Leitnaker, et al., Ref. 9).

Table 66

Intermediate Phases in the Tantalum - Boron System

Phase	Structure	Parameters(Å)	Reference
Ta_2B	Tetragonal	a = 5.778 c = 4.864	17
	Tetragonal	a = 5.785 c = 4.867	13
	Tetragonal(C16)	———	8
	Tetragonal	a = 5.779 c = 4.8644	9
	Tetragonal	a = 5.778 c = 4.864	19
Ta_3B_2	Tetragonal	a = 6.18_4 c = 3.28_6	20
	Tetragonal(U_3Si_2)	a = 6.172 c = 3.280	8
	Tetragonal	a = 6.175 c = 3.284	9
TaB	Orthorhombic	a = 3.276 b = 8.669 c = 3.157	17
	Orthorhombic	same as above	13
	Orthorhombic(CrB type)	———	8
Ta_3B_4	Orthorhombic(Mn_3B_4type)	———	8
	Orthorhombic	———	17
	Orthorhombic	———	13

Table 66 (Cont'd)

Phase	Structure	Parameters(Å)	Reference
$TaB_{2.57}$	Hexagonal(C32)	a = 3.060 c = 3.290	13
	Hexagonal(C32)	a = 3.057 c = 3.291	17
$TaB_{1.78}$	Hexagonal(C32)	a = 3.097 c = 3.227	13
	Hexagonal(C32)	a = 3.099 c = 3.224	17
TaB_2	Hexagonal(C32)	———	8
TaB_2	Hexagonal(C32)*	a = 3.085 c = 3.240	— —

*66.1 a/o B, See Section VIII.

d. The assembled jigs are then heated to the desired temperatures for a time sufficient to allow the diffusion interface to move approximately 0.020 inch.

e. Initial examination is metallographic. The diffusion couple is sectioned perpendicular to the polished surface, then metallographically prepared, etched, and examined, for weld soundness, diffusion depth, and appearance of intermediate phases.

f. The diffusion couples are prepared for microprobe analysis using mechanical polishing techniques. The diboride phases are then scanned perpendicular to the interfaces by an electron microprobe analyzer. A plot of composition versus distance from the interface, extrapolated to both the metallic and boron interfaces will give the terminal compositions of the diboride at the equilibrating temperature.

2. Off-Stoichiometric Alloys

A complementary method for studying the compositional limits of the diboride phases is to make a series of alloys in the two phase fields to the left and right of the diboride phase. The compositional limits are given directly by electron microprobe analysis; in the two phase field only the amounts of the two phases change with composition.

In the course of the program on the zone refining subtask, several samples of two-phase alloys were prepared in the preliminary experiments for a given diboride. Such high purity material can be useful for the phase boundary determinations. This supply of two phase alloys must be complemented by a series of arc-melted samples. The two-phase alloys are equilibrated at temperature. Metallographic analysis before and after equilibration is used to check the samples prior to the electron microprobe analysis.

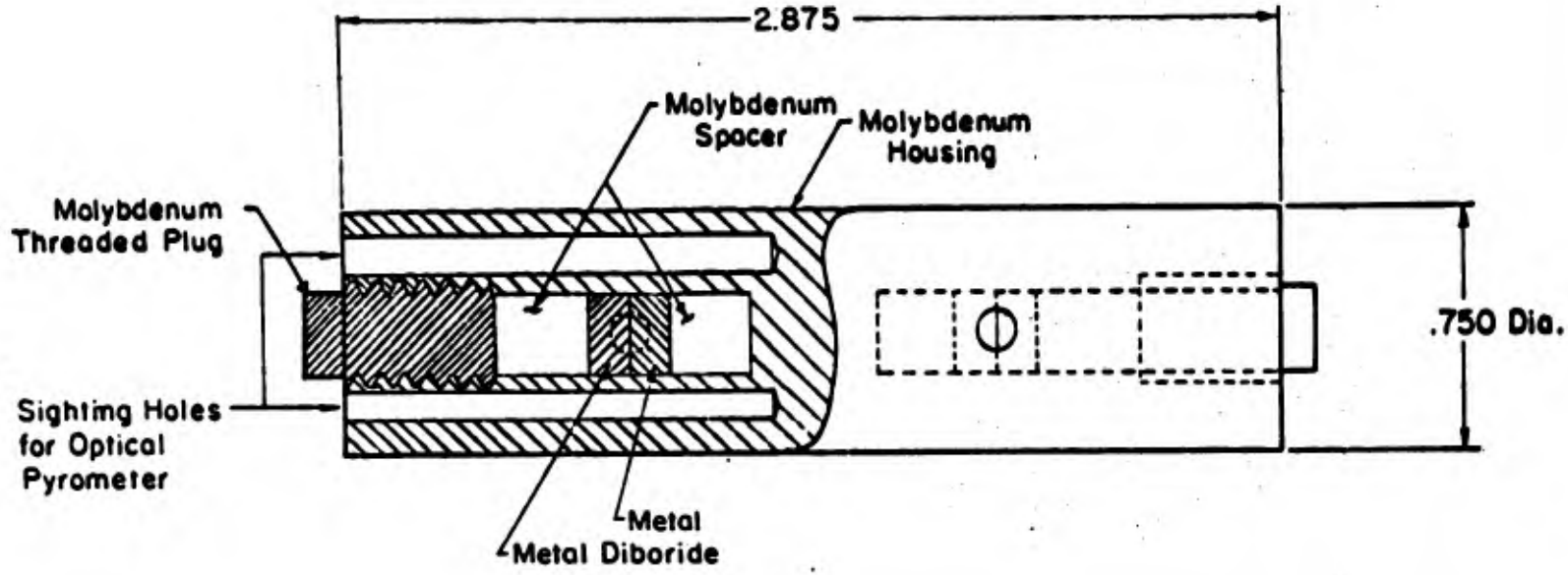

Fig. 93 - Molybdenum Pressure Welding Apparatus for Diffusion Couples.

3. Vapor Pressure Measurements

In principle, the measurement of vapor pressure as a function of composition and temperature can be used to obtain phase boundary data. In practice this may be the only technique for obtaining such data at very high temperatures, but the measuring technique does not lend itself to applications which involve a large number of samples. Accurate and precise measurements are extremely difficult to obtain; the nature of the measurements require a considerable length of time for completion.

D. Results and Discussion

1. General Considerations

Before discussing the available results it is appropriate to consider the experimental limitations of the techniques that are applicable to phase boundary determinations. High temperature limits for the diffusion couple technique are set by the eutectic temperatures which lie between metal and diboride and between boron and diboride. The two-phase alloy technique can be used to extend the temperature range up to a region where a liquid phase becomes the second phase in equilibrium with the diboride. In practice, still lower operating temperatures may be fixed by the relatively higher vapor pressure of boron. Low temperature limits are set by time requirements for the attainment of equilibrium for either technique. The limitations of the vapor pressure technique are operational as discussed in the previous section.

In the present study the diffusion couple technique was chosen for the lower temperature regions. The physical characteristics of the available zone refined material limited the application of this technique to the Hf-B and the Zr-B systems. As an alternate procedure an attempt was made to prepare

diffusion couples between boron and metal. The high vapor pressure of boron caused a reaction on the surface of the metal which produced the diboride phase but a diffusion couple as such did not form. From these results (Table 65) it now appears that neither boron/diboride couples nor two phase alloys involving boron as a second phase would be feasible for these systems.

In the light of the variety of experimental difficulties concerning the attainment of equilibrium and the limited availability of physically sound diboride samples, the problems in the determination of the compositional limits of the diboride phases in particular and the problems in the determination of the phase diagrams in general should be investigated from the semi-theoretical approach which has been successfully applied to the refractory metal carbides[22]. In this report the extreme phase boundary limits of the diboride phase were calculated from the previously reported thermodynamic model[22] and the available experimental data. The calculation of the more important aspects of the metal-boron phase diagrams must await the determination of several points from experimental phase diagram work and the compilation of additional thermodynamic data.

2. Zirconium-Boron System

The experimental program for the phase boundary determinations in the Zr-B system was planned on the basis of the available phase diagram data. The zone refining subtask supplied both physically sound single phase material and a limited quantity of high purity two phase alloys. High purity zirconium metal was available from ManLabs inventory; this material was characterized by qualitative spectroscopic analysis, vacuum fusion analysis for hydrogen

and nitrogen, and metallographic procedures. High purity zone refined boron was purchased from the Eagle Picher Co. Accordingly, both the two phase alloy technique and the diffusion couple experiments were initiated for this system.

As indicated in the section on phase diagrams, the available information suggests twodifferent temperature ranges of stability for the monoboride phase, and two different crystal structures. The latter disagreement is also found in the Hf-B and the Ti-B systems.

Experimental conditions and results for diffusion couple experiments and for two phase alloy equilibration are presented in Table 67. The formation of a liquid phase in the attempted diffusion couples, Zr/ZrB_2, at temperatures above 1650°C and the consequent loss of metal and boron prevented the attainment of equilibrium in these experiments. Metallographic examination of the original Zr/ZrB_2 interfaces for the latter experiments showed a eutectic structure. The photomicrograph of a typical area is presented in Fig. 94. These results demonstrate that the eutectic temperature between Zr and the metal-boron phase is less than 1650°C; this conclusion is contrary to both of the reported phase diagrams (see Figs. 87 and 88) for this system. The indentification of a face centered cubic monoboride in the quenched specimens and possibly in the eutectic can not be related to the equilibrium at 1650°C at this time. Further, in any attempt to draw conclusions from these results concerning the controversy over the structure of the monoboride, it is important to note that these experiments were performed in argon in a carbon tube furnace. Accordingly, the phase identified by X-ray diffraction as face centered cubic in the experiments summarized in Table 67. as the monoboride, could also be a ternary cubic phase of metal, boron and carbon with a slightly different lattice parameter. Carbon stabilization of cubic phases of the metals of Groups IVa and Va is well known.

Table 67

Phase Boundary Experiments* in Metal-Boron Systems

Exp.	Components	Temp. (°C)	Time (Hrs.)	Post Quenching Analysis		
				Metallographic	X-ray Diffraction	Electron Probe
D-2	Zr/ZrB_2	1850	3	Zr melted	----------	-
d-2	ZrB_2 + 2nd phase	1850	3	Two phases	----------	-
D-4	Zr/ZrB_2	1750	8	Zr melted	----------	-
d-3	ZrB_2 + 2nd phase	1730	12	Two phases	----------	Matrix: 80.8 w/oZr, B/Me = 2.02 2nd phase: < 0.1 w/oZr
d-5	Zr/ZrB_2	1770	12	Zr melted, Eutectic formed	ZrB_2 ZrB (cubic) No Zr	-
D-6	Zr/ZrB_2	1650	11	Zr melted, Eutectic formed	ZrB_2 ZrB (cubic) No Zr	-
D-7	Zr/ZrB_2	1500	24	Sound couple No intermediate phase	----------	-
D-8	Zr/ZrB_2	1400	24	Sound couple No intermediate phase	----------	ZrB_2: 81.1 w/oZr, B/Me = 1.97
D-9	Zr/ZrB_2	1000	116	Sound couple No intermediate phase	----------	ZrB_2: 80.9 w/oZr, B/Me = 1.99
D-10	Nb/B	1400	24	No couple, diboride formed on Nb surface	NbB_2	-
D-11	Nb/B	1400	114	No couple, diboride formed on Nb surface	NbB_2	-
D-12	Ta/B	1400	114	No couple, diboride formed on Ta surface	TaB_2	-

*All experiments at temperatures above 1500°C were performed in an argon atmosphere inside the molybdenum sample holder (see Fig. 93) in a carbon tube furnace; all experiments at 1500°C and lower temperatures, in an argon atmosphere inside the same sample holder in a globar type furnace.

The results of the two phase alloy equilibration at 1730°C and the Zr/ZrB_2 diffusion couple experiments at 1000°C and 1400°C confirm the reported narrow range of homogeneity for ZrB_2 but are not in accord with the proposed[4,5] eutectoid temperature for ZrB_{12}. In addition, metallographic inspection of the two-phase alloy equilibrated at 1730°C show some evidence for a eutectoid structure. The average zirconium composition in the region of this structure is 43 w/o Zr, $^{B}/_{Me}$ = 11. The absence of one intermediate phase between Zr and ZrB_2 in the diffusion couple experiment at 1000°C is in accord with the phase diagram reported by Schedler[5]. The composition limits determined at 1000° ($^{B}/_{Me}$ = 1.99) and 1400°C ($^{B}/_{Me}$ = 1.97) are in reasonable agreement with the calculated maximum limits for these temperatures, $^{B}/_{Me}$ = 1.97 and $^{B}/_{Me}$ = 1.93 respectively in Table 68. The composition limit determined at 1730°C, ($^{B}/_{Me}$ = 2.02), is considerably below the maximum calculated limit, ($^{B}/_{Me}$ = 2.10), in Table 68. This latter difference may be due to the appearance of a liquid phase or ZrB_{12} will be investigated when more data are available.

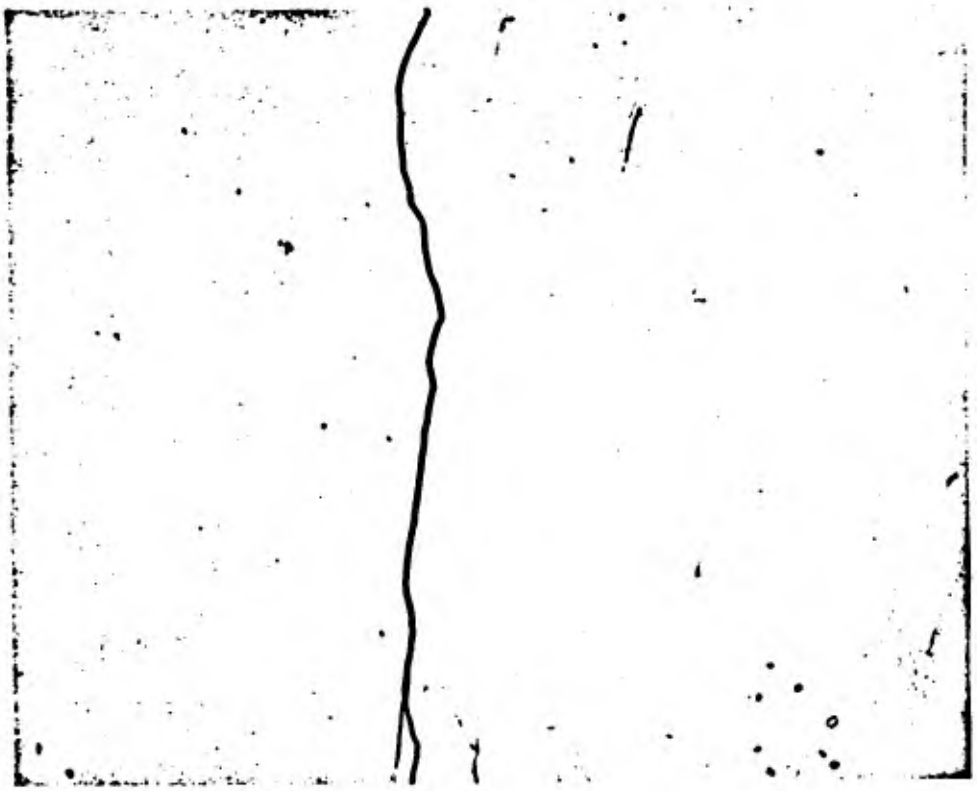

Fig. 94 - Zr/ZrB_2 interface after 12 hours at 1770°C.
(Note: eutectic structure on metal rich side)

3. Calculation of Maximum Limits of Solubility of the MeB_2^{η} Phase

This calculation is made ignoring any intermediate compound phases which may exist between pure metal Me, the η phase, and pure B on the phase diagram, and assumes that there is little solubility of Me in B and B in Me. The quantity $x_{\eta 1}$ is defined as the true metal rich boundary and $x_{\eta 2}$ as the true boron rich boundary of the MeB_2^{η} phase on the real phase diagram. If $x_{\eta Me}$ and $x_{\eta B}$ are the phase boundaries of the η phase, calculated by assuming no intermediate compound phases and little solubility of Me in pure B and B in pure Me then

$$x_{\eta Me} < x_{\eta 1} < 2/3 \qquad (1)$$

and

$$x_{\eta B} > x_{\eta 2} > 2/3 \qquad (2)$$

Eqs. 6 and 11 of Section XX yield

$$\ln(2-3x_{\eta Me})\,4^{-1/6} = -(RT)^{-1}(-13,000-\Delta H^{\eta}[0^{\circ}K]-0.75\gamma^{\eta}T^{2}-0.5\phi^{o}_{Me}) - \frac{3}{2}\ln\theta^{\eta}_{Me}\theta^{-1}_{Me} \qquad (3)$$

while Eqs. 7 and 14 of Section XX yield

$$\ln(3x_{\eta B}-2)4^{-1/6} = -(RT)^{-1}(26,000+0.5\Delta H^{\eta}[0^{\circ}K]-2\phi^{o}_{B})-6\ln\theta^{\eta}_{B}\theta^{-1}_{B} \qquad (4)$$

By using Eqs. 3 and 4 along with the numerical results for the parameters detailed in Sections XVI, XVII, and XX, values of $x_{\eta Me}$ and $x_{\eta B}$ for the diborides of interest can be computed over the range 800° - $2000^{\circ}K$.

Table 68

Calculated Maximum Limits of the MeB_2^{η} Phase

$x_{\eta Me}$:(B/Me) at $x_{\eta Me}$

	800°K	1200°K	1600°K	2000°K
TiB_2	0.666(1.99)	0.662(1.96)	0.656(1.91)	0.650(1.86)
ZrB_2	0.666(1.99)	0.664(1.98)	0.660(1.94)	0.655(1.90)
HfB_2	0.666(1.99)	0.664(1.98)	0.659(1.93)	0.655(1.90)
NbB_2	0.664(1.98)	0.653(1.88)	0.640(1.78)	0.625(1.67)
TaB_2	0.660(1.94)	0.646(1.82)	0.629(1.70)	0.589(1.43)

$x_{\eta B}$: (B/Me) at $x_{\eta B}$

TiB_2	0.668(2.01)	0.668(2.01)	0.669(2.02)	0.674(2.07)
ZrB_2	0.668(2.01)	0.668(2.01)	0.671(2.04)	0.679(2.10)
HfB_2	0.668(2.01)	0.668(2.01)	0.670(2.03)	0.677(2.10)
NbB_2	0.668(2.01)	0.668(2.01)	0.670(2.03)	0.675(2.08)
TaB_2	0.668(2.01)	0.668(2.01)	0.669(2.02)	0.673(2.06)

These values are based on the considerations of Section XX and are tentative.

REFERENCES

1. Samsonov, G.V. and Portnoy, K.I., "Alloys Based on High Melting Compounds", FTD-TT-62-430.
2. Paltry, A.E., Margolin, H. and Nielsen, J.P., Trans. ASM, (1954) 46 312.
3. Decker, B.F. and Kasper, J.S., Acta. Cryst., (1954) 7 77.
4. Glaser, F.W. and Post, B., Trans. AIME, (1953) 197 1117.
5. Schedler, W., Dissert. Techn. Hochsch, Graz. (1952).
6. Nowotny, H., Braun, H. and Benesovsky, F., Radex-Rundschau, (1960) 6 367.
7. Rudy, E. and Benesovsky, F., Monat. Chem., (1961) 92 415.
8. Nowotny, H., Benesovsky, F. and Kieffer, R., Zeit. Metalkde., (1959) 50 417.
9. Leitnaker, J.M., "Thermodynamic Properties of Refractory Borides", Los Alamos Scientific Laboratory, Report LA-2402, 13 April 1960.
10. Glaser, F.W., Trans. AIME, (1952) 194 391.
11. Ehrlich, P., Zeit. anorg. allgem. Chem., (1949) 259 1.
12. Norton, J.T., Blumenthal, H. and Sindeband, S.J., Trans. AIME, (1949) 185 749.
13. Brewer, L., et al, J. Am. Cer. Soc., (1951) 34 173.
14. Kiessling, R., Acta Chem. Scand., (1949) 3 90.
15. Post, B. and Glaser, F.W., Trans. AIME, (1952) 194 631.
16. Glaser, F.W., Moskowitz, D. and Post, B. Trans. AIME, (1953) 197 1119.
17. Kiessling, R., Acta. Chem. Scand., (1949) 3 603.
18. Nowotny, H., et al, Monat. Chem., (1960) 91 975.
19. Anderson, L.H. and Kiessling, R., Acta. Chem. Scand., (1950) 4 1960.

20. Nowotny, H. and Wittman, A., Monat. Chem., (1958) 89 220.

21. Passmore, E.M., et al, "Investigation of Diffusion Barriers for Refractory Metals", TR-60-343, ManLabs, Inc., August, 1960.

22. Kaufman, L. and Clougherty, E.V., "Thermodynamic Factors Controlling the Stability of Solid Phases at High Temperatures and Pressures" to be published by AIME and Interscience Publishers in "Metallurgy at High Temperatures and Pressures" (1963).

23. Post, B. and Glaser, F.W., J. Chem. Phys., (1952) 20 1050.

XIX. VAPOR PRESSURE*

A. Introduction

The purpose of vapor pressure measurements on the diborides is two-fold: (1) to establish the boundaries of the diboride phase, and (2) to determine the vapor pressure over this phase and the associated thermodynamic properties.

For niobium diboride, the first material to be investigated in the present program, the vapor pressure of each element changes with composition in the single phase NbB_2 region and remains constant over the two phase regions, NbB_2-B and Nb_3B_4-NbB_2. The limits of the diboride phase may be found by measuring the rate of evaporation, or of effusion, of NbB_2 starting with the two phase system NbB_2-B. Boron will evaporate preferentially moving the system into the two phase region Nb_3B_4-NbB_2. During this experiment the isothermal evaporation rate curves will consist of three parts: (1) a constant rate controlled by the boron pressure over boron saturated with niobium and by the niobium pressure in equilibrium with boron rich NbB_2, (2) a decreasing rate of boron evaporation commencing with the disappearance of the boron phase and an increasing niobium vaporization rate, where evaporation is governed by partial pressures in equilibrium with the single phase NbB_2 of changing composition, (3) a constant rate controlled by the boron pressure over the metal rich limit of NbB_2 and by the niobium pressure over boron rich Nb_3B_4.

In general, the vapor composition over the two phase regions could be established either by analyzing the initial material and the unevaporated sample

---

* P. E. Blackburn, Arthur D. Little, Inc., Cambridge, Mass.

or by analysis of the condensate. If the weight fraction of boron in the condensate from the two phase region is X_B and the total evaporation rate is G, the pressures of boron and metal over the two phase field will be given by

$$P_B = X_B G \sqrt{\frac{2\pi RT}{M_b}} \qquad (1)$$

and

$$P_M = (1 - X_B) G \sqrt{\frac{2\pi RT}{M_{Me}}} \qquad (2)$$

where G is in $g/cm^2/sec$, R is the gas constant, T the absolute temperature and M_{Me} and M_B the atomic weight of metal and boron respectively. Since the vapor pressure of pure niobium is sufficiently lower than that of pure boron, very little error is introduced by assuming that the total pressure is equal to the vapor pressure of boron over niobium diboride.

All of the data obtained on the diborides of titanium, zirconium, and hafnium have been found by the Knudsen method using tungsten, graphite and B_4C cells. This method has been used because it was found that the diborides appear t. have low evaporation coefficients (from 0.025 to 0.1). Since evaporation rates may be influenced by reaction with the cell, pressure measurements were made by the Langmuir method. A series of experiments on niobium rich NbB_2 has been made and the results are reported below. Measurements have also been made on pure niobium for two purposes: (1) to check the apparatus, and (2) to obtain data on niobium which is more consistent with the diboride data for the calculation of activities than are the literature values based on measurements in other laboratories using other equipment.

B. Apparatus

The equipment for this research may be conveniently divided into three parts: (1) vacuum balance, (2) vacuum system, and (3) furnace and controls. The apparatus is shown in Figs. 95, 96 and 97.

1. Vacuum Balance

The rate of evaporation (or effusion) is detected by measuring the rate of condensation of vapor on a target suspended from an automatic recording vacuum microbalance. The balance consists of a quartz truss beam supported vertically at the fulcrum by fine quartz fibers. The hangdowns at the end of each arm are also quartz fibers sealed directly to the beam and to quartz hooks. The balance is held at the null position automatically by an electromagnet acting on a magnet rod suspended from one arm of the balance. The null position is detected with a variable permeance transducer which surrounds a steel rod hanging below the magnet rod. When the balance is displaced from its null a signal is generated by the transducer controller which drives a potentiometer through a servo mechanism. The potentiometer changes the current flowing in the electromagnet restoring the balance to its null. The current which is proportional to the weight change is recorded continuously.

Measurements on niobium were made using a one mil platinum target on a quartz frame. Interaction of the target with the magnetic field of the induction coil produced an apparent weight loss of around 0.5 $\mu g/^{o}C$ sample temperature. This effect was appreciably reduced by replacing the platinum foil with thin cover glass. Since the generator output is controlled during an experiment, variations in apparent weight with the magnetic field are minimized.

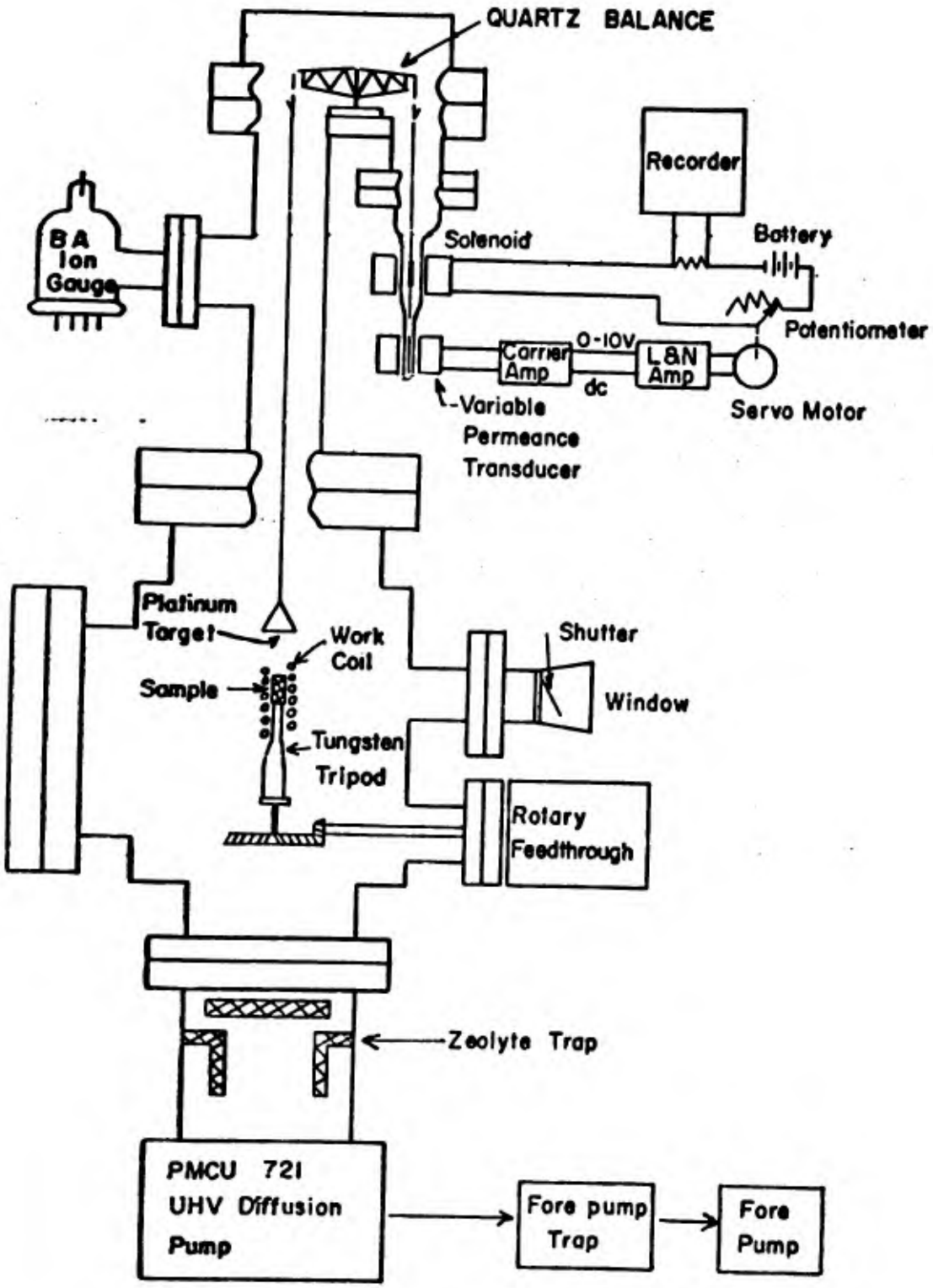

Fig. 95 - Vacuum Microbalance, Induction Furnace and Pumping System.

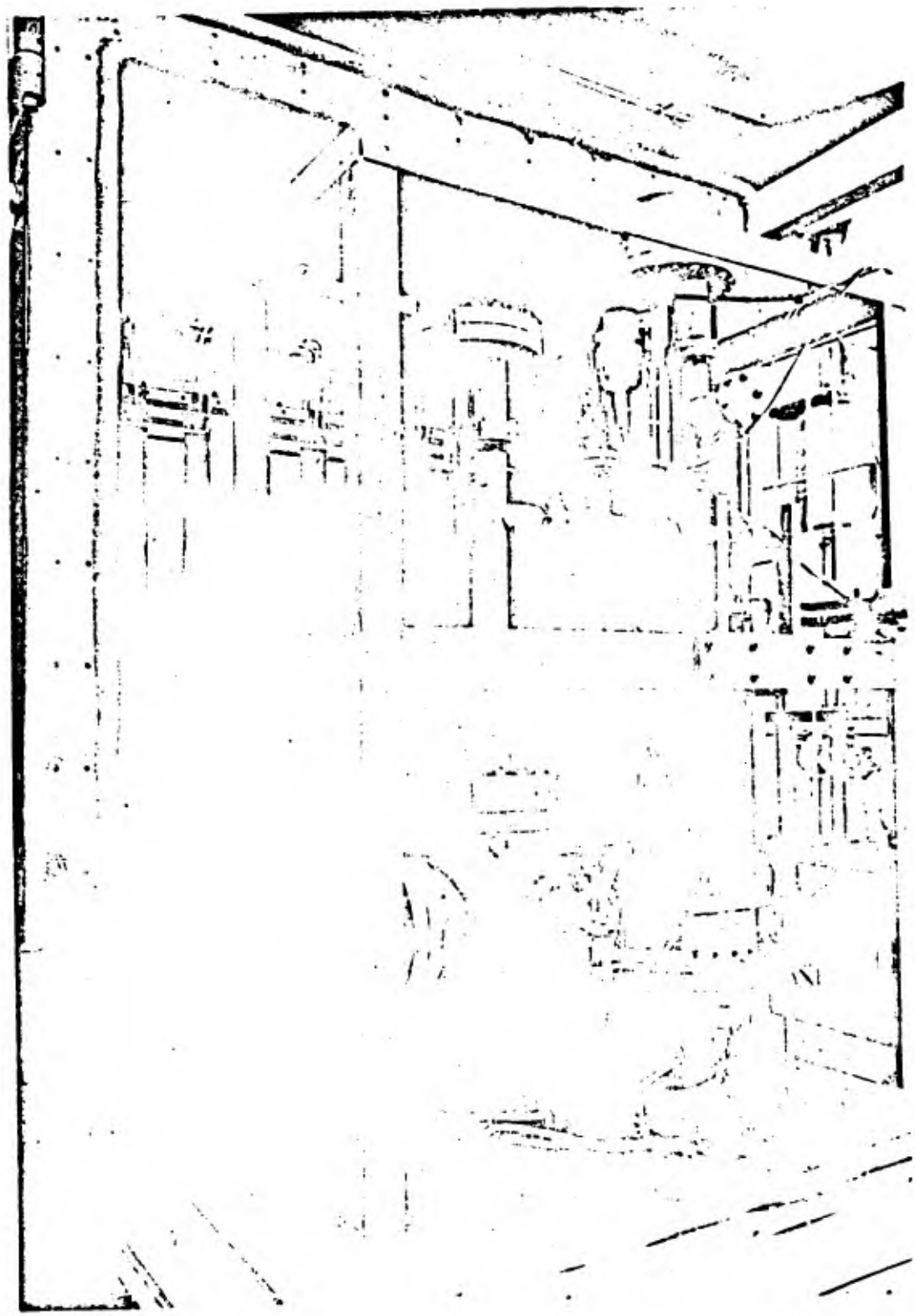

Fig. 96 - Vacuum Microbalance, Induction Furnace and Degassing Oven.

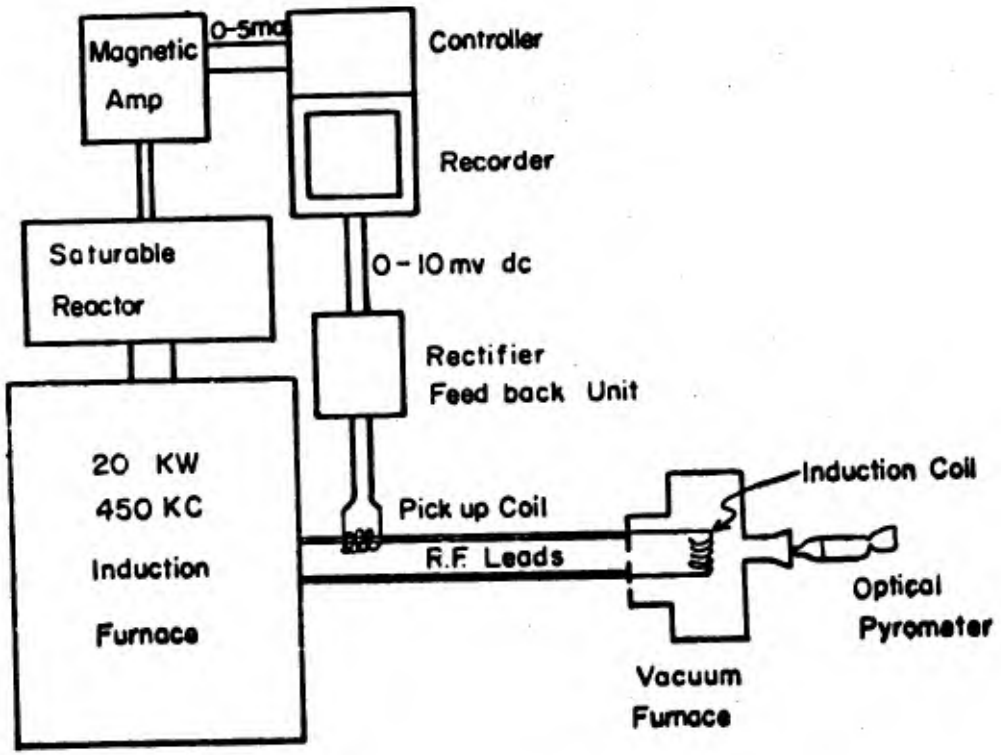

Fig. 97 - Automatic Control of Induction Furnace Output.

2. Vacuum System

The vacuum system is designed to achieve pressures in the ultrahigh vacuum range 10^{-8} torr or better. It consists of a Consolidated PMCU 721 diffusion pump, a foreline trap, and a 5 cubic foot/min mechanical pump. The pump is isolated from the vacuum system by a zeolyte trap which adsorbs any oil vapor which may back diffuse into the system. Dow 705 fluid with a room temperature vapor pressure of 3×10^{-10} torr is used in the diffusion pump.

The zeolyte trap and the rest of the system is built inside a large degassing oven capable of reaching a temperature of 500°C. The vacuum system is made of stainless steel, Pyrex glass and kovar. All joints are sealed with metal gaskets of gold or copper. Both the electromagnet and the transducer mentioned above are mounted outside the balance so that they may be removed during bakeout. The system has been pumped to pressures as low as 2×10^{-9} torr.

3. Vacuum Induction Furnace

The furnace is shown in Fig. 95. It is constructed of 304 stainless steel with a water jacket welded around the body of the furnace. All seams were heliarc welded and all flanges (Varian and Ultek vacuum flanges) are sealed with copper gaskets as are the joints in the rest of the system. There are two observation ports with shutters to eliminate coating of the windows by the evaporating sample. One window is on the side of the furnace permitting the sample to be sighted through the turns of the work coil. The other window (not shown) is on top of the furnace. A high vacuum rotary feedthrough, manufactured by Varian, drives the base of the sample tripod through a beveled gear. This allows the sample to be rotated about its vertical axis.

The latter feature may be used to determine the difference, if any, between effusion of the diboride from a diboride Knudsen cell and evaporation from the sample surface. This difference may be studied in the following way. A diboride cell is made with an effusion orifice near its edge, and screens are placed between the sample and the target. The screens have holes in them which are placed so that they are between the orifice and the target. With the screen aligned over the orifice both molecules from the surface and the orifice strike the target, but the fraction from the surface may be calculated from the earlier measurement of the surface alone.

The furnace also has a six-inch access port on the side and a demountable induction lead feedthrough. The latter, made by Varian, is attached to the system through a four inch port (not shown) and consists of a four-inch, high purity alumina disk sealed to a copper cylinder which is welded to the stainless flange. The radio frequency leads go through two holes in the alumina disk and are sealed with copper gaskets.

4. Degassing Oven

The degassing oven may be seen in the photograph of the equipment (Fig. 96). The oven which is four feet high, five feet wide and three feet deep rolls over and around the equipment on rails. A door swings across the front to completely enclose the system. This oven, capable of reaching 500°C, is heated with strip heaters totaling 22.5 kilowatts. It is controlled by a Chromolux thermostat to $\pm 10^{\circ}$C. The oven has stainless sheet interior, five inches of insulation and aluminum sheet exterior. The bottom of the oven remains stationary around the tube leading from the induction furnace to the diffusion pump located below and outside the degassing oven.

5. Induction Furnace Controls

The sample temperature is maintained constant by fixing the power input to the work coil. This is achieved by attaching a feedback coil to the induction furnace output leads as shown in Fig. 97. The output from the pickup coil, rectified and attenuated is fed to a recorder-controller. Output from the controller is used to regulate the induction furnace through a magnetic amplifier and saturable reactors. Since the output of the generator is recorded, it is possible to determine the constancy of power to the sample. In the experiments on niobium this system maintained the sample temperature above 2000°C to $\pm$ 4°C as determined by optical pyrometer readings. Inasmuch as the temperature is held constant, frequent optical temperature measurements are unnecessary during an experiment.

C. Experimental Results

Measurements have been made on the evaporation rate, melting point and emissivity of niobium. Results have also been obtained on the evaporation rate of boron rich NbB_2 over a range of composition.

1. Niobium Vapor Pressure, Melting Point and Emissivity

A high purity niobium sample furnished by ManLabs* was machined into a cylinder 0.632 cm in diameter and 1.436 cm high. Two blackbody holes, each 0.0089 cm in diameter and 0.4 cm deep were drilled in the side of the sample, one above the other. One hole was approximately 0.4 cm from the top, the other was an equal distance from the bottom. The sample had three small holes drilled in the bottom to facilitate mounting it on the points of a tungsten

*Spectroscopic analysis indicate faint traces of Mg, Si, Fe, Cu, Mo, and Ag.

tripod. The weighed sample was centered inside a half inch diameter, seven-turn work coil. A weighed target consisting of a square quartz frame covered by 1 mil platinum sheet was suspended 5 cm above the sample from one arm of the balance.

After evacuating the system the sample was gradually degassed. During degassing the pressure never exceeded 3×10^{-6} torr. The vacuum level at measurement temperature for evaporation rates was between 1×10^{-7} and 4×10^{-8} torr. In calculating the amount of vapor striking the target, both atoms evaporating from the side and from the top of the sample were considered. The cosine law is assumed to apply, so that the contribution from the side of the sample constituted a small fraction of the total. Atoms striking the water-cooled copper work coil were not reflected to the target. Rather, sharp shadows were observed within the apparatus indicating a niobium condensation coefficient near unity. At the conclusion of this series of experiments the sample and target were weighed on an analytical microbalance to establish the condensation coefficient of niobium vapor on platinum. The ratio of the measured weight gain of the target to that calculated is 0.959. This value seems to be well within the experimental errors involved, which include the deviations from uniform temperatures over the sample surface.

The sample was placed in the apparatus a second time to measure its melting point. The sample was heated gradually to the melting point by increasing the control point on the recorder-controller. During this experiment temperatures of the two blackbody holes and the surface were measured. It was found that the hole nearer the top of the cylinder was 11° higher in temperature than the lower hole. The temperature was increased until the top

hole filled in while the bottom hole remained intact. The sample was held at this temperature for ten minutes during which several readings were made of the bottom hole. The evaporation rate was determined simultaneously. The pressure in the system during the melting point experiment was 1×10^{-6} torr. At the completion of this investigation the window was calibrated for absorption over a wide range of temperatures. The temperature read in the bottom hole was corrected for the eleven degree difference between the two holes and for the window absorption. A new Leeds and Northrup optical pyrometer which had been calibrated by L&N against a Bureau of Standards calibrated lamp was used for all the preceding temperature measurements. Literature values for the melting point of niobium may be compared with results from this study in Table 69. Little agreement between investigators is to be noted.

Table 69

Niobium Melting Point

Authors	Date	Principal Impurities	Melting Point °C
This Research	1963		2414
Riemann & Grant[1] (Stull & Sinke)	1936	0.02% Sn	2498 ± 40
Hansen, et al[2]	1951		2410
Wilhelm, Carlson & Dickenson[3]	1954	0.18% C	2420
Rogers & Atkins[4]	1955	0.5% Ta, 0.25% C	2435
Schofield[5]	1957	1.9% Ta	2468 ± 10
Dushman[5b]			2415

All but one of these melting points are above the temperature found in this research. Riemann and Grant made two measurements of melting point using

niobium wire. The first of these was done by increasing the current through the wire and observing the current at which melting occurred. From their current-temperature plot obtained by using an optical pyrometer and Whitney's value of 0.374 for the emissivity, they obtained a melting point of 2517°C. A second measurement was made in which the temperature of the wire was measured optically just before melting occurred. This time they found 2457°C for the melting point. Giving more weight to the first measurement, they chose 2498°C (or 2770°K) as the melting point.

The relatively high tantalum content (1.9%) in Schofield's sample should result in a higher melting point, although it seems unlikely that this could increase the melting temperature enough to account for the difference between his measurements and those found by most other investigators.

The emissivity of niobium as measured in this research is compared to literature values in Table 70.

Table 70

Emissivity of Niobium

Author	Temp. Range °C	Wave Length Microns	Emissivity
This Research	1700-2400	0.65	0.365
Whitney[6]	1300-2000	0.667	0.374
Smithells[7]	< mp	0.65	0.49

The vapor pressure data are given in Table 71 and plotted in Fig. 98. Values from Riemann and Grant[1], and from Speiser, Blackburn and Johnston[8] are also plotted.

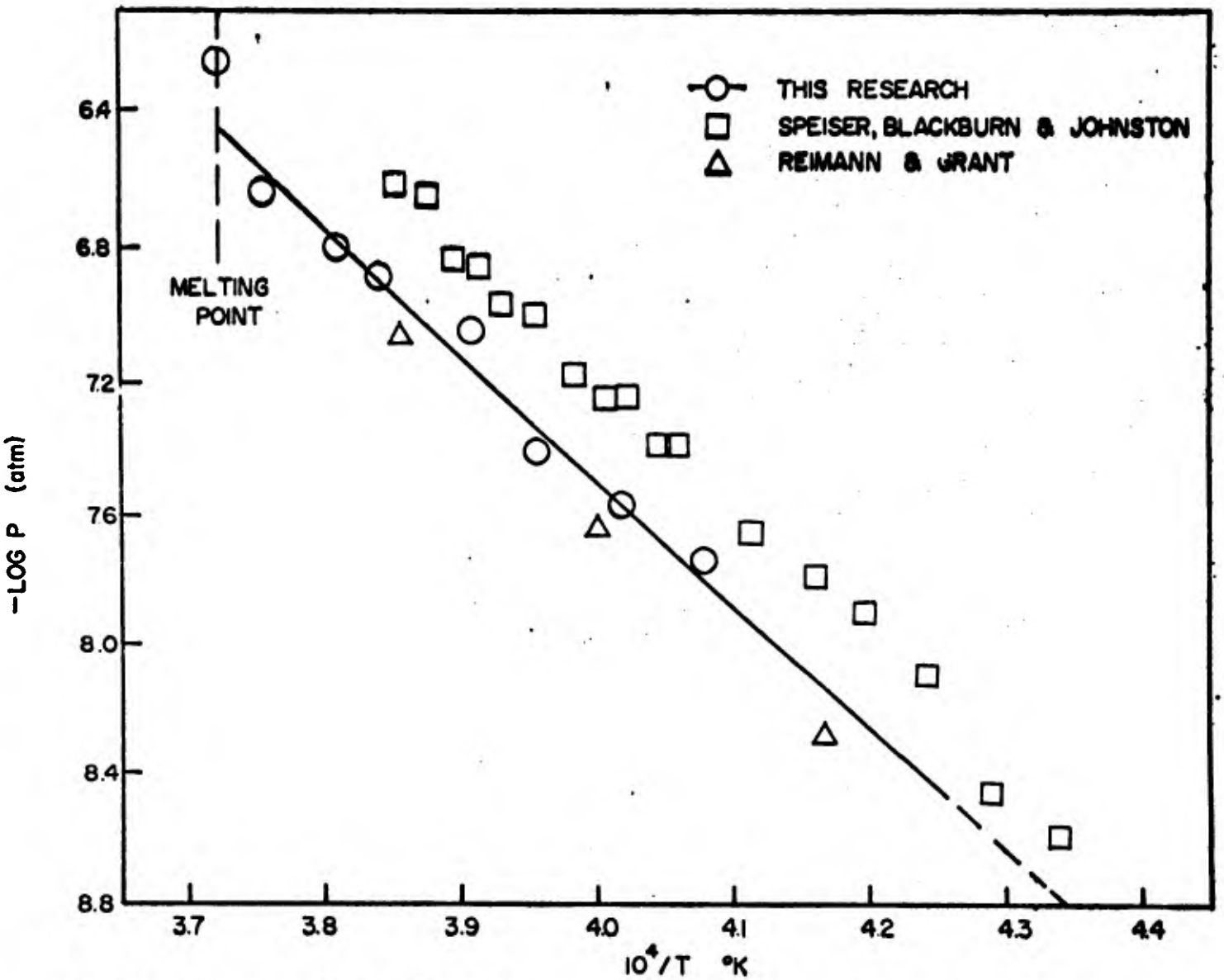

Fig. 98 - Logarithm of the Niobium Pressure in Atmospheres vs, the Reciprocal of the Absolute Temperature

Table 71

The Vapor Pressure of Niobium

Run No.	T, °K	Time, Sec.	Weight gain of target, μg	Rate of Evap. of Nb $g/cm^2/sec \times 10^7$	Pressure atm $\times 10^8$
1	2602	4500	124	10.9	12.7
2	2663	2340	116	19.7	23.1
3	2529	6600	57	3.42	3.92
4	2489	18600	110	2.35	2.66
5	2452	24600	101	1.63	1.83
6	2624	3300	115	13.8	15.5
7	2559	5880	116	7.82	9.0
8	2687	660	78	46.9	55.3

Table 72 gives the thermodynamic functions for niobium using Stull and Sinke's[9] values for the gas and solid. The heat of vaporization, ΔH_{298} = 174.8 kcal/g-atom may be compared to that calculated by Stull and Sinke, from Riemann and Grant,[1] ΔH_{298} = 176.8 kcal/g-atom and to Speiser, Blackburn and Johnston's[8] value, ΔH_{298} = 171.8 kcal/g-atom.

Table 72

Thermodynamic Calculations for Niobium

Run No.	T, °K	-R ln P cal/mole/deg.	$-\Delta$ fef (gas-solid) cal/mole/deg	ΔH_{298}: kcal/g-atom
1	2602	31.56	35.69	175.0
2	2663	30.37	35.68	175.9
3	2529	33.89	35.70	176.0
4	2489	34.66	35.70	175.1
5	2452	35.40	35.71	174.4
6	2624	31.16	35.73	175.5
7	2559	32.24	35.69	173.8
8	2687	28.63	35.68	172.8
				Avg. 174.8 ± 0.8

Speiser, et al. suggested that the difference between their data and that of Riemann and Grant could be due to the fact that the latter authors used emissivities to determine their temperatures. In the present research values for the emissivity were measured in good agreement with those used by Riemann. At 2500°K, Riemann's temperatures would be about 5° lower than those in the present work based on the slight differences in emissivity (see Table 70).

The spread in the heats of vaporization found in the two previous studies and the present one is within that found for many other elements and compounds. Although pressure measurements with a particular set of instruments can be reproduced quite precisely, the agreement between laboratories is rarely this good. The difficulty can be appreciated if one considers the melting points reported for niobium (Table 69). Here a scatter of 88°C. has been found by a number of careful investigators. Sample impurities could account for many of the differences but the samples reported melting at the extremes of the range appear to be very pure. An error in the temperature of 88°C would change the heat of vaporization, ΔH , by about 6 kcal/mole. This is slightly greater than the spread of 5 kcal/mole between the three sets of measurements.

Temperature, however, is only one of the variables. A factor of two in the pressure (lumping the remaining variables) would result in a change of more than 3 kcal/mole in ΔH at the temperatures studied here.

2. Vaporization of Single Phase NbB_2

A boron rich sample of NbB_2 zone refined at Arthur D. Little, Inc. was machined with a spark gap tool. Two blackbody holes (1 mm diameter) were drilled, one above the other in the side of the cylindrical sample. The

sample was 0.68 cm in diameter and 1.85 cm high. A portion of the bar from which this sample was machined was set aside for chemical and X-ray analysis.

After sealing the weighed sample in the furnace the system was pumped to the 10^{-8} torr range and slowly heated to temperature in order to degas it. During the initial heating the pressure rose to the 10^{-6} torr range, but soon dropped to 10^{-7} and 10^{-8} torr. Six measurements were made between 1940 and 2140°K. The chronological activity of boron for these experiments decreased rather sharply. From the shape of the curves (target weight gain vs time) it appeared that the boron evaporation was diffusion limited. Thus, to uniformly distribute the boron in the sample it was annealed for one hour at 1900°K between each successive measurement. The remaining measurements were made between 2100 and 2200°K for periods usually less than 30 minutes.

Since it was thought that the condensation coefficient of boron on the glass target was less than one, both the sample and target were weighed after a number of measurements. The fraction of vapor adhering to the target compared to that striking it was calculated from the geometry of the system, using the cosine law, the sample weight loss, and the target weight gain. This fraction is computed to be 1.078 ± 0.033 indicating that virtually no vaporization from the target occurs. Since targets were replaced frequently, the boron layer forming on them was probably too thin to peel and flake off. The deviation from unity is within experimental error.

Table 73 gives the results of measurements on the single phase diboride sample. Each series corresponds to a set of measurements made without breaking the vacuum. The sample to target distance varied from series to series

Table 73

The Vapor Pressure of Boron Over Single Phase NbB_2

Series*	B/Nb Ratio	T, °K	Time sec.	Weight Gain of Target ug	$p_B^{\eta}[x]$ atm x 10^9
I	2.093	1998	1560	74	55.6
	2.084	2105	600	87	175.0
II	2.061	2068	660	87	162.0
	2.040	2128	786	100	159.0
III	2.020	2134	1314	180	161.0
	2.017	2089	804	68	98.1
	2.014	2097	558	35	73.0
	2.004	2107	552	37	86.8
	1.997	2095	1380	62	52.2
	1.996	2186	558	70	149.0
	1.990	2163	1410	40	33.6
IV	1.982	2171	1860	280	18.4
V	1.971	2102	5400	190	8.58
	1.963	2100	8100	270	8.13
	1.939	2109	4350	230	12.9
	1.922	2128	2850	110	9.48
	1.912	2119	1470	150	2.50
	1.897	2135	4500	100	5.47
	1.896	2133	4650	50	2.64
	1.889	2129	8100	130	3.94
	1.883	2143	4920	150	7.51

*Total sample area = 4.67 cm^2. The percentage of the total vapor adhering to the target varies with the distance to the sample. These percentages determined experimentally are as follows: I, 5.60; II, 5.41; III, 5.79; IV, 5.60; V, 2.76.

resulting in different fractions of vapor adhering to the target. The pressure was calculated from equation (1), where X_B was considered equal to one.

Two sets of chemical analyses at different laboratories were obtained to determine the composition of the sample. A piece cut from the end of the sample yielded the following results: niobium, 83.27%; boron, 15.66%. Since the boron content found was inconsistent with X-ray analysis (indicating only NbB_2 present) a second analysis was sought. Two small metallographic specimens taken from the same bar as the vapor pressure sample were analyzed giving: niobium, 78.3%; boron, 20.9%. These results diverged so much from the earlier analysis that it was necessary to use another approach for establishing the composition.

To calculate composition, data was used from measurements made on the two-phase system NbB_2-Nb_3B_4. Results from these experiments are given in Table 74. Nowotny et al.[10] have measured the lattice parameters as a function of composition for NbB_2 and have established the phase limits as $NbB_{1.90}$ and $NbB_{2.36}$ at 1600°C. Using these authors' lower limit for the diboride, the two phase experiments and single phase measurements, it is possible to establish a composition of $NbB_{1.90}$ for the intersection of the two sets of data. With this fixed point and the sample weight losses, the compositions were computed for all the single phase material. The boron concentrations are tabulated in Table 73. On the basis of Fig. 99, and Table 66 it appears that the reported[10] boron rich limit corresponding to $NbB_{2.36}$ is incorrect and that the true value lies closer to $NbB_{2.08}$.

Table 74

The Vapor Pressure of Boron Over Nb_3B_4-NbB_2

Run	T, °K	Time sec.	Weight Gain of Target μg	Press. of B* atm x 10^8	$\log P_B^n/P_B^o$
1	2285	3600	75	6.41	1.874
2	2266	5940	90	4.62	1.899
3	2296	2400	70	9.00	1.789
4	2288	10320	330	9.85	1.699
5	2279	4800	140	8.96	1.696

*Total sample area is 4.35 cm^2. Weight change of the sample and target showed that 2.48% of the total vapor adheres to the target.

A number of Knudsen vapor pressure studies have been made on boron with a considerable spread in the heat of vaporization. Recently Paule and Margrave[11] measured the vapor pressure by the Langmuir method. They calculated a heat of vaporization of 136.9 kcal/mole. Since the present study was also done by this method it is believed that more consistent results would be obtained if Paul and Margrave's pressures were used to determine the activity of boron than if the Knudsen measurements were used.

Table 75 lists the logarithm of the boron activities normalized to 2150°K. The corrections necessary to convert α_T to α_{2150} were made by using Kaufman's equations (see section XX, Table 76).

$$\text{for } x < 2/3 \qquad \log \alpha = -\frac{36,500}{2.3\,RT} + C_1 = \log p_B^n / p_B^o \tag{3}$$

and

$$\text{for } x > 2/3 \qquad \log \alpha = +\frac{8050}{2.3\,RT} + C_2 = \log p_B^n / p_B^o \tag{4}$$

where C_1 and C_2 are constant at constant x.

Table 75

Boron Activity in NbB_2 at 2150°K

B/Nb Ratio	$-\log a_B = -\log p_B^{\eta}/p_B^{\circ}$
2.093	0.114
2.084	0.384
2.061	0.149
2.040	0.532
2.020	0.569
2.017	0.494
2.014	0.676
2.004	0.772
1.997	0.802
1.996	0.907
1.990	1.450
1.982	1.780
1.971	1.529
1.963	1.536
1.939	1.413
1.922	1.703
1.912	2.209
1.897	2.009
1.896	2.304
1.889	2.095
1.883	1.935
*	2.116
*	2.109
*	2.049
*	1.946
*	1.928

* Boron activity in two-phase region NbB_2-Nb_3B_4 at 2150°K from data in Table 74.

The data in Table 75 are plotted in Fig. 99 where they may be compared to the activity curves predicted by Kaufman:

for $x < 2/3$

$$\ln p_B^{\eta} / p_B^{o} = -\frac{36,500}{RT} + 3 \ln \theta_B^{\eta} \, \theta_B^{-1} + \ln 3x/(2-3x)4^{1/3} \qquad (5)$$

for $x > 2/3$

$$\ln p_B^{\eta} / p_B^{o} = +\frac{8050}{RT} + 3 \ln \theta_B^{\eta} \, \theta_B^{-1} + 2^{-1} \ln \frac{4^{1/3}(3x-2)}{3x} \qquad (6)$$

The derivation of these equations is explained in Section XX. There is good agreement between the measured values and those calculated by Kaufman.

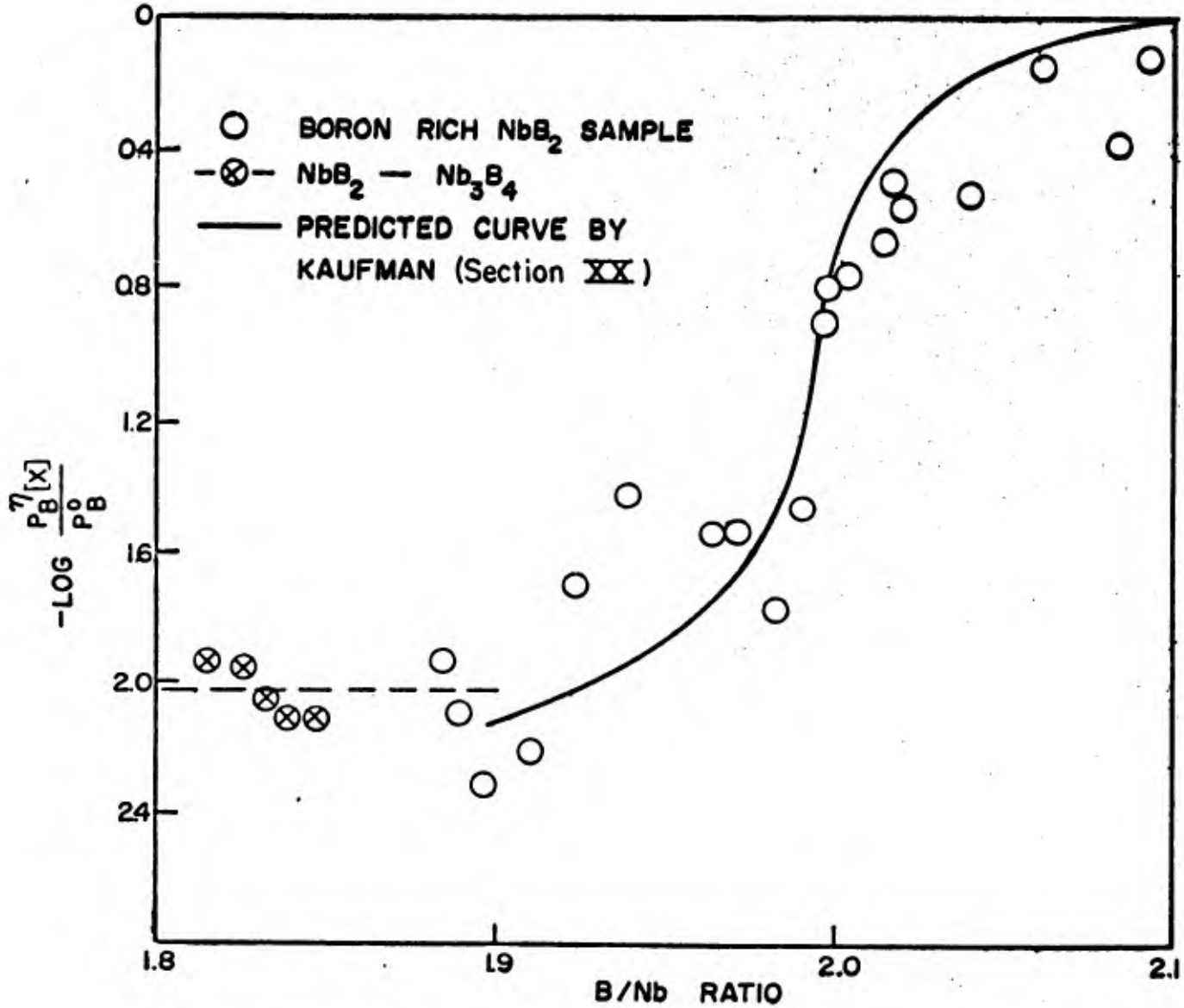

Fig. 99 - Activity of Boron in NbB_2 at 2150°K.

REFERENCES

1. Riemann, L.L. and Grant, C.K., Phil. Mag., (1963) 22 34.

2. Hanson, M., Kamen, E.L., Kessler, H.D. and McPherson, J.D., Trans. AIME, (1951) 191 881.

3. Wilhelm, H.A., Carlson, O.N., and Dickinson, J.M., Trans. AIME, (1954) 200 915.

4. Rogers, B.A., and Atkins, D.F., Trans. AIME, (1955) 203 1034.

5. Schofield, T.H., J. Inst. Metals, (1956-7) 85 372.

5b. Dushman, referred to in 5.

6. Whitney, L.V., Phys. Rev., (1935) 48 458.

7. Smithells, C.J., Metals Reference Book, Vol. II, Butterworths, London, 1955.

8. Speiser, R., Blackburn, P. and Johnston, H.L., J. Electrochem. Soc., (1959) 106 52.

9. Stull, D.R. and Sinke, G.C., Thermodynamic Properties of the Elements, American Chemical Society, Washington, D.C., 1956.

10. Nowotny, N., Benesovsky, F., Rudy, E., and Wittman, Monatshefte für Chemie (1960) 91 975.

11. Paule, R.C. and Margrave, J.L., J. Phys. Chem., (1963) 67 1368.

12. Kaufman, L., Section XX of this report.

XX. THERMODYNAMICS OF STABILITY*

A. Introduction

Sections XV to XVII of this report deal with the integral thermodynamic properties of the diborides such as specific heat, enthalpy, and free energy of formation. This section is concerned with a more detailed consideration of the "shape" of the free energy-composition curve which in effect determines the vapor pressure of both species over the compound and hence, congruency conditions, phase boundaries and several other important properties. The thermodynamic model proposed[1] for a two sublattice compound phase has been specified for the diborides in order to permit calculation of the temperature and compositional dependences of the vapor pressure of metal and boron atoms over the diborides. These calculations although tentative in nature do provide a semi-quantitative assessment of the current state of knowledge of these important properties. In addition they permit calculation of the composition of congruent vaporization of the diborides.

B. Implementation of the Thermodynamic Model

The thermodynamic development[1] consists of an application of the Schottky-Wagner model[2, 3] to a two-sublattice compound where vacancies of both components are the only defects allowed. If the fraction of B and Me sites which are vacant at stoichiometry is small then[1],

$$\Delta F^{\eta}[T, 2/3] = -1/3F_{Me+} - 2/3F_{B+} + RT \ln 4^{1/3}/3\alpha \qquad (1)$$

where $\Delta F^{\eta}[T, 2/3]$ is the free energy of formation of the compound in calories/g.at.

---

*L. Kaufman, ManLabs, Inc.

as a function of temperature at $x=2/3$. In Eq.(1), F_{Me+} and F_{B+} are the free energies of formation of Me and B vacancies in MeB_2^{η}, while $3\alpha/4^{1/3}$ is the fraction of metal and/or boron sites vacant at stoichiometry.

Reference to Sections XVI and XVII of this report indicates that

$$\Delta F^{\eta}[T,2/3] = \Delta H^{\eta}[0^{\circ}K] + RT \ln \theta_{Me}^{\eta} \theta_{Me}^{-1} (\theta_B^{\eta})^2 \theta_B^{-2} - 0.5\gamma^{\eta} T^2 - 1/3\phi_{Me}^{o} - 2/3\phi_B^{o} \quad (2)$$

where γ^{η}, ϕ_{Me}^{o}, ϕ_B^{o} and the appropriate θ's are specified in Table (56) Section XVI.

Analysis[1] of the NaCl type phases TiC, ZrC, TaC, ZrN, TiN, and TiO resulted in values of $-RT \ln \alpha/(1-2\alpha)$ of about 40,000 cal/g.at. for the carbides, 28,000 cal/g.at. for the nitrides, and 8000 cal/g.at. for TiO. A value of 38,000 cal/g.at. was obtained for ZrO_2. From the analysis of the Schissel-Trulson vapor pressure data for TiB_2[4]

$$RT \ln \alpha \simeq -32,000 \text{ cal/g.at.}, \quad (3)$$

$$F_{Ti+}[2300^{\circ}K] \simeq 61,800 \text{ cal/g.at.}, \quad (4)$$

and

$$F_{B+}[2300^{\circ}K] \simeq 35,000 \text{ cal/g.at.} \quad (5)$$

If these values are taken to be representative of all of the diborides then

$$F_{Me+} = -2.5\Delta H^{\eta}[0^{\circ}K] + 26,000 + 3RT \ln \theta_{Me}(\theta_{Me}^{\eta})^{-1} 4^{1/9} 3^{-1/3} + 1.5T^2\gamma^{\eta} + \phi_{Me}^{o} \text{ cal/g.at.} \quad (6)$$

$$F_{B+} = -2.5\Delta H^{\eta}[0^{\circ}K] - 13,000 + 3RT \ln \theta_B(\theta_B^{\eta})^{-1} 4^{1/9} 3^{-1/3} + \phi_B^{o} \text{ cal/g.at.} \quad (7)$$

and

$$RT \ln \alpha \simeq 1.5\Delta H^{\eta}[0^{\circ}K] \text{ cal/g.at.} \quad (8)$$

Combination of Eqs., 6 to 8 above permit explicit calculation of the vapor pressure of metal and boron as a function of temperature and composition over the diborides. This calculation can be performed by using the values tabulated in Sections XVI and XVII of this report along with the relations derived in reference 1. The results are

$$F^{\eta}_{Me} - F^{o}_{Me} = RT \ln p^{\eta}_{Me}[2/3]/p^{o}_{Me} = -F_{Me+} - RT \ln 3\alpha 4^{-1/3} \qquad (9)$$

and

$$F^{\eta}_{B} - F^{o}_{B} = RT \ln p^{\eta}_{B}[2/3]/p^{o}_{B} = -F_{B+} - RT \ln 3\alpha 4^{-1/3} \qquad (10)$$

These equations give the pressure of metal, $p^{\eta}_{Me}[2/3]$, and boron $p^{\eta}_{B}[2/3]$ as a function of temperature for the stoichiometric compound. In these equations, p^{o}_{Me} and p^{o}_{B} are the vapor pressures of pure Me and pure B at the temperature in question.

Numerical calculation of the vapor pressures for $x \neq 2/3$ can be performed when α^2 is much smaller than $(2/3-x)^2$ by using the following equations[1]. For $x < 2/3$.

$$F^{\eta}_{Me} - F^{o}_{Me} = RT \ln p^{\eta}_{Me}[x]/p^{o}_{Me} = -F_{Me+} + RT \ln (2-3x)^2\, 27^{-1}\, \alpha^{-3} (1-x)^{-2} \qquad (11)$$

$$F^{\eta}_{B} - F^{o}_{B} = RT \ln p^{\eta}_{B}[x]/p^{o}_{B} = -F_{B+} + RT \ln x(2-3x)^{-1} \qquad (12)$$

while for $x > 2/3$

$$F^{\eta}_{Me} - F^{o}_{Me} = RT \ln p^{\eta}_{Me}[x]/p^{o}_{Me} = -F_{Me+} + RT \ln 2(1-x)(3x-2)^{-1} \qquad (13)$$

$$F^{\eta}_{B} - F^{o}_{B} = RT \ln p^{\eta}_{B}[x]/p^{o}_{B} = -F_{B+} + 2^{-1} RT \ln 4(3x-2)\, 27^{-1}\, x^{-1}\, \alpha^{-3} \qquad (14)$$

Thus Eqs. (1-14) completely specify the thermodynamic properties. These equations are approximate and some of the parameters may be changed as

more data (i.e., experimental $\Delta H^{\eta}[0^{\circ}K]$ values, see Section XVII) develop. However, for the present they reproduce the information available for the free energy of formation (and its temperature dependence) of the diborides to within 5%. In addition, they reproduce individual vapor pressures of the elemental components over the diborides (presently available) to within a factor of 1.3.

C. Calculation of the Vapor Pressure of the Diborides as a Function of Temperature and Composition

In order to calculate the vapor pressure of both components it is convenient to rearrange Eqs. 9-14 as shown in Table 76. Values for the vapor pressure of the pure elements used in these calculations are given in Table 77, while the values for the other parameters are given in Sections XVI and XVII. Table 78 contains a tabulation of the compositional dependent terms in Eqs. 8 - 14 for convenience in performing the computations. The computed log p-x-T curves for the diborides are shown in Figs. 100 through 104. These curves have been drawn without taking into account the actual phase boundaries of the diboride. Naturally the equilibrium between the diboride with higher and lower borides will limit the compositional range over which these calculated curves apply. Conversely, the curves can be used in the calculation of the phase boundaries of the diborides.

It must also be pointed out rather strenuously that these curves are tentative and although they do represent the best current description of the situation, they are subject to revision as new enthalpy of formation data become available.

Nevertheless a consideration of the general features of these curves provides considerable insight into some of the important thermodynamic features of the compounds under consideration. Examination of Figs. 100 to 104 indicates

Table 76

Approximations for Calculating the Temperature and Compositional Dependence of the Vapor Pressure of Diborides

	$\ln p^{\eta}_{Me}/p^{o}_{Me}$	$\ln p^{\eta}_{B}/p^{o}_{B}$
x less than 2/3 (B/Me less than 2)	$(-26,000 - 2\Delta H^{\eta}[0^{o}K]$ $-1.5\gamma^{\eta}T^{2} - \phi^{o}_{Me})/RT$ $+ 3\ln\theta^{\eta}_{Me}\theta^{-1}_{Me}$ $+ \ln(2-3x)^{2}/9(1-x)^{2}4^{1/3}$	$(+13,000 + 2.5\Delta H^{\eta}[0^{o}K]$ $-\phi^{o}_{B})/RT$ $+ 3\ln\theta^{\eta}_{B}\theta^{-1}_{B}$ $+ \ln 3x/(2-3x)4^{1/3}$
x = 2/3 (B/Me = 2)	$(-26,000 + \Delta H^{\eta}[0^{o}K]$ $-1.5\gamma^{\eta}T^{2} - \phi^{o}_{Me})/RT$ $+ 3\ln\theta^{\eta}_{Me}\theta^{-1}_{Me}$	$(+13,000 + \Delta H^{\eta}[0^{o}K]$ $-\phi^{o}_{B})/RT$ $+ 3\ln\theta^{\eta}_{B}\theta^{-1}_{B}$
x greater than 2/3 (B/Me greater than 2)	$(-26,000 + 2.5\Delta H^{\eta}[0^{o}K]$ $-1.5\gamma^{\eta}T^{2} - \phi^{o}_{Me})/RT$ $+ 3\ln\theta^{\eta}_{Me}\theta^{-1}_{Me}$ $+ \ln 6(1-x)/4^{1/3}(3x-2)$	$(+13,000 + 0.25\Delta H^{\eta}[0^{o}K]$ $-\phi^{o}_{B})/RT$ $+ 3\ln\theta^{\eta}_{B}\theta^{-1}_{B}$ $+ 2^{-1}\ln 4^{1/3}(3x-2)/3x$

Table 7?

Vapor Pressure of the Pure Elements

(Values Tabulated are for, -log p(atm))

$T^{\circ}K$	B*	Ti^{+}	$Zr^{\dagger}$	Nb**	Ta^{++}	$Hf^{\dagger\dagger}$
1000	21.192	16.894	24.376	30.889	33.436	24.667
1200	16.366	12.853	19.112	24.417	26.649	19.378
1400	12.927	9.999	15.379	19.797	21.799	15.602
1600	10.354	7.870	12.585	16.335	18.159	12.771
1800	8.360	6.222	10.415	13.646	15.327	10.575
2000	6.769	4.921	8.683	11.499	13.061	8.817
2200	5.473	3.889	7.284	9.746	11.206	7.382
2400	4.414	3.032	6.148	8.289	9.657	6.217
2600	3.539	2.309	5.188	7.058	8.346	5.246
2800	2.792	1.691	4.366	6.011	7.219	4.412
3000	2.147	1.157	3.655	5.131	6.243	3.692
3200	1.585	0.690	3.033	4.381	5.387	3.062

---

* JANAF 31 December 1960, ΔH_f° = 131.399 kcal/mol. (ref. 5)

\+ JANAF 31 December 1960, ΔH_f° = 111.838 kcal/mol. (ref. 5)

† JANAF 30 June 1961, ΔH_f° = 145.105 kcal/mol. (ref. 5)

** STULL & SINKE 1956, ΔH_f° = 177.500 kcal/mol. (ref. 6)

++ STULL & SINKE 1956, ΔH_f° = 186.800 kcal/mol. (ref. 6)

†† STULL & SINKE 1956, pressure values <u>recalculated</u> using ΔH_f° = 146 kcal/mol. (ref. 7)

Table 78

Numerical Values of Compositional Terms

B/Me	x	$\ln(2-3x)^2/9(1-x)^2 4^{1/3}$	$\ln 3x/4^{1/3}(2-3x)$
1.85	0.649	- 6.44	3.14
1.86	0.650	- 6.56	3.20
1.87	0.652	- 6.80	3.33
1.88	0.653	- 6.92	3.40
1.89	0.654	- 7.14	3.51
1.90	0.655	- 7.23	3.57
1.91	0.656	- 7.40	3.66
1.92	0.658	- 7.82	3.87
1.93	0.659	- 8.05	3.99
1.94	0.660	- 8.32	4.13
1.95	0.661	- 8.64	4.30
1.96	0.662	- 9.02	4.49
1.97	0.663	- 9.50	4.74
1.98	0.664	-10.14	5.06
1.99	0.666	-11.07	5.53

		$\ln 6(1-x)/4^{1/3}(3x-2)$	$2^{-1}\ln 4^{1/3}(3x-2)/3x$
2.01	0.668	5.77	-2.78
2.02	0.669	5.21	-2.60
2.03	0.670	4.87	-2.42
2.04	0.671	4.58	-2.29
2.05	0.672	4.37	-2.19
2.06	0.673	4.20	-2.10
2.07	0.674	4.05	-2.02
2.08	0.675	3.92	-1.97
2.09	0.676	3.80	-1.91
2.10	0.677	3.70	-1.86
2.11	0.678	3.60	-1.81
2.12	0.679	3.51	-1.77
2.13	0.681	3.36	-1.70
2.14	0.682	3.29	-1.67
2.15	0.683	3.22	-1.63

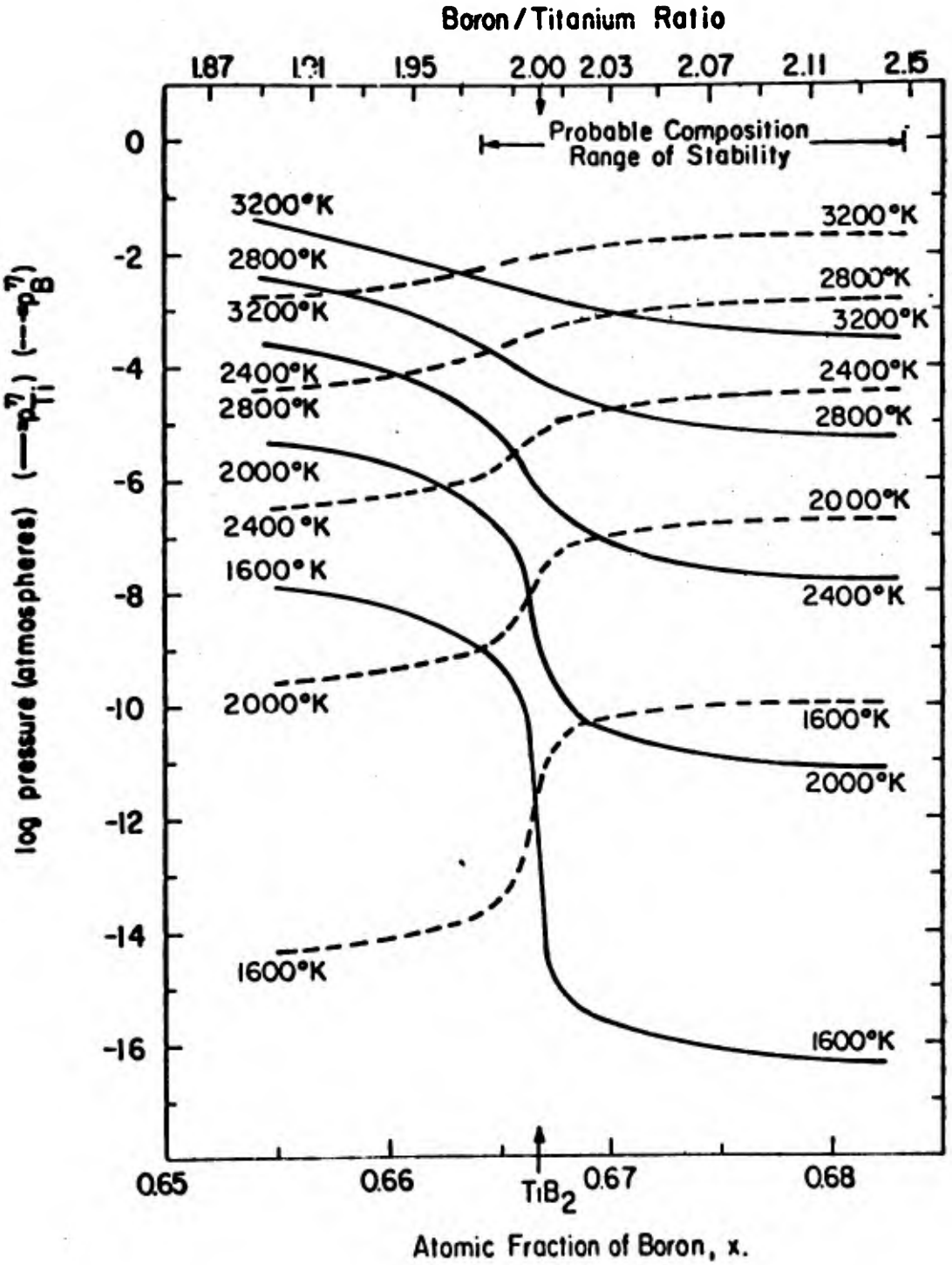

Fig. 100 - Tentative Calculated Vapor Pressure of Titanium (p_{Ti}^{η}) and Boron (p_{B}^{η}) over TiB_2

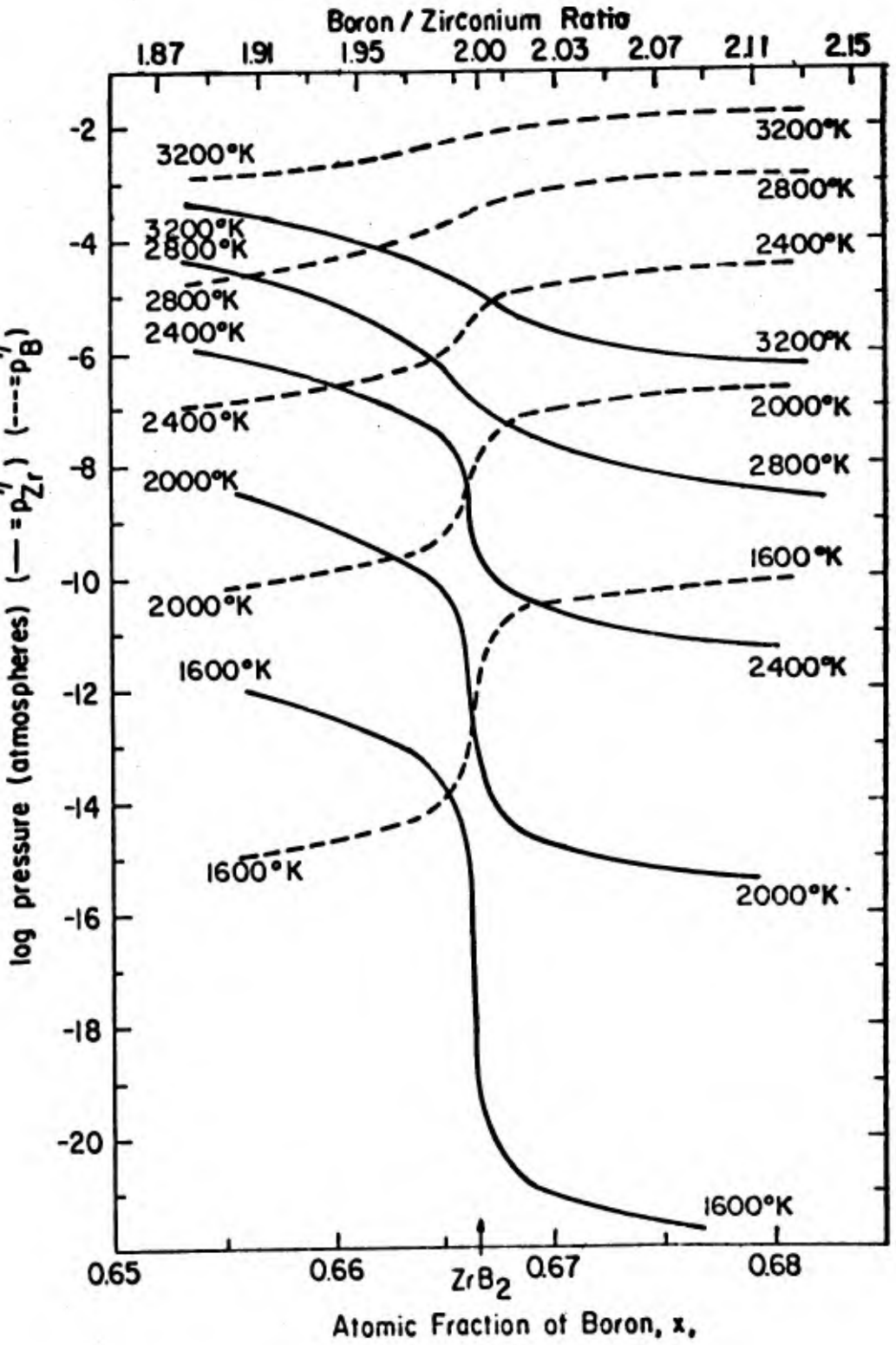

Fig. 101 - Tentative Calculated Vapor Pressure of Zirconium (p_{Zr}^{η}) and Boron (p_B^{η}) over (ZrB_2).

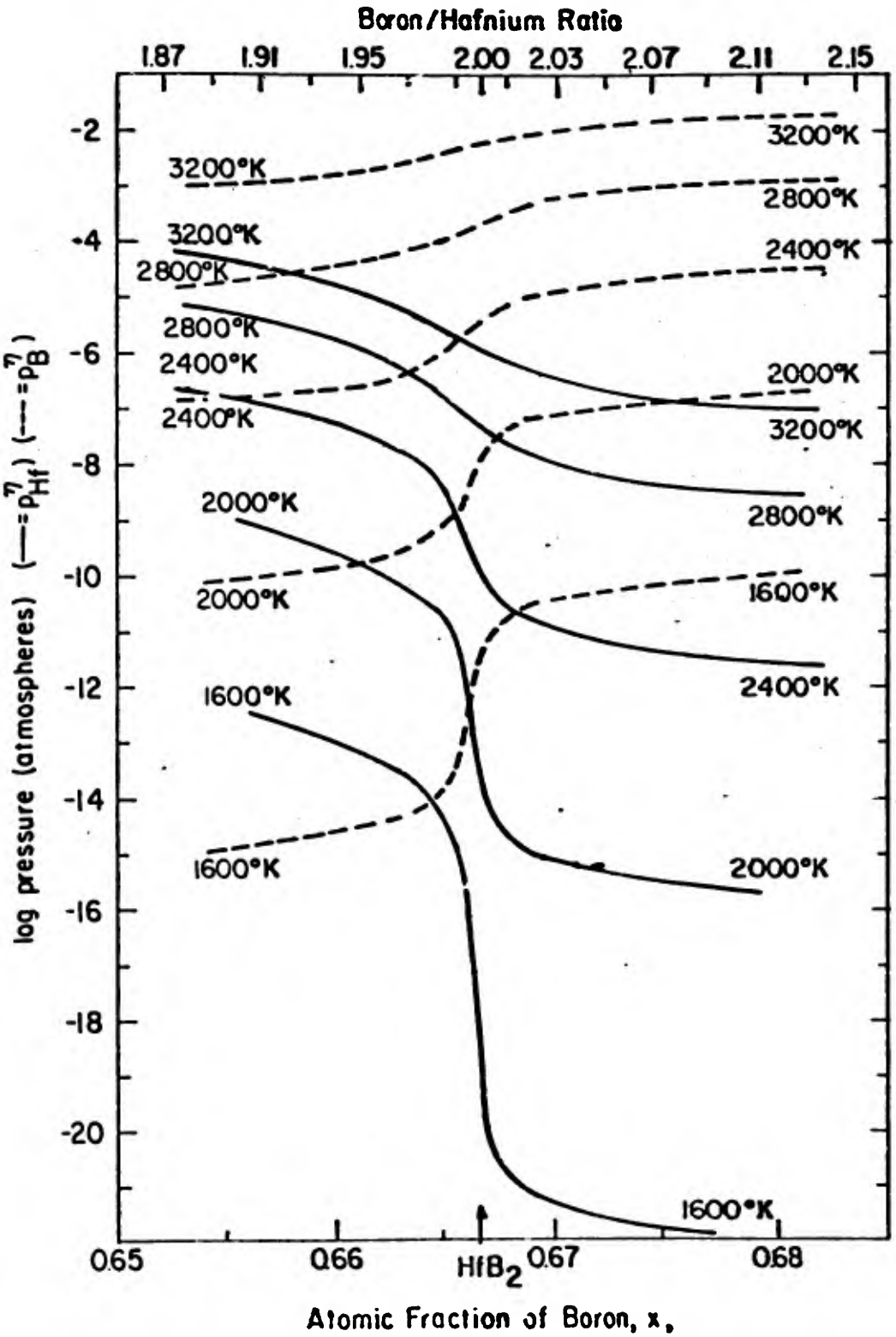

Fig. 102 - Tentative Calculated Vapor Pressure of Hafnium (p^{η}_{Hf}) and Boron (p^{η}_{B}) over HfB_2.

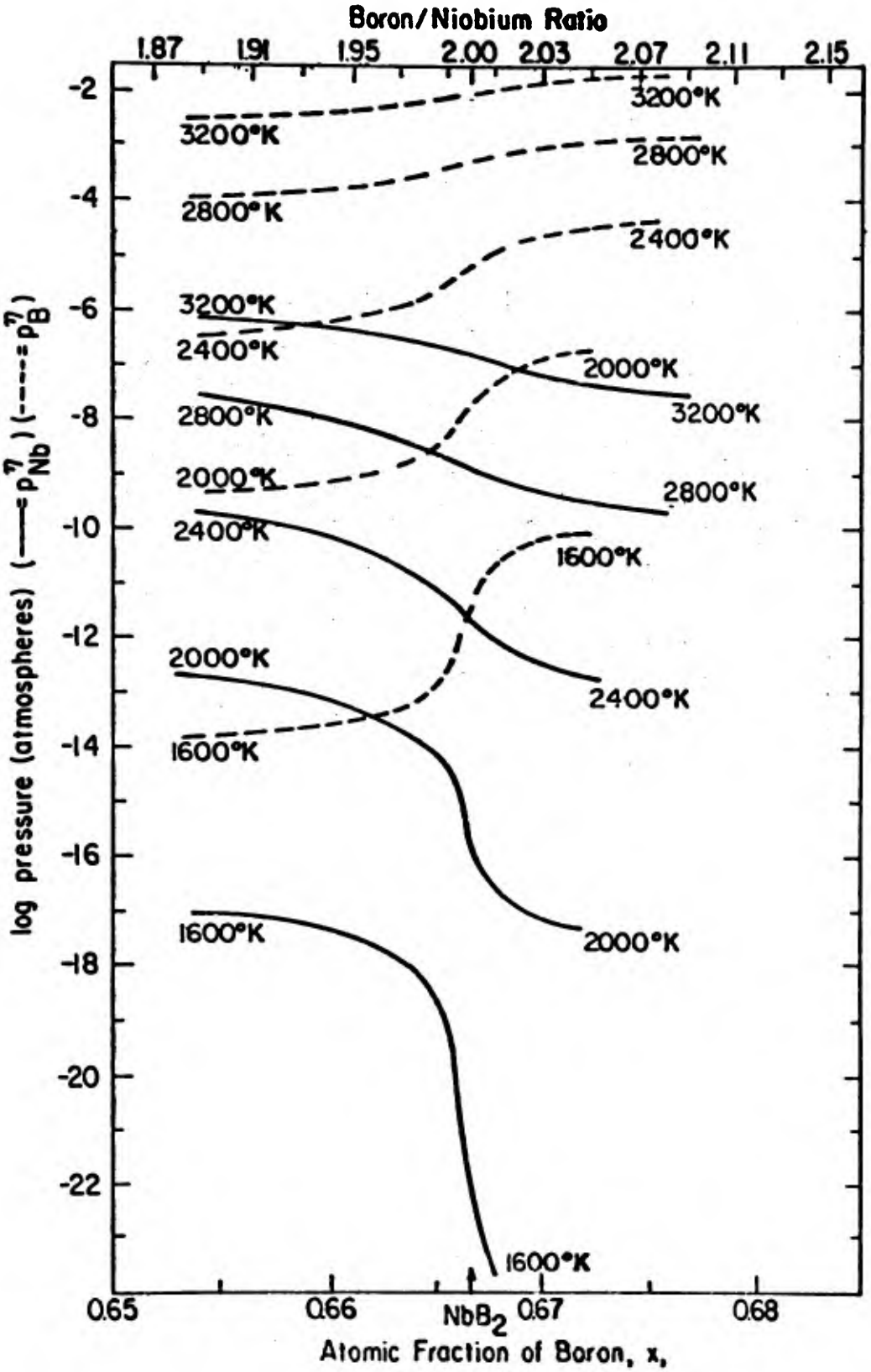

Fig. 103 - Tentative Calculated Vapor Pressure of Niobium (p^{η}_{Nb}) and Boron (p^{η}_{B}) over NbB_2.

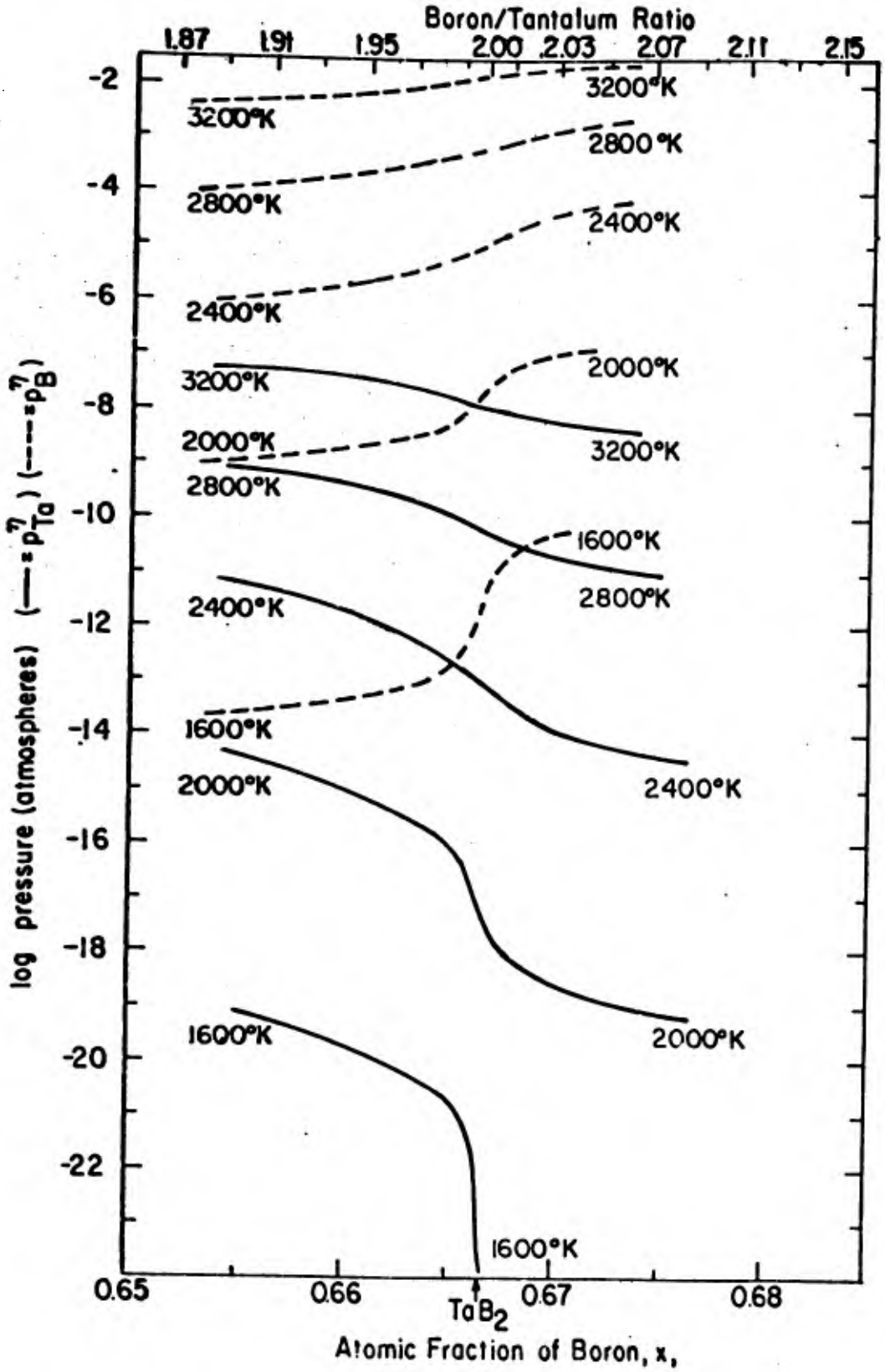

Fig. 104 - Tentative Calculated Vapor Pressure of Tantalum (p_{Ta}^{η}) and Boron (p_B^{η}) over TaB_2.

that the compounds under present consideration fall into three groups i.e., TiB_2, ZrB_2 and HfB_2, and NbB_2 and TaB_2.

Reference to Fig. 100 indicates that over the temperature range $1600^oK \leq T \leq 3200^oK$, the vapor pressure of Ti and B are of comparable magnitudes and that the $p^{\eta}_{Ti}[x]$ and $p^{\eta}_{B}[x]$ curves cross at values of B/Ti less than, but close to 2.00. However, for ZrB_2 and HfB_2, Figs. 101 and 102, the vapor pressure of Me is lower than that of B and although the curves do cross in the range $1600\text{-}2400^oK$, the composition of intersection is farther from 2.00 (on the metal rich side). Moreover, this composition moves farther from 2.00 with increasing temperature until at $2800\text{-}3200^oK$ the curves do not cross. In the case of NbB_2 and TaB_2, Figs. 103 and 104 , the vapor pressure of metal is so much lower than that of boron that there is no crossover. The significance of the crossover is associated with congruent vaporization and will be discussed in detail below.

Apart from the use of these curves in predicting and interpreting congruent vaporization, they can also be used in phase boundary calculations and in designing the best "non-stoichiometric" compositions for oxidation resistance. Now that these curves are available, (albeit tentative) an effort will be made to use them in the abovementioned applications.

It must be re-emphasized that these curves, based on Eqs. 1-14 are tentative and are based on fragmentary data. However, they do represent a complete description of all of the currently available data. As new information becomes availabe, modifications of the assumptions made earlier will undoubtedly be necessary.

D. Calculation of the Composition of Congruent Vaporization

The condition for congruent vaporization is

$$p^{\eta}_{B}[x]/p^{\eta}_{Me}[x] = 2(M_B/M_{Me})^{1/2} \qquad (15)$$

The factor 2 in Eq. 15 should more accurately be replaced by $x/(1-x)$. However for the present considerations, this quantity will be close enough to 2 to make this refinement unnecessary. Eq. 15 shows the significance of the crossover point in Figs. 100 to 104 since the r.h.s. of Eq. 15 varies between $\simeq 1$ for TiB_2 to $\simeq 1/2$ for HfB_2. Eqs. 1 to 14 can be substituted into Eq. 15 to obtain an analytical expression for the congruently vaporizing composition (x_c) which is

$$-3\ln(2-3x_c) = 0.5\ln M_B M_{Me}^{-1} + \ln p^o_{Me}(p^o_B)^{-1} + 3\ln \theta^{\eta}_{Me}\theta^{-1}_{Me}\theta_B(\theta^{\eta}_B)^{-1} - \frac{(39,000 + 4.5\Delta H^{\eta}[0^oK] - \phi^o_B + \phi^o_{Me} - 1.5\gamma^{\eta}T^2)}{RT} \qquad (16)$$

Reference to Figs. 100 to 102 shows that x_c is a function of temperature. Eq. 16 can be used to compute x_c. At 2400°K calculations for TiB_2, ZrB_2 and HfB_2 yield $x_c/1-x_c$ equal to 1.99, 1.92, and 1.89 respectively as compared with values of 1.91 for ZrB_2 reported by Leitnaker*[8] and 1.96 for HfB_2 reported by Krupka[9]. Although the agreement between the calculated and observed values of x_c is not as good as what might be desired, the large temperature dependence of this quantity indicated by Figs. 101 and 102 and Eq. 16 illustrate the difficulties which must be anticipated in attempting to determine x_c experimentally.

Finally, it is worth pointing out a consequence of these calculations that has already been noted experimentally. Reference to Figs. 100 and 101 shows that small changes in composition in the vicinity of the crossover point can yield large changes in the ratio p^{η}_B/p^{η}_{Me}.

---

*On 29 Jan. 1963 at a meeting Symposium on "Preparation and Thermodynamic Properties of the Group IVa Diborides" Jointly sponsored by Arthur D. Little Inc. and ManLabs and held at Acorn Park, Cambridge, Leitnaker indicated that his previously reported value of 1.91 should be revised to 1.97.

REFERENCES

1. Kaufman, L. and Clougherty, E.V., "Thermodynamic Factors Controlling the Stability of Solid Phases at High Temperatures and Pressures" published by A.I.M.E. and Interscience Publishers New York, N.Y. in the book Metallurgy at High Temperatures and Pressures in 1963.

2. Schottky, W. and Wagner, C.; Z. Phys. Chem. (1930) B11 163.

3. Wagner, C.; Thermodynamics of Alloys, Addison-Wesley Cambridge, Mass., (1952) pp. 56-60.

4. Schissel, P.O. and Trulson, O.C., J. Phys. Chem. (1962) 66 1492.

5. JANAF Thermochemical Tables, Dow Chemical Co., Midland, Michigan.

6. Stull, D.R. and Sinke, G.C. Thermodynamic Properties of the Elements, Am. Chem. Soc. #18 Advances in Chemistry Series, Washington, D.C. 1956.

7. Kibler, G.M., Lyons, T.F., Linevsky, M.J., and Desantis, V.J., General Electric Company, Cincinnati, Ohio, WADD, TR-60-466 Part III, Vol. 2 (1963).

8. Leitnaker, J., "Thermodynamic Properties of Refractory Borides," Los Alamos Scientific Laboratory Report #LA-2402 13 April 1960.

9. Krupka, M.C., "High Temperature Vaporization Behavior and Thermodynamic Properties of Hafnium Diboride," Los Alamos Scientific Laboratory Report #LA-2611 16 April 1962.

APPENDIX A

Tables 79 through 90 contain analysis of the materials procured for this program. A full description of the suppliers providing these materials is as follows:

U. S. Borax Research Corp. - New Products Division
412 Crescent Way,
Anaheim, California
Attn: Mr. Grover Collins

Kawecki Chemical Company
220 East 42nd Street
New York 17, N. Y.
Attn: Mr. Michael C. Weston

Millmaster Chemical Corporation
99 Park Avenue
New York 16, N.Y.
Attn: Mr. George F. Smith

Wah Chang Corporation
100 Church Street
New York 7, N. Y.

Table 79

Preliminary Analysis of U. S. Borax TiB_2 (#1)

(Jarrell Ash Co., Newtonville, Mass.)

Na	0.001%
Mg	0.001%
Al	0.001-0.01%
Si	0.001%
Ca	0.001-0.01%
Cr	0.001%
Mn	0.001%
Fe	0.01-1%
Co	0.01-1%
Ni	0.001%
Cu	0.001-0.01%

The following elements were not detected:

Li, Be, K, V, Zn, Ga, Ge, As, Rb, Sr, Y, Zr, Nb, Mo, Ru, Rh, Pd, Ag, Cd, In, Sn, Sb, Te, Cs, Ba, La, Ce, Pr, Nd, Sm, Eu, Gd, Tb, Dy, Ho, Er, Tm, Yb, Lu, Hf, Ta, W, Re, Os, Ir, Pt, Au, Hg, Tl, Pb, Bi, Th, U.

Table 80

Chemical Analysis of U.S. Borax TiB_2 (#1), w/o
(LeDoux and Co., Teaneck, New Jersey)

	Sample #F	Sample #G	Sample F*
Ti	68.61	68.50	68.94
B	31.17	30.85	30.88
C	0.094	0.099	0.11
Fe	0.10	0.09	0.11
O	0.43	0.43	0.46
N	0.073	0.066	0.058
Total	100.47	100.25	100.56
Ti+B	99.78	99.35	99.82
B/Ti	2.003	1.99	1.985

Quantitative Spectrographic Analysis, w/o
(LeDoux and Co., Teaneck, New Jersey)

	Sample F*
Al	0.005
Cr	0.001
Cu	0.001
Fe	0.11
Mg	0.001
Mn	0.002
Si	0.005
V	0.01
Zr	0.001
K	0.001

Sample F was taken from the same batch as samples F and G.

Table 81

Preliminary Analysis of Millmaster TiB_2 (#2)

(Jarrell Ash Co., Newtonville, Mass.

The following elements were detected at the indicated impurity levels (weight percent):

0.1	Cr, Fe, Co
0.01	Si, Ni
0.001-0.01	Mg, Al, Mo
0.001	Cu, Ge, Sn
0.001	Mn, Ag, Cd

The following elements were not detected: Li, Be, Na, K, Ca, V, Zn, Ga, As, Rb, Sr, Y, Zr, Nb, Ru, Rh, Pd, In, Sb, Te, Cs, Ba, La, Ce, Pr, Nd, Sm, Eu, Gd, Tb, Dy, Ho, Er, Tm, Yb, Lu, Hf, Ta, W, Re, Os, Ir, Pt, Au, Hg, Tl, Pb, Bi, Th, V.

Table 82

Chemical Analysis of Millmaster TiB_2 (#2)

(Donald Gurnsey, Metallurgy Dept., M.I.T.)

Element	w/o
Ti	69.0
B	30.0
C	0.10
O	0.06
N	0.18
Fe	0.06
Total	100.00

Boron to Metal Atomic Ratio: 1.965

(National Spectrographic Laboratories, Inc. 6300 Euclid Avenue, Cleveland 3, Ohio)

Element	w/o
Ti	68.71
B	30.96
N	0.02
C	0.13
O	0.15

Boron to Metal Atomic Ratio: 1.997

Table 83

Preliminary Analysis of U.S. Borax ZrB_2 (#1)

(Jarrell Ash Co., Newtonville, Mass.)

Be	0.001%	Cd	0.001%
Na	0.001-0.01%	Sn	0.001-0.01%
Mg	0.001-0.01%	Hf	0.001-0.01%
Al	0.001-0.1%	The following elements were not	
Si	0.001-0.1%	detected (i.e. below 0.0001%):	
Ca	0.01-1%	Li, K, V, Zn, Ga, Ge, As, Rb,	
Ti	0.001-0.1%	Sr, Y, Ru, Rh, Pd, In, Sb, Te,	
Cr	0.01-1%	Cs, Ba, La, Ce, Pr, Nb, Sm,	
Mn	0.001%	Eu, Gd, Tb, Dy, Ho, Er, Tm,	
Fe	0.01-0.1%	Yb, Lu, Ta, W, Re, Os, Ir, Pt,	
Co	0.001-0.01%	Au, Hg, Tl, Pb, Bi, Th, U.	
Ni	0.001-0.1%		
Cu	0.001-0.1%		
Nb	0.001%		
Mo	0.001%		
Ag	0.0001-0.001%		

Table 84

Chemical Analyses of U. S. Borax ZrB_2 (#1), $^{w}/_{o}$

(LeDoux and Co., Teaneck, New Jersey)

	Sample #1	Sample #2	Sample #3
Zr	80.42	80.56	81.04
B	18.01	17.87	18,27
C	0.35	0.34	0.31
N	0.20	0.20	0.17
O	0.52	0.52	0.55
Fe	0.048	0.051	0.04
Total	99.548	99.541	100.38
B+Zr	98.43	98.43	99.31
B/Zr	1.889	1.871	1.902

(Note: Hf = 0.01 - 0.001%)

Quantitative Spectrographic Analysis ($^{w}/_{o}$)

(LeDoux and Co., Teaneck, New Jersey)

	Sample #3
Co	0.001
Cr	0.007
Cu	0.001
Fe	0.04
Mg	0.002
Mn	0.001
Mo	0.01
Ni	0.005
Si	0.001
Ti	0.05
V	0.001

Table 85

Preliminary Analysis of Kawecki TaB_2 (#1)
(Jarrell Ash Co., Newtonville, Mass.)

>10%: Ta, B

0.1%: Fe

0.01 - 0.1%: Al, Ni

0.001 - 0.01%: Mg, Si, Ca, Ti, Mn, Zr, Cu,

The following elements were not detected: Li, Be, Na, K, V, Cr, Co, Zn, Ga, Ge, As, Rb, Sr, Y, Nb, Mo, Ru, Rh, Pd, Ag, Cd, In, Sb, Sn, Te, Cs, Ba, La, Ce, Pr, Nd, Sm, Eu, Gd, Tb, Dy, Ho, Er, Tm, Yb, Lu, Hf, W, Re, Os, Ir, Pt, Au, Hg, Tl, Pb, Bi, Th, U.

Table 86

Chemical Analysis of Kawecki TaB_2 (#1), w/o

Element	(Donald Gurnsey, Metallurgy Dept., M.I.T.) Sample A	Sample B	(LeDoux and Co., Teaneck, New Jersey) Sample B	Sample C
Ta	89.4	89.3	88.31	88.19
B	10.38	10.35	10.38	10.25
C	0.36	0.34	0.38	0.36
N	0.01[illegible]	0.013	0.0064	0.0038
O	0.55	0.52	0.83	0.83
Fe	0.12	0.11	0.13*	0.09*
Total	100.83	100.63	100.04	99.72
Boron to Metal Atomic Ratio	1.942		1.967	

Quantitative Spectrographic Analysis (w/o)

(LeDoux and Co., Teaneck, New Jersey)

Element	Sample B	Sample C
Al	0.005	0.005
Ca	0.01	0.01
Cr	0.01	0.01
Fe	0.13	0.09
Mg	0.007	0.005
Mo	0.01	0.01
Na	0.001	0.001
Nb	0.25	0.19
Ni	0.01	0.01
Si	0.003	0.003
Ti	0.005	0.005
V	0.001	0.001
Zr	0.08	0.06
K	0.001	0.001

*Analyzed by quantitative spectrographic technique.

Table 87

Preliminary Analysis of Wah Chang HfB_2 (#1)
(Jarrell Ash Co., Newtonville, Mass.)

The following elements were detected at the indicated impurity level (weight percent):

Fe	0.1%
Al	0.001-0.01%
Ti	0.001-0.01%
Mn	0.001-0.01%
Cu	0.001%
Mg	0.001%
Cr	0.001%
Si	<0.0001%

The following elements were not detected:

Li, Be, Na, K, C, V, Co, Ni, Zn, Ga, Ge, As, Rb, Sr, Y, Zr, Nb, Mo, Ru, Rh, Pd, Ag, Cd, In, Sn, Sb, Te, Cs, Ce, Ba, La, Pr, Nd, Sm, Eu, Gd, Tb, Dy, Ho, Er, Tm, Yb, Lu, Ta, W, Re, Os, Ir, Pt, Au, Hg, Tl, Pb, Bi, Th, U.

Table 88

Chemical Analysis of Wah Chang HfB_2 (#1)
(Analysis by Donald Gurnsey, Metallurgical Dept., M.I.T.)

Element	w/o	
Hf	89.0	(Duplicate)
B	10.6	(Triplicate)
N	0.017	
C	0.14	
Fe	0.083	
O	0.10	
Total	99.84	

Boron to Metal Atomic Ratio 1.967

Table 89

Preliminary Analysis of U.S. Borax NbB_2 (#2)
(Jarrell Ash Co., Newtonville, Mass.)

The following elements were detected at the indicated impurity levels (weight percent):

0.1	- Fe, Ti
0.01 - 0.10	- Al, Si, Cr
0.01	- Ni, Mg
0.001 - 0.01	- Sn, Ag, Cu
0.001	- Ge, Mn
<0.001	- Be

The following elements were not detected:

Li, Na, K, Ca, V, Co, Zn, Ga, As, Rb, Sr, Y, Zr, Mo, Ru, Rh, Pd, Cd, In, Sb, Te, Cs, Ba, La, Ce, Pr, Nd, Sm, Eu, Gd, Tb, Dy, Ho, Er, Tm, Yb, Lu, Hf, Ta, W, Re, Os, Ir, Pt, Au, Hg, Tl, Pb, Bi, Th, U.

Table 90

Chemical Analysis of U.S. Borax NbB_2 (#2)
(Donald Gurnsey, Metallurgy Dept., M.I.T.)

Element	w/o
Nb	80.75
B	18.6
N	0.05
O	0.11
Fe	0.10
C	0.09
Total	99.70

Boron to Metal Atomic Ratio: 1.987

(National Spectrographic Laboratories, Inc.,
6300 Euclid Avenue, Cleveland 3, Ohio)

Element	w/o
Nb	80.85
B	18.77
N	0.013
C	0.12

Boron to Metal Atomic Ratio: 1.995

UNCLASSIFIED